Exoplanetary Systems Dynamics

Virginie Faramaz

UNIVERSITÉ DE GRENOBLE

THÈSE

Pour obtenir le grade de

DOCTEUR DE L'UNIVERSITÉ DE GRENOBLE

Spécialité : **Astronomie & Astrophysique**

Arrêté ministériel : du 7 Août 2006

Présentée par

Virginie FARAMAZ

Thèse dirigée par **Hervé BEUST**
et codirigée par **Jean-Charles AUGEREAU**

préparée au sein **l'Institut de Planétologie et d'Astrophysique de Grenoble**
et de **l'École doctorale de Physique de Grenoble**

Dynamique des systèmes exoplanétaires

Thèse soutenue publiquement le **16 Octobre 2014**,
devant le jury composé de :

M. Jonathan FERREIRA
Professeur UJF, IPAG, Président
M. Sean RAYMOND
CR1, Laboratoire d'Astrophysique de Bordeaux, Rapporteur
M. Karl STAPELFELDT
Chargé de recherche, GSFC-NASA, Rapporteur
M. Alain LECAVELIER DES ETANGS
Directeur de recherche, Institut d'Astrophysique de Paris, Examinateur
M. Carlos EIROA
Professeur adjoint, Universidad Autónoma de Madrid, Examinateur
M. Hervé BEUST
Astronome, IPAG, Directeur de thèse
M. Jean-Charles AUGEREAU
Astronome adjoint, IPAG, Co-Directeur de thèse

Ecole doctorale de Physique de Grenoble – Université Joseph Fourier

PhD dissertation in Astronomy & Astrophysics

Exoplanetary Systems Dynamics

by

Virginie FARAMAZ

Defended on October 16$^{\text{th}}$, 2014

PhD Degree prepared at Institut de Planétologie et d'Astrophysique de Grenoble

Résumé

Au moins 20% des étoiles de la séquence principale abritent des disques de débris, analogues à la ceinture de Kuiper. Ces disques sont la preuve que l'accumulation de solides a au moins permis la formation de corps de taille kilométrique. Il n'est donc pas surprenant que plusieurs de ces disques soient accompagnés de planètes, qui, en laissant leur empreinte dynamique sur la structure spatiale de ces disques, révèlent leur présence. Par conséquent, la détection d'un disque de débris excentrique entourant ζ^2 Ret par le télescope spatial *Herschel* indique la présence d'un perturbateur massif dans ce système. ζ^2 Ret étant un système mature, âgé de 2-3 Gyr, et en ce sens, analogue à notre propre système solaire, il offre un exemple différent d'évolution dynamique à long terme. Cette thèse comprend une modélisation détaillée de la structure du disque de débris de ζ^2 Ret, ce qui conduit à des contraintes sur la masse et l'orbite du perturbateur suspecté. Cette étude révèle également que les structures excentriques dans les disques de débris peuvent survivre sur des échelles de temps Gyr.

La modélisation de disques de débris peut permettre la découverte postérieure de planètes comme c'est le cas pour le système de Fomalhaut. La forme excentrique de son disque de débris fut d'abord attribuée à Fom b, un compagnon détecté près du bord interne du disque, mais qui se révèle finalement trop excentrique ($e \sim 0.6 - 0.9$) pour lui donner sa forme, indiquant la présence d'un autre corps massif, Fom c. Le système planétaire qui en résulte est très instable, ce qui implique une diffusion récente de Fom b sur son orbite actuelle, éventuellement par Fom c. L'étude de ce scénario révèle qu'en ayant résidé dans une résonance de moyen-mouvement interne avec une Fom c excentrique et de masse comparable à Neptune ou Saturne, Fom b aurait subi une augmentation progressive de son excentricité sur des périodes comparables à l'âge du système ($\sim 440\,\mathrm{Myr}$), ce qui l'aurait amenée assez proche de Fom c pour subir une diffusion récente, qui, complétée par une évolution séculaire avec Fom c, explique sa configuration orbitale actuelle. Ce mécanisme en trois étapes pourrait également avoir généré d'importantes quantités de matériel en orbites très excentriques, ce qui en retour pourrait alimenter en poussière les parties internes du système. Par conséquent, ce mécanisme pourrait aussi expliquer la présence de ceintures de poussières internes dans le système de Fomalhaut, mais aussi la découverte d'une importante population de ceintures de poussières chaudes et massives dans les systèmes âgés de plus de 100 Myr.

Les systèmes planétaires découverts jusqu'ici présentent une grande variété d'architectures, et notre système solaire est loin d'être un modèle générique. Un des principaux mécanismes déterminant la morphologie d'un système planétaire est la migration planétaire. On attend d'un compagnon stellaire - ce que notre système solaire ne possède pas - qu'il affecte les conditions de migration planétaire, et conduise potentiellement à la formation de systèmes planétaires très différents. Ce phénomène est évidemment non négligeable puisque les systèmes binaires représentent au moins la moitié des systèmes stellaires. Dans les systèmes planétaires matures, la migration planétaire peut se produire suite à l'interaction avec le matériel solide et l'impact de la binarité sur cette migration tardive est exploré dans cette thèse. Un compagnon circumstellaire pourrait inverser la tendance à la migration interne des planètes dans les systèmes stellaires simples, et rapprocher ces planètes des régions perturbées par le compagnon binaire, où elles ne pourraient pas s'être formées in situ. Cela pourrait fournir une explication à la détection de planètes qui présentent des signes de migration externe dans les systèmes binaires de faible séparation.

Abstract

At least 20% of Main-Sequence stars are known to harbor debris disks analogs to the Kuiper Belt. These disks are proof that the accretion of solids has permitted the formation of at least km-sized bodies. It is thus not surprising that several of these disks are accompanied by planets, which may reveal themselves by setting their dynamical imprints on the spatial structure of debris disks. Therefore, the detection of an eccentric debris disk surrounding ζ^2 Ret by the *Herschel* space telescope provides evidence for the presence of a massive perturber in this system. ζ^2 Ret being a mature Gyr-old system, and in that sense, analogous to our own Solar System, it offers a different example of long-term dynamical evolution. This thesis includes a detailed modelling of the structure of the debris disk of ζ^2 Ret, which leads to constraints on the mass and orbital characteristics of the putative perturber. This study also reveals that eccentric structures in debris disks can survive on Gyr timescales.

Detailed modelling of the structure of debris disks can allow the posterior discovery of hidden planets as is the case for the Fomalhaut system. The eccentric shape of the debris disk observed around this star was first attributed to Fom b, a companion detected near the belt inner-edge, which revealed to be highly eccentric ($e \sim 0.6-0.9$), and thus very unlikely shaping the belt. This hints at the presence of another massive body in this system, Fom c, which drives the debris disk shape. The resulting planetary system is highly unstable, which involves a recent scattering of Fom b on its current orbit, potentially with the yet undetected Fom c. This scenario is investigated in this thesis and its study reveals that by having resided in inner mean-motion resonance with a Neptune or Saturn-mass belt-shaping eccentric Fom c and therefore have suffered a gradual resonant eccentricity increase on timescales comparable to the age of the system ($\sim$ 440 Myr), Fom b could have been brought close enough to Fom c and suffered a recent scattering event, which, complemented by a secular evolution with Fom c, explains its current orbital configuration. This three-step scenario also implies that significant amounts of material may have been set on extremely eccentric orbits such as this of Fom b through this mechanism, which in return could feed in dust the inner parts of the system. Therefore, this mechanism may also explain the presence of inner dust belts in the Fomalhaut system, but also the discovery a significant population of very bright hot dust belts in systems older than 100 Myr.

The planetary systems discovered so far exhibit a great variety of architectures, and our solar system is far from being a generic model. One of the main mechanism that determines a planetary system morphology is planetary migration. The presence of a stellar binary companion - which our solar system is deprived of - is expected to affect planetary migration conditions, and potentially lead to the formation of very different planetary systems. This phenomenon is obviously non-negligible since binary systems represent at least half of stellar systems. At late stages of planetary systems evolution, planetary migration may occur as the result of interactions with remaining solid planetesimals and the impact of binarity on this planetesimal-driven migration is explored in this thesis. A stellar binary companion may in fact reverse the tendency for planets in single star systems to migrate inwards, and bring them closer to regions perturbed by the binary companion, where they could not have formed in situ. This may give an explanation for the detection of planets which present signs of outward migration in close binary systems.

Contents

Chapter 1

Context and thesis outline

Contents

> "I would answer to Blaise Pascal, who said that the eternal silence of infinite spaces were frightening him, that it is exactly the eternity of space that has allowed the molecular complexity we are made of... We are the children of eternal silences and infinite spaces."
>
> Alexandre Astier, *La physique quantique.*

1.1 Introduction

More than a thousand exoplanets are known as I am currently writing this thesis [1]. I will not make here any attempt to give a precise number. It is indeed constantly increasing, at such point that it can change within a Master students lecture. I had just begun this thesis when a team of my home lab, Bonfils et al. (2013), published the results of a statistical study on the presence of "Super-Earths" in the habitable zone around the Red Dwarves, which are the most common stars in our Galaxy ($\sim 80-85\,\%$ of stars). Their conclusion was spectacular: our Galaxy would house tens of billions of them. A little less than twenty years ago, the only known planetary system was the Solar System. The term "Super-Earth" did not even exist.

Would we have to say that planetary formation is in fact nothing more than a banality? Certainly not! It is actually amazingly diverse. The first exoplanets were detected around the pulsar PSR 1257 +12, that is, a star at the end of its life, and which has left the Main Sequence of stellar evolution (Wolszczan & Frail 1992). However, it was not believed that planets could survive the death of their host star, because this one explodes into a supernova, which generates a gigantic shockwave that passes through the planetary system. For this reason, these planets are now considered as second generation planets, which would have formed from remnants after the explosion of the star (Hamilton & Miller 2001).

[1] See `www.exoplanets.org`

The first exoplanet around a main-sequence star was discovered in 1995 (Mayor & Queloz 1995). It was also surprising : 51 Peg b is a Jupiter-like giant planet, which orbital period is only four days. It therefore orbits very close to its star, precisely where the materials necessary for its solid core to assemble are sublimated, and where this planet could in fact not have formed. This indicates that it has formed further out from the star, and then migrated inwards. Such migration had in fact been predicted by Ward (1986), and 51 Peg b brought in a confirmation. Many other so-called "hot" planets have been discovered since, and this is in fact not surprising because most techniques used to detect exoplanets are biased towards massive planets and planets which are close to their star. Many technical advances have been and remain to be made to broaden the spectrum of masses and planetary distances accessible to instruments, and thus obtain a more complete picture of the composition of planetary systems.

It is fascinating to see how the inventory of planetary systems has grown in nearly two decades. Their typology is complex: a wide range of masses and sizes, planets very close to or, on the opposite, very far from their star, sometimes even lonely and adrift, planets orbiting their stars retrogradly, that is, in the direction opposite to the rotation of the star. More specifically, eccentric exoplanets appear to be much more common than expected (see Figure 1.1). This is in contrast with our Solar System, so familiarly consistent: terrestrial planets in the inner parts, giant planets in the outer parts, neatly separated by the asteroid belt, nearly all contained in the same plane with prograde and almost circular orbits (see Figure 1.2).

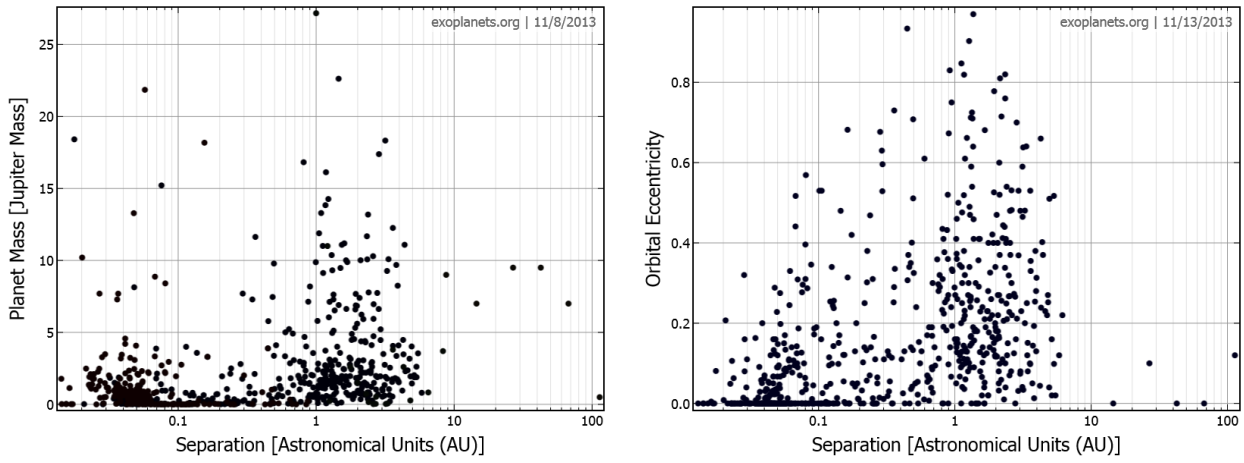

(a) Separation-mass diagram

(b) Separation-eccentricity diagram

Figure 1.1 – Diversity of known exoplanets. *Source: www. exoplanets. org*

However, the contrast is not total, and despite the diversity of the detected systems, it is now clear that the formation of a planetary system is a robust mechanism underpinned by some generic principles, which were first suggested by the study of our own Solar System. The idea that planetary systems form in a disk of gas and dust rotating around a star, now called protoplanetary disk, and within which the material accretes to give birth to planets, dates back to the XVIII $^{\text{th}}$ century, with the models of Swedenborg (1734), Kant (1755) and Laplace (1796).

The development of this hypothesis over time eventually led to the current model of planetary systems formation: the gradual accretion of solids leads to the formation of so-called proto-planetary cores of a few Earth masses, which, according to their position in the system and their ability to accrete the gaseous material of the disk will give rise to terrestrial planets, icy planets or gas giants. These ones could also be the result of an instability in the protoplanetary disk, in the same way an instability in a molecular cloud causes it to collapse and leads to the formation of a star, although at a larger scale (See, e. g., Armitage 2010).

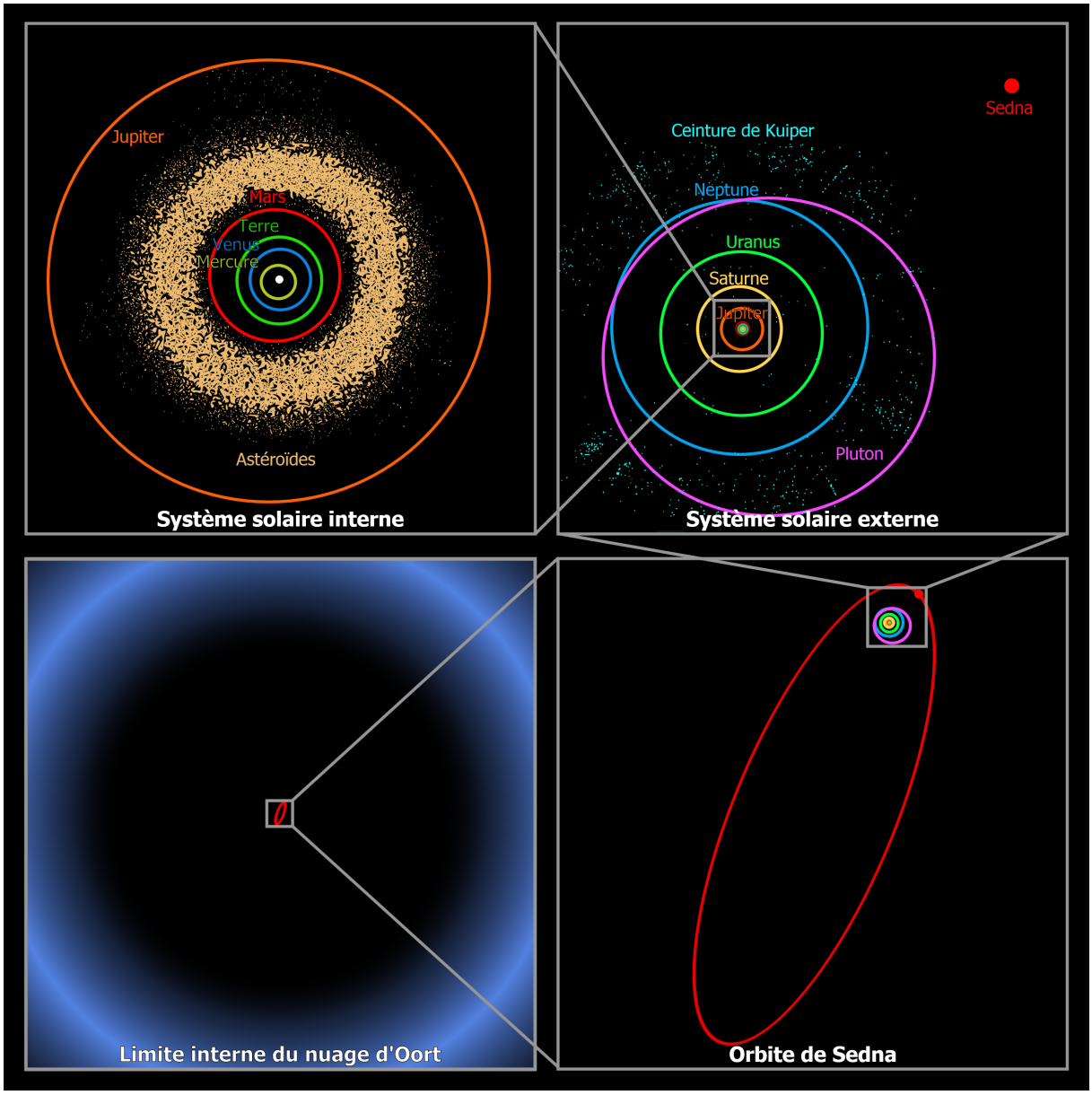

Figure 1.2 – The Solar System, a first model: planets on quasi-circular orbits, and almost all contained in the same plane, along with solids remnants that are the Main Asteroid and Kuiper Belts. *Courtesy of NASA/JPL-Caltech/R. Hurt*

With such a model, it is obvious that the system once formed is similar to ours : since the planets are all born in the same rotating disk around the star, it can be expected that, as in our Solar System, they are more or less all contained in the same plane, and that their orbits are almost circular and prograde. In fact, besides the action of gaseous material, which, by friction, tends to circularise the orbits of solids which agglomerate to form planets, eccentric orbits naturally tend to be eliminated, since they are more likely to cross other orbits and are therefore extremely unstable, so that the remaining bodies possess nearly circular orbits. In addition, the further from its host star the material is located, the less it benefits from the warmth of it, so that beyond the so-called "ice line", part of the gaseous material condenses into ices, which thereby increases the amount of solid material available to form protoplanetary cores. Therefore, it is expected that giant icy planets are preferentially found in the outer parts of a planetary system, along with giant gaseous planets, since more massive protoplanetary cores will be able to accrete the surrounding gas. On the other hand, less massive Earth-like planets are preferentially expected in the inner parts of a planetary system.
One can also expect that a planetary system contains one or more populations of small solids that have not found their place in the process of planetary formation, called debris disks. The size of the solids varies from micron-size, such as in the Zodiacal Cloud (see Figure 1.3), to kilometer-size, with bodies such as asteroids or comets, as in the Main Asteroid or Kuiper Belts (see Figure 1.2). These bodies endure collisional activity and their dynamical behaviour is closely related to the planetary system with which they coexist, as evidenced for instance in the Main asteroid Belt, by populations of asteroids trapped in stable orbits thanks to the dynamical influence of Jupiter (See Figure 1.4).

All this is supported by numerous observations : the detection of protoplanetary disks and debris disks [2] (see Figure 1.5), and, of course the discovery of numerous planets, show the robustness of the planetary system formation process itself, but also of the proposed model.

However, every model has its limitations. Indeed, as mentioned earlier, our own Solar System is far from being a generic example of planetary system, and in particular, eccentric planets appear to be very common. Therefore, models derived from the study of our own Solar System probably do not represent all the complexity that can be expected in a more generic planetary system. In addition to its almost circular orbits our Solar System is also distinguished by the fact that it contains a single star, whereas more than half of the stars are not isolated but part of binary or even more multiple systems. Therefore, studying the dynamics of systems containing eccentric planets or a binary companion is crucial to have a more representative picture of exoplanetary systems, and this is what this thesis is devoted to.

1.2 Eccentric planets and debris disks

At least $\sim 20\%$ of the extrasolar planetary systems are known to harbor debris disks (Marshall et al. 2014). The first debris disk was discovered in 1984, when the InfraRed Astronomical Satellite (IRAS) found a strong IR excess around Vega, revealing the presence of micron-sized dust grains (Aumann et al. 1984). Because of collisions and stellar radiation effects, these grains have a limited lifetime, which is shorter than the system's age. Consequently, this dust is assumed to be replenished by collisional grinding of much larger parent bodies, which are at least kilometre-sized for this collisional cascade to be sustained over the system's age (Backman & Paresce 1993; Löhne et al. 2008). Therefore, these disks are proof that the accretion of solid material around a star has permitted the formation of at least kilometer-sized bodies. It is thus not surprising that several of these disks are accompanied by planets.

[2] See `www.circumstellardisks.org`

Figure 1.3 – Zodiacal light, seen from the Cerro Paranal Observatory, Chile.
Source: ESO/Y.Beltetsky

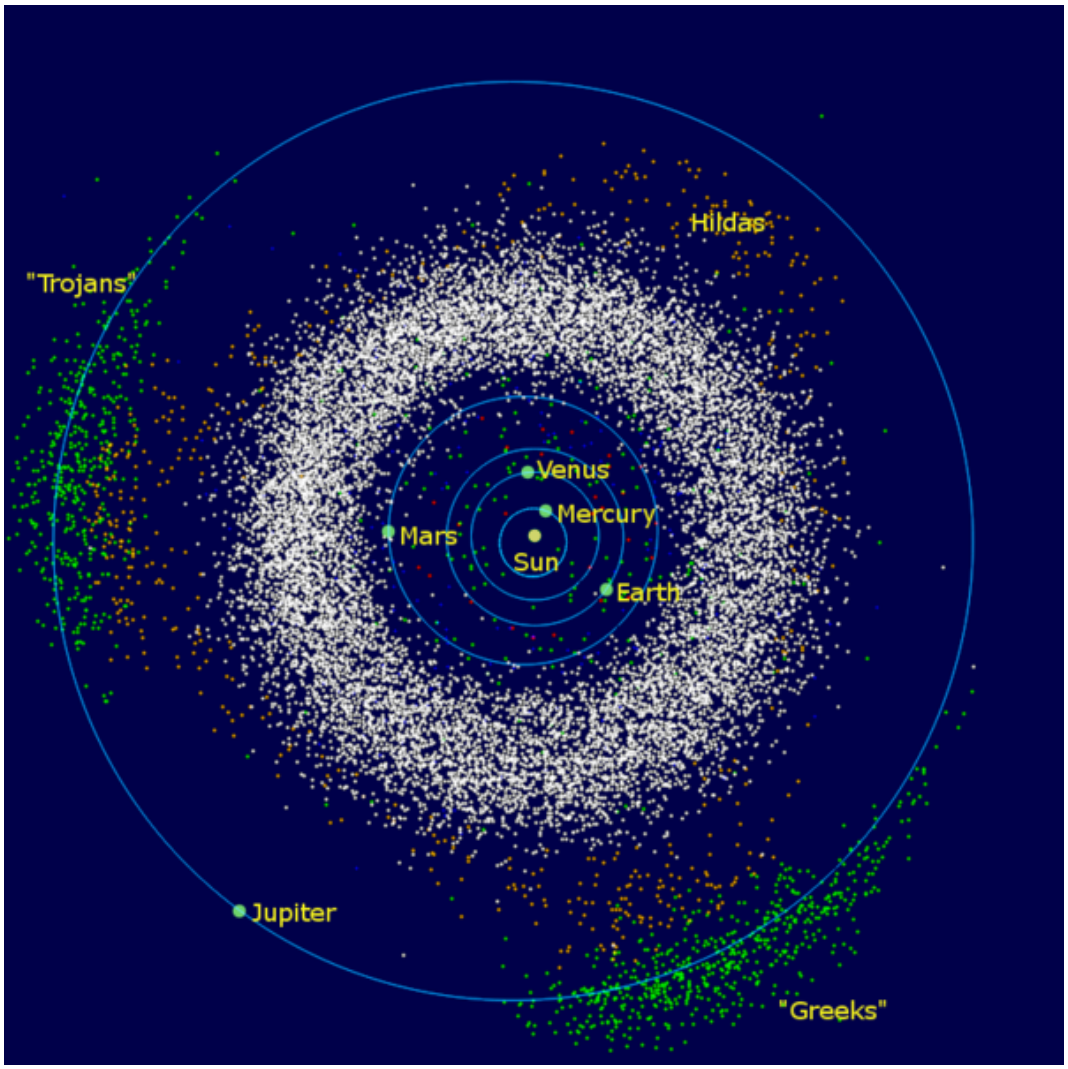

Figure 1.4 – Examples of planet-planetesimals interactions: populations of asteroids trapped on stable orbits by Jupiter, with the Greeks and the Troyans in *green*, and the Hildas in *red*.

Spatially resolved structures in debris disks can provide clues to the invisible planetary components of those systems. Indeed, planets may be responsible for sculpting these disks and may leave their signature through various asymmetries such as wing asymmetries, resonant clumpy structures, warps, spirals, gaps, or eccentric ring structures (see, e.g., Wyatt 1999).

The diversity of these asymmetries is to be compared with the variety of exoplanetary systems discovered around Main Sequence stars since 1995 (51 Peg b, Mayor & Queloz 1995). In particular, the common discovery of significantly eccentric planets is in complete contrast with the circular planetary orbits of our Solar System. According to Udry & Santos (2007), the median eccentricity of planets with orbital period greater than 6 days is ~ 0.3. This has revealed that our own Solar System is far from being a reference, and that our current planetary systems formation and evolution models, which were naturally built from its study, require refinements. Therefore, the study of systems containing eccentric perturbers and their dynamical history is crucial to achieve these refinements.

This thesis will firstly focus on the eccentric debris disk resolved around ζ^2 Reticuli by the *Herschel* space telescope and its PACS instrument (Eiroa et al. 2010). This case is particularly interesting because ζ^2 Reticuli is a Gyr-old system. These systems are rarely accessible to observations, because debris disks tend to lose luminosity on long-term periods: the dust grains emitting at infrared wavelengths are continuously blown away by stellar radiations effects (see e.g. Thébault & Augereau 2007) while replenished via collisional processes among the km-sized parent bodies (Backman & Paresce 1993). Since the parent bodies population is not replenished, the amounts of dust, and thus the disk luminosity in mid-far IR decreases adiabatically (Krivov 2010), until instrument sensitivity does not allow us to detect them anymore.

Therefore, the debris disk of ζ^2 Reticuli illustrates one aspect of mature systems as ours, and is a particularly useful example to understand the long-term history of exoplanetary systems, especially as its disk bears signs for the presence of an eccentric massive body in this system. The first question that arises then is what type of perturber creates this eccentric pattern, and what constraints one might set on it. In addition to retrieve constraints on this companion, one might also question whether the disk asymmetry can be sustained on Gyr timescales, or whether the dynamical history of this system would rather involve a recent setting of the belt-shaping massive perturber on its eccentric orbit. One of the goals of this thesis is to provide answers to these questions through a detailed modelling of the structure of this debris disk, which consists in performing extensive N-body simulations with trial eccentric perturbers, exploring their dynamical influence on massless planetesimals on Gyr timescales, in order to determine which of these perturbers can produce the corresponding observed eccentric pattern, and finally clarify whether this pattern can be sustained on Gyr timescales (Chapter 3).

Another system of major interest is that of Fomalhaut (See Figure 1.5 and Kalas et al. 2005). The eccentric-ring shape of its debris disk was quickly attributed to the dynamic action of a massive and eccentric perturber orbiting near the inner edge of the ring (Quillen 2006; Chiang et al. 2009). This hypothesis was apparently confirmed by the direct detection of a companion near the inner edge of the belt, as predicted, called Fomalhaut b (hereafter Fom b) (Kalas et al. 2008), but new constraints on its orbit revealed that it is belt-crossing, highly eccentric ($e \sim 0.69 - 0.98$), and can hardly account for the shape of the belt (Graham et al. 2013; Beust et al. 2014). The best scenario to explain this paradox is that there is another massive body in this system, Fom c, which drives the debris disk shape. The resulting planetary system is highly unstable, which hints at a dynamical scenario involving a recent scattering of Fom b on its current orbit, potentially with the putative Fom c.

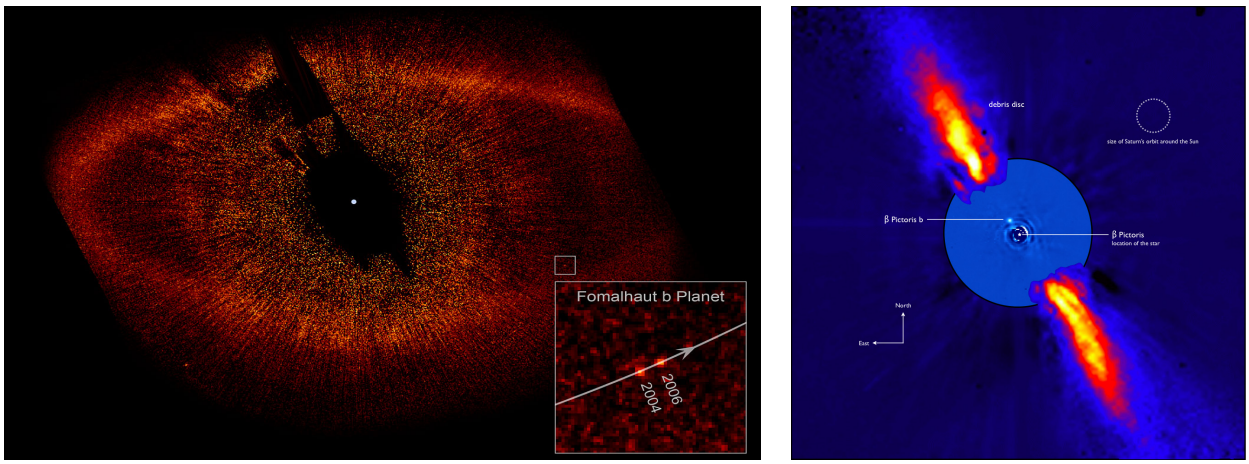

(a) The Fomalhaut system, NASA-ESA/HST

(b) The β Pictoris system, ESO/A.-M. Lagrange et al.

Figure 1.5 – Examples of debris disks, around the stars Fomalhaut **(a)** and β Pictoris **(b)**.

One of the goals of this thesis is to investigate the dynamics of this hypothetical two planets system, and in particular, to give insights on the probability for Fom b to have been set on its highly eccentric orbit by a close-encounter with the putative Fom c (Chapter 4).

The two systems Fomalhaut and ζ^2 Reticuli possess eccentric perturbers, and thus offer a wider picture of exoplanetary systems than our Solar System has so far. The study of their dynamical history is crucial to refine the models of formation and evolution of planetary systems, which were built from the study of our Solar System.

1.3 Planetary migration and stellar binary companion

Finally, this thesis will discuss the impact of a binary companion on planetary migration (Chapter 5). Planetary migration is a phenomenon that can significantly alter the distance of a planet to its star, and is therefore a key element of the morphology of planetary systems. One of its most famous manifestations is certainly the class of so-called "hot" planets that orbit too close to their star to have formed in-situ, which includes 51 Peg b (Lin et al. 1996). Migration results from interactions between the planet and the material of the disk in which it has formed, that is, gas and/or solids depending on the age of the system.

In a protoplanetary disk, interactions with the gaseous material will be predominant and generate migration. This type of migration has been extensively studied in the past years. However, in several Myr, a protoplanetary disk is emptied of most of its gas, and it is ultimately the interactions with the remaining km-sized solids, asteroid- or comet-like, and called planetesimals, which may generate migration in systems typically older than ten million years. It is on this late migration, called *Planestesimal-driven migration* (PDM), and which gives its final architecture to planetary system, that this thesis will focus on. More specifically, it is the impact of a stellar binary companion on this migration process that will be explored numerically. It is obviously expected that a secondary star perturbs the material orbiting the primary star, and therefore any migration process. Therefore, one can expect that a binary companion influences the final architecture of a planetary system. In addition, the impact of a stellar companion on the formation and evolution of planetary systems is by no means negligible, since more than half of the stars possess one.

1.4 Summary

Five centuries ago, Copernicus revolutionised astronomy by extricating it from geocentrism. Today, thanks to a collective effort involving actors from the whole world in search for new planetary worlds, we know that our Solar System is not a generic model, and witness another major revolution, one that will lead astronomy out of heliomorphism.

The diversity of exoplanetary systems often questions our formation and evolution models, however, these models have been primarily built from the study of our Solar System, which turns out to be quite exceptional, because it contains nearly circular orbits and involves a single star.

Highlighting all stages of formation and evolution of planetary systems, being able to describe all the processes at work from their birth to their death, and explain their diversity, is a large and ambitious project of modern astronomy, to which this thesis aims to contribute.

By focusing on the dynamical history of systems containing eccentric perturbers, and the impact of a second star on the architecture of exoplanetary systems, this thesis opens the way to a more appropriate view of exoplanetary systems.

Chapter 2

Modelling planet-debris disks interactions

Contents

I will review here essential features of the dynamics of planetary systems with particular focus on the models and methods that are classically used to investigate planet-debris disk interactions, and which were used throughout this thesis. I will describe the possible gravitational effects of a massive planet on much less massive bodies, therefore named "test-particles", and which include all the component of debris disks, from micron-sized dust grains to km-sized planetesimals. I will also describe the radiative effects of the central star on these solid components, and will explain how planet-debris disks interactions can lead to observable features in debris disks.

2.1 Keplerian motion

A single test-particle of mass m and a star of mass $M_\star$ will mutually attract each other with a gravitational force $\vec{F}_{\rm grav} = GmM_\star\vec{r}/r^3$, $\vec{r}$ being the position vector of the test-particle in the frame centered on the star. It follows, from the application of Newton's second law, that the differential equation which describes the motion of the test-particle is given by :

$$\ddot{\vec{r}} + \mu\frac{\vec{r}}{r^3} = 0 \qquad , \tag{2.1}$$

where $\mu = G(m + M_\star)$.

The test-particle will thus adopt a Keplerian motion, that is, it will describe an ellipse which one of the foci is occupied by the star. This motion is defined by six parameters $(a, e, i, \Omega, \omega, \tau)$, called orbital elements (see Figure 2.1).

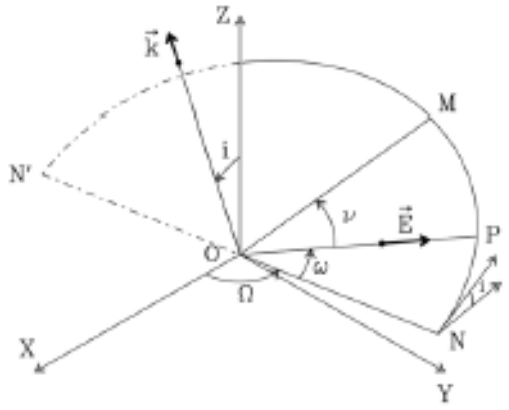

Figure 2.1 – Orbital elements

- a is the semi-major axis. It represents the size of the orbit ;
- e is the eccentricity, with value between 0 and 1, and gives an idea of the shape of the orbit : the greater e is, the more elliptic the orbit is ;
- $i = (\vec{OZ}, \vec{k})$ is the inclination of the orbit ;
- $\Omega = (\vec{OX}, \vec{ON})$ is the longitude of the ascending node. This permits, with the inclination, to specify the position of the plane of the orbit in space ;
- $\omega = (\vec{ON}, \vec{OP})$ is the argument of periastron, and specifies the position of the orbit in its plane ;
- τ is the time of passage of the test-particle at its periastron.

The position of the test-particle on its orbit is specified by the true anomaly ν, i.e., the angle between the position vector $\vec{r}$ of the test-particle and the direction of its periastron. The trajectory itself, that is, the equation that defines the orbit in its plane and relates the distance r of the test-particle to the star, and its angular position on its orbit ν, reads :

$$r(\nu) = \frac{a(1-e^2)}{1+e\cos\nu} \quad . \tag{2.2}$$

The test-particle will have an orbital period T which depends only on a, m, and $M_\star$, as defined with Kepler's third law by :

$$T^2 = \frac{4\pi}{\mu}a^3 \quad . \tag{2.3}$$

Finally, the equation which gives the position of the test-particle on its orbit as a function of the time is the Kepler's equation, and reads :

$$M = E - e\sin E \quad , \tag{2.4}$$

where E and M are respectively the eccentric and mean anomalies, being defined by:

$$\tan\frac{\nu}{2} = \sqrt{\frac{1+e}{1-e}}\tan\frac{E}{2} \quad , \tag{2.5}$$

and

$$M = n(t-\tau) \quad . \tag{2.6}$$

This last equation contains the mean-motion n, simply defined by $2\pi/T$.

If the test-particle was to be effectively alone in the system, the shape and orientation of its orbit would be constant. Of course, this situation is ideal, and Keplerian orbits are in fact perturbed by various phenomena. In particular, it will be affected by the presence of a massive body such as a planet. If effectively acted upon by a planet, a whole population of small solids such as the components of a debris disk may bear the imprint of this planet in its spatial distribution, and lead to observable features in debris disks.

2.2 Planetary patterns in debris disks

Spatially resolved structures in debris disks can provide clues to the invisible planetary component of those systems. Such planets may be responsible for sculpting these disks and may leave their signature through various asymmetries such as wing asymmetries, resonant clumpy structures, warps, spirals, gaps, or eccentric ring structures (see, e.g., Wyatt 1999). Dynamical modelling of such asymmetries is the only method to place constraints on the masses and orbital parameters of planets in systems where direct observations are not possible (see, e.g., Mouillet et al. 1997b; Wyatt et al. 1999; Augereau et al. 2001; Moro-Martín & Malhotra 2002; Wyatt 2004; Kalas et al. 2005; Quillen 2006; Stark & Kuchner 2008; Chiang et al. 2009; Ertel et al. 2011; Boley et al. 2012; Ertel et al. 2012; Thebault et al. 2012).

Most images of resolved debris disks have been obtained so far in the visible or near-IR. At these wavelengths, the emission is dominated by sub-micron to micron-sized grains, which are released by larger km-sized bodies as these suffer collisions. The smallest a solid component is, the more sensitive it is to stellar radiation effects. Radiation pressure tends to blow material out of the system. As the gravitational force, it is a radial force, that scales as the inverse square of the radius, but it is directed outwards and therefore counteracts gravitational attraction. Using the parameter β, which is the radiation pressure to gravity ratio, a particle is submitted to a total force:

$$\vec{F} = -\frac{GM_\star(1-\beta)m}{r^3}\vec{r} \quad . \tag{2.7}$$

One can see that this is equivalent to a gravitational force ponderated by a factor $(1-\beta)$. Therefore if $\beta > 1$, the particle will no longer be bound to the system and be expelled from it. In fact, a particle becomes unbound as soon as $\beta > 0.5$ (Augereau & Beust 2006). This means that a planetesimal on a circular orbit will release bound dust grains on eccentric orbits, as long as the value of β for these dust grains does not exceed 0.5 (See for instance Figure 1 of Krivov 2010).

An expression for β was given by Burns et al. (1979) in the ideal case where the body subject to radiation pressure is spherical with radius s and density ρ, and absorbs the totality of the radiation it is exposed to:

$$\beta = 0.574 \left(\frac{L_\star}{L_\odot}\right)\left(\frac{M_\odot}{M_\star}\right)\left(\frac{1\mathrm{g.cm}^{-3}}{\rho}\right)\left(\frac{1\mu\mathrm{m}}{s}\right) \quad , \tag{2.8}$$

where $L_\star$ and $M_\star$ are the star luminosity and mass, respectively.

As one can see from Eq. (2.8), β depends on the size of the particle : the larger it is, the smaller β is, which characterizes the fact that the largest components of a debris disk, that is, km-sized planetesimals, are unsensitive to radiation pressure and suffer gravitational effects only, while smaller grains tend to be blown out of the system.

Therefore, the grains observed in the visible or near-IR are close to the blow-out limit imposed by stellar radiation. However, since these grains are the product of collisions of larger bodies which endure gravitational effects only, planetary perturbations among a collisionally active population of planetesimals will thus infer on the zone of production of dust grains, which explains why large-scale asymmetries can be visible among a population of short-lived dust grains, which will eventually leave the system. The effect of radiation pressure is that it may strongly alter or even mask the dynamical structures imparted by a massive perturber on a debris disk (See for instance Figure 1 of Krivov 2010).

Observations of larger bodies, less affected by radiation pressure effects, that is, observations at longer wavelegths (mid-IR to sub-mm), allow one to obtain better constraints on the structure of debris disks and its potential large-scale asymmetries. These observations were made possible by the Herschel Space Telescope and the interferometer ALMA.

In any case, by using constraints derived from resolved observations of large-scale asymmetries in debris disks, one can then proceed to a dynamical modelling work: using analytical and/or numerical tools, and more precisely N-body simulations, it is possible to explore a given space of parameters for any disturbing planet within a system and study its gravitational effect on a population of planetesimals. The goal is to try to reproduce the asymmetries observed, and thus constrain the parameters of the planetary system. It is precisely this type of work that I have conducted in my thesis for the case of the debris disk of ζ^2 Reticuli and that I will present in Chapter 3. In the following sections, I will give more details on the general modelling assumptions, the analytical methods, and the numerical methods used throughout this thesis.

2.3 Perturbed Keplerian motion : introduction

The usual assumption that is made when trying to relate a large-scale asymmetry among an observed dust population to a planetary perturber, is that this asymmetry already exists amongst the parent planetesimal population that produces the observed dust and result from pure gravitational perturbations. Another usual assumption is that at the end of the protoplanetary phase, the planetesimals start from almost circular orbits because of orbital eccentricity-damping by primordial gas, and that any perturbing planet in the system is fully formed by the time the gas disappears. Thus, one can consider the disappearance of the gas as time zero for the onset of planetesimal perturbations by a planetary companion.

In this context, one can study the influence of different perturbers in a simplified way, neglecting the effect of radiation pressure and considering initially cold parent planetesimals as mass-less and collision-less particles in orbit around their host star and perturbed by a companion.

When a particle suffers perturbations due to the presence of a planet in the system, the context is this of the three-body problem, which has unfortunately no exact solution. As shown by Burns (1976), perturbing forces in the plane of the orbit of the particle will induce changes on its semi-major axis a, eccentricity e, and argument of periastron ω, while forces normal to the plane of the orbit will induce changes in the inclination i and longitude of ascending node Ω. The orbital elements of the particle are no longer constant, and the goal is then to find the equations describing their behaviour. This is best achieved using a Hamiltonian formulation of the problem, which is a global and energetic approach.

Indeed, the Hamiltonian H is a function that describes the system as a whole, and is the sum of the kinetic and potential energies at play. In the case the system studied is conservative, the total energy and thus the Hamiltonian of this system are constants. This function can be defined with any set of variables (q_i, p_i) with $i = 1...N$, as soon as these variables are conjugated, which means that they allow the equations of motion to be written in a very simple form, that is, a system of $2N$ first order equations, instead of N second order equations :

$$\frac{dq_i}{dt} = \frac{\partial H}{\partial p_i} \quad ; \quad \frac{dp_i}{dt} = -\frac{\partial H}{\partial q_i} \quad , \tag{2.9}$$

where q_i are called the generalized coordinates, and p_i are their conjugated impulsions.

It can be easily verified in the frame of the two-body problem that $\vec{r}$ and $\vec{p} = m\dot{\vec{r}}$ are conjugated. Indeed, in this case, one has :

$$H_0 = E_{kin} + E_{pot} = \frac{p^2}{2m} - \frac{\mu}{r} = \frac{p_x^2 + p_y^2 + p_z^2}{2m} - \frac{\mu}{r} \quad , \tag{2.10}$$

and thus,

$$\nabla_{\vec{p}} H_0 = \frac{\partial H_0}{\partial p_x}\vec{u}_x + \frac{\partial H_0}{\partial p_y}\vec{u}_y + \frac{\partial H_0}{\partial p_y}\vec{u}_z = \frac{p_x}{m}\vec{u}_x + \frac{p_y}{m}\vec{u}_y + \frac{p_z}{m}\vec{u}_z = \frac{\vec{p}}{m} = \dot{\vec{r}} \quad , \tag{2.11}$$

$$-\nabla_{\vec{r}} H_0 = -\frac{\partial H_0}{\partial r}\vec{u}_r = -\frac{\mu}{r^2}\vec{u}_r = \vec{F}_{\text{grav}} = m\ddot{\vec{r}} = \dot{\vec{p}} \quad . \tag{2.12}$$

The three second order differential equations contained in Eq. (2.1) are now transformed into six first order equations.

The three-body problem can be treated with this approach to retrieve the Lagrange equations, which describe the variations of the orbital elements. The orbital elements themselves are not conjugated, however, several combinations of them are. This is the case for the Delaunay elements :

$$l = M \qquad L = \sqrt{\mu a} \tag{2.13}$$

$$g = \omega \qquad G = L\sqrt{1 - e^2} \tag{2.14}$$

$$\theta = \Omega \qquad \Theta = G\cos i \quad , \tag{2.15}$$

where the Hamiltonian now reads $H_0 = -\mu^2/2L^2$ with these new variables, and the equations of the Keplerian motion now are :

$$\frac{dl}{dt} = \frac{\partial H_0}{\partial L} = \frac{\mu^2}{L^3} \qquad \frac{dL}{dt} = -\frac{\partial H_0}{\partial l} = 0 \tag{2.16}$$

$$\frac{dg}{dt} = \frac{\partial H_0}{\partial G} = 0 \qquad \frac{dG}{dt} = -\frac{\partial H_0}{\partial g} = 0 \tag{2.17}$$

$$\frac{d\theta}{dt} = \frac{\partial H_0}{\partial \Theta} = 0 \qquad \frac{d\Theta}{dt} = -\frac{\partial H_0}{\partial \theta} = 0 \quad . \tag{2.18}$$

With a perturbing force $\vec{P}$, the equation of the perturbed Keplerian motion now reads :

$$\ddot{\vec{r}} = -\mu\frac{\vec{r}}{r^3} + \vec{P} \quad . \tag{2.19}$$

Laplace-Lagrange theory, which dates back from the XIX$^{\text{th}}$ century, consists in considering a perturbing force $\vec{P}$ that derives from a potential, with $P = \vec{\nabla} U$. Therefore, the corresponding Hamiltonian reads $H_1 = H_0 - U$, and the equations of the motion are :

$$\frac{dl}{dt} = \frac{\partial H_1}{\partial L} = \frac{\mu^2}{L^3} - \frac{\partial U}{\partial L} \qquad \frac{dL}{dt} = -\frac{\partial H_1}{\partial l} = \frac{\partial U}{\partial l} \tag{2.20}$$

$$\frac{dg}{dt} = \frac{\partial H_1}{\partial G} = -\frac{\partial U}{\partial G} \qquad \frac{dG}{dt} = -\frac{\partial H_1}{\partial g} = \frac{\partial U}{\partial g} \tag{2.21}$$

$$\frac{d\theta}{dt} = \frac{\partial H_1}{\partial \Theta} = -\frac{\partial U}{\partial \Theta} \qquad \frac{d\Theta}{dt} = -\frac{\partial H_1}{\partial \theta} = \frac{\partial U}{\partial \theta} \quad . \tag{2.22}$$

From these equations, one can then retrieve the Lagrange equations :

$$\sqrt{\mu a}\frac{da}{dt} = 2a\frac{\partial U}{\partial M} \quad ; \tag{2.23}$$

$$\sqrt{\mu a}e\frac{de}{dt} = (1-e^2)\frac{\partial U}{\partial M} - \sqrt{1-e^2}\frac{\partial U}{\partial \omega} \quad ; \tag{2.24}$$

$$\sqrt{\mu a(1-e^2)}\sin i\frac{di}{dt} = \cos i\frac{\partial U}{\partial \omega} - \frac{\partial U}{\partial \Omega} \quad ; \tag{2.25}$$

$$\frac{dM}{dt} = n - \frac{1}{\sqrt{\mu a}}\left[2a\frac{\partial U}{\partial a} + \sqrt{\mu a(1-e^2)}\left(\frac{d\omega}{dt} + \cos i\frac{d\Omega}{dt}\right)\right] \quad ; \tag{2.26}$$

$$\sqrt{\mu a(1-e^2)}e\left(\frac{d\omega}{dt} + \cos i\frac{d\Omega}{dt}\right) = (1-e^2)\frac{\partial U}{\partial e} \quad ; \tag{2.27}$$

$$\sqrt{\mu a(1-e^2)}e\sin i\frac{d\omega}{dt} = (1-e^2)\sin i\frac{\partial U}{\partial e} - e\cos i\frac{\partial U}{\partial i} \quad . \tag{2.28}$$

There is still no exact solution to the Lagrange equations, but the most classical way to derive solutions to these equations is to apply the linear Laplace-Lagrange theory, as will be explained in Section 2.4. However, this approach is valid only for low eccentricities, and as we shall see for the case of the system of ζ^2 Reticuli (Chapter 3), investigating small eccentricities may not be appropriate for extrasolar systems. Moreover, this theory relies on an averaging method that does work only if the mutual positions of the bodies on their orbits are random, which is not the case in a mean-motion resonance situation, as will be seen in Section 2.5.

2.4 Secular perturbations

The secular theory of Laplace-Lagrange was developped to find solutions to the Lagrange equations, which are impossible to solve as they are. The secular theory is based on simplifications of the problem by considering small eccentricities and inclinations, as observed in our own Solar System, and by considering the average influence of the considered bodies on each other.

However, Delaunay's elements or classical orbital elements are not adapted to small eccentricities and inclinations, since when this quantities are zero, the longitude of ascending node Ω and the argument of the periastron ω become undefined. One can use instead variables which depend on these angles, but which become zero instead of being undefined when the eccentricity or inclination tend to zero, such as the mean longitude $\lambda = \Omega + \omega + M$ and the longitude of periastron $\varpi = \Omega + \omega$.

The orbits, and thus the Hamiltonian of the system, are described thanks to the semi-major axis, the mean longitude λ and the following quantities :

$$h = e \sin \varpi \qquad p = \sin \frac{i}{2} \sin \Omega \tag{2.29}$$

$$k = e \cos \varpi \qquad q = \sin \frac{i}{2} \cos \Omega \quad . \tag{2.30}$$

The first step of the Laplace-Lagrange theory consists in replacing rapidly oscillating terms of the Hamiltonian by their mean value, so that the varying terms which remain represent the slow secular variations of the system. This is done by averaging the Hamiltonian over the mean longitudes of the test-particle λ and that of the perturbing planet λ_p, which are rapidly evolving variables compared to the other orbital elements. In the following, the variables with subscript p refer to the planet, while unsubscripted variables are those of the test-particle. This averaging is justified as soon as the positions of the bodies on their orbit are mutually independent, which involves that conjunctions between the two bodies can occur anywhere on their orbits, and thus λ and λ_p are independent variables, with all the configurations (λ, λ_p) in $[0, 2\pi] \times [0, 2\pi]$ being equiprobable. This is not the case when the bodies are in a resonant configuration, as we shall see in Section 2.5.

The second step consists in an expansion of the averaged Hamiltonian to second order in ascending powers of the eccentricities of the two bodies, that is concretely, to second order in ascending powers of k, h, p and q. These two steps eventually allow one to transform the system of Lagrange equations into a linear differential system which describes the long-term variations of the orbital elements of the test-particles, and thus, their secular evolution. At first order, the semi-major axis a of the test-particle will remain constant, while the evolutions of its eccentricity e and longitude of periastron ϖ will be coupled, as well as those of the inclination i and longitude of ascending node Ω. These elements will oscillate with a given amplitude around a value imposed by the perturber.

This thesis largely involves the dynamical modelling of systems containing eccentric perturbers which shape debris disks into eccentric ring belts thanks to secular interactions. Therefore, I use the example of secular interactions between an eccentric perturber and planetesimals to explain how large scale structures, here eccentric patterns, may arise in debris disks as a result of these interactions. Examples of such eccentric debris disks are displayed in Figure 2.2.

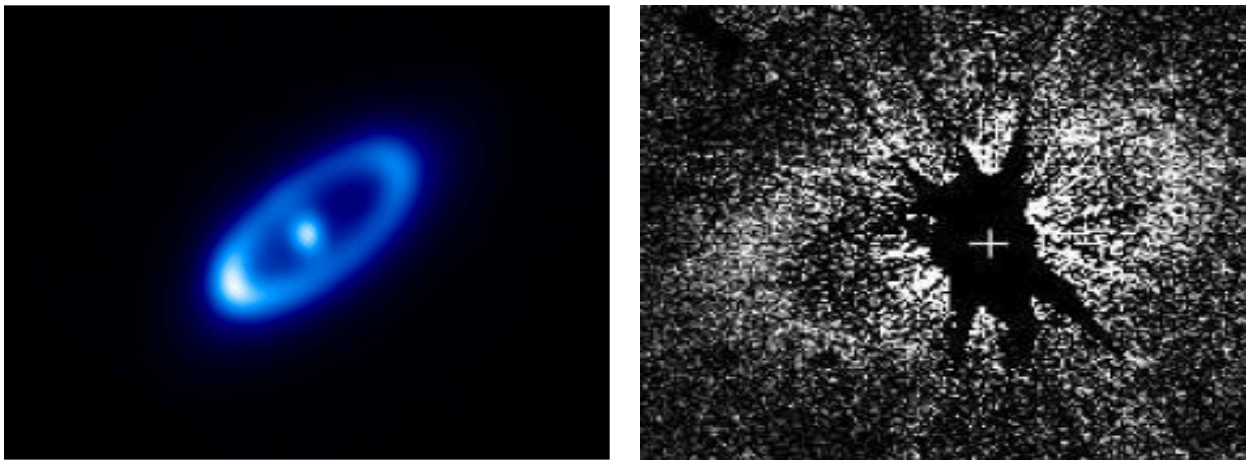

(a) Fomalhaut seen with *Herschel* (Acke et al. 2012) (b) HD 202628 seen with HST (Krist et al. 2012)

Figure 2.2 – Eccentric debris disks resolved around Fomalhaut **(a)**, and HD 202628 **(b)**.

When secularly perturbed by an eccentric perturber, the eccentricity of a planetesimal evolves cyclically in a coupled manner with the longitude of periastron : it oscillates around an eccentricity e_f imposed by the perturber, with a frequency that depends on the distance of the test-particle to the perturber, but also on the mass of the perturber, and which is the same at which the longitude of periastron evolves. This is the result of the Laplace-Lagrange theory, where one can then define the complex eccentricity of a planetesimal, $z(t) = e\cos(\varpi - \varpi_p) + I\sin(\varpi - \varpi_p)$, where $\varpi - \varpi_p$ is the longitude of periastron of the test-particles with respect to the direction of the perturber's periastron, that is, the planet and planetesimal have their periastra aligned when $\varpi - \varpi_p = 0$ and anti-aligned when $\varpi - \varpi_p = \pi$.

This complex ecentricity can also be written:

$$z(t) = e_f \left\{1 - \exp(IAt)\right\} \qquad , \tag{2.31}$$

where $I^2 = -1$, and $A = \frac{\mathrm{d}(\varpi - \varpi_p)}{\mathrm{d}t}$ is the secular precession rate. One can see from this expression that the maximum induced eccentricity for a planetesimal is twice the forced eccentricity, that is, $e_{f,max} = 2e_f$. This occurs when $At = \pi\,[2\pi]$, that is, when the longitudes of periastra of the planetesimal and the perturber are equal ($\varpi - \varpi_p = 0$, see Figure 2.3(b) and, for more details, see e.g., Wyatt 2005; Beust et al. 2014). As a consequence, when an eccentric perturber acts upon a disk of planetesimals, the eccentricity of these planetesimals appear to be maximum when these are apsidally aligned with the perturber, and thus, the disk is shaped into an eccentric ring.

This result is probably best visualised by using phase-space diagrams, of which an example is shown in Figure 2.3(a). These are produced by reducing the Hamiltonian to one degree of freedom, i.e., by obtaining $H(e, \varpi)$ and tracing isovalue curves of this Hamiltonian in the (e, ϖ) space. The reduction of the Hamiltonian to one degree of freedom is achieved by considering a coplanar problem, which first reduces the Hamiltonian to $H(a, a_p, e, e_p, \varpi, \varpi_p, \lambda, \lambda_p)$. One first averages this Hamiltonian over the mean-longitudes λ and λ_p, and thus consider that the semi-major axes a and a_p are constant. The perturber being much more massive and dynamically predominant over a planetesimal, this allows one to further consider a perturber of fixed orbit, with e_p and ϖ_p being constants. In particular, its longitude of periastron ϖ_p can be taken for reference and set to zero for sake of simplicity. This finally reduces the Hamiltonian to $H(e, \varpi)$.

Since the disk initally contains planetesimals in almost circular orbits, the forced elliptic ring structure takes some time to settle in, and it is preceded by the appearance and disappearance of transient spiral features, which can appear on observations, as shown in Figure 2.4(a). These are due to differential precession within the disk: all the planetesimals in the disk have different precession rates – because of their different orbital distances – such that these spiral structures are expected to wind up and finally generate an eccentric ring, as shown by Augereau & Papaloizou (2004) and Wyatt (2005). The characteristic time for reaching this state is of the order of a few precession timescales t_{prec} at the considered semi-major axis a (Wyatt 2005) :

$$t_{\mathrm{prec}} = \frac{2\pi}{(\mathrm{d}\varpi/\mathrm{d}t)_a} \qquad , \tag{2.32}$$

The eccentricity of the ring finally causes the disk centre of symmetry to be offset from the star, and the disk pericentre to be brighter than the apocentre, since it is closer to the star and thus hotter. This feature was studied by Wyatt et al. (1999) for a planetary companion, and was called the pericentre-glow phenomenon. This phenomenon will be investigated in this thesis on Gyr timescales and for significantly eccentric debris disks through the study of the ζ^2 Reticuli system (Chapter 3).

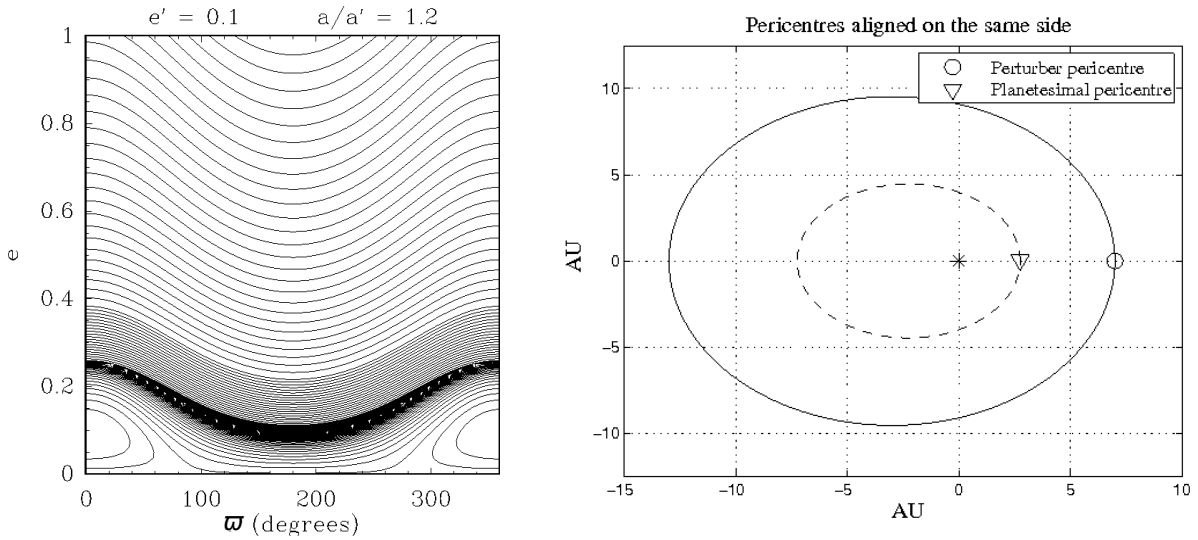

(a) Iso-Hamiltonian curves in the (e, ϖ) space (b) Configuration of maximum induced eccentricity with $\varpi = 0$

Figure 2.3 – **(a)** Phase-space diagram which displays the trajectories of a planetesimal in the (e, ϖ) space when acted upon by an eccentric perturber, and thus represents the co-evolution of its eccentricity e and longitude of periastron ϖ. **(b)** Since the planetesimal orbit precesses, its periastron will eventually be aligned with that of the perturber on the same side of the massive central body, that is, the longitudes of periastra of the planetesimal and the perturber are equal ($\varpi = 0$). In this configuration, the planetesimal eccentricity is maximum.

Here the behaviour of the eccentricity and the longitude of periastron are coupled. In the case of perturbations from an inclined planet, it is the inclination and the longitude of ascending node which are coupled in the exact same manner, and the resulting large scale structure that can arise is a warp, as shown in Figure 2.4(b).

However, this secular behaviour, expected when the mutual positions of the bodies on their orbit are independent and which allows to average the Hamiltonian, becomes non valid as soon as the conjunctions between the planet and the test-particle occur at non-random locations, as is the case when the test-particle and the planet are in mean-motion resonance. This requires another treatment of the Hamiltonian, since averaging is not permitted there, which we describe further in the next section.

2.5 Resonant interactions

Mean motion resonances (hereafter MMR) between a test-particle and a planet, usually noted $p+q : p$, where p is an integer and q is a relative integer, concern particles with orbital periods achieving the $p/p+q$ commensurability with that of the perturber. Resonances with $q > 0$ correspond to inner resonances, that is, particles orbiting inside the orbit of the perturber, while $q < 0$ denotes outer resonances. This commensurability leads conjunctions between the particle and the planet to be non-random and occur more or less always in the same configuration. The integer $|q|$ is called the order of the resonance, and specifies the number of conjunctions between the two bodies.

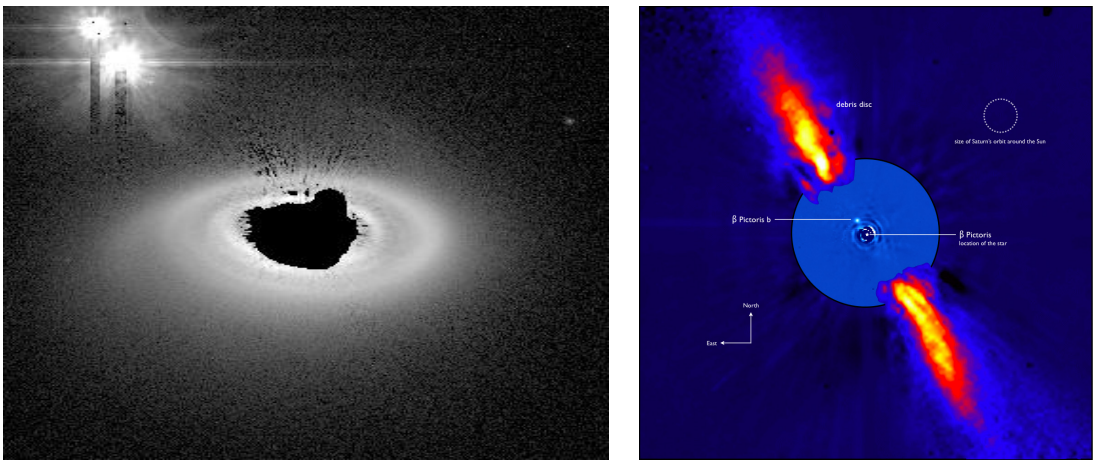

(a) Spirals around HD 141 569 (Clampin et al. 2003) (b) Warp around β Pictoris, ESO/A.-M. Lagrange et al.

Figure 2.4 – Example observations of spirals, in the debris disk of HD 141 569 **(a)**, and of a warp, in the debris disks of β Pictoris **(b)**.

The averaging method used to treat the secular effect of a planetary perturber on a test-particle is valid only if the positions of the planet and the particle are independent, that is, if the conjunctions between both bodies are random. This is not the case if the bodies are in mean-motion resonance, and the problem must be treated differently. The problem here is plane, and thus, as for the secular problem at small inclinations, the angles Ω and ω are no longer defined, while $\varpi = \omega + \Omega$ is always defined. The problem is thus treated with the use of the plane Delaunay's elements :

$$\lambda = \varpi + M \qquad L = \sqrt{aGM_\star} \tag{2.33}$$
$$\varpi = \Omega + \omega \qquad P = L(\sqrt{1-e^2} - 1) \quad . \tag{2.34}$$

The equations of motion are then :

$$\frac{d\lambda}{dt} = \frac{\partial H}{\partial L} \qquad \frac{dL}{dt} = -\frac{\partial H}{\partial \lambda} \tag{2.35}$$
$$\frac{d\varpi}{dt} = \frac{\partial H}{\partial P} \qquad \frac{dP}{dt} = -\frac{\partial H}{\partial \varpi} = 0 \quad . \tag{2.36}$$

As for the secular case, the Hamiltonien H is a function of both λ and λ_p, however, in this case, the configurations (λ, λ_p) in $[0, 2\pi] \times [0, 2\pi]$ are not equiprobable, and λ and λ_p depend on each other, and as a consequence, one cannot average the Hamiltonian separately on both λ and λ_p as in the Laplace-Lagrange secular theory. Indeed, in the case of a MMR, $p\lambda_p - (p+q)\lambda_p = p\varpi - (p+q)\varpi_p$ can be considered a constant in a very good approxiamation over an orbital period, since orbits precess much slowlier, on secular timescales. One must first proceed to a change in variables in order to take into account this dependency in an explicit manner before being able to proceed to an averaging.

One introduces the conjugated variables :

$$\sigma = \frac{p+q}{q}\lambda_p - \frac{p}{q}\lambda - \varpi \qquad S = L(1-\sqrt{1-e^2}) \tag{2.37}$$

$$\nu = \frac{p+q}{q}\lambda_p + \frac{p}{q}\lambda + \varpi_p \qquad N = L(\sqrt{1-e^2} - \frac{p+q}{p}) \quad . \tag{2.38}$$

The corresponding Hamiltonian is $K = H - \frac{p+q}{p}n_p L$ where n_p is the perturbing planet mean-motion, and the equations of motion now read :

$$\frac{d\sigma}{dt} = \frac{\partial K}{\partial S} \qquad \frac{dS}{dt} = -\frac{\partial K}{\partial \sigma} \tag{2.39}$$

$$\frac{d\nu}{dt} = \frac{\partial K}{\partial N} \qquad \frac{dN}{dt} = -\frac{\partial K}{\partial \nu} = 0 \quad . \tag{2.40}$$

The only remaining rapidly varying variable is λ_p, and one can then average the Hamiltonian over this variable, and make this Hamiltonian become a constant of the motion. Additionally, if the perturbing planet is on a circular orbit, ϖ_p becomes zero and ν becomes a constant. Therefore, the Hamiltonian does not depend on ν, and as a consequence, $N = \sqrt{a}\left(\frac{p+q}{p} - \sqrt{1-e^2}\right)$ also becomes a constant of the motion. Since the eccentricity e will vary, the result is that a will also vary, and both will suffer oscillations. N characterises the maximum amplitude of these oscillations : the greater N is, the larger is the amplitude of the oscillations.

σ specifies the position of the conjunction between both bodies with respect to the periastron of the test-particle, while ν is the equivalent for the perturbing planet. The mutual orientation of the periastron of both orbits is $\sigma + \nu$. If the planetary perturber is considered to be on a circular orbit, N and ν are constants, which reduces the Hamiltonian to one degree of freedom, with a dependency in (e, σ). Therfore one can understand the behaviour of a test-particle in MMR by considering isovalues of the Hamiltonian in the $(X = e\cos\sigma, Y = e\sin\sigma)$ plane and for a fixed value of the constant N, which thus represents the conjunctions between both bodies in the polar (e, σ) plane.

We show an example of such diagram in Figure 2.5(a) with the well-known example of the 3:4 MMR between Titan and Hyperion. Each close curve represents a possible trajectory determined by the value of the Hamiltonian. One can see two different types of curves. For small or great eccentricities, the curves exhibit a tendency to be circular, which means that σ can take any possible value in $[0, 2\pi]$, and is thus said to circulate. This means that the conjunction between both bodies can occcur anywhere on the orbit of the test-particle, that is, it is not in MMR. Other curves rather have a horseshoe shape, which means in this case that σ oscillates with a more or less great amplitude around a given value, and thus, the conjunctions between both bodies occur more or less always in the same configuration. σ is then said to librate, and the test-particle is in MMR with the perturbing planet. Particles trapped in MMRs are thus characterized by the libration of σ (see Beust & Morbidelli 1996; Morbidelli & Moons 1995, for details). This analysis and the production of these phase-space diagrams are restrained to the case where the perturber is on a circular orbit, since it allows the Hamiltonian to be reduced to one degree of freedom. However, the study of interactions with eccentric planets is necessary.

Indeed, if the eccentricity of the perturber is zero (or very small), then the eccentricity of the test-particle only undergoes small amplitude variations. But if the eccentricity of the perturber is non-zero, the eccentricity modulations can have much larger amplitudes. Yoshikawa (1989) showed that this is particularly relevant for inner MMRs like the 4:1, 3:1 or 5:2.

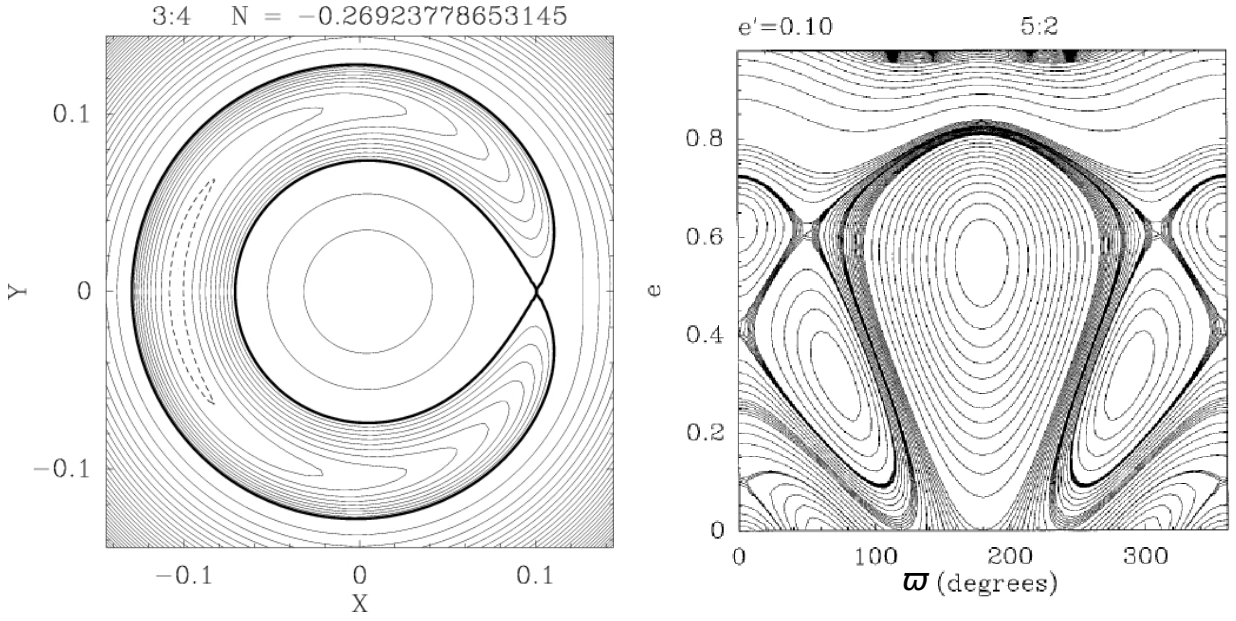

(a) Map of conjunctions between Titan and Hyperion (b) Iso-Hamiltonian curves in the (e, ϖ) space

Figure 2.5 – **(a)** Phase-space diagram representing the conjunctions σ between Hyperion and Titan in the polar (e, σ) plane, and which are in 3:4 MMR. **(b)** Phase-space diagram representing the co-evolution of a planetesimal eccentricity e and longitude of periastron ϖ when in 5:2 MMR with an eccentric perturber ($e_p = 0.1$).

This mechanism is thought to be responsible for the generation of the Kirkwood gaps in the solar system (see Figure 2.6(a) and Wisdom 1983), and it has been claimed to trigger the Falling Evaporating Bodies (FEBs, that is, star-grazing evaporating planetesimals, or comets) mechanism towards β Pictoris (Beust & Morbidelli 1996, 2000).

As for the secular case, the dynamical behaviour of a particle in MMR is characterized by a co-evolution of e, the eccentricity of a test-particle, and $\sigma + \nu$, the orientation of the periastron of the test-particle compared to that of the perturbing planet, which in fact, corresponds to $\varpi - \varpi_p$ as defined in Section 2.4. Again, if the longitude of periastron of the perturber is taken as reference and set to zero, this quantity simply reduces to ϖ. Of course, the dynamical behaviour of a particle in MMR is constrained to a given evolution which depends on the conditions in which the particle enters in MMR with a planet, but also on the MMR itself. However, in the case the perturber is on an eccentric orbit, N is not a constant any longer, and the Hamiltonian has two degrees of freedom. To derive a one degree of freedom Hamiltonian, one can then choose to fix the value of N to zero, that is, to consider that the amplitude of libration, and thus, of the oscillations in semi-major axis and eccentricity, is zero.

This allows one to produce phase-diagrams which show the trajectory followed by a test particle along time in the (e, ϖ) space when in a given MMR with an eccentric perturber, as shown in Figure 2.5(b). As we shall see in Chapter 4, such diagrams were of great use in the study of the Fomalhaut system. When N is not zero, the amplitude of the libration is preserved with a good approximation (See Beust & Morbidelli 2000, and in particular, their Figure 13). Indeed, MMRs have little effect on the semi-major axis of the particle, which suffers only small amplitude librations ($\lesssim 0.1$AU) around the exact resonance location.

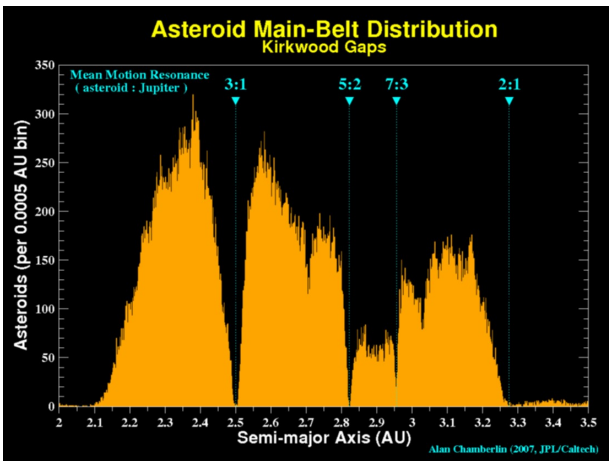

(a) Kirkwood gaps, by Alan Chamberlain, JPL/Caltech

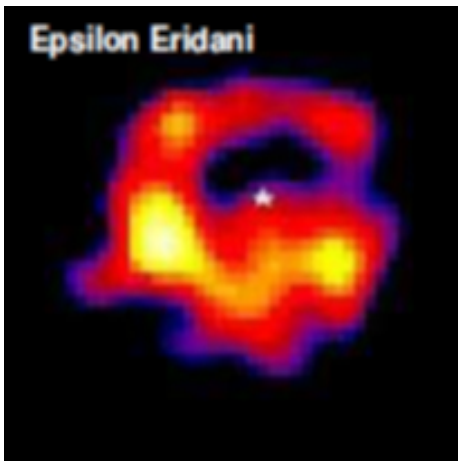

(b) Debris disk of ϵ Eridani, Greaves et al. (1998).

Figure 2.6 – **(a)** Distribution in semi-major axis of the asteroids in the Main Asteroid belt, which shows gaps at MMR locations with Jupiter, called the Kirkwood gaps. **(b)** Clumps in the debris disk of ϵ Eridani, which have been interpreted as resonant structures.

Stabilization effects of several MMRs can lead to overdensities of material which are suspected to appear on observation as clumpy structures in debris disks (see for instance Figure 2.6(b) and Greaves et al. 1998; Moran et al. 2004). In particular, planetary migration can lead to the resonant trapping of planetesimals (see, e.g., Wyatt 2003). However, the typical size of such structures (<1AU) is difficultly accessible to current instrumental sensitivities and resolution (Reche et al. 2008). As will be found in this thesis, MMRs with an eccentric perturber are also a crucial mechanism that can lead to the late production of eccentric orbits, which may be linked with the production of inner dust belts. Finally, another major type of interactions between test-particles and planets are close-encounters. These occur when a test-particle enters the chaotic zone of a planet, which is defined as the region where MMRs overlap (Wisdom 1980). We characterise close-encounters further in the next section.

2.6 Close-encounters

A particle will endure a strong deflection of its orbit and suffer a close-encounter with a planet, if it enters the chaotic zone of the planet. The width Δa of this zone depends on the mass ratio between the central star and the planet,

$$\frac{\Delta a}{a_p} = \frac{|a_{\rm edge} - a_p|}{a_p} = 1.5\mu^{2/7} \quad , \tag{2.41}$$

where $\mu = m_p/m_*$, and a_p and $a_{\rm edge}$ are the semi-major axis of the planet and the semi-major axis at which the disk is truncated, respectively (Wisdom 1980; Duncan et al. 1989).

This is in agreement with other studies which showed that the chaotic zone extends radially up to $\sim 3 - 3.5\, R_H$ around the planet's orbit (Ida et al. 2000; Kirsh et al. 2009), where R_H is the Hill radius defined by

$$R_H = a_p \left(\frac{m_p}{3M_\star} \right)^{1/3} \quad . \tag{2.42}$$

If a particle approaches the planet at a distance smaller than a Hill radius, it will enter the Hill's sphere of the planet and may be trapped in 1:1 MMR with the planet, and thus be stabilized on a horseshoe orbit. Therefore, close encounters occur in the vicinity of a planet, beyond 1 Hill radius and below $\sim 3 - 3.5\,R_H$ from the planet. Beyond the chaotic zone, particle will suffer only small deflections of their orbits and will be in secular evolution with the planet, excepted if at a specific MMR location.

This allows to determine the width of the gap created by a planet in a debris disk, and consequently, this is widely used to derive constraints on the location of a planet which is suspected to shape a disk edge, as was done for instance by Quillen (2006); Chiang et al. (2009). One can deduce the semi-major axis of a planet of a given mass that generates a disk inner edge at a given distance retrieved from resolved observations :

$$a_p = \frac{a_{\rm edge}}{1 + 1.5\mu^{2/7}} \quad . \tag{2.43}$$

A close encounter itself can be studied using the Tisserand parameter, which relates the orbital elements of a particle before and after the encounter (see for instance Murray & Dermott 1999), and defined by :

$$C_T = \frac{a_p}{a} + 2\sqrt{\frac{a}{a_p}}\sqrt{1-e^2}\cos i \quad . \tag{2.44}$$

The Tisserand parameter is closely related to the Jacobi invariant which is a conserved quantity in the framework of the circular restricted 3-body system, even after close encounters. Strictly speaking, C_T is not conserved if the perturber is on a non-zero eccentricity orbit, but detailed studies focusing on Jupiter perturbed comets showed that in most cases, C_T remained preserved within $\sim 1\,\%$ despite the eccentricity of Jupiter (Carusi et al. 1995). This tool will be used for cases of moderate eccentricity – 0.1 maximum, in the case of Fomalhaut, which is only twice that of Jupiter – so that we expect C_T to be preserved within a few percents in close encounters. This accuracy is sufficient for our analysis.

Finally, although due to the mass ratio between a particle and a planet, one can in first instance neglect the gravitational effect of a particle on the planet, repeated close encounters with many particles lead to significant exchanges of angular momentum with the planet and planetary migration, and as we shall see in Chapter 5.

2.7 Numerical methods : N-body symplectic codes

Analytical approaches allow one to evaluate the effect of a perturbing planet on a test particle, but since the goal is to study how large-scale asymmetries arise among a population of planetesimals as a collective result of the perturbations on each planetesimal, the use of N-body numerical simulations becomes crucial. Moreover, as was seen in the previous section, analytical tools always suffer more or less approximations, which is very useful to predict qualitative results, but will eventually fail into giving more detailed and exact results. An ideal way to study the dynamics of planetary systems would be of course to be able to solve the equations exactly, but involves of course very extensive computations. Here again, the use of numerical methods enables to reach this goal in a reasonable amount of time.

The basic idea is to treat a whole population of massless test-particles perturbed by a planet, and which do not interact between themselves, nor backreact on the planet, that is, to treat a collection of individual 3-body problems.

This can be achieved using symplectic N-body codes, which are numerical methods specifically dedicated to the long-term integration of the N-body problem, and which have the crucial properties of not accumulating errors on long term and reduce the computational time required for integration, contrary to traditional integration techniques.

As shown in Yoshida (1993), if one considers the following differential equation:

$$\frac{dz}{dt} = f(z) \qquad , \tag{2.45}$$

one can find an approximate solution under the form $z' = \phi(z, \tau)$, from z at $t = 0$ to z' at $t = \tau$, where τ is the timestep. The first method developped to achieve this is the Euler method :

$$z' = \phi(z, \tau) = z + \tau f(z) \qquad . \tag{2.46}$$

This mehod is precise at the first order since this solution is equivalent to the Taylor development of the exact solution:

$$z' = z + \tau f(z) + \frac{\tau^2}{2} f'(z) f(z) + \frac{\tau^2}{6}(f''(z) f(z) + f'(z)^2) f(z) + ... \qquad , \tag{2.47}$$

up to the first order in τ. Therefore, one calls an application $z' = \phi(z, \tau)$ a n^{th} order integrator if it is equivalent to the Taylor development up to τ^n. For instance, the Runge-Kutta integration is of the 4th order.

However, the problem with such traditional integration techniques is that they accumulate errors on long term. If one considers the simple one dimension example of the pendulum, the Hamiltonian of the system reads :

$$H = \frac{1}{2}(p^2 + q^2) \qquad . \tag{2.48}$$

The exact solution is known to be :

$$\begin{pmatrix} q(\tau) \\ p(\tau) \end{pmatrix} = \begin{pmatrix} \cos\tau & \sin\tau \\ -\sin\tau & \cos\tau \end{pmatrix} \begin{pmatrix} q(0) \\ p(0) \end{pmatrix} \qquad , \tag{2.49}$$

and the Hamiltonian, and thus the energy, is a conserved quantity.

However, Euler's technique approximates this solution with :

$$\begin{pmatrix} q' \\ p' \end{pmatrix} = \begin{pmatrix} 1 & \tau \\ -\tau & 1 \end{pmatrix} \begin{pmatrix} q \\ p \end{pmatrix} \qquad , \tag{2.50}$$

and with which the value of the energy is multiplied by a factor $(1 + \tau^2)$ at each timestep. Therefore, the solution eventually diverges from the exact solution during long-term integrations. In order to reduce the error, one can of course reduce the timestep, however, this will require much longer computational time.

N-body symplectic codes address both the problem of error accumulation and computational expense, and as a consequence, the use of these methods has now become mandatory in order to study planetary systems dynamics. Their common origin is the mapping method, introduced by Wisdom & Holman (1991, 1992), based on the following idea: in a long-term evolution, the terms of the Hamiltonian undergoing slow changes become significant, while oscillating terms, if their frequency is high enough, tend to a mean value and no longer significantly contribute to the evolution of the system (Arnold 1978). The method exploits this phenomenon by using a separation of the Hamiltonian system in a sum of terms operating at different timescales.

One can then replace the rapidly oscillating terms by a more easily integrable term without having any effect on the dynamic evolution.

The basic idea is to rewrite the Hamiltonian in a sum of terms easily integrable. For instance, Euler's integration technique applied to a Hamiltonian of the form $H = T(p) + V(q)$, can become symplectic if the two parts of the Hamiltonian are integrated succesively with :

$$q' = q + \tau \left(\frac{\partial T}{\partial p} \right)_{p=p} \quad , \quad p' = p - \tau \left(\frac{\partial V}{\partial q} \right)_{q=q'} \quad , \tag{2.51}$$

and where the second transformation is made at $q = q'$ and not at the initial position, such as in the traditional integration techniques. The entire transformation from the initial state (q, p) to the final state of the system (q', p') is canonical, because it is obtained via the composition of two canonical applications $(q, p) \longrightarrow (q', p)$ et $(q', p) \longrightarrow (q', p')$. This means that the coordinates remained conjugated at each step, and that the shape of the equations and the phase-space structure is always preserved.

As a consequence, the error on the total energy is bound and of the order τ^n for a n order integrator, which makes these integration techniques stable on long timescales. Since it is also not necessary to reduce the timestep to increase the precision of these codes on long-term, symplectic N-body codes enable the use of an integration timestep of the order of the shortest orbital period time involved. A typical timestep of $\sim 1/20$ of the smallest orbital period ensures a conservation of energy with a typical error of $\sim 10^{-6}$ on relative energy. This saves computation time by an order of magnitude and therefore, makes long-term integration much easier to achieve in reasonable amounts of CPU time. For comparison, an identical level of precision would be achieved with the Runge-Kutta method with typical timestep of 1/1000th of the orbital period.

The splitting of the Hamiltonian into easily integrable terms can be achieved in particular using the Jacobian coordinates, as in the MVS (Mixed Variable Symplectic) code. These coordinates consist in successive nestings and are defined by :

$$\vec{x}_1' = \vec{r}_1 \quad , \tag{2.52}$$

and

$$\vec{x}_i' = \vec{x}_i - \vec{r}_{i-1} \qquad 2 \leq i \leq N \quad , \tag{2.53}$$

where $\vec{r}_i$ is the position of the center of mass of the first i bodies.

The use of this coordinate set allows to write the Hamiltonian of the system under the form :

$$H = H_{\text{Keplerian}}(q, p) + H_{\text{interactions}}(q) \quad , \tag{2.54}$$

where $H_{Keplerian}$ is composed of terms of the form $H = p^2/2 - 1/q$. This separation is often used as a natural starting point for various theories disturbances Keplerian motion, because in this case, $H_{\text{Keplerian}} >> H_{\text{interactions}}$, and thus $H_{\text{interactions}} = \epsilon H_{\text{Keplerian}}$, with $\epsilon << 1$. This allows one to use an even longer timestep and achieve N-body simulations faster, with reasonable errors. It is therefore obvious that this splitting of the Hamiltonian was used in the development of numerical methods.

The second order symplectic integration scheme, called KDK (Kick-Drift-Kick) consists in:

- Integrate $H_{interactions}$ over a $\tau/2$ timestep,
- Integrate $H_{Keplerian}$ over a τ timestep,
- Integrate $H_{interactions}$ over a $\tau/2$ timestep.

However, the following conditions must be met:

- the central mass must be the only dominant mass of the system.
- the distance between the bodies must not be too small, that is, the method can not be applied in the case of close encounters.

When these conditions are not fulfilled, the interaction Hamiltonian is of the same order of magnitude as the Keplerian Hamiltonian and the integration method fails. Several solutions were first proposed to solve this last problem:

- the integration step is initially reduced during close-encounters with the RMVS code (Levison & Duncan 1994).
- MERCURY integrator incorporates the interaction terms that become too large during close-encounters into the Keplerian part, but the integration speed is greatly reduced (Chambers 1999).
- SyMBA integrator uses a technique that manages multiple encounters while remaining symplectic, but does not yet support close-encounters with the central mass (Duncan et al. 1998). This problem will be solved by Levison & Duncan (2000) even if the calculations take longer.
- the HJS integrator of Beust (2003) allows to simulate systems in which the central star is not the only dominant mass, that is in multiple stellar systems.

Planetesimals are usually treated as massless test-particles, which removes self-gravity in the disk, as well as a back-reaction of the disk on the planet. In general, both of these phenomena are significant when the planet mass is similar to the disk mass. Debris disk usually contain several Earth masses of material, and the situations investigated in this thesis generally involve planets significantly more massive than the debris disk they coexist with. However, in the case the back-reaction of particles are important in a given problem, as is the case when studying planetesimal-driven migration, since it results precisely from repeated and numerous interactions between planetesimals and a planet, one can use codes such as SyMBA, which still neglects interactions of planetesimals between themselves.

These codes allow to achieve accurate dynamical modelling of planetary systems, and show how planets can generate more or less large scale structures in debris disks. We show the examples of structures mentioned throughout this chapter as revealed by the use of N-body numerical simulations on Figure 2.7.

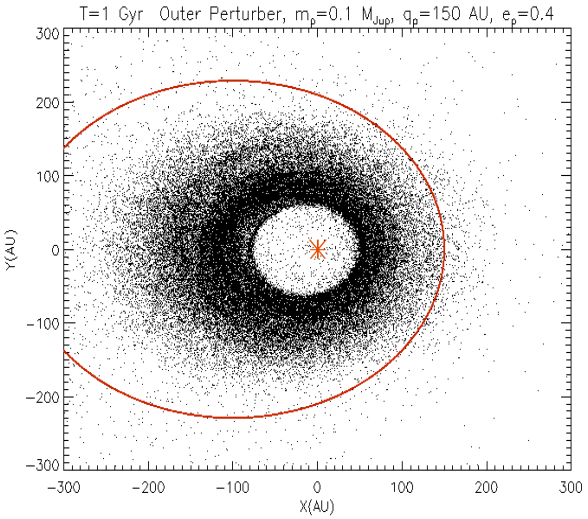

(a) Eccentric pattern

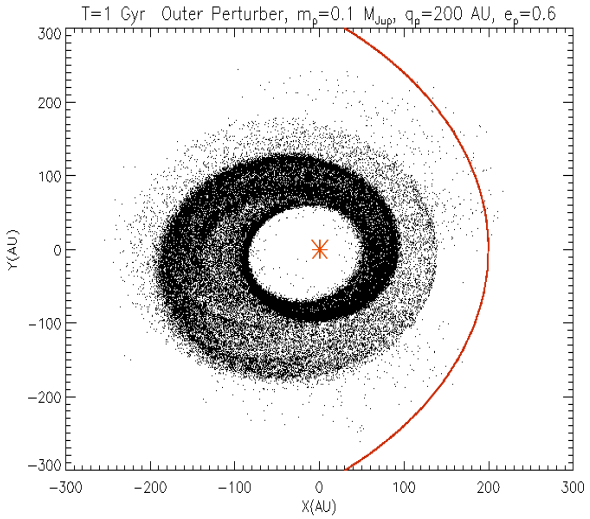

(b) Spirals

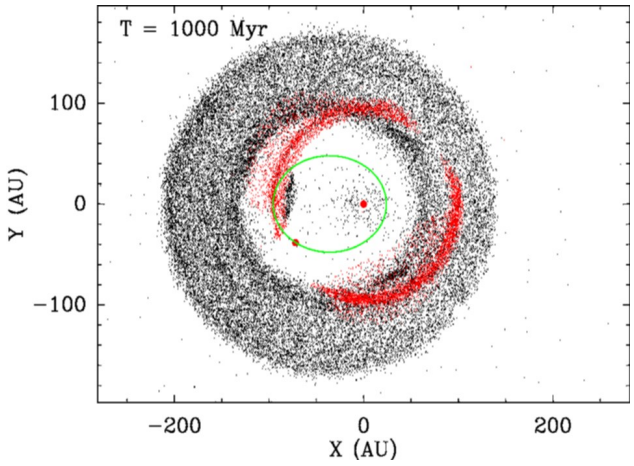

(c) Clumpy resonant structures

Figure 2.7 – **(a)** Eccentric patterns, **(b)** spirals, and **(c)** clumpy resonant structures in debris disks, as evidenced by N-body numerical simulations.

Chapter 3

Picture of a mature Gyr-old system, Faramaz et al. (2014b)

Contents

3.1 The eccentric debris disk of ζ^2 Reticuli

The G1V solar-type star ζ^2 Reticuli (HR 1010, HIP 15371) (Eiroa et al. 2013) is located at 12 pc (van Leeuwen 2007b), has a luminosity $L_\star = 0.97 L_\odot$, $\log g = 4.51$, and is $\sim 2-3$ Gyr old (Eiroa et al. 2013). It has a binary companion ζ^1Reticuli, a G2-4V (Gray et al. 2006; Torres et al. 2006) star located at a projected distance of 3713 AU from ζ^2 Reticuli (Mason et al. 2001). Bayesian analysis by Shaya & Olling (2011) of the proper motions of these stars indicates a very high (near 100%) probability that the pair are physically connected.
The presence of dust around ζ^2 Reticuli has been probed with *Spitzer* (Trilling et al. 2008); the results suggest a $\sim$ 150 K emission at $\sim$ 4.3 AU. However, the angular resolution of *Spitzer* is limited, and the dust spatial distribution remained unconstrained. New observations with *Herschel*/PACS completed the spectral energy distribution (SED), providing the suggestion of an optically thin, $\sim$ 40 K, emission at $\sim$ 100 AU, with fractional luminosity $L_{\rm dust}/L_\star \approx 10^{-5}$ (Eiroa et al. 2010). Moreover, *Herschel*/PACS provided spatially resolved images of the dust thermal emission surrounding ζ^2 Reticuli at 70 μm and 100 μm (Eiroa et al. 2010).

Newly reduced *Herschel*/PACS images are shown in Figure 3.1. The images show a double-lobe feature, asymmetric both in position and brightness. Note that at 70 μm, the probability for alignment with a background source within 10″ is extremely low, namely 10^{-3} (Eiroa et al. 2010). As suggested by Eiroa et al. (2010), the asymmetry revealed by *Herschel*/PACS in the disk of ζ^2 Reticuli can be interpreted as a ring-like elliptical structure with $e \gtrsim 0.3$ seen close to edge-on and extending from $\sim$ 70 to $\sim$ 120 AU, which is fully consistent with the information derived from the SED (Eiroa et al. 2010) and with the best fit inclination of the system, that is 65° with respect to the pole (See Appendix A).

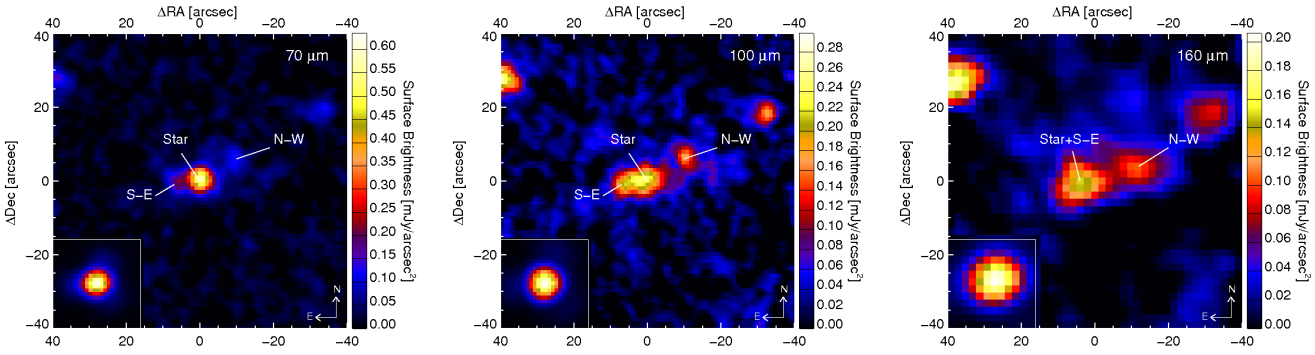

(a) At 70 microns (b) At 100 microns (c) At 160 microns

Figure 3.1 – *Herschel*/PACS images of ζ^2 Reticuli at **(a)** 70, **(b)** 100, and **(c)** 160 microns. North is up and east is left. The inset in the bottom-left corner shows the PSF. The north-west lobe is noted N-W, while the south-east lobe is noted S-E.

Without a doubt, this asymmetric structure provides evidence that "something" is dynamically sculpting the disk. This may be the stellar companion ζ^1Reticuli or a (as yet undetected) planet. The latter hypothesis is fully compatible with radial velocity measurements of ζ^2 Reticuli , which suggest there is no Jupiter-mass (or larger) planet interior to $\sim 5-10$ AU (Mayor et al. 2003), but which put no contraints on a small planet or a Jupiter-like planet at larger radii. It is also compatible with growing observational evidence for planets at large orbital separation, that is, several tens to a few hundreds of AU from their host star (see, e.g., Luhman et al. 2007; Kalas et al. 2008; Marois et al. 2008, 2010). Constraints from direct imaging do not provide constraints on companions beyond a projected distance of $\sim$ 30 AU, and the presence of a brown dwarf within $\sim$ 20 AU is still compatible with observations (See Appendix A).

The modelling of eccentric patterns in debris disks and their possible link with the dynamical influence of eccentric companions has been investigated in several earlier studies: authoritative work was carried out by Wyatt et al. (1999, 2000) for the case of HR 4796. Another case of interest is the debris disk of Fomalhaut (Stapelfeldt et al. 2004; Kalas et al. 2005; Quillen 2006; Chiang et al. 2009; Boley et al. 2012; Kalas et al. 2013; Beust et al. 2014). However, these studies considered low eccentricity rings ($e \gtrsim 0.02$ for HR4796 and $e = 0.11 \pm 0.1$ for Fomalhaut), and were limited to timescales smaller than the typical ages of mature disks ($\leq$ 10 Myr for HR4796 simulations and $\leq$ 100 Myr for Fomalhaut). The issue of whether highly eccentric ring structures could be sustained over very long timescales has not been addressed thus far in the literature. This issue has become very topical because of the discovery of at least two Gyr-old and significantly eccentric debris disks: that around ζ^2 Reticuli , and another one around HD 202628 ($e \sim 0.18$ Stapelfeldt et al. 2012; Krist et al. 2012). These systems are both older than Fomalhaut or HR 4796, with disks that are also much more eccentric.

The ζ^2 Ret system provides an excellent proxy to investigate the long-term evolution of highly eccentric structures in debris disks, and their relation to planetary or stellar perturbers, by investigating their Gyr timescales. In addition with the setting of constraints on the belt-shaping perturber, the question we would like to address is whether this structure is really Gyr-old, or might have originated from a more recent event, be it a flyby or the late excitement of a sherpherding planet's eccentricity.

3.2 Modelling approach

The goal of this work is to set constraints on the belt-shaping pertuber evidenced in the ζ^2 Reticuli system, and determine whether this perturber is able to shape and maintain a disk into a significantly eccentric ring structure on Gyr timescales. This involves the development of a dynamical model to investigate the shaping of a debris disk into an eccentric ring, and the timescales associated with its onset and survival, based on the current understanding on how eccentric ring structures arise as a result of the dynamical effect of an eccentric perturber. This dynamical model includes analytical predictions, which as will be shown, must be complemented by numerical studies.

3.2.1 Analytical model

As seen in Section 2.4, the onset of an eccentric ring structure is a matter of few precession timescales $t_{\rm prec}$, as seen in Eq. (2.32), while the value of the disk global eccentricity is to be linked with the planetesimals' forced eccentricity e_f, and thus to the perturber's eccentricity e_p. There are several ways to analytically derive the forced eccentricity e_f and the precession rate $t_{\rm prec}$. The most classical one, exposed in Section 2.4, is to apply the linear Laplace-Lagrange theory, which is an expansion of the interaction Hamiltonian to second order in ascending powers of the eccentricities of the two bodies and an averaging over the two orbits. However, this approach is valid only for low eccentricities, but the perturber's orbital eccentricity e_p is not necessarily low. Therefore, restricting the analytical study to small e_p may not be appropriate here in the case of the modelling of a debris disk as eccentric as that of the ζ^2 Reticuli system.

Another way to proceed is to expand the interaction Hamiltonian in spherical harmonics and truncate it at some order in α, where α is the ratio[1] between a and a_p, the planetesimal and the perturber's semi-major axis, respectively, and to average after over the two orbits. This permits us to perform an analysis without any restriction on the eccentricities. The resulting Hamiltonian is given by Krymolowski & Mazeh (1999), Ford et al. (2000), or Beust & Dutrey (2006). To the lowest order in α (second order, quadrupolar), it yields a forced eccentricity e_f :

$$e_f \simeq \frac{5}{4}\frac{\alpha e_p}{1-e_p^2} \quad . \tag{3.1}$$

This expression is given by Augereau & Papaloizou (2004) and Mustill & Wyatt (Eq. (8) of 2009).

The method given by Mardling & Lin (2002) was used to derive the precession rate $\mathrm{d}\varpi/\mathrm{d}t$ in the spherical harmonic expansion case :

$$\begin{aligned}\frac{\mathrm{d}\varpi}{\mathrm{d}t} &= \frac{3n}{4}\frac{m_p}{M_\star}\alpha^3\frac{\sqrt{1-e^2}}{(1-e_p^2)^{3/2}} \\ &\quad + \frac{45n}{256}\frac{m_p}{M_\star}\alpha^5\frac{(4+3e^2)(2+3e_p^2)\sqrt{1-e^2}}{(1-e_p^2)^{7/2}} \quad .\end{aligned} \tag{3.2}$$

which allows to retrieve $t_{\rm prec}$ thanks to Eq. (2.32).

With this we analytically predict the effect of a perturber on a debris disk, that is, for a given set of values of e_p and of the planet periastron q_p, one can derive the precession timescale $t_{\rm prec}$. Conversely, one can set this dynamical timescale and the forced eccentricity for a particle with semi-major axis a to correspond to those derived from observations of an eccentric debris disk, and thus initially estimate the perturber's characteristics (see Figure 3.2).

[1] α is such that $\alpha < 1$, always, and thus $\alpha = a_p/a$ if $a_p < a$, and inversely, $\alpha = a/a_p$ if $a_p > a$.

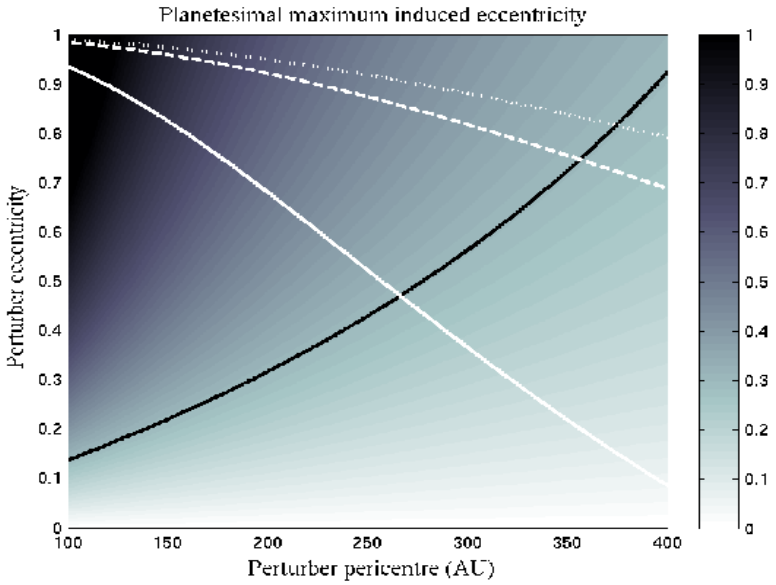

Figure 3.2 – Example colour map of the maximum induced eccentricity $2e_f$ imposed by a planetary perturber on a particle with semi-major axis 100 AU and eccentricity $e = 0$ as a function of its periastron and eccentricity, as estimated from Eq. (3.1). The black line corresponds to a $2e_f = 0.3$ condition, which was set to mimic the condition for the disk of ζ^2 Reticuli . Note that it does not depend on the mass of the planet. The white lines show the parameters for which the typical timescale to reach a steady state at 100 AU is $t_{\rm prec} = 1\,$Gyr, using Eq. (2.32). This timescales depends on the mass: $m_p = 0.1\,M_{\rm Jup}$ *(solid line)*, $1\,M_{\rm Jup}$ *(dashed line)* and $2\,M_{\rm Jup}$ *(dotted line)*. For example, a perturber of mass $0.1\,M_{\rm Jup}$, periastron $q_p = 150\,$AU and eccentricity $e_p = 0.4$ is expected to produce a significantly eccentric ring in shorter than 1 Gyr, although spiral patterns may remain since it can take several precession timescales for them to vanish, as was shown by Wyatt (2005).

However, the problem is more complex for real disks, which have a finite spatial extension, since these estimates depend on radial locations. To first order, it can be seen from Eqs. (3.1), (3.2), and (2.32), that the forced eccentricity and the secular timescale scale as :

$$e_f \propto \alpha \quad , \tag{3.3}$$

and

$$t_{\rm prec} \propto \frac{1}{m_p \alpha^3} \quad . \tag{3.4}$$

If $a_{\rm in}$ and $a_{\rm out}$ are the inner and outer limits of the disk in the semi-major axis, and $e_{f,\rm min}$ and $e_{f,\rm max}$ are the minimum and maximum eccentricities induced across the disk[2], and the minimum and maximum precession timescales, $t_{\rm prec,min}$ and $t_{\rm prec,max}$, are defined in the same manner, then, using Eq. (3.3) and Eq. (3.4), one obtains :

$$\frac{e_{f,\rm max}}{e_{f,\rm min}} = \frac{a_{\rm out}}{a_{\rm in}} \quad , \tag{3.5}$$

and

$$\frac{t_{\rm prec,max}}{t_{\rm prec,min}} = \left(\frac{a_{\rm out}}{a_{\rm in}}\right)^3 \quad . \tag{3.6}$$

It is easy to see from these equations that the secular precession timescale spans a wide range of values across the disk. This means that making analytical predictions by setting the desired values for the forced eccentricity and the secular precession timescale for a particle with semi-major axis at the centre of the distribution suffers limitations when applied to an extended disk, especially concerning the timescale.

Eqs. (3.5) and (3.6) can be rewritten using Δa, the half width of the disk extent, along with $e_{f,c}$ and $t_{\rm prec,c}$, the forced eccentricity and secular precession timescale at a_c, the typical semi-major axis of a test-particle in the ring, respectively :

$$e_{f,\rm max/min} = \left(\frac{a_c \pm \Delta a}{a_c}\right) e_{f,c} \quad , \tag{3.7}$$

and

$$t_{\rm prec,max/min} = \left(\frac{a_c \pm \Delta a}{a_c}\right)^3 t_{\rm prec,c} \quad . \tag{3.8}$$

Applying this to the ζ^2 Reticuli system by setting $a_c = 100$ AU, $\Delta a = 25$ AU, $2e_c = 0.3$ and $t_{\rm prec,c} = 1$ Gyr, one obtains :

$$\begin{cases} 2e_{f,\rm min/max} = 0.225 - 0.375 \\ t_{\rm prec,min/max} = 0.42 - 1.95\,{\rm Gyr} \end{cases} \quad . \tag{3.9}$$

In these conditions, the extent of the disk is not expected to affect the global eccentricity of the disk too much, that is, it is expected that the global eccentricity recovered on average corresponds to the forced eccentricity at a_c after the steady state is reached. But the problem is that the extent of the disk strongly affects the timescale to reach this steady state. This is a limitation of the analytic approach that can be overcome by the use of numerical simulations.

[2] $e_{f,\rm min} = e_{f,\rm in}$ and $e_{f,\rm max} = e_{f,\rm out}$ for an inner perturber and vice versa for an outer one.

3.2.2 N-body simulations

Numerical N-body simulations can be used to move beyond the simplified analytical approach and explore the high-eccentricity case on Gyr timescales. The frame chosen is this of the three-body problem, that is, one central star, a planet, and a mass-less planetesimal. The symplectic N-body code SWIFT-RMVS of Levison & Duncan (1994) was used to integrate the evolution of a ring of 150,000 mass-less planetesimals around a solar-mass star, over 1 Gyr.

The radial extent of the model disk was configured to closely match the observed properties of the disk around ζ^2 Reticuli , that is, these planetesimals were uniformly distributed between 70 and 140 AU (except when specified otherwise).

Their initial eccentricities were randomly distributed between 0 and 0.05, and initial inclinations between $\pm 3°$, while the remaining angles (longitudes of nodes and periastra) were randomly distributed between 0 and 2π. These values are summarised in Table 3.1. This reasonably well mimics the low eccentricities and inclinations expected at the end of the protoplanetary phase.

Using mass-less test particles removes self-gravity in the disk, as well as a back-reaction of the disk on the planet. In general, both of these phenomena are significant when the planet mass is similar to the disk mass. There is no mass estimate for the debris disk of ζ^2 Reticuli . However, a well-studied case is the debris disk of Fomalhaut, whose mass was estimated to be $\sim 3-20\,M_\oplus$ (Wyatt & Dent 2002; Chiang et al. 2009). Since a debris disk loses material over time due to the combined effects of collisional evolution, Poynting-Robertson drag, and radiation pressure, and since ζ^2 Reticuli is much older than Fomalhaut (440 Myr; Mamajek 2012), it is reasonable to assume that the debris disk surrounding ζ^2 Reticuli does not contain more than a few Earth masses. In this case, it is also reasonable to assume that the disk self-gravity and back-reaction are negligible, and the planet will still be able to imprint on the disk structure if its mass is at least $0.1 M_{\rm Jup} \sim 32\,M_\oplus$.

Parameters	Values
Number of particles	150,000
Semi-major axis (AU)	$a_{\rm min} = 70$; $a_{\rm max} = 140$
Eccentricity	$e_{\rm min} = 0$; $e_{\rm max} = 0.05$
Inclination (°)	$i_{\rm min} = -3$; $i_{\rm max} = 3$

Table 3.1 – Initial parameters for the planetesimals used in our N-body simulations

Two planet-disk configurations were considered, inside and outside the planetesimal belt, and parametric exploration of their influent orbital elements were conducted. In all cases, the perturber was considered to be coplanar to the disk. In the case of a planet interior to the initial ring, the inner edge of the disk was considered to be located at 70 AU, and assumed to be truncated by the chaotic zone generated by a coplanar planet. Consequently, both the mass and eccentricity of the perturber were explored, fixing its semi-major axis to the value deduced from Eq. (2.43). Here the disk initial inner edge was fixed halfway between 70 AU and the planet semi-major axis. The case of a more massive perturber such as a brown dwarf, located farther inside the system, was also considered. The second case considered is that of a planet exterior to the ring. While an inner edge is in general considered as a clue for the presence of inner perturbers, it is obviously more of a conjecture to assume that an outer edge is formed in the same manner, since a disk instrinsically has an outer limit. Therefore, the outer edge was not assumed here to be formed because of resonance overlap, and the planet periastron was fixed instead, to ensure that it does not cross the disk.

The ability of the binary companion ζ^1 Ret to produce the observed pattern was also tested. In this case, the orbital characteristics of ζ^1 Ret were chosen by considering the eccentricity it should have given its projected distance to ζ^2 Reticuli in order to force the eccentricity of the disk test-particles to 0.3, thanks to Eq. (3.1) (See Faramaz et al. 2014b, for more details). All the configurations explored are summarised in Table 3.4.

The global aspect of the disks at 1 Gyr will be examined, and in the case an eccentric pattern has arisen, the global eccentricity of the disk will be evaluated considering the geometry of an ellipse: the offset δ of the centre of symmetry from one of the foci of an ellipse is simply the product of its semi-major axis a by its eccentricity e, that is, $\delta = ae$.

For a disk from our simulations, δ can be obtained by calculating the centre of symmetry of the disk, using the positions of the test particles in the asterocentric frame : δ is the distance of this centre of symmetry to the star. The disk semi-major axis a is determined as follows : the disk was divided into superimposed angular sectors of 3°. For each of these sectors, the radial distribution of the particles is fitted to a Gaussian. This provides the radial position of the maximum density for each angular sector, and thus a set of points defining the global shape of the disk. It is then straightforward to retrieve a from this set of points by seeking for the major axis, that is, the maximum distance between two opposite points. Finally, the disk eccentricity is simply $e = \delta/a$.

3.2.3 Synthetic images

The modelling process can be furthermore completed by using results of the best-fit N-body simulations to produce a realistic dust population and synthetic images, in order to achieve full comparison with *Herschel*/PACS observations. The procedure followed to create synthetic images is straightforward: a population of dust can be created from the position of their parent planetesimals, retrieved from a simulation that leads to a clear and significantly eccentric disk.

The main difference between dust particles and planetesimals is that the former are small enough to be affected by stellar radiation pressure. Radiation pressure is usually described for a particle by its constant ratio β to stellar gravity. The dust particles are assumed to be released by planetesimals, which feel no radiation pressure. Hence the daugther particles assume an orbit that is very different from that of their parent bodies. It is well known that if the parent bodies move on circular orbits, the dust particles are unbound from the star as soon as $\beta \geq 0.5$. In our case, however, dust particles may be released by planetesimals orbiting on more or less eccentric orbits, which may slightly change this threshold. Because planetesimal eccentricities are expected to be moderate on average, $\beta = 0.5$ can nevertheless be considered as a reasonable approximation. Small grains are released from seed planetesimal positions at the planetesimal velocity, and are then spread along the orbits determined by these initial conditions and their β value. The dust grain sizes range was set from 0.5 μm to 1 mm, with a classical Dohnanyi (1969) power-law distribution (index -3.5), which covers the β distribution from 0 to 0.5 well, since this parameter depends on grain size. Their emission was computed using the radiative transfer code GRaTeR (see, e.g., Lebreton et al. 2012). To do this, the following parameters are required: distance of the star (12 pc), magnitude in band V ($V = 5.24$), and total luminosity $0.96\,L_\odot$.

Because the disk is optically thin, its mass is linearly linked to the flux emission intensity, and it can be easily scaled to fit the observed intensity (see Table 3.2). It is important to note that these fluxes are only lower limits. The mass needed for the disk to produce a flux as observed on *Herschel*/PACS will vary with the dust grain composition, and thus its density.

Wavelength (μm)	Stellar flux (mJy)	Disk flux (mJy)
70	24.9 ± 0.8	8.9 ± 0.8
100	13.4 ± 1.0	13.5 ± 1.0
160	19.4 ± 1.5	
	~ 4.7	~ 14.7

Table 3.2 – Stellar and disk fluxes at 70, 100, and 160 μm (Eiroa et al. 2010). The fluxes at 70 and 100 μm, along with the total flux of the star-disk system at 160 μm are PACS measurements. The individual star and disk fluxes at 160 μm result from predictions.

But because there is no constraints on the dust composition, astrosilicate grains were used (Draine 2003), and the mass of the disk was simply scaled to obtain intensities compatible with observational constraints for a given wavelength.

Thermal emission images were produced with a resolution of $1''$/pixel at 70 and 100 μm and $2''$/pixel at 160 μm. Before convolving these images with the point spread function (PSF), the star was added at the central pixel with a flux intensity matching the predicted stellar photosphere flux density in each waveband. The position angles of the disk observed with *Herschel*/PACS and of the disk in the synthetic images, as well as the orientation of the telescope during the observations were taken into account (see Table 3.3). The disk inclination was set to its best fit, that is 65.5°.

	Wavelength (μm)	PA(°)
Observed disk	-	110
Simulated disk	-	110
PSF	70/160	127
PSF	100/160	127
ζ^2 Reticuli	70/160	281
ζ^2 Reticuli	100/160	281

Table 3.3 – Disk position angle observed with *Herschel*/PACS, disk position angle in our synthetic images, and telescope orientation during *Herschel*/PACS observations and PSF.

3.3 New constraints on the ζ^2 Reticuli system

3.3.1 Constraints on perturbers : N-body simulations

In Faramaz et al. (2014b), we used ζ^2 Reticuli as an example to discuss the shaping of a disk into an eccentric ring on Gyr timescales. Firstly, we showed that the binary companion ζ^1 Ret cannot be directly responsible for the eccentric ring structure. Indeed, the disk is truncated at ~ 80 AU, as seen in Figure 3.3(a), which is incompatible with observational constraints of the debris disk of ζ^2 Reticuli , since it radially extends up to ~ 120 AU. Moreover, the final disk has a highly symmetric shape and no clear offset from the star, as seen in Figure 3.3(b). These results suggest that the disk asymmetry is instead caused by a closer companion, either interior or exterior to the disk.

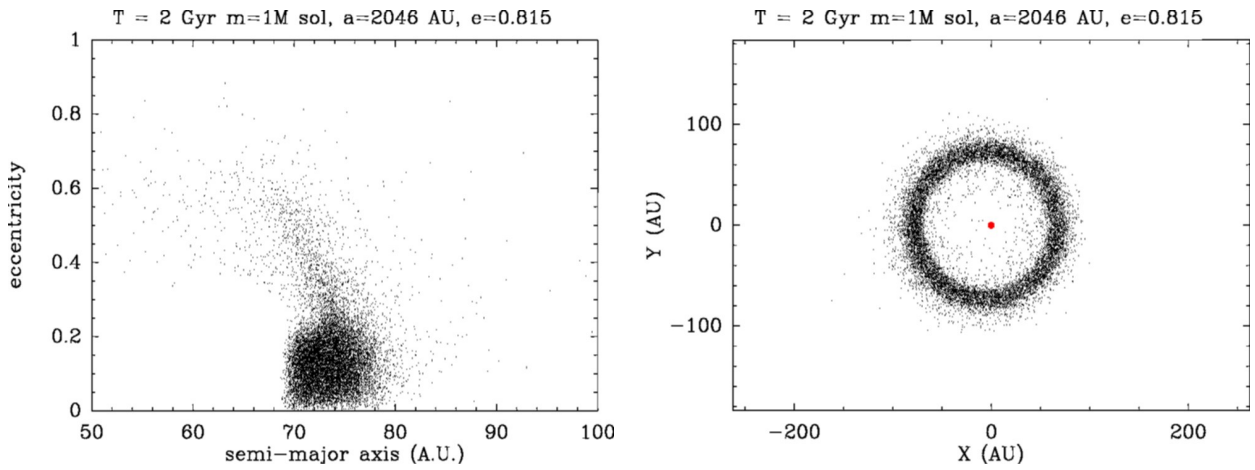

(a) Semi-major axis vs eccentricity diagram (b) Upper view

Figure 3.3 – **(a)** Semi-major axis vs eccentricity diagram, and **(b)** pole-on projection of a disk of planetesimals after 2 Gyr under the influence of a one-solar-mass star of semi-major axis 2046 AU on an orbit of eccentricity 0.815. The disk is truncated at ~ 80 AU and nearly circular. It has no clear offset: its centre of symmetry is offset by ~ 6 AU from the star along the perturber major axis. With a disk mean semi-major axis of ~ 70 AU, this gives a global eccentricity of ~ 0.08.

We showed that eccentric patterns in debris disks can be maintained on Gyr timescales, but also that eccentric perturbers can produce patterns other than eccentric rings. Our results can be classified in five categories, which we describe hereafter, along with the constraints these allow to set on the perturber at the origin of the eccentric pattern in the disk. A summary of these results can be found in Table 3.4.

Steady state with $e < 0.2$ or $e > 0.2$

In our simulations, none of our 0.2 eccentric perturbers created the desired eccentric structure, even in the limit case predicted analytically, where a 0.1 $M_{\rm Jup}$ perturber has a pericentre $q_p = 150$ AU and eccentricity $e_p = 0.2$ (see Figure 3.2). Eiroa et al. (2010) derived a lower limit for the eccentricity of the disk in ζ^2 Reticuli of 0.3. Therefore, given the uncertainties in the estimation of the disk global eccentricity we computed from our simulations, a disk global eccentricity lower than 0.2 was discarded in our analysis. As a consequence, the best candidates have eccentricities $\sim 0.4 - 0.6$. We show such examples in Figure 3.4. Constraints can also be set on the mass of the putative perturber, which we detail hereafter in the next sections.

Scattered disks

The general results of our simulations show that both inner and outer perturbers can generate extremely significant scattering processes. They can cause a disk to adopt structures that show no clear elliptic ring : the inner part of the disk is either filled in the case the inner perturber is not massive enough to scatter material out of the system, as shown in Figure 3.5(a), or the structure is destroyed in the case the outer perturber is too massive, shown in Figure 3.5(b). These scattering processes endanger the survival of an eccentric ring, and investigating these processes with numerical experiments allowed us to put constraints on potential perturbers. From these constraints, we derived an upper-mass limit of 2 $M_{\rm Jup}$ for an outer perturber located in a range of periastra $150 - 250$ AU, whereas a lower-mass limit of 0.1 $M_{\rm Jup}$ is associated with inner perturbers in the ζ^2 Reticuli system.

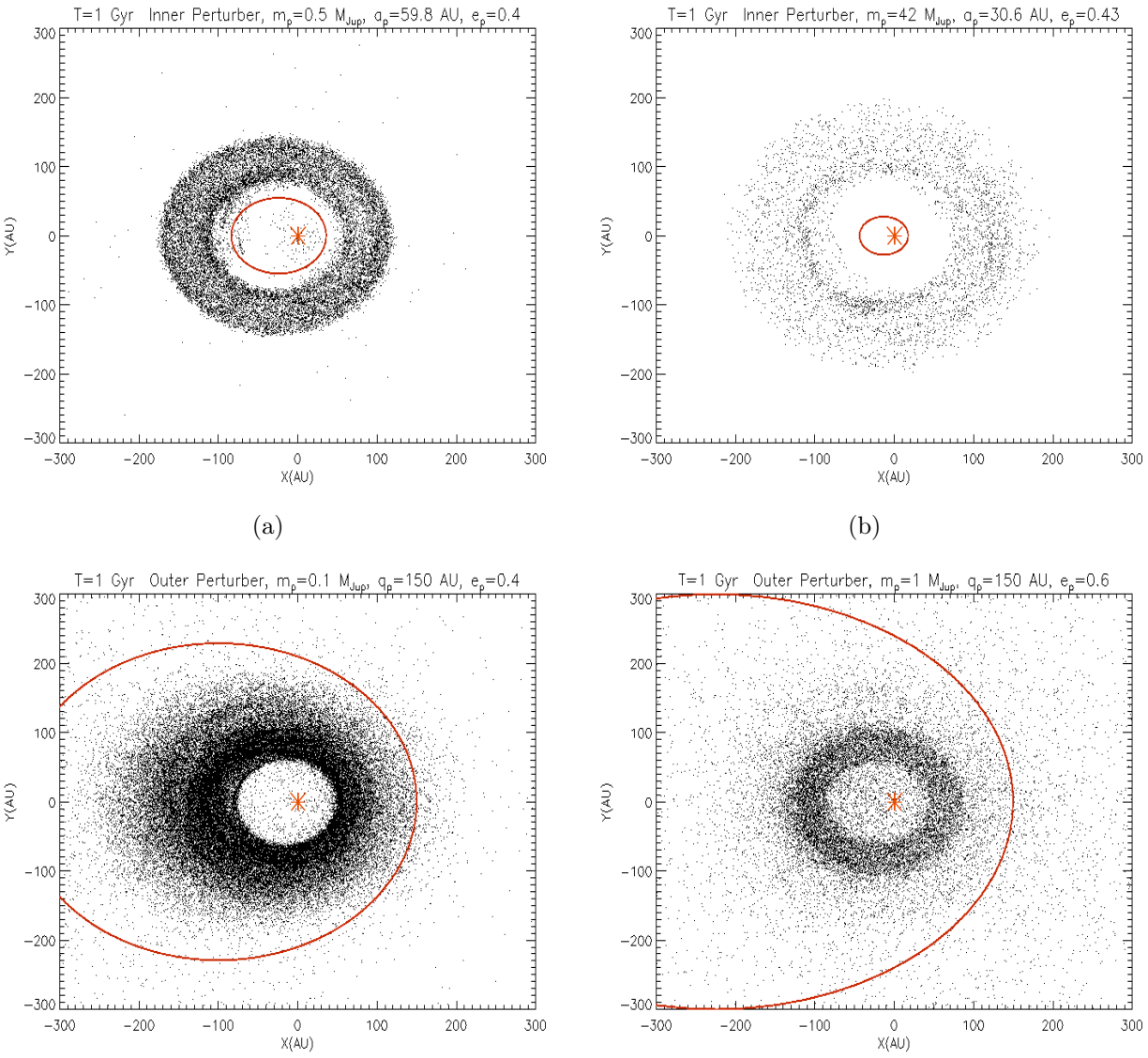

(a) (b)

(c) (d)

Figure 3.4 – Example views from above the plane of disks at 1 Gyr, under the influence of best candidates perturbers. **(a)** Case B. **(b)** Brown-dwarf case. **(c)** Case D. **(d)** Case F. One might question the contribution of the scattered material to the disk emission.

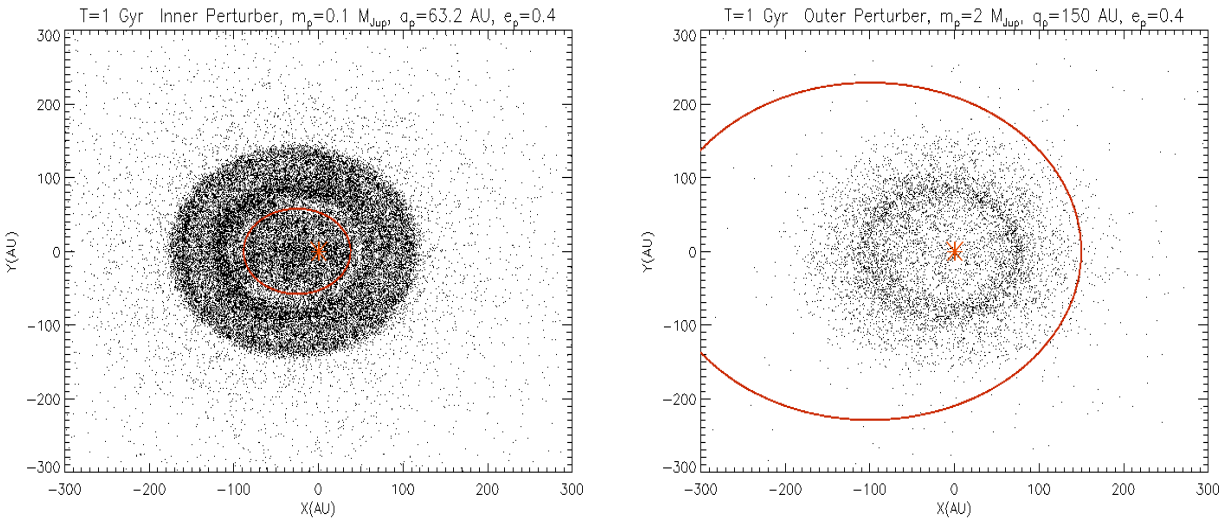

(a) Inner perturber, Case A

(b) Outer perturber, Case G

Figure 3.5 – Example views from above the plane of scattered disks at 1 Gyr, generated by **(a)** an inner perturber and **(b)** an outer perturber.

Resonant patterns

Remarkarbly, for very eccentric ($e_p = 0.6$) inner perturbers of mass between 0.5 and 1 $M_{\rm Jup}$, resonant clumpy structures may arise. An example is Case C, shown in Figure 3.6, where two populations in resonance with the planet, namely the 3:2 and 2:1 mean-motion resonances, are highlighted. Typically, a population in 3:2 resonance is associated with capture during outward planetary migration, as is the case in our own solar system (Malhotra 1993, 1995). But here, these structures most probably appear because we used the chaotic-zone formula defined by Eq. (2.43) to determine the perturber semi-major axis, which was derived for perturbers on circular orbits.

Therefore, it is expected that this formula works less efficiently with increasing orbital eccentricity of the perturber : the result is that the planet digs into the disk, and consequently, planetesimals unprotected against close encounters by mean-motion resonance are scattered out, leaving the resonant structures apparent. This is supported by the fact that these resonant structures disappear when the constraint given by the chaotic-zone formula is applied to the perturber's apastron instead of its semi-major axis, as for an inner brown-dwarf-type companion. Interestingly, the observation of these resonant structures in a system may provide other clues on the dynamical history of a perturber than an outward migration : it may mean that the planet was originally shaping the inner edge of the disk before it was set on an eccentric orbit. However, these are thin structures, and when the disk is seen close to edge-on, as is the case for ζ^2 Reticuli , they would most probably be hidden by the non-resonant population.

Spiral patterns

Case E is shown in Figure 3.7. The system shows a spiral pattern at 1 Gyr, which, according to analytical predictions, corresponds to one precession timescale (see Figure 3.2). Thus, our N-body integrations confirm what was noted by Wyatt (2005): the analytical formula appears to be a lower limit and several precession timescales are sometimes necessary for spiral patterns to vanish. The effect of spirals can also be seen in the evolution of the disk offset, which oscillates, as can be seen in Figure 3.8(b).

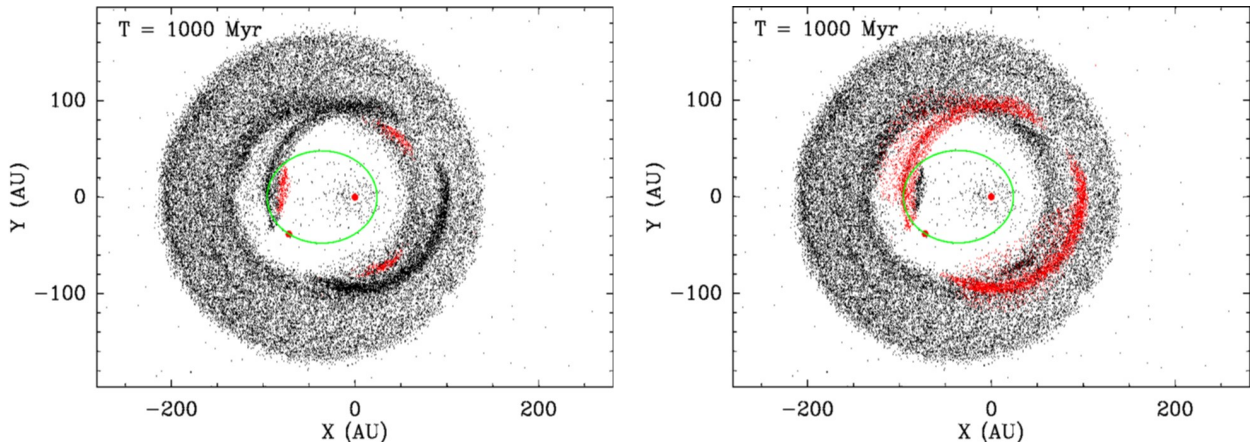

(a) 3:2 MMR (b) 2:1 MMR

Figure 3.6 – Views from above the plane of disks at 1 Gyr in Case C, i.e., where resonant patterns appear. Planetesimals in **(a)** 3:2 and **(b)** 2:1 mean-motion resonance with the perturber are shown in red.

If we had observational proof that the disk of ζ^2 Reticuli has reached steady state and contains no spiral pattern, the results of our numerical investigation would allow us to place a lower mass limit of 0.1 $M_{\rm Jup}$ on an outer perturber in a range of periastra from 150 to 250 AU, based on a dynamical timescales criterion, otherwise it takes longer than 1 Gyr to generate a steady-state eccentric disk. This limit still holds for larger periastra than the range explored, since dynamical timescales increase with distance. But because of the slightly edge-on orientation of the disk and the resolution of the *Herschel*/PACS images, it is extremely difficult to discard a possible spiral pattern in this disk, and no lower mass limit can be clearly defined for an outer perturber.

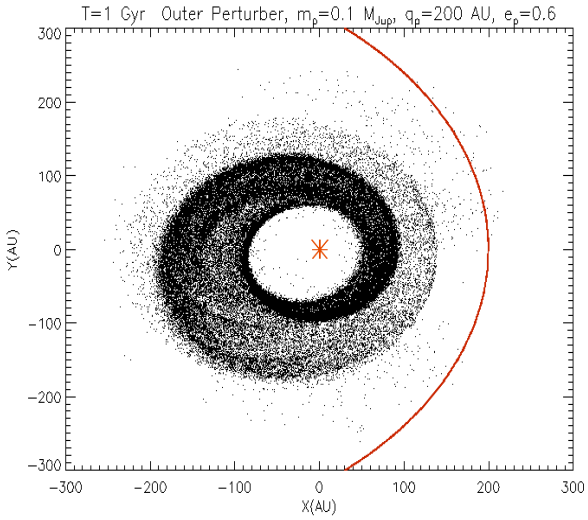

Figure 3.7 – Example view from above the disk plane at 1 Gyr, under the influence of the Case E perturber : spirals are still apparent.

Finally, the offset of the disk centre with respect to the star is mostly stable; however, we note that it seems to relax very slowly in rare cases, as shown in Figures 3.8(c) and 3.8(d). While the former evolution is characteristic for pericentre glow dynamics, the latter one is surprising. The relaxation of the eccentric structure is not expected in the first-order secular analysis described by Wyatt et al. (1999) and Wyatt (2005).

It may be the result of higher-order terms that have been neglected in the analytical study, and is more probably caused by erratic short-term variations of the planetesimals' semi-major axes due to moderately distant approaches to the planet. These effects, which can lead to scattering of the planetesimals, are eliminated in the analytical averaging process of the perturbations, and thus cannot be predicted analytically in the secular approximations used here.
In summary, we showed that eccentric patterns in debris disks can be maintained on Gyr timescales, but also that eccentric perturbers can produce patterns other than eccentric rings. Inspection of these patterns in the context of the modelling of the eccentric debris disk of ζ^2 Reticuli has allowed us to set constraints on the mass, distance, and eccentricity of the suspected perturber at play in this system. This perturber is in any case distant of several tens of AU from its host star, and is on an orbit of eccentricity $\gtrsim 0.3$. It could be either an inner or an outer perturber. An inner perturber as massive as a brown dwarf can create the desired pattern, but should have a mass $> 0.1\ M_{\rm Jup}$, whereas an outer perturber with a periastron in the range $150 - 250$ AU should have a mass $\lesssim 2\ M_{\rm Jup}$.

Table 3.4 – Summary of numerical experiments with an inner and outer perturber, and for a brown dwarf and the stellar binary companion ζ^1 Reticuli. Description of the disk at 1 Gyr: I) steady state, $e < 0.2$, II) steady state, $e > 0.2$, III) scattered disk, IV) resonant pattern, V) spiral pattern. The example cases highlighted in more detail in Section 3.3.1 are labelled from A to G.

Inner perturbers				
$m_p\,(M_{\rm Jup})$	a_p (AU)	$e_p = 0.2$	$e_p = 0.4$	$e_p = 0.6$
0.1	63.2	I	III,A	III
0.5	59.8	I	II,B	IV,C
1	57.9	I	II	IV

Outer perturbers				
$m_p\ (M_{\rm Jup})$	q_p (AU)	$e_p = 0.2$	$e_p = 0.4$	$e_p = 0.6$
	150	I	II,D	V
0.1	200	I	V	V,E
	250	V	V	V
	150	I	II	III,F
1	200	I	II	II
	250	I	I	II
	150	I	III,G	III
2	200	I	I	I
	250	I	I	II

Other perturbers			
Perturber	m_p	Orbital parameters	Result
Brown dwarf	$42\,M_{\rm Jup}$	$a_p = 30.6$ AU ; $e_p = 0.43$	II
ζ^1 Reticuli	$1\,M_\odot$	$a_p = 2046$ AU ; $e_p = 0.815$	I

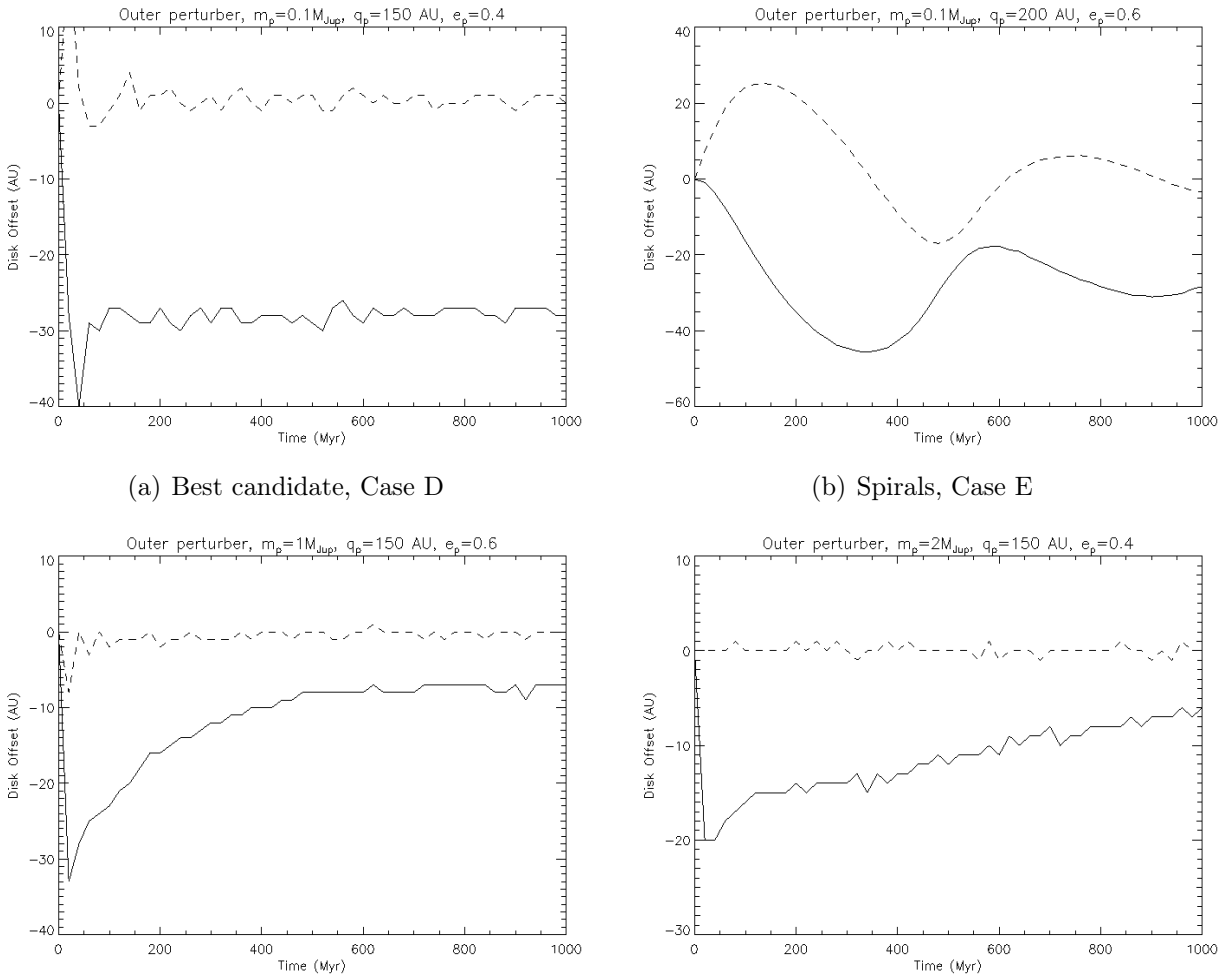

(a) Best candidate, Case D

(b) Spirals, Case E

(c) Relaxation, Case F

(d) Relaxation, Case G

Figure 3.8 – Example of the time evolution on 1 Gyr of the disk offset coordinates (X *(solid line)* and Y *(dashed line)*) for outer perturbers. **(a)** One of the best candidates (Case D). Because of the orientation of the perturber orbit, where its semi-major axis is along the X-axis with positive periastron, this corresponds to a negative X-offset $\Delta X \sim -30\,\mathrm{AU}$ and a zero Y-offset for a disk located at $a_c \sim 100\,\mathrm{AU}$. **(b)** The oscillations of the offset coordinates reveal the spiral-winding regime (Case E). **(c)** and **(d)** The offset seems to relax (Cases F and G).

3.3.2 Constraints on the disk : Synthetic images

We chose a simulation that led to a clear and significantly eccentric disk at 1 Gyr, namely our Case A, to reproduce the *Herschel*/PACS image at 100 μm. The mass of the disk was scaled so that a total flux of 13.5 mJy as observed with *Herschel*/PACS at 100 μm was spread all over the disk. These first images show no difference between a symmetric and an asymmetric state because of the contrast between the star and the disk emission. Moreover, the disk flux per pixel is one order of magnitude lower than the fluxes observed in *Herschel*/PACS images. This is not surprising, however : to estimate the total disk flux, the flux was measured in a small region of the disk before applying aperture correction. Even if the correct aperture correction for a point source were used, it would always be a lower limit, and the total disk flux would be underestimated. The parent ring may also be narrower, which would increase the flux per pixel.

Therefore, we investigated the impact of the width and of the total flux of the disk on the features visible with PACS and produced convolved images of a dusty disk produced by an asymmetric eccentric parent ring of diverse total fluxes (1, 2, and 5 times the flux measured by *Herschel*/PACS) and of diverse widths (semi-major axis centred on 100 AU, widths 5, 10, and 20 AU). To do this, particles from a range of semi-major axes from our N-body simulation output were selected. The fluxes per pixel recovered in convolved images with a disk five times more massive than the mass initially derived from observations match the observations better. This provides a better constraint on the disk mass and total flux.

Finally, investigation of the location of the disk by producing convolved images of a ring of dust produced by a narrow eccentric parent ring of width 5 AU and semi-major axis centred on 120, 130, and 140 AU, and comparison with the *Herschel*/PACS image, reveals that a parent ring located slightly farther away than derived by Eiroa et al. (2010), such that its a semi-major axis distribution is centred between 120 and 140 AU, gives the best fit to observations, as shown in Figure 3.9.

This slightly changes the constraints derived on potential perturbers, but the forced eccentricity only depends on the ratio between the planet and planetesimal semi-major axis, and in a linear way at lowest-order approximation. This means that in this approximation the constraints can be completely scaled in a linear way, that is, the potential semi-major axis for planets must also be increased by 20–40 % and the disk needs to be centred on 120–140 AU, while the constraint on the perturber eccentricity ($e \gtrsim 0.3$) remains identical.

By producing synthetic images, we showed that the original interpretation of the double-lobed feature around ζ^2 Reticuli , that is, the observed eccentric ring $e \gtrsim 0.3$, is clearly supported, although the disk is located slightly farther away (20–40%) than originally derived. Moreover, we found that the dusty disk is probably created by a narrow parent ring (width <10 AU), which should have a slight inclination with the line of sight, compatible with the most probable inclination derived for the system, and it also has a significantly higher flux than that estimated from the *Herschel*/PACS measurements (at least five times).

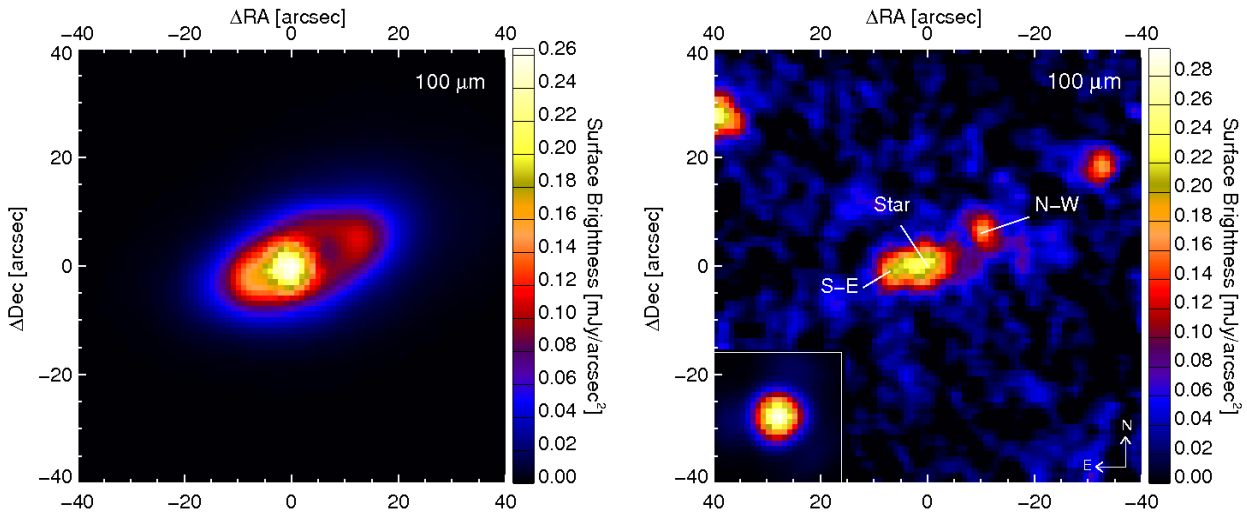

(a) Synthetic image at 100 microns

(b) *Herschel*/PACS image at 100 microns

Figure 3.9 – **(a)** Synthetic image of Case A (see Table 3.4) at 100 μm and convolved with the PSF. The parent ring is centred on 130 AU, has a width of 5 AU and is seen with an inclination of 65°. The disk total flux is five times the flux measured by *Herschel*/PACS. The star is at the centre of the image and the flux scale is set to match that of *Herschel*/PACS image. **(b)** *Herschel*/PACS image at 100μm.

3.4 Conclusions and perspectives

3.4.1 Conclusion

Transient spiral structures, filled inner holes, sparsely populated scattered disks, and resonant clumpy structures are all possible results when an eccentric perturber acts on a debris disk. They can be shown with numerical simulations, but more importantly, used to derive constraints on a perturber in a system (mass and eccentricity). The production of synthetic images may further allows one to set additional constraints on the spatial distribution and mass of an eccentric debris disk.

Therefore, we provided a method for investigating and modelling eccentric ring structures based on a complementary analytic and numerical approach, where one can derive potential orbits from analytics and test them numerically using N-body codes and syntetic images. This method can be easily applied to other systems and is expected to be useful in the near future.

Indeed, Kaib et al. (2013) have pointed out that wide binary star systems, that is, systems with separations greater than 1000 AU, can produce eccentric planets around a primary star on Gyr timescales. This is due to Galactic tides and passing star perturbations, which are able, sooner or later, to set the secondary star on a highly eccentric orbit. The proportion of wide binary systems is by no means negligible ($\sim$ 50%, Duquennoy & Mayor 1991), and although debris disks which are several Gyr old are faint and difficult to detect, this will be overcome with the unique capabilities of ALMA, JWST, and SPICA. Therefore, old eccentric patterns in debris disks are expected to be commonly observed in the future.

The ζ^2 Reticuli disk is one such example of such a Gyr-old eccentric debris disk. Moreover, ζ^2 Reticuli is part of a wide binary star system, which may provide an explanation for the presence of an eccentric perturber around ζ^2 Reticuli. Other scenarios can be envisaged. For instance, an inner perturber might acquire its eccentricity via a planet-planet scattering event.

However, this event should be such that a single perturber remains in the system. Otherwise, additional perturbations of a second planet would generate an orbital precession of the eccentric perturber, which in turn would not be able to sculpt the disk into an eccentric shape. This is compatible with observational constraints, since as previously mentioned radial velocity measurements rule out a massive perturber in the inner system.

3.4.2 Towards better knowledge of the ζ^2 Reticuli system with ALMA

At Herschel/PACS wavelengths, resolved emission at 70μm and 100μm comes from short-lived dust grains affected by radiation pressure. The dust spatial distribution is somewhat related to its parent bodies under pure gravitational influence, but it is more extended. Thus gravitational prints are somewhat smeared and constraints on a potential planetary perturber suffer uncertainties. Herschel images at 160μm show better tracers of parent bodies, but unfortunately, the disk is not resolved at this wavelength. Since the ring limits or global eccentricity of the debris disk of ζ^2 Reticuli are not well constrained, the space of parameters explored is large, that is, there is solution degeneracy.

ALMA observations could place more detailed limits on the disk geometry and combining them with the other available dataset break the solution degeneracy, and thus make a clean investigation to search for a potential planetary perturber. Excellent tracers for parent bodies will be seen using ALMA at 1300 microns (see Figure 3.10). As a consequence, our data will not be polluted by non-gravitational effects, and better constraints will be placed on the planetary companion.

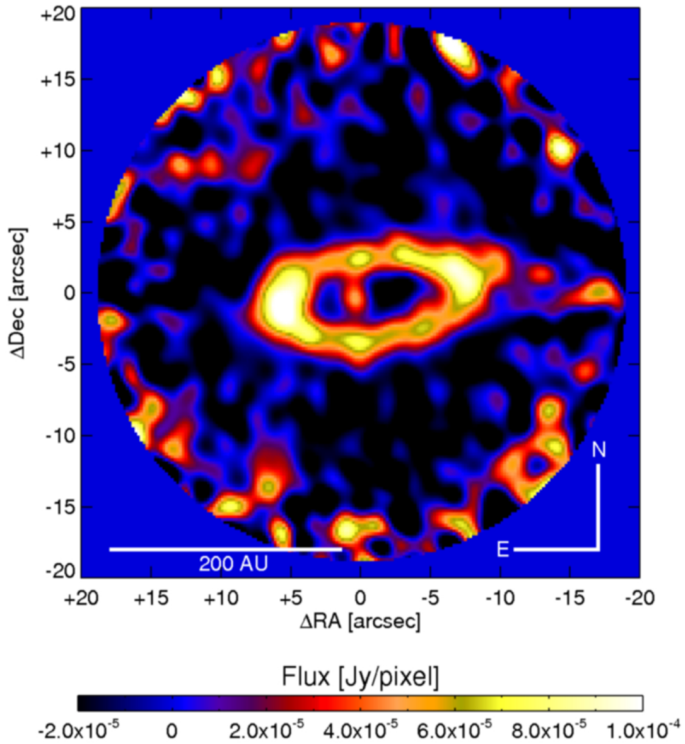

Figure 3.10 – Synthetic observations at 1300 microns with ALMA of the debris disk of ζ^2 Reticuli .

With such data, it will be possible to constrain :

- the inclination and position angle of the parent ring: models suggest the planetary companion is coplanar (or almost) to the disk. Obtaining the disk inclinations will allow us in turn to constrain the planet inclination.
- the offset of the parent ring, and thus its eccentricity: the ring eccentricity is only constrained by a lower limit (0.3), and thus it is the eccentricity of the planetary companion which creates this structure. Better constraints on the ring eccentricity will allow to reduce significantly the space of parameters explored and potentially break down the solution degeneracy while searching for a suitable planetary perturber.
- its radial extent, inner and outer radius.

We may also be able to investigate the sharpness of its edges, and thus discriminate between inner and outer companion. This information will feed our dynamical models, allowing us to reduce the space of parameters explored. This will place better constraints on the planetary system at work in shaping this disk asymmetrically. A proposal was submitted for ALMA Cycle 1 (2012.1.00730.S, PI: Virginie Faramaz).

However, the observation time required to achieve these observations – (~ 5 hours) – was judged relatively long compared to the average time allowed per project. Moreover, the time required was computed assuming that the disk would behave as a blackbody, whereas it was brought to our attention that at ALMA wavelengths, the disk would rather behave as a gray-body, that is, its emissivity at a given wavelength is lower than this of a blackbody. Therefore, the observation time derived under the blackbody assumption probably underestimates the time actually required to achieve our imaging goals. We hope that we will be able to submit our project again in the future, applying the necessary corrections under the gray-body assumption, but also that we will benefit from recent instrumental improvements with instruments such as SPHERE or JWST (see Sect. 6.2).

Article : Can eccentric debris disks be long-lived? – A first numerical investigation and application to ζ^2 Reticuli

Astronomy & Astrophysics manuscript no. zetaRet
April 14, 2014

Can eccentric debris disks be long-lived?

A first numerical investigation and application to ζ^2 Reticuli

V. Faramaz[1], H. Beust[1], P. Thébault[2], J.-C. Augereau[1], A. Bonsor[1], C. del Burgo[3], S. Ertel[1], J.P. Marshall[4], J. Milli [1,5], B. Montesinos[6], A. Mora[7], G. Bryden[8], W. Danchi[9], C. Eiroa[4], G.J. White[10,11], and S. Wolf[12]

(Affiliations can be found after the references)

Received; Accepted

ABSTRACT

Context. Imaging of debris disks has found evidence for both eccentric and offset disks. One hypothesis is that they provide evidence for massive perturbers, for example, planets or binary companions, which sculpt the observed structures. One such disk was recently observed in the far-IR by the *Herschel*⋆ Space Observatory around ζ^2 Reticuli. In contrast with previously reported systems, the disk is significantly eccentric, and the system is several Gyr old.

Aims. We aim to investigate the long-term evolution of eccentric structures in debris disks caused by a perturber on an eccentric orbit around the star. We hypothesise that the observed eccentric disk around ζ^2 Reticuli might be evidence of such a scenario. If so, we are able to constrain the mass and orbit of a potential perturber, either a giant planet or a binary companion.

Methods. Analytical techniques were used to predict the effects of a perturber on a debris disk. Numerical N-body simulations were used to verify these results and further investigate the observable structures that may be produced by eccentric perturbers. The long-term evolution of the disk geometry was examined, with particular application to the ζ^2 Reticuli system. In addition, synthetic images of the disk were produced for direct comparison with *Herschel* observations.

Results. We show that an eccentric companion can produce both the observed offsets and eccentric disks. These effects are not immediate, and we characterise the timescale required for the disk to develop to an eccentric state (and any spirals to vanish). For ζ^2 Reticuli, we derive limits on the mass and orbit of the companion required to produce the observations. Synthetic images show that the pattern observed around ζ^2 Reticuli can be produced by an eccentric disk seen close to edge-on, and allow us to bring additional constraints on the disk parameters of our model (disk flux and extent).

Conclusions. We conclude that eccentric planets or stellar companions can induce long-lived eccentric structures in debris disks. Observations of such eccentric structures thus provide potential evidence of the presence of such a companion in a planetary system. We considered the specific example of ζ^2 Reticuli, whose observed eccentric disk can be explained by a distant companion (at tens of AU) on an eccentric orbit ($e_p \gtrsim 0.3$).

Key words. Circumstellar matter – Methods: N-body Simulations – Celestial mechanics – Stars: ζ^2 Reticuli, planetary systems

1. Introduction

The first debris disk was discovered in 1984, when the Infrared Astronomical Satellite (IRAS) found a strong IR excess around Vega, revealing the presence of micron-sized dust grains (Aumann et al. 1984). For most debris disks, these grains have a limited lifetime, which is shorter than the system's age because of Poynting Robertson drag and collisions. Therefore, this dust is assumed to be replenished by collisional grinding of much larger parent bodies, which are at least kilometre-sized for this collisional cascade to be sustained over the system's age (Backman & Paresce 1993; Löhne et al. 2008). Consequently, debris disks provide evidence for the existence of solid bodies that have reached km-size, and potentially the planetary-size level.

Spatially resolved structures in debris disks can provide clues to the invisible planetary component of those systems. Such planets may be responsible for sculpting these disks and may leave their signature through various asymmetries such as wing asymmetries, resonant clumpy structures, warps, spirals, gaps, or eccentric ring structures (see, e.g., Wyatt 1999). This diversity is to be compared with the variety of exoplanetary systems[1] discovered around main sequence stars since 1995 (51 Peg b, Mayor & Queloz 1995). Dynamical modelling of such asymmetries is the only method to place constraints on the masses and orbital parameters of planets in systems where direct observations are not possible (see, e.g., Mouillet et al. 1997; Wyatt et al. 1999; Augereau et al. 2001; Moro-Martín & Malhotra 2002; Wyatt 2004; Kalas et al. 2005; Quillen 2006; Stark & Kuchner 2008; Chiang et al. 2009; Ertel et al. 2011; Boley et al. 2012; Ertel et al. 2012; Thebault et al. 2012).

We focus here on cases of eccentric patterns in debris disks. The modelling of this type of asymmetry and its possible link with the dynamical influence of eccentric companions has been investigated in several previous studies: authoritative work was carried out by Wyatt et al. (1999, 2000) for HR 4796. Another case of interest is the debris disk of Fomalhaut (Stapelfeldt et al. 2004; Kalas et al. 2005; Quillen 2006; Chiang et al. 2009; Boley et al. 2012; Kalas et al. 2013, Beust et al, in revision).

Send offprint requests to: V. Faramaz

⋆ *Herschel* Space Observatory is an ESA space observatory with science instruments provided by European-led Principal Investigator consortia and with important participation from NASA.

Correspondence to: Virginie.Faramaz@obs.ujf-grenoble.fr

[1] see www.exoplanets.org

This pioneering work showed that these large-scale structures arise in systems where debris disks are perturbed by an eccentric companion on a low-inclination orbit relative to the disk (Wyatt et al. 1999). The disk centre of symmetry is offset from the star, which may be measured explicitly in high-resolution images (e.g., HST scattered light). Furthermore, its periastron is closer to the star and thus hotter and brighter, which results in a two-sided brightness asymmetry.

However, it is important to emphasize that previous studies considered low-eccentricity rings ($e \gtrsim 0.02$ for HR4796 and $e = 0.11 \pm 0.01$ for Fomalhaut), and were limited to timescales shorter than the typical ages of mature disks ($\leq$ 10 Myr for HR4796 simulations and $\leq$ 100 Myr for Fomalhaut). The question of whether highly eccentric ring structures could be sustained over very long timescales has not been addressed thus far in the literature. This question has become very topical because of the discovery of at least two several Gyr old and significantly eccentric debris disks: one around ζ^2 Reticuli ($e \gtrsim 0.3$ Eiroa et al. 2010), which is used as a reference case in this paper, and another one around HD 202628 ($e \sim 0.18$ Stapelfeldt et al. 2012; Krist et al. 2012). These systems are older than either Fomalhaut or HR 4796, and their disks are also much more eccentric.

In the present work, we investigate the long-term evolution of highly eccentric structures in debris disks and their relation to planetary or stellar perturbers by investigating their evolution over Gyr timescales. One of the questions we address is whether these structures are indeed several Gyr old, or if they might have originated from a more recent event, either a flyby or the late excitement of a sherpherding planet's eccentricity. We also summarise a general modelling method, based on complementary analytical and numerical tools, which we apply to the specific case of ζ^2 Reticuli.

This paper is structured as follows: Sect. 2 presents how a perturber can generate an eccentric ring structure. Useful analytical expressions are derived to study under which conditions such a pattern can be created. We also show that these predictions can be complemented by numerical studies. Sect. 3 describes the debris disk of ζ^2 Reticuli, along with newly reduced *Herschel*/PACS images. This debris disk is used as a proxy to determine a numerical set-up. Then, in Sect. 4, the numerical investigation is carried out. From N-body simulations, we examine both the onset and suvival of an eccentric pattern and explore their dependencies on the perturber's characteristics. This modelling approach allows one to put constraints on a perturber at work in shaping a debris disk into an eccentric ring over Gyr timescales, and it is applied to the debris disk of ζ^2 Reticuli. Sect. 5 shows synthetic images on which we perform a full comparison with observations of ζ^2 Reticuli, and retrieve additional constraints on this disk. Finally, Sect. 6 is devoted to conclusions, discussions, and propositions for **future** work.

2. Footprints of eccentric companions on debris disks

We have developed a dynamical model to investigate the shaping of a debris disk into an eccentric ring, and the timescales associated with its onset and survival. More specifically, we seek to determine whether perturbers are able to shape and maintain a disk into a significantly eccentric ring structure on Gyr timescales, and whether the asymmetry relaxes or not.

Before presenting our model and our results in detail for this as yet unexplored case, we present the current understanding on how eccentric ring structures arise as a result of the dynamical effect of an eccentric perturber.

2.1. Basic principle

For a disk to be shaped into an eccentric ring, it must be perturbed in such a way that the eccentricity of its components are forced to higher values, and that the orbits of these components are more or less oriented in a common direction. These conditions are both fulfilled if the disk is under the gravitational influence of a perturber, namely a planetary or a stellar companion (nearly) coplanar to the disk and on an eccentric orbit. The eccentricity of the ring causes the disk centre of symmetry to be offset from the star, and the disk pericentre to be brighter than the apocentre, since it is closer to the star and thus hotter. This feature was studied by Wyatt et al. (1999) for a planetary companion, and was called the pericentre glow phenomenon.

Spatially resolved imaging is required to determine the structure of debris disks, and therefore renewed efforts have been made to image as many debris disks as possible[2]. Most images of resolved debris disks have been obtained so far in the visible or near-IR. At these wavelengths, the emission is dominated by small grains close to the blow-out limit imposed by stellar radiation (sub-micron to micron, depending on stellar luminosity). These grains exhibit a complex evolution because of the coupled effects of collisions and radiation pressure (see, e.g., Thébault & Augereau 2007). This may strongly alter or even mask the dynamical structures imparted by a massive perturber (Thébault et al. 2012). Observations at longer wavelengths detect larger grains that are less affected by stellar radiation (a few tens to a few hundreds of micron in size, depending on the observing wavelength). These directly trace the distribution of larger parent bodies and thus more directly reflect the dynamical effect of a perturber (see, e.g., Krivov 2010; Moro-Martín 2012, for exhaustive reviews).

Since the origin of an eccentric pattern is gravitational, we can reasonably assume that large-scale asymmetries among an observed dust population already exist amongst the parent planetesimal population that produces it and result from pure gravitational perturbations. This assumption allows us to study the influence of different eccentric perturbers in a simplified way, neglecting the effect of radiation pressure and considering parent planetesimals as mass-less and collision-less particles in orbit around their host star and perturbed by a companion, either stellar or planetary.

We assumed that at the end of the protoplanetary phase, the planetesimals start from almost circular orbits because of orbital eccentricity-damping by primordial gas. We furthermore assumed that any perturbing planet in the system is fully formed by the time the gas disappears, and evolves on a significantly eccentric orbit, because of a major perturbing event such as planet-planet scattering. Thus, we can consider the disappearance of the gas as time zero for the onset of planetesimal perturbations by an eccentric companion. From this moment, the planetesimal eccentricities start to increase and their lines of apsides tend to align with this of the planet. Under these assumptions, the forced elliptic ring structure takes some time to settle in, and it is preceded by the appearance and disappearance of transient spiral features. These are due to differential precession within the disk: all the planetesimals in the disk have different precession rates (because of their different orbital distances), such that these spiral structures are expected to wind up and finally generate an eccentric ring, as shown by Augereau & Papaloizou (2004) and Wyatt (2005). The characteristic time for reaching this state is of the order of a few precession timescales at the considered dis-

[2] see, e.g., www.circumstellardisks.org

tance (Wyatt 2005). Consequently, the onset of an eccentric ring structure is a matter of timescales, while the value of the disk global eccentricity is to be linked with the planetesimals' forced eccentricity, and thus to the companion's eccentricity.

2.2. Analytical approach

We show here how the onset of these structures can be understood from analytical considerations. Planetesimals are considered to be mass-less particles. We focus on the secular response of a debris disk to a coplanar perturbing body, either a planet or a star. More specifically, both the forced secular eccentricity e_f and the apsidal precession rate $d\varpi/dt$ of test planetesimals are examined, where ϖ is the longitude of periastron with respect to the direction of the perturber's periastron, that is, the planet and planetesimal have their periastra aligned when $\varpi = 0$ and anti-aligned when $\varpi = \pi$.

When secularly perturbed, the eccentricity of a planetesimal evolves cyclically; its period is related to the rate of orbital precession. This holds in particular when we consider a dynamically cold disk of planetesimals as an initial condition, which is a reasonable and classical assumption considering the damping effect of the gas during the protoplanetary phase. In that case, the secular behaviour of a planetesimal can be understood considering the analytical solution for its eccentricity. In the Laplace-Lagrange theory, the complex eccentricity of a planetesimal, $z(t)$, can be written

$$z(t) = e_f \{1 - \exp(IAt)\} \quad , \tag{1}$$

where $I^2 = -1$, and $A = \frac{d\varpi}{dt}$ is the secular precession rate.

One can see from this expression that the maximum induced eccentricity for a planetesimal is twice the forced eccentricity, that is, $e_{f,max} = 2e_f$. This occurs when $At = \pi[2\pi]$, that is, when the longitudes of periastra of the planetesimal and the perturber are equal ($\varpi = 0$, see Fig. 1 and, for more details, see e.g., Wyatt 2005; Beust et al. 2014).

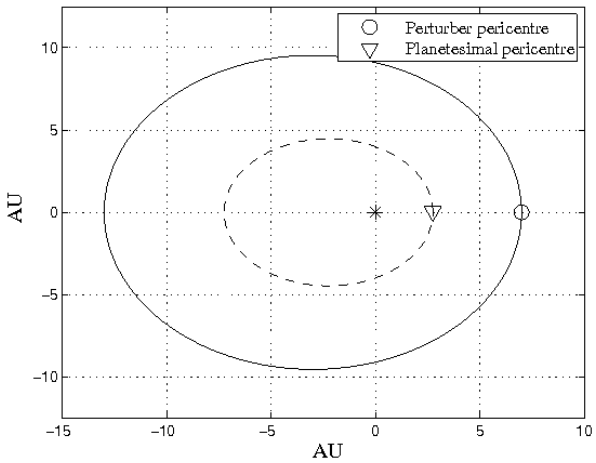

Fig. 1. Co-evolution of a planetesimal eccentricity and orbital precession when acted upon by an eccentric perturber. Since the planetesimal orbit precesses, its periastron will eventually be aligned with that of the perturber on the same side of the massive central body, that is, the longitudes of periastra of the planetesimal and the perturber are equal ($\varpi = 0$). In this configuration, the planetesimal eccentricity is maximum.

There are several ways to analytically derive e_f and $d\varpi/dt$. The most classical one is to apply the linear Laplace-Lagrange theory, which is an expansion of the interaction Hamiltonian to second order in ascending powers of the eccentricities of the two bodies and an averaging over the two orbits (see, e.g., Eq. 6 of Mustill & Wyatt 2009). However, this approach is valid only for low eccentricities, but the perturber's orbital eccentricity e_p is not necessarily low. Therefore, restricting our analytical study to small e_p may not be appropriate.

Another way to proceed is to expand the interaction Hamiltonian in spherical harmonics and truncate it at some order in α, where α is the ratio[3] between a and a_p, the planetesimal and the perturber's semi-major axis, respectively, and to average after over the two orbits. This permits us to perform an analysis without any restriction on the eccentricities. The resulting Hamiltonian is given by Krymolowski & Mazeh (1999), Ford et al. (2000), or Beust & Dutrey (2006).

To the lowest order in α (second order, quadrupolar), it yields a forced eccentricity e_f:

$$e_f \simeq \frac{5}{4}\frac{\alpha e_p}{1-e_p^2} \quad . \tag{2}$$

This expression is given by Augereau & Papaloizou (2004) and Mustill & Wyatt (Eq. 8 of 2009). Note that this approach is only valid for low enough values of α to ensure a fast convergence of the expansion, that is, for orbits with significantly different sizes. It is also only valid far from mean-motion resonances. However, these resonances' spatial extension along the semi-major axis (of the order of ~ 0.1 AU) is typically two orders of magnitude smaller than the extent of the observed structures (of the order of ~ 10 AU), although when the particles are on eccentric orbits, these resonances may span much wider ranges in terms of radial distance to the star than their span in semi-major axis may have hinted at. But in any case, the amount of material trapped in resonance can reasonably be assumed to be much smaller than the amount of non-resonant material, all the more so because we did not assume here that the planet has migrated, and thus excluded resonant capture during migration. Therefore, these structures are assumed to result from non-resonant material, and our approach is appropriate. Moreover, resonances were be treated in our N-body integrations, and were confirmed to be only important for limited parameter combinations (see Sect. 4).

To derive the precession rate in the spherical harmonic expansion case, we followed the method given by Mardling & Lin (2002). The variation rate for the Runge-Lenz vector of the orbit was computed, expanded to any given order, and integrated over one orbital period.

After the numerical tests, there were fewer than two orders of magnitude between terms of the second and the fourth order (the third-order terms cancel out), therefore we retained terms up to fourth order in the spherical harmonic expansion, and averaged the resulting precession rate over the longitude of periastron. The precession rate is

$$\frac{d\varpi}{dt} = \frac{3n}{4}\frac{m_p}{M_\star}\alpha^3\frac{\sqrt{1-e^2}}{(1-e_p^2)^{3/2}} + \frac{45n}{256}\frac{m_p}{M_\star}\alpha^5\frac{(4+3e^2)(2+3e_p^2)\sqrt{1-e^2}}{(1-e_p^2)^{7/2}} \quad . \tag{3}$$

[3] α is such that $\alpha < 1$, always, and thus $\alpha = a_p/a$ if $a_p < a$, and inversely, $\alpha = a/a_p$ if $a_p > a$.

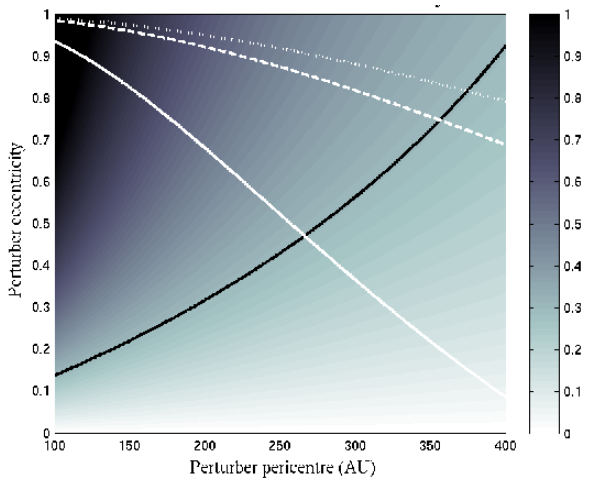

Fig. 2. Example colour map of the maximum induced eccentricity $2e_f$ imposed by a planetary perturber on a particle with semi-major axis 100 AU and eccentricity $e = 0$ as a function of its periastron and eccentricity, as estimated from Eq. (2). The black line corresponds to a $2e_f = 0.3$ condition, which was set to mimic the condition for the disk of ζ^2 Reticuli. Note that it does not depend on the mass of the planet. The white lines show the parameters for which the typical timescale to reach a steady state at 100 AU is $t_{prec} = 1$ Gyr, using Eq. (4). This timescales depends on the mass: $m_p = 0.1\,M_{Jup}$ *(solid line)*, $1\,M_{Jup}$ *(dashed line)* and $2\,M_{Jup}$ *(dotted line)*. For example, a perturber of mass $0.1\,M_{Jup}$, periastron $q_p = 150$ AU and eccentricity $e_p = 0.4$ is expected to produce a significantly eccentric ring in shorter than 1 Gyr, although spiral patterns may remain since it can take several precession timescales for them to vanish, as was shown by Wyatt (2005).

We then followed Wyatt et al. (1999) and assumed that the precession timescale, t_{prec}, corresponds to the lower limit of the typical dynamical timescale for setting a dynamical steady state:

$$t_{prec} = \frac{2\pi}{(d\varpi/dt)_{a_c}} \quad , \tag{4}$$

where a_c is the typical semi-major axis of a particle in the ring.

With this we analytically predict the effect of a perturber on a debris disk, that is, for a given set of values of e_p and of the planet periastron q_p, one can derive the precession rate $(d\varpi/dt)_{a_c}$ corresponding to planetesimals that orbit at this distance. Conversely, one can set this dynamical timescale and the forced eccentricity for a particle with semi-major axis a_c to correspond to those derived from observations of an eccentric debris disk, and thus initially estimate the perturber's characteristics (see Fig. 2).

However, the problem is more complex for real disks, which have a finite spatial extension, since these estimates depend on radial locations. To first order, it can be seen from Eqs. 2, to 4 that the forced eccentricity and the secular timescale scale as

$$e_f \propto \alpha \quad , \tag{5}$$

and

$$t_{prec} \propto \frac{1}{m_p \alpha^3} \quad . \tag{6}$$

We now define a_{in} and a_{out} as the inner and outer limits of the disk in the semi-major axis and define $e_{f,min}$ and $e_{f,max}$ as the minimum and maximum eccentricities induced across the disk.[4]

[4] $e_{f,min} = e_{f,in}$ and $e_{f,max} = e_{f,out}$ for an inner perturber and vice versa for an outer one.

The minimum and maximum precession timescales, $t_{prec,min}$ and $t_{prec,max}$, are defined in the same manner. Then, using Eq. 5 and Eq. 6, one obtains

$$\frac{e_{f,max}}{e_{f,min}} = \frac{a_{out}}{a_{in}} \quad , \tag{7}$$

and

$$\frac{t_{prec,max}}{t_{prec,min}} = \left(\frac{a_{out}}{a_{in}}\right)^3 \quad . \tag{8}$$

It is easy to see from these equations that the secular precession timescale spans a wide range of values across the disk. This means that making analytical predictions by setting the desired values for the forced eccentricity and the secular precession timescale for a particle with semi-major axis at the centre of the distribution suffers limitations when applied to an extended disk, especially concerning the timescale.

Eqs. 7 and 8 can be rewritten using Δa, the half width of the disk extent, along with $e_{f,c}$ and $t_{prec,c}$, the forced eccentricity and secular precession timescale at a_c, respectively:

$$e_{f,max/min} = \left(\frac{a_c \pm \Delta a}{a_c}\right) e_{f,c} \quad , \tag{9}$$

and

$$t_{prec,max/min} = \left(\frac{a_c \pm \Delta a}{a_c}\right)^3 t_{prec,c} \quad . \tag{10}$$

As an example, we set $a_c = 100$ AU, $\Delta a = 25$ AU, $2e_c = 0.3$ and $t_{prec,c} = 1$ Gyr. These values are close to those derived for the disk of ζ^2 Reticuli ($e \gtrsim 0.3$ and extent 70-120 AU: Eiroa et al. 2010, and Sect. 3 of the present work). One obtains

$$\begin{cases} 2e_{f,min/max} = 0.225 - 0.375 \\ t_{prec,min/max} = 0.42 - 1.95\,\text{Gyr} \end{cases} \quad . \tag{11}$$

In these conditions, the extent of the disk is not expected to affect the global eccentricity of the disk too much, that is, we expect to recover on average a global eccentricity corresponding to the forced eccentricity at a_c after the steady state is reached. But the problem is that the extent of the disk strongly affects the timescale to reach this steady state. This is a limitation of the analytic approach that can be overcome by the use of numerical simulations.

3. Numerical investigation: a typical set-up, the highly eccentric, old disk of ζ^2 Reticuli

To move beyond the simplified analytical approach and explore the high-eccentricity case on Gyr timescales, we resorted to numerical tools. We placed ourselves in the frame of the restricted three-body problem, thatb is, one central star, a planet, and a mass-less planetesimal. The symplectic N-body code SWIFT-RMVS of Levison & Duncan (1994) was used to integrate the evolution of a ring of planetesimals around a solar-mass star, over 1 Gyr. We used a typical timestep of $\sim 1/20$ of the shortest orbital period and ensured a conservation of energy with a typical error of $\sim 10^{-6}$ on relative energy. This code has a crucial advantage over an analytical approach: it is able to handle close encounters and scattering processes, along with the short-term variations of the planetesimals orbital elements, whereas these effects were ignored in the analytical approach, for which orbits

were averaged, short-term variations were los,t and the approach is valid only for $\alpha << 1$, that is, far from close encounters. As we show in Sect. 4, the scattering events play a crucial role in the system's evolution.

For the sake of clarity, the ζ^2 Reticuli system was considered as a proxy for a typical mature and significantly eccentric debris ring. We explore different planet-disk configurations, and produce synthetic images for comparison with *Herschel*/PACS observations. We show that the hypothesis of an eccentric debris disk around ζ^2 Reticuli is fully consistent with the observations.

3.1. The ζ^2 Reticuli system

The G1V solar-type star ζ^2 Reticuli (HR 1010, HIP 15371) (Eiroa et al. 2013) is located at 12 pc (van Leeuwen 2007), has a luminosity $L_\star = 0.97 L_\odot$, $\log g = 4.51$, and is $\sim 2-3$ Gyr old (Eiroa et al. 2013). It has a binary companion ζ^1Reticuli, a G2-4V (Gray et al. 2006; Torres et al. 2006) star located at a projected distance of 3713 AU from ζ^2 Reticuli (Mason et al. 2001). Bayesian analysis by Shaya & Olling (2011) of the proper motions of these stars indicates a very high (near 100%) probability that the pair are physically connected.

The presence of dust around ζ^2 Reticuli has been probed with *Spitzer* (Trilling et al. 2008); the results suggest a $\sim$ 150 K emission at $\sim$ 4.3 AU. However, the angular resolution of *Spitzer* is limited, and the dust spatial distribution remained unconstrained. New observations with *Herschel*/PACS completed the spectral energy distribution (SED), providing the suggestion of an optically thin, $\sim$ 40 K, emission at $\sim$ 100 AU, with fractional luminosity $L_{\rm dust}/L_\star \approx 10^{-5}$ (Eiroa et al. 2010). Moreover, *Herschel*/PACS provided spatially resolved images of the dust thermal emission surrounding ζ^2 Reticuli at 70 μm and 100 μm (Eiroa et al. 2010). We present here newly reduced *Herschel*/PACS images (see Fig. 3). The images show a double-lobe feature, asymmetric both in position and brightness. Note that at 70 μm, the probability for alignment with a background source within 10″ is extremely low, namely 10^{-3} (Eiroa et al. 2010). The disk is not resolved at *Herschel*/SPIRE wavelengths: newly reduced images and star-disk flux measurements are presented in Appendix A.

As suggested by Eiroa et al. (2010), the asymmetry revealed by *Herschel*/PACS in the disk of ζ^2 Reticuli can be interpreted as a ring-like elliptical structure with $e \gtrsim 0.3$ seen close to edge-on and extending from $\sim$ 70 to $\sim$ 120 AU, which is fully consistent with the information derived from the SED (Eiroa et al. 2010). Alternatively, it might also be interpreted as two clumps from an over-density of dust and planetesimals. In Appendix B, we investigate the system inclination on the line of sight, a crucial parameter required for correctly interpreting the observed structures. More precisely, we determined the star inclination and assumed that the disk and the star are coplanar. The 50% probability value is $i = 65.5°$, meaning that the system is highly inclined to the line of sight, which tends to support the eccentric-ring scenario.

Without a doubt, this asymmetric structure provides evidence that "something" is dynamically sculpting the disk. This may be the stellar companion ζ^1Reticuli or a (as yet undetected) planet. The latter hypothesis is fully compatible with radial velocity measurements of ζ^2 Reticuli, which suggest there is no Jupiter-mass (or larger) planet interior to $\sim 5-10$ AU (Mayor et al. 2003), but which put no contraints on a small planet or a Jupiter-like planet at larger radii. It is also compatible with growing observational evidence for planets at large orbital separation, that is, several tens to a few hundreds of AU from their host star

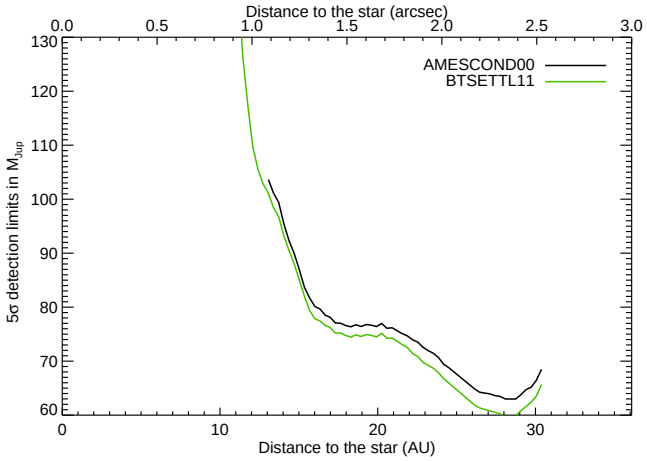

Fig. 4. Detection limits set by direct imaging on the presence of brown dwarf / close binary between 1″ and 2.5″ in projected separation.

(see, e.g., Luhman et al. 2007; Kalas et al. 2008; Marois et al. 2008, 2010).

Constraints from direct imaging are presented in Fig. 4 using the two evolutionary models COND 2003 (Baraffe et al. 2003) or BT-settl 2011 (Allard et al. 2011). Details of the reduction procedure are presented in Appendix C. These constraints were obtained from VLT/NaCo archival data taken in November 2010 in the Ks band. These data do not provide constraints on companions beyond a projected distance of $\sim$ 30 AU. The presence of a brown dwarf within $\sim$ 20 AU is still compatible with observations.

3.2. Numerical set-up

We considered a ring of 150,000 mass-less planetesimals uniformly distributed between 70 and 140 AU (except when specified otherwise) around a solar-mass host star, with initial eccentricities randomly distributed between 0 and 0.05, and initial inclinations between $\pm 3°$, while the remaining angles (longitudes of nodes and periastra) were randomly distributed between 0 and 2π. These values are summarised in Table 1. This reasonably well mimics the low eccentricities and inclinations expected at the end of the protoplanetary phase. The radial extent of the model disk was configured to closely match the observed properties of the disk around ζ^2 Reticuli.

Using mass-less test particles removes self-gravity in the disk, as well as a back-reaction of the disk on the planet. In general, both of these phenomena are significant when the planet mass is similar to the disk mass. We have no mass estimate for the debris disk of ζ^2 Reticuli. However, a well-studied case is the debris disk of Fomalhaut, whose mass was estimated to be $\sim 3-20 M_\oplus$ (Wyatt & Dent 2002; Chiang et al. 2009). Since a debris disk loses material over time due to the combined effects of collisional evolution, Poynting-Robertson drag, and radiation pressure, and since ζ^2 Reticuli is much older than Fomalhaut (440 Myr; Mamajek 2012), it is reasonable to assume that the debris disk surrounding ζ^2 Reticuli does not contain more than a few Earth masses. In this case, it is also reasonable to assume that the disk self-gravity and back-reaction are negligible, and the planet will still be able to imprint on the disk structure if its mass is at least $0.1 M_{\rm Jup} \sim 32 M_\oplus$.

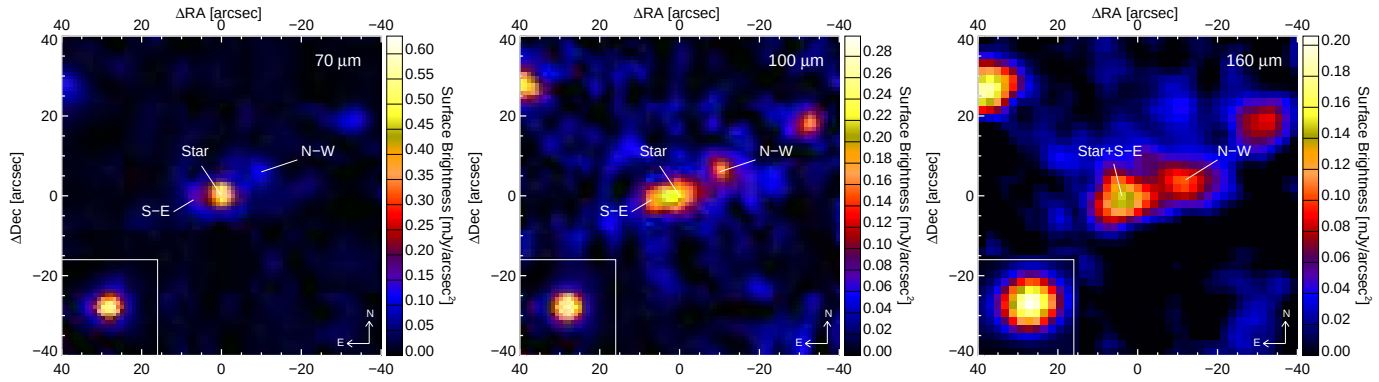

Fig. 3. *Herschel*/PACS images of ζ^2 Reticuli at 70, 100 and 160 microns from left to right. North is up and east is left. The inset in the bottom-left corner shows the PSF. The north-west lobe is noted N-W, while the south-east lobe is noted S-E.

Parameters	Values
Number of particles	150,000
Semi-major axis (AU)	$a_{\rm min} = 70$; $a_{\rm max} = 140$
Eccentricity	$e_{\rm min} = 0$; $e_{\rm max} = 0.05$
Inclination (°)	$i_{\rm min} = -3$; $i_{\rm max} = 3$

Table 1. Initial parameters for the planetesimals used in our N-body simulations

We considered two planet-disk configurations, inside and outside the planetesimal belt, and performing parametrically explored their influent orbital elements.

3.2.1. Inner perturber

The first case is that of a planet interior to the initial ring. In this case, we considered that the inner edge of the disk is located at 70 AU, and made the classical assumption that it is truncated by the chaotic zone generated by a coplanar planet (see, e.g., the approach used by Chiang et al. 2009). The chaotic zone is defined as the region where mean-motion resonances overlap. The width of this zone depends on the mass ratio between the central star and the perturber,

$$\frac{\Delta a}{a_{\rm planet}} = \frac{a_{\rm edge} - a_{\rm planet}}{a_{\rm planet}} = 1.5\mu^{2/7} \quad , \tag{12}$$

where $\mu = m_{\rm planet}/m_*$ (Wisdom 1980; Duncan et al. 1989). Consequently, one can deduce the semi-major axis of a planet of a given mass that generates a disk inner edge at 70 AU:

$$a_{\rm planet} = \frac{a_{\rm edge}}{1 + 1.5\mu^{2/7}} \quad . \tag{13}$$

We chose to perform a parametric exploration of the mass and eccentricity of the perturber, fixing its semi-major axis to the value deduced from the formula above. The values explored were 0.1 $M_{\rm Jup}$, 0.5$M_{\rm Jup}$, and 1 $M_{\rm Jup}$ for the mass and 0.2, 0.4 and 0.6 for the eccentricity (see Table 2). Here the disk initial inner edge was fixed halfway between 70 AU and the planet semi-major axis.

In addition, we also considered a more massive perturber such as a brown dwarf, located farther inside the system. This was motivated by the observation of a suspicious point source on observations in Ks-band data from the ESO archive (ID 086.C-0732(A); PI: Löhne,71574), which disappeared after re-reduction of the data, and consequently, since its existence is controversial, we chose not to show these images. However, if it were confirmed, this point source was showing a 42 $M_{\rm Jup}$ brown dwarf located at a projected distance of 17.5 AU from the star. Therefore, we investigated the possibility for the presence of a brown dwarf in the inner parts of the system. For an inner edge to be produced at 70 AU, the planet's semi-major axis need to be 43.8 AU. Since this constraint is less relevant for very eccentric inner perturbers (see Sect. 4), we chose here to set this value to the perturber's apastron and not its semi-major axis. We fixed its periastron to 17.5 AU, which led to an orbital eccentricity of 0.43 and a semi-major axis of 30.6 AU. With this orbit, analytical predictions indicate that the perturberexcites planetesimals eccentricities up to 0.4. Therefore, this orbit was chosen for numerical tests (see Table 2).

3.2.2. Outer perturber

The second case considered is that of a planet exterior to the ring. There is indeed growing evidence for planets at large orbital separations, that is, several tens to a few hundreds of AU away from their host star (see e.g. Luhman et al. 2007; Kalas et al. 2008; Marois et al. 2008, 2010), and the mass constraints set by direct imaging are loose given the age of the system (see Sect. 4.1.3). Therefore, we also investigated the ability of an *external* perturber to shape a disk.

We considered coplanar outer planetary companions and explored the impact of the eccentricity, mass, and periastron on the disk asymmetry. While an inner edge is in general considered as a clue for the presence of inner perturbers, it is obviously more of a conjecture to assume that an outer edge is formed in the same manner, since a disk instrinsically has an outer limit. Therefore, the outer edge was not assumed here to be formed because of resonance overlap, and the planet periastron was fixed instead, to ensure that it does not cross the disk. To explore a great variety of situations despite the CPU-time limitations, we considered a rough parameter space consisting of all the possible combinations between masses $m_{\rm p} = 0.1 - 1 - 2\,{\rm M_{Jup}}$, periastra $q_{\rm p} = 150 - 200 - 250$ AU, and eccentricities $e_{\rm p} = 0.2 - 0.4 - 0.6$ (see Table 2).

Note that the perturbers were set on an initially eccentric orbit, which requires an explanation, because we assumed that the disk is initally symmetric. Indeed, this pictures a situation where the process that sets the perturber on its eccentric orbit leaves the disk unperturbed. This may seem rather unrealistic, even though some scenarios can be envisaged. For instance, an inner perturber might acquire its eccentricity via a planet-planet

Table 2. Summary of numerical experiments with an inner and outer perturber, and for a brown dwarf and the stellar binary companion ζ^1 Reticuli. Description of the disk at 1 Gyr: I) steady state, $e < 0.2$, II) steady state, $e > 0.2$, III) scattered disk, IV) resonant pattern, V) spiral pattern. The example cases highlighted in more detail in Sect. 4 are labelled from A to G.

Inner perturbers				
m_p (M_{Jup})	a_p (AU)	$e_p = 0.2$	$e_p = 0.4$	$e_p = 0.6$
0.1	63.2	I	III,A	III
0.5	59.8	I	II,B	IV,C
1	57.9	I	II	IV

Outer perturbers				
m_p (M_{Jup})	q_p (AU)	$e_p = 0.2$	$e_p = 0.4$	$e_p = 0.6$
0.1	150	I	II,D	V
	200	I	V	V,E
	250	V	V	V
1	150	I	II	III,F
	200	I	II	II
	250	I	I	II
2	150	I	III,G	III
	200	I	I	I
	250	I	I	II

Other perturbers			
Perturber	m_p	Orbital parameters	Result
Brown dwarf	$42 M_{Jup}$	$a_p = 30.6$ AU ; $e_p = 0.43$	II
ζ^1 Reticuli	$1 M_\odot$	$a_p = 2046$ AU ; $e_p = 0.815$	I

scattering event. However, this event should be such that a single perturber remains in the system. Otherwise, additional perturbations of a second planet would generate an orbital precession of the eccentric perturber, which in turn would not be able to sculpt the disk into an eccentric shape. This is compatible with observational constraints, since as previously mentioned radial velocity measurements rule out a massive perturber in the inner system. For an outer perturber, an eccentric outer binary companion may be able to generate these initial conditions (see Sect. 6). In summary, retrieving realistic initial conditions relies on a complete study of the perturbations induced on the disk for multiple scenarios and, most probably, an extensive parameter space exploration. This is beyond the scope of the present paper, and will be the subject of future work; this motivated us to choose simple initial conditions.

4. Numerical investigation: results

We present here results obtained for the two disk-planet set-ups we considered: an inner and outer planet, and when the perturber is the stellar companion ζ^1 Ret. For each case, we aimed to find the result that gives an eccentric disk compatible with observational constraints.

Eiroa et al. (2010) derived a lower limit for the eccentricity of the disk in ζ^2 Reticuli of 0.3. Therefore, given the uncertainties in the estimation of the disk global eccentricity we computed from our simulations, a disk global eccentricity lower than 0.2 was discarded in our analysis. This global eccentricity was evaluated considering the geometry of an ellipse: the offset δ of the centre of symmetry from one of the foci of an ellipse is simply the product of its semi-major axis a by its eccentricity e, that is, $\delta = ae$. For a disk from our simulations, δ can be obtained by calculating the centre of symmetry of the disk, using the positions of the test particles in the heliocentric frame: δ is the distance of this centre of symmetry to the star. The disk semi-major axis a was determined as follows: the disk was divided into superimposed angular sectors of 3°. For each of these sectors, the radial distribution of the particles was fitted to a Gaussian. This provided the radial position of the maximum density for each angular sector, and thus a set of points defining the global shape of the disk. It is then straightforward to retrieve a from this set of points by seeking for the major axis, that is, the maximum distance between two opposite points. Finally, the disk eccentricity is simply $e = \delta/a$.

4.1. Inner perturber

We chose four illustrative results (see Table 2). For each, we show pole-on projections of the system at 1 Gyr in Fig. 7. We also summarise the results of our simulations in Table 2.

The best candidates needed a significant orbital eccentricity of ~ 0.4. The example of Case B is shown in Fig. 7 (upper-right panel). However, scattering processes may be important, and studying them allowed us to place constraints on the mass of the perturber.

4.1.1. Scattered disks

Inner perturbers may lead to very significant scattering processes. Namely, they can fill the inner parts of the disk instead of producing a well-defined ring. Such effects are presented with Case A in Fig 7 (upper-left panel).

This effect appears for low-mass perturbers. These perturbers do not scatter material efficiently enough. This material then tends to populate the inner parts of the system.

As a consequence, there is a lower mass limit for inner perturbers, and in the specific case of the ζ^2 Reticuli system, this lower limit is between 0.1 and 0.5 M_{Jup}. However, one cannot exclude that another more massive planet produces scattering of the material, blowing it out and leaving an inner hole, therefore a more correct way to express this constraint would be that perturbers with masses as low as 0.1 M_{Jup} should be accompanied by another more massive planet to create this pattern. But this scenario presents difficulties: while this second planet must be massive enough to clear the inner parts of the system of its material, it also must have a limited dynamical effect on the first planet that sculpts the disk: this second planet must be distant and not too massive for the orbit of the first planet to remain unperturbed. Otherwise, this orbit would precess and no longer lead to an eccentric pattern. It is not our purpose here to investigate this scenario, but based on the previous arguments, it would most probably work in a very limited parameter space.

4.1.2. Resonant patterns

Remarkarbly, for very eccentric ($e_p = 0.6$) inner perturbers of mass between 0.5 and 1 M_{Jup}, resonant clumpy structures may arise. An example is Case C, shown in Fig. 7 (bottom-left panel). In Fig. 5, we show a semi-major axis vs eccentricity diagram of the disk: it reveals two populations in resonance with the planet, namely the 3:2 and 2:1 mean-motion resonances, at ~ 79 AU and ~ 95 AU, respectively. These resonant populations are shown in Fig. 6. Typically, a population in 3:2 resonance is associated with capture during outward planetary migration, as is the case in our own solar system (Malhotra 1993, 1995). But here, these struc-

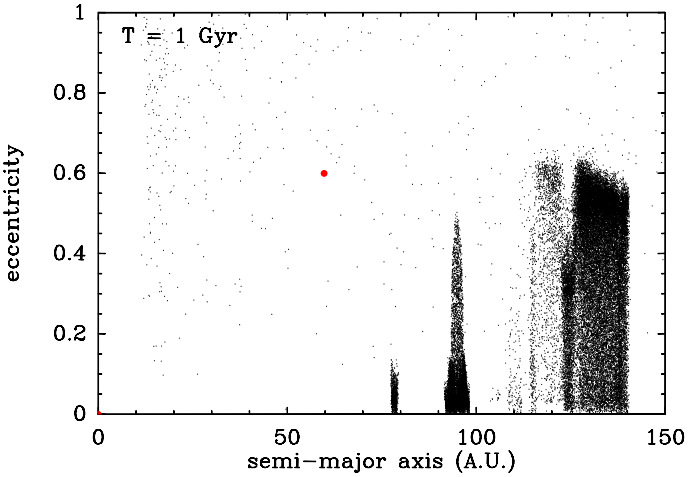

Fig. 5. Semi-major axis versus eccentricity diagram of the disk at 1 Gyr for the Case C perturber. Overdensities of planetesimals at ∼ 79 and ∼ 95 AU correspond to planetesimals in 3:2 and 2:1 mean-motion resonance with the perturber.

tures is most probably appear because we used the chaotic-zone formula (Eq. 13) to determine the perturber semi-major axis, which was derived for perturbers on circular orbits. Therefore, it is expected that this formula works less efficiently with increasing orbital eccentricity of the perturber: the result is that the planet digs into the disk, and consequently, planetesimals unprotected against close encounters by mean-motion resonance are scattered out, leaving the resonant structures apparent. This is supported by the fact that these resonant structures disappear when the constraint given by the chaotic-zone formula is applied to the perturber's apastron instead of its semi-major axis, as for an inner brown-dwarf-type companion. Interestingly, the observation of these resonant structures in a system may provide other clues on the dynamical history of a perturber than an outward migration: it may mean that the planet was originally shaping the inner edge of the disk before it was set on an eccentric orbit. However, these are thin structures, and when the disk is seen close to edge-on, as is the case for ζ^2 Reticuli, they would most probably be hidden by the non-resonant population.

4.1.3. Brown dwarf

Additionally, we investigated the possibility for the presence of a brown dwarf in the inner parts of the system, on an orbit such that the perturber excites planetesimal eccentricities up to 0.4. The disk at 1 Gyr is shown in Fig 7 (bottom-right panel). Its global eccentricity is $\sim 0.2-0.25$, which shows that very massive perturbers in the inner parts of the system can create the desired pattern.

4.2. Outer perturber

We chose four illustrative results (see Table 2) and show pole-on projections of the system at 1 Gyr on Fig. 8 for each, along with the evolution of the disk offset on 1 Gyr in Fig. 9. The results of our simulations are summarised in Table 2.

4.2.1. Good candidates

Case D is shown in Fig. 8 (upper left panel). The corresponding evolution of the offset clearly shows that the disk is at steady state and significantly eccentric (see Fig. 9). The best candidates must have significant eccentricities: none of our 0.2 eccentric perturbers creates the desired eccentric structure, even in the limit case predicted analytically, where a 0.1 $M_{\rm Jup}$ perturber has a pericentre $q_{\rm p}$ = 150 AU and eccentricity $e_{\rm p}$ = 0.2 (see Fig. 2). As a consequence, the best outer candidates have eccentricities $\sim 0.4 - 0.6$.

4.2.2. Spiral patterns

Case E is shown in Fig. 8 (upper-right panel). The system shows a spiral pattern at 1 Gyr, which, according to analytical predictions, corresponds to one precession timescale (see Fig. 2). Thus, our N-body integrations confirm what was noted by Wyatt (2005): the analytical formula appears to be a lower limit and several precession timescales are sometimes necessary for spiral patterns to vanish. The effect of spirals can also be seen in the evolution of the disk offset, which oscillates (see Fig. 9).

If we had observational proof that the disk of ζ^2 Reticuli has reached steady state and contains no spiral pattern, the results of our numerical investigation would allow us to place a lower mass limit of 0.1 $M_{\rm Jup}$ on an outer perturber in a range of periastra from 150 to 250 AU, based on a dynamical timescales criterion, otherwise it takes longer than 1 Gyr to generate a steady-state eccentric disk. This limit still holds for larger periastra than the range explored, since dynamical timescales increase with distance. But because of the slightly edge-on orientation of the disk and the resolution of the *Herschel*/PACS images, it is extremely difficult to discard a possible spiral pattern in this disk, and no lower mass limit can be clearly defined for an outer perturber.

4.2.3. Scattered disks

Outer perturbers may lead to very significant scattering processes. We present such effects in Fig. 8 (lower panels), where Case F and Case G are considered.

These processes are even more significant when the mass of the perturber increases. Indeed, as physically expected, more massive perturbers tend to scatter small bodies more efficiently. The distance to the disk plays a major part in this effect too, since close perturbers also tend to scatter more material. Additionally, when a perturber is on an eccentric orbit, it approaches even closer to the disk. In the most dramatic cases, the disk is completely destroyed. Consequently, for a given distance to the disk, there is an upper limit to the mass of an outer companion.

For Case F, one might question the contribution of the scattered inner material to the emission of the disk, and whether it would be visible on resolved images. In this case, the potential visibility of material on real observations relies on the sensitivity and resolution of the instrument used for these observations, as well as on the distance of the object, the radiative properties of the material itself and the quantity of light it receives, that is, on the host star properties. Therefore, only the production of synthetic images for direct comparison with observations can reveal whether this material is apparent or not, and refine constraints on the potential perturbers at work in the system. Additionally, the evolution of the offset clearly suggests that the asymmetry relaxes asymptotically to a low but non-zero value, and indeed, the apparent ring structure shows little eccentricity.

More specifically, our results allow us to place an upper mass limit of 2 $M_{\rm Jup}$ on an outer perturber in a range of periastra from 150 to 250 AU for the ζ^2 Reticuli system. However, this upper mass limit is expected to increase for periastra higher than those

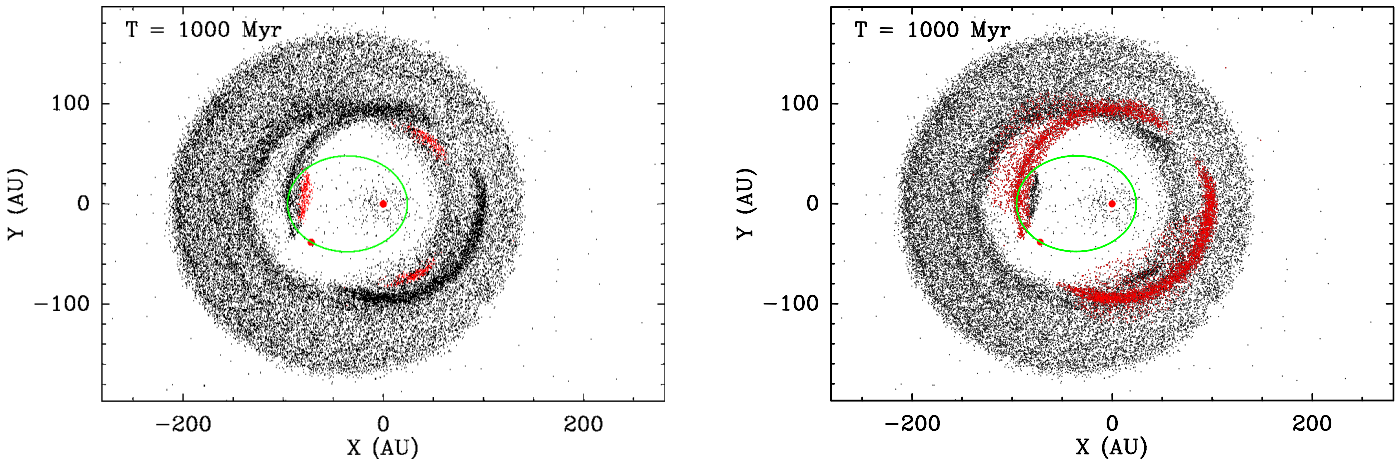

Fig. 6. Views from above the plane of disks at 1 Gyr in Case C, i.e., where resonant patterns appear. Planetesimals in 3:2 *(left)* and 2:1 *(right)* mean-motion resonance with the perturber are shown in red.

explored, since scattering processes are expected to be less efficient for a given mass when the companion is farther away from the disk.

4.3. Stellar binary companion

We investigated the influence of the binary companion ζ^1Reticuli on the debris disk surrounding ζ^2 Reticuli. The aim was to determine whether it alone could generate the observed asymmetry. If this were to be the case, the companion must be on an eccentric orbit. The only observational constraint available so far on the relative orbit of the binary system is the projected distance between the two stars, namely 3713 AU (Mason et al. 2001). Consequently, we cannot exclude the possibility that its orbit is eccentric, with a present-day location near apastron. We investigated whether a binary companion on an eccentric orbit at this distance might account alone for the observed structure of the disk, which would mean an elliptic ring with a minimum global eccentricity of 0.3, without any constraint on the binary eccentricity. We used analytical and numerical methods.

We first examined the forced secular eccentricity applied to the planetesimals by an eccentric binary companion, which was assumed to be coplanar. The debris disk surrounding ζ^2 Reticuli is approximately centred on $a = 100$ AU, and the binary perturber is at 3713 AU from ζ^2 Reticuli. This is only a projected distance, not a semi-major axis. We assumed that the binary companion is currently located at a distance $r_\star$ from ζ^2 Reticuli. The equation of its orbit around ζ^2 Reticuli reads

$$r_\star = \frac{a_\star(1-e_\star^2)}{1+e_\star \cos v_\star} \quad , \tag{14}$$

where $v_\star$, $a_\star$ and $e_\star$ are the binary companion current true anomaly, semi-major axis, and orbital eccentricity, respectively. The observed distance $d = 3713$ AU is related to $r_\star$ by $d = r_\star \cos\psi$, where ψ is a projection angle. This gives

$$a_\star = \frac{d(1+e_\star \cos v_\star)}{(1-e_\star^2)\cos\psi} \quad . \tag{15}$$

From this result Eqs. 15 and 2, where a_p and e_p are substituted by $a_\star$ and $e_\star$,

$$2e_\mathrm{f} \simeq \frac{5}{2}\frac{a}{d}\frac{e_\star \cos\psi}{1+e_\star \cos v_\star} \quad . \tag{16}$$

It is clear from this equation that the highest possible e_f values ware obtained for $\cos v_\star = -1$ (binary currently at apastron) and $\cos\psi = 1$ (no projection factor). With these assumptions, one derives

$$2e_{\mathrm{f,max}} \simeq 0.068\frac{e_\star}{1-e_\star} \quad . \tag{17}$$

For $2e_{\mathrm{f,max}}$ to reach at least 0.3, $e_\star \geq 0.815$ is required.

This seems highly eccentric and very unlikely at first sight. Yet, Duquennoy & Mayor (1991, see their Fig. 6.b) have shown that almost 25% of binaries with orbital periods longer than 10^3 days have orbital eccentricities $e_\star = 0.825 \pm 0.075$. In the present case, $d = 3713$ AU and $e_\star = 0.815$ lead to $a_\star = 2046$ AU and an orbital period $T_\star \sim 10^5$ yrs. Therefore it is possible that ζ^1 Reticuli is on an eccentric orbit, if not a highly eccentric one. However, the derived orbit should also have an apoastron value of $q_\star = 379$ AU and one might question the disk survival at $\sim 70-120$ AU with a stellar-type perturber approaching so close to the system.

Eq. 1 of Holman & Wiegert (1999) gives the critical semi-major axis a_crit for orbital stability around a star perturbed by a binary. This is

$$\begin{aligned} a_\mathrm{crit} = [&(0.464 \pm 0.006) + (-0.380 \pm 0.010)\mu \\ &+(-0.631 \pm 0.034)e_\star + (0.586 \pm 0.061)\mu e_\star \\ &+(0.150 \pm 0.041)e_\star^2 + (-0.198 \pm 0.074)\mu e_\star^2]a_\star \end{aligned} \tag{18}$$

where $\mu = m_\star/(m_{\zeta^2\,\mathrm{Reticuli}} + m_\star)$ is the star mass ratio of value 1/2 if we assume here $m_\star = m_{\zeta^2\,\mathrm{Reticuli}} = 1M_\odot$. Material with $a \geq a_\mathrm{crit}$ will be on an unstable orbit, and most probably scattered out of the system.

Applying this to our case leads to $a_\mathrm{crit} = 66^{+236}_{-66}$ AU. Uncertainties on a_crit are very large, and this result shows that within uncertainties, the disk could exist at the observed distances, or, in contrast, not exist at all. Therefore, this orbit was tested numerically. We considered a ring of 150,000 mass-less planetesimals uniformly distributed between 70 and 140 AU from their solar-mass host star, with proper initial eccentricities randomly distributed between 0 and 0.05, and initial inclinations between ±3°.

The test particles are perturbed by another solar-mass star in orbit around the primary with a semi-major axis 2046 AU and

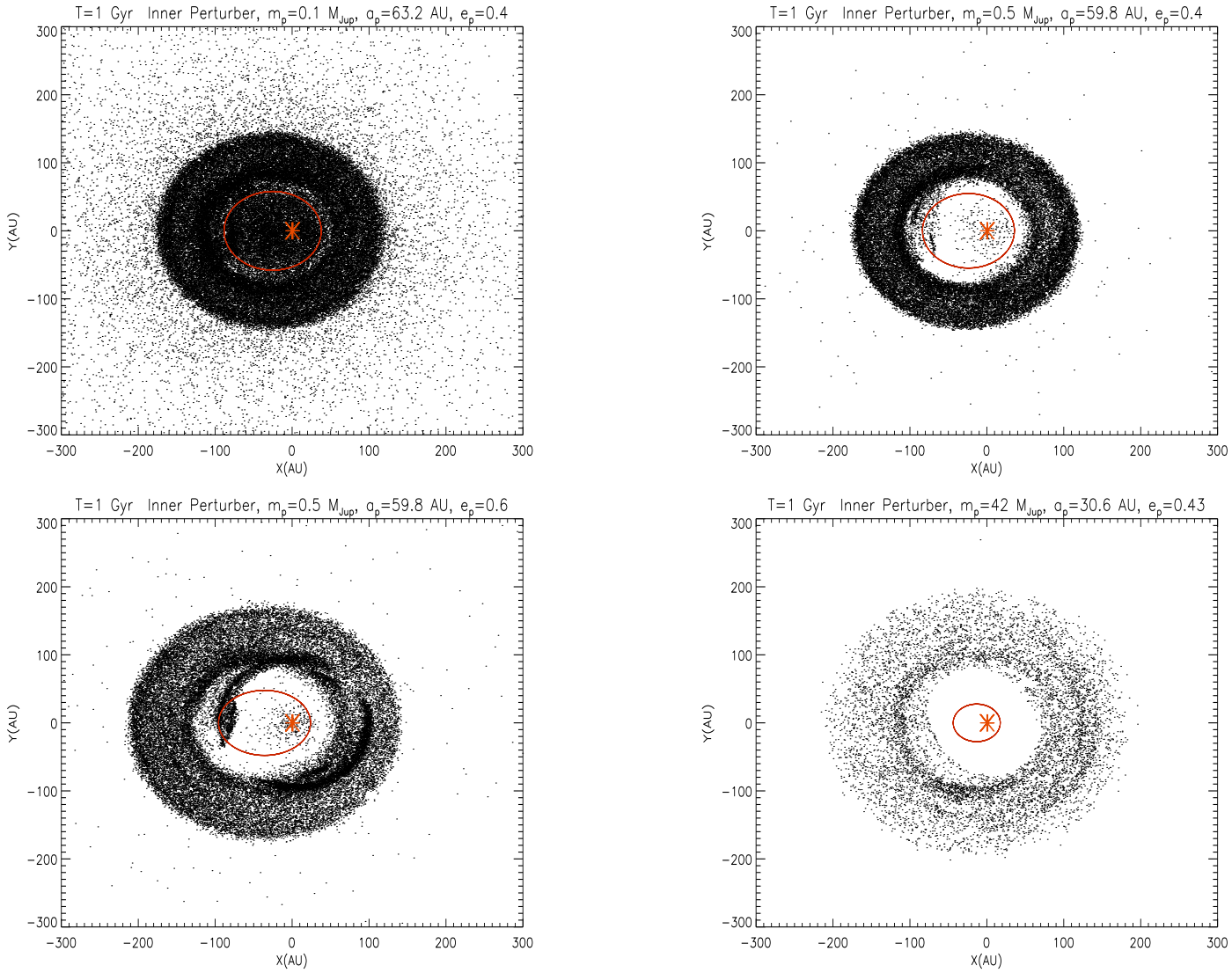

Fig. 7. Example views from above the plane of disks at 1 Gyr, under the influence of inner perturbers.**TOP** *Left:* the perturber scatters material in the inner parts of the system (Case A). *Right:* one of the best candidates (Case B). **BOTTOM** *Left:* resonant patterns appear (Case C). *Right:* a brown-dwarf perturber can be a good candidate.

eccentricity 0.815, coplanar to the disk. We used the SWIFT-RMVS N-body symplectic code of Levison & Duncan (1994) to compute their orbital evolution for 2 Gyr.

Our results are consistent with the predictions of Holman & Wiegert (1999): the disk is truncated at $\sim$ 80 AU (see Fig. 10, left panel), which is incompatible with observational constraints of the debris disk of ζ^2 Reticuli, since it radially extends up to $\sim$ 120 AU.

Moreover, at 2 Gyr, the disk has a highly symmetric shape and no clear offset from the star (see Fig. 10, right panel). These results suggest that the binary companion on an eccentric orbit can not account for the disk structure, and that an unseen eccentric companion is more likely responsible for shaping the disk.

Another possible way for a stellar binary companion to generate high-eccentricity orbiting bodies around a primary is the Kozai mechanism (Kozai 1962). This would occur if the disk and the binary orbit were mutually inclined by more than $\sim 39°$. In that case, the orbit of a particle in the disk would suffer coupled modulations in inclination and eccentricity, that is, a particle would periodically switch from a highly eccentric orbit, coplanar with the binary companion's orbit, to a circular orbit, highly inclined with respect to the orbit of the binary companion. However, we can discard this mechanism as a possible explanation for the eccentric global structure of the disk of ζ^2 Reticuli: indeed, the Kozai Hamiltonian is invariant by rotation, meaning that, if this mechanism is able to excite planetesimal eccentricities to high values, their longitudes of periastra remain uniformely distributed, while they should be preferentially aligned for an eccentric and offset disk to be generated.

5. Synthetic images

In this section, we use the results of our best-fit N-body simulations to produce a realistic dust population and synthetic images for comparison with *Herschel*/PACS observations. The procedure followed to create synthetic images is straightforward: a population of dust was created from the position of the parent planetesimals.

The main difference between dust particles and planetesimals is that the former are small enough to be affected by stellar radiation pressure. Radiation pressure is usually described for a particle by its constant ratio β to stellar gravity. The dust particles

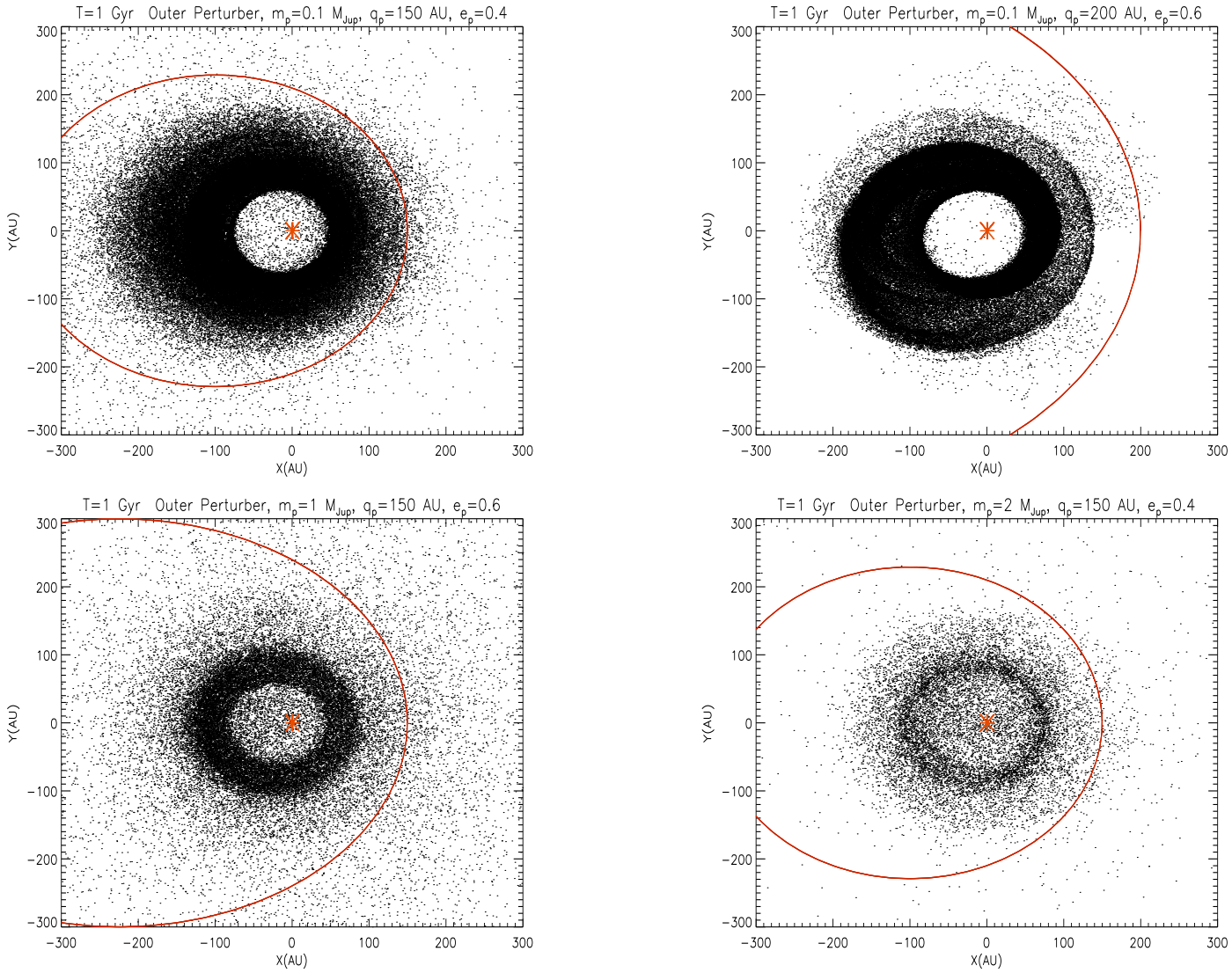

Fig. 8. Example views from above the disk plane at 1 Gyr, under the influence of outer perturbers. **TOP** *Left:* one of the best candidates (Case D). *Right:* spirals are still apparent (Case E). **BOTTOM** *Left:* one might question the contribution of the scattered material to the disk emission (Case F). *Right:* scattering processes tend to destroy the structure (Case G).

are assumed to be released by planetesimals, which feel no radiation pressure. Hence the daugther particles assume an orbit that is very different from that of their parent bodies. It is well known that if the parent bodies move on circular orbits, the dust particles are unbound from the star as soon as $\beta \geq 0.5$. In our case, however, dust particles may be released by planetesimals orbiting on more or less eccentric orbits, which may slightly change this threshold. Because planetesimal eccentricities are expected to be moderate on average, $\beta = 0.5$ can nevertheless be considered as a reasonable approximation.

Small grains are released from seed planetesimal positions at the planetesimal velocity, and are then spread along the orbits determined by these initial conditions and their β value. We are aware that this simple procedure cannot accurately evaluate the spatial distribution of the smallest grains. To do this, complex models such as the DyCoSS code of Thébault (2012), the CGA of Stark & Kuchner (2009), or the LIDT-DD ode by Kral et al. (2013) have to be used to evaluate the complex interplay between the rate at which grains are collisionally produced from parent planetesimals, the time they spend (because of their highly eccentric orbits) in empty collisionally inactive regions and the rate at which they can be affected or even ejected by close encounters with the perturbing planet (see Sect. 4 of Thebault et al. 2012), not to mention the Poynting-Robertson drag these small grains are subject to.

However, this caveat is acceptable for the present problem, because the role played by small micron-sized grains close to the blow-out size is very minor at wavelengths > 70 μm, so that our synthetic images are not strongly affected by errors in their spatial distribution.

We set the dust grain sizes range from 0.5 μm to 1 mm, with a classical Dohnanyi (1969) power-law distribution (index -3.5), which covers the β distribution from 0 to 0.5 well, since this parameter depends on grain size.

Their emission was computed using the radiative transfer code GRaTeR (see, e.g., Lebreton et al. 2012). To do this, the following parameters are required: distance of the star (12 pc), magnitude in band V (V = 5.24), and total luminosity 0.96 $L_{\odot}$.

Because the disk is optically thin, its mass is linearly linked to the flux emission intensity, and it can be easily scaled to fit the observed intensity (see Table 3). The mass needed for the disk to produce a flux as observed on *Herschel*/PACS will vary with the

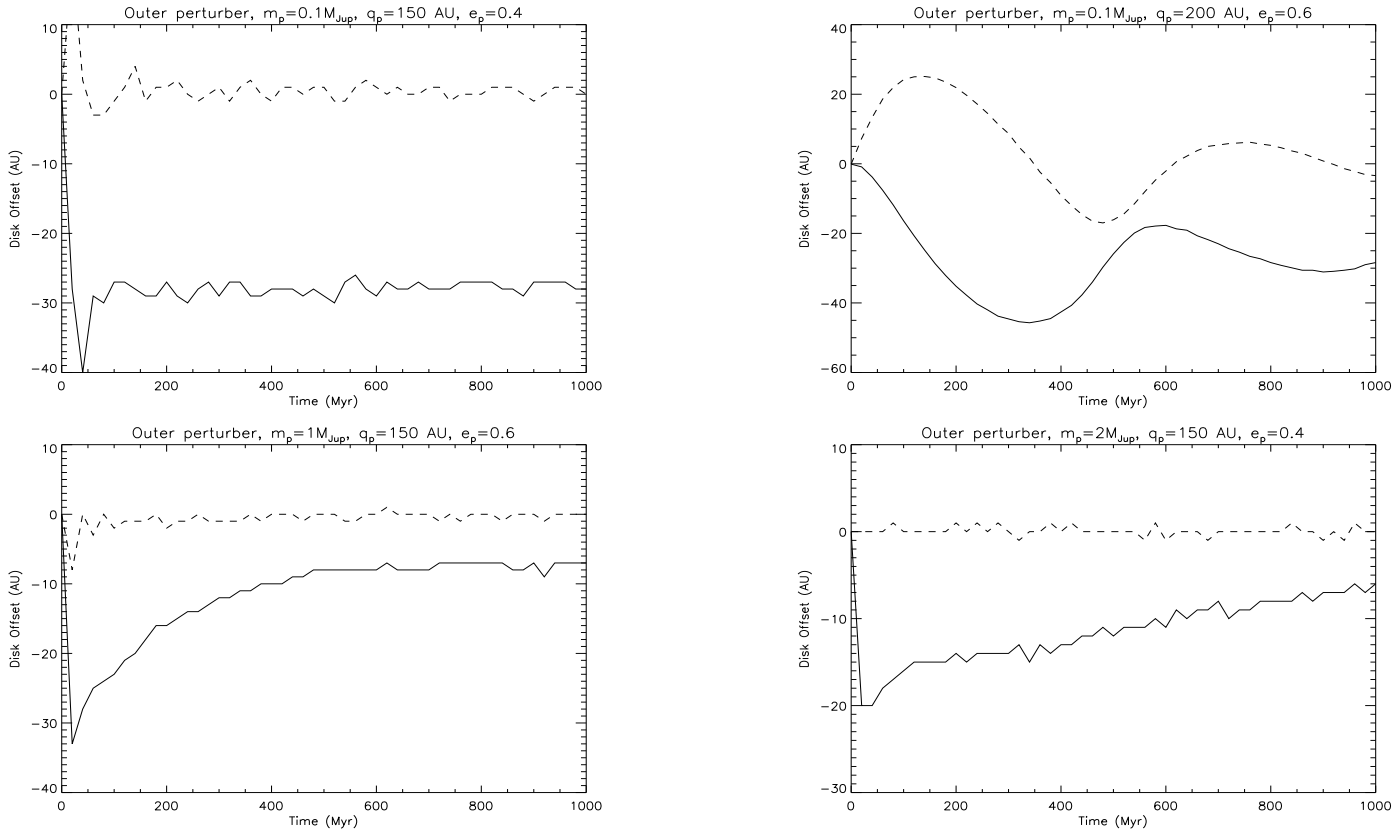

Fig. 9. Example of the time evolution on 1 Gyr of the disk offset coordinates (X *(solid line)* and Y *(dashed line)*) for outer perturbers. **TOP** *Left:* one of the best candidates (Case D). Because of the orientation of the perturber orbit, where its semi-major axis is along the X-axis with positive periastron, this corresponds to a negative X-offset $\Delta X \sim -30$ AU and a zero Y-offset for a disk located at $a_c \sim 100$ AU. *Right:* the oscillations of the offset coordinates reveal the spiral-winding regime (Case E). **BOTTOM** The offset seems to relax. *Left:* Case F. *Right:* Case G.

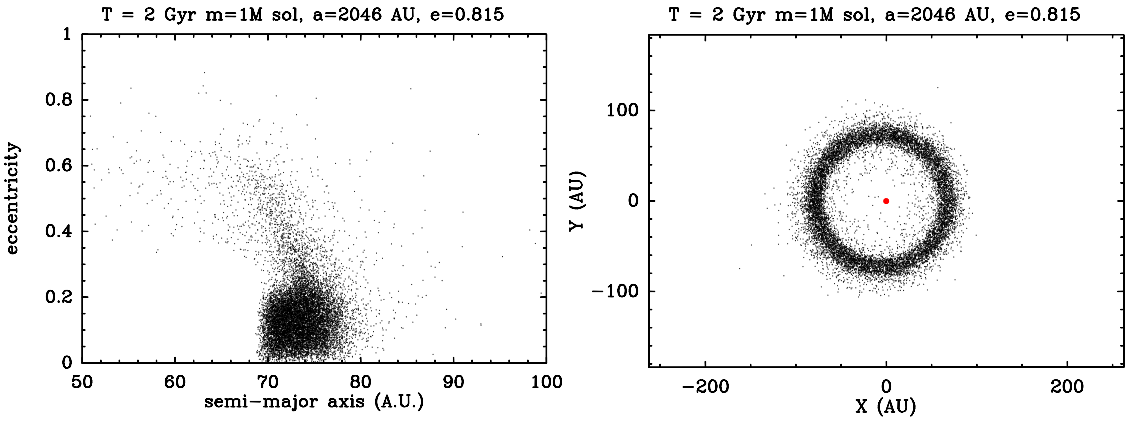

Fig. 10. Semi-major axis vs eccentricity diagram (left) and pole-on projection(right) of a disk of planetesimals after 2 Gyr under the influence of a one-solar-mass star of semi-major axis 2046AU on an orbit of eccentricity 0.815. The disk is truncated at ~ 80 AU and nearly circular. It has no clear offset: its centre of symmetry is offset by ~ 6 AU from the star along the perturber major axis. With a disk mean semi-major axis of ~ 70 AU, this gives a global eccentricity of ~ 0.08.

dust grain composition, and thus its density. But because we have no constraints on the dust composition, astrosilicate grains were used (Draine 2003), and the mass of the disk was simply scaled to obtain intensities compatible with observational constraints for a given wavelength.

Thermal emission images were produced with a resolution of 1″/pixel at 70 and 100 μm and 2″/pixel at 160 μm. Before convolving these images with the point spread function (PSF), the star was added at the central pixel with a flux intensity matching the predicted stellar photosphere flux density in each waveband. The position angles of the disk observed with *Herschel*/PACS and of the disk in our synthetic images, as well as the orientation of the telescope during the observations were taken into account (see Table 4). Our purpose was to match the observations.

We chose the simulation that led to a clear and significantly eccentric disk at 1 Gyr, namely our Case A (see Table 2, and upper-left panels of Fig. 8 and Fig. 9) to reproduce the *Herschel*/PACS image at 100 μm. The mass of the disk was scaled so that a total flux of 13.5 mJy as observed with *Herschel*/PACS at 100 μm was spread all over the disk. The last

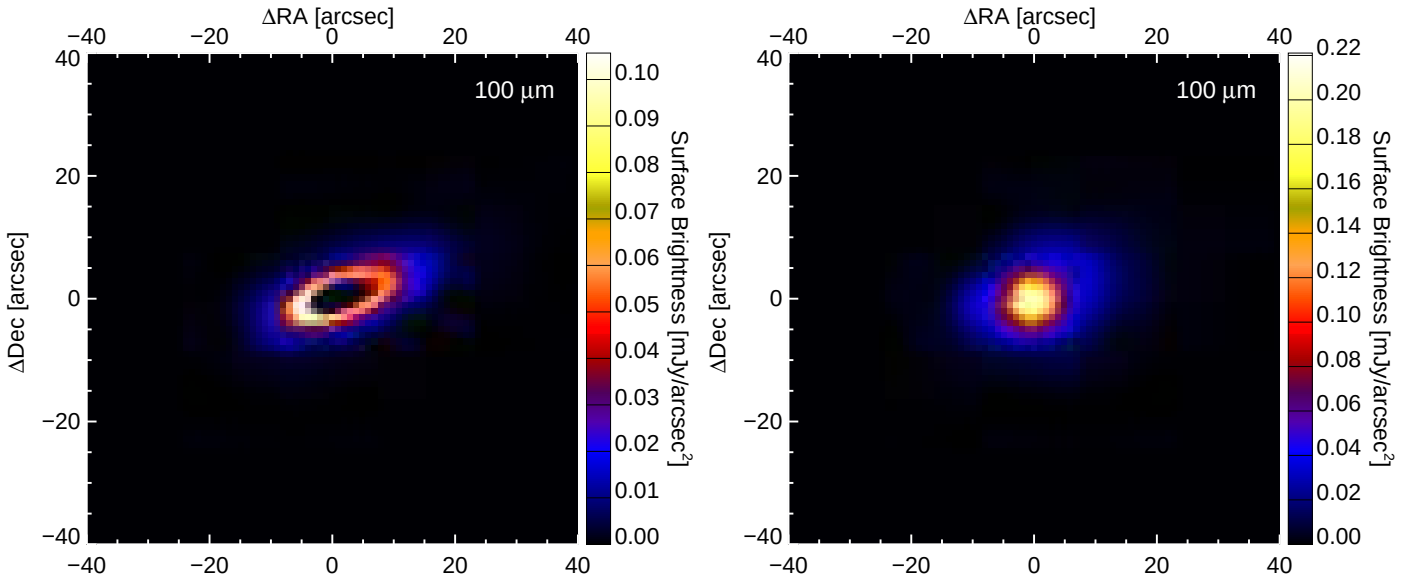

Fig. 11. Synthetic images at $\lambda = 100\,\mu$m, unconvolved disk (no star) *(left)* and convolved disk and star image with the PSF *(right)*. Disk at 1 Gyr in Case A (see Table 2), seen with inclination 65°. The star is at the centre of the image, and in the convolved image, the flux scale is set to match that in the *Herschel*/PACS image.

Wavelength (μm)	Stellar flux (mJy)	Disk flux (mJy)
70	24.9 ± 0.8	8.9 ± 0.8
100	13.4 ± 1.0	13.5 ± 1.0
160	19.4 ± 1.5	
	~ 4.7	~ 14.7

Table 3. Stellar and disk fluxes at 70, 100, and 160 μm (Eiroa et al. 2010). The fluxes at 70 and 100 μm, along with the total flux of the star-disk system at 160 μm are PACS measurements. The individual star and disk fluxes at 160 μm result from predictions.

	Wavelength (μm)	PA(°)
Observed disk	-	110
Simulated disk	-	110
PSF	70/160	127
PSF	100/160	127
ζ^2 Reticuli	70/160	281
ζ^2 Reticuli	100/160	281

Table 4. Disk position angle observed with *Herschel*/PACS, disk position angle in our synthetic images, and telescope orientation during *Herschel*/PACS observations and PSF.

parameter needed is the system inclination. Our best fit gives 65.5° (see Appendix B).

We present an unconvolved and convolved image of this disk in Fig. 11. The disk offset is clearly visible in unconvolved images. However, there seem to be no difference between the symmetric **and** asymmetric state after the images are convolved because of the contrast between the star and the disk emission. Moreover, the disk flux per pixel is one order of magnitude lower than the fluxes observed in *Herschel*/PACS images.

This is not surprising, however: to estimate the total disk flux, the flux was measured in a small region of the disk before applying aperture correction. Even if the correct aperture correction for a point source were used, it would always be a lower limit, and the total disk flux would be underestimated. The parent ring may also be narrower, which would increase the flux per pixel.

Therefore, we investigated the impact of the width and of the total flux of the disk on the features visible with PACS and produced convolved images of a dusty disk produced by an asymmetric eccentric parent ring of diverse total fluxes (1, 2, and 5 times the flux measured by *Herschel*/PACS) and of diverse widths (semi-major axis centred on 100 AU, widths 5, 10, and 20 AU). To do this, particles from a range of semi-major axes from our *N*-body simulation output were selected. An inclination angle of 65° was chosen, which is the most probable inclination derived for the system.

The fluxes per pixel recovered in convolved images with a disk five times more massive than the mass initially derived from observations match the observations better. This provides a better constraint on the disk mass and total flux. We show this example in Fig. 12 (left panel): the asymmetric double-lobe structure now appears clearly.

It is worth noting that the width of the parent ring has a more limited influence on the flux per pixel than the mass of the disk. But it has an influence on the appearance of the disk: a narrow parent ring (< 10 AU) leads to a resolved apastron lobe, which is more consistent with *Herschel*/PACS images, although this lobe does not seem to be located as far from the star as it is in the *Herschel*/PACS images.

Therefore, we also investigated the location of the disk by producing convolved images of a ring of dust produced by a narrow eccentric parent ring of width 5 AU and semi-major axis centred on 120, 130, and 140 AU . The disk total flux was set to be five times the flux derived from observations. The inclination angle was here again set to 65°. As expected, the farther away the disk is located, the clearer the lobes appear (see Fig. 12).

Finally, with all these insights, we conclude that the hypothesis of an eccentric dusty disk around ζ^2 Reticuli is indeed compatible with *Herschel*/PACS images, provided that the dust is produced by a narrow parent ring with width less than 10 AU and located slightly farther away than derived by Eiroa et al. (2010),

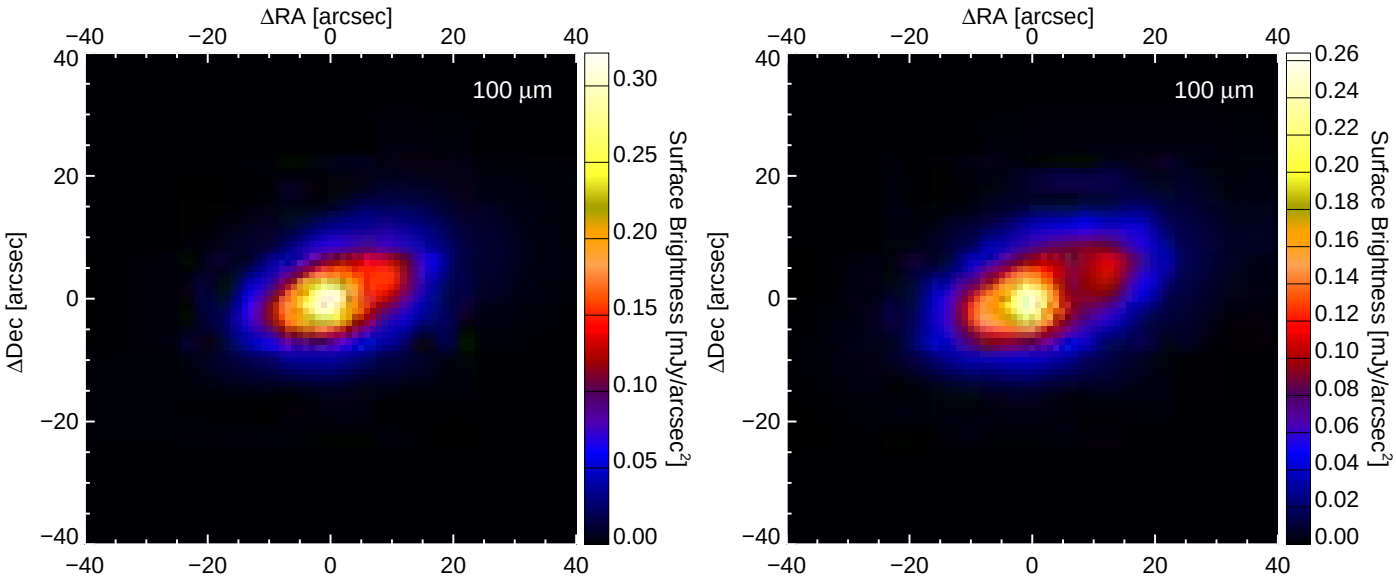

Fig. 12. Synthetic images of Case A (see Table 2) at 100 μm and convolved with the PSF. The parent ring is centred on 100 AU (left) and 130 AU (right), has a width of 5 AU and is seen with an inclination of 65°. The disk total flux is five times the flux measured by *Herschel*/PACS. The star is at the centre of the image and the flux scale is set to match that of *Herschel*/PACS image.

such that its a semi-major axis distribution is centred between 120 and 140 AU.

This slightly changes the constraints derived on potential perturbers, but the forced eccentricity only depends on the ratio between the planet and planetesimal semi-major axis, and in a linear way at lowest-order approximation. This means that in this approximation the constraints can be completely scaled in a linear way, that is, the potential semi-major axis for planets must also be increased by 20–40 % and the disk needs to be centred on 120–140 AU, while the constraint on the perturber eccentricity ($e \gtrsim 0.3$) remains identical.

6. Discussion and conclusion

We used ζ^2 Reticuli as an example to discuss the shaping of a disk into an eccentric ring on Gyr timescales.

We showed that eccentric patterns in debris disks can be maintained on Gyr timescales, but also that eccentric perturbers can produce patterns other than eccentric rings.

The general results of our simulations show that both inner and outer perturbers can generate extremely significant scattering processes. They can cause a disk to adopt structures that show no clear elliptic ring: the inner part of the disk is either filled or the structure is destroyed. These scattering processes endanger the survival of an eccentric ring, and investigating these processes with numerical experiments allowed us to put constraints on potential perturbers. From these constraints, we derived an upper-mass limit for outer perturbers in a certain range of periastra and a lower-mass limit for inner perturbers.

Moreover, the timescale for spiral structures to vanish is longer with smaller-mass perturbers, and thus, investigating this timescale with numerical experiments permitted us to place a lower-mass limit on perturbers, provided that spiral structures in a disk can definitely be ruled out from observations. The role of numerical experiments is crucial here, since the analytical timescale at the disk centre of distribution underestimates the effective timescale in a real extended disk.

The offset of the disk centre with respect to the star is mostly stable; however, we note that it seems to relax very slowly in rare cases. While the former evolution is characteristic for pericentre glow dynamics, the latter one is surprising. The relaxation of the eccentric structure is not expected in the first-order secular analysis described by Wyatt et al. (1999) and Wyatt (2005). It may be the result of higher-order terms that have been neglected in the analytical study, and is more probably caused by erratic short-term variations of the planetesimals' semi-major axes due to moderately distant approaches to the planet. These effects, which can lead to scattering of the planetesimals, are eliminated in the analytical averaging process of the perturbations, and thus cannot be predicted analytically in the secular approximations used here. A more detailed study of this relaxation phenomenon of pericentre glow structures is nevertheless beyond the scope of the present paper and will be the purpose of future work.

Transient spiral structures, filled inner holes, sparsely populated scattered disks, and resonant clumpy structures are all possible results when an eccentric perturber acts on a debris disk. They can be shown with numerical simulations, but more importantly, used to derive constraints on a perturber in a system (mass and eccentricity). Therefore, we provided a method for investigating and modelling eccentric ring structures based on a complementary analytic and numerical approach, where one can derive potential orbits from analytics and test them numerically using N-body codes. This method can be easily applied to other systems and is expected to be useful in the near future.

Indeed, Kaib et al. (2013) have pointed out that wide binary star systems, that is, systems with separations greater than 1000 AU, can produce eccentric planets around a primary star on Gyr timescales. This is due to Galactic tides and passing star perturbations, which are able, sooner or later, to set the secondary star on a highly eccentric orbit. The proportion of wide binary systems is by no means negligible ($\sim$ 50%, Duquennoy & Mayor 1991), and although debris disks which are several Gyr old are faint and difficult to detect, this will be overcome with the unique capabilities of ALMA, JWST, and SPICA. Therefore, old eccen-

tric patterns in debris disks are expected to be commonly observed in the future.

The ζ^2 Reticuli disk is one such example of such a Gyr-old eccentric debris disk. Moreover, ζ^2 Reticuli is part of a wide binary star system, which may provide an explanation for the presence of an eccentric perturber around ζ^2 Reticuli. We showed that the binary companion cannot be directly responsible for the eccentric ring structure, and also that the asymmetry is instead caused by a closer companion, either interior or exterior to the disk. In all cases, the eccentric companion is expected to have an eccentricity $e \gtrsim 0.3$ to produce this pattern.

Investigation of the disk structure generated by the scattering processes provided an upper-mass limit of 2 $M_{\rm Jup}$ for an outer perturber located in a range of periastra 150 – 250AU, whereas a lower-mass limit of 0.1 $M_{\rm Jup}$ is associated with inner perturbers in the ζ^2 Reticuli system.

By producing synthetic images, we showed that the original interpretation of the double-lobed feature around ζ^2 Reticuli, that is, the observed eccentric ring $e \gtrsim 0.3$, is clearly supported, although the disk is located slightly farther away (20–40%) than originally derived. Moreover, we found that the dusty disk is probably created by a narrow parent ring (width <10 AU), which should have a slight inclination with the line of sight, compatible with the most probable inclination derived for the system, and it also has a significantly higher flux than that estimated from the *Herschel*/PACS measurements (at least five times).

Aknowledgements:

We thank the referee, A. Mustill, for very useful comments that contributed to clarity of this paper. Computations presented in this paper were performed at the Service Commun de Calcul Intensif de l'Observatoire de Grenoble (SCCI) on the supercomputer funded by the Agence Nationale pour la Recherche under contracts ANR-07-BLAN-0221, ANR-2010-JCJC-0504-01 and ANR-2010-JCJC-0501-01. B. Montesinos, C. Eiroa and J.P. Marshall are supported by Spanish grant AYA 2011-26202. A. Bonsor and S. Ertel acknowledge the support of the ANR-2010 BLAN-0505- 01 (EXOZODI). The authors wish to thank the PNP/CNES for their financial support. This work has also greatly benefited from the software resulting from Thomas Tintillier's training project.

References

Allard, F., Homeier, D., & Freytag, B. 2011, in Astronomical Society of the Pacific Conference Series, Vol. 448, 16th Cambridge Workshop on Cool Stars, Stellar Systems, and the Sun, ed. C. Johns-Krull, M. K. Browning, & A. A. West, 91
Augereau, J. C., Nelson, R. P., Lagrange, A. M., Papaloizou, J. C. B., & Mouillet, D. 2001, A&A, 370, 447
Augereau, J. C. & Papaloizou, J. C. B. 2004, A&A, 414, 1153
Aumann, H. H., Beichman, C. A., Gillett, F. C., et al. 1984, ApJ, 278, L23
Backman, D. E. & Paresce, F. 1993, in Protostars and Planets III, ed. E. H. Levy & J. I. Lunine, 1253–1304
Baraffe, I., Chabrier, G., Barman, T. S., Allard, F., & Hauschildt, P. H. 2003, A&A, 402, 701
Beust, H., Augereau, J.-C., Bonsor, A., et al. 2014, A&A, 561, A43
Beust, H. & Dutrey, A. 2006, A&A, 446, 137
Boley, A. C., Payne, M. J., Corder, S., et al. 2012, ApJ, 750, L21
Chiang, E., Kite, E., Kalas, P., Graham, J. R., & Clampin, M. 2009, ApJ, 693, 734
Dohnanyi, J. S. 1969, J. Geophys. Res., 74, 2531
Draine, B. T. 2003, ARA&A, 41, 241
Duncan, M., Quinn, T., & Tremaine, S. 1989, Icarus, 82, 402
Duquennoy, A. & Mayor, M. 1991, A&A, 248, 485
Eiroa, C., Fedele, D., Maldonado, J., et al. 2010, A&A, 518, L131
Eiroa, C., Marshall, J. P., Mora, A., et al. 2013, A&A, 555, A11
Ertel, S., Wolf, S., Eiroa, C., et al. 2011, in EPSC-DPS Joint Meeting 2011, 678
Ertel, S., Wolf, S., & Rodmann, J. 2012, A&A, 544, A61
Ford, E. B., Kozinsky, B., & Rasio, F. A. 2000, ApJ, 535, 385
Gray, R. O., Corbally, C. J., Garrison, R. F., et al. 2006, AJ, 132, 161
Guilloteau, S., Dutrey, A., Piétu, V., & Boehler, Y. 2011, A&A, 529, A105
Henry, T. J., Soderblom, D. R., Donahue, R. A., & Baliunas, S. L. 1996, AJ, 111, 439
Holman, M. J. & Wiegert, P. A. 1999, AJ, 117, 621
Johnson, H. L., Mitchell, R. I., Iriarte, B., & Wisniewski, W. Z. 1966, Communications of the Lunar and Planetary Laboratory, 4, 99
Kaib, N. A., Raymond, S. N., & Duncan, M. 2013, Nature, 493, 381
Kalas, P., Graham, J. R., Chiang, E., et al. 2008, Science, 322, 1345
Kalas, P., Graham, J. R., & Clampin, M. 2005, Nature, 435, 1067
Kalas, P., Graham, J. R., Fitzgerald, M. P., & Clampin, M. 2013, ArXiv e-prints
Kozai, Y. 1962, AJ, 67, 591
Kral, Q., Thébault, P., & Charnoz, S. 2013, A&A, 558, A121
Krist, J. E., Stapelfeldt, K. R., Bryden, G., & Plavchan, P. 2012, AJ, 144, 45
Krivov, A. V. 2010, Research in Astronomy and Astrophysics, 10, 383
Krymolowski, Y. & Mazeh, T. 1999, MNRAS, 304, 720
Lebreton, J., Augereau, J.-C., Thi, W.-F., et al. 2012, A&A, 539, A17
Lenzen, R., Hartung, M., Brandner, W., et al. 2003, in Society of Photo-Optical Instrumentation Engineers (SPIE) Conference Series, Vol. 4841, Society of Photo-Optical Instrumentation Engineers (SPIE) Conference Series, ed. M. Iye & A. F. M. Moorwood, 944–952
Levison, H. F. & Duncan, M. J. 1994, Icarus, 108, 18
Löhne, T., Krivov, A. V., & Rodmann, J. 2008, ApJ, 673, 1123
Luhman, K. L., Patten, B. M., Marengo, M., et al. 2007, ApJ, 654, 570
Malhotra, R. 1993, Nature, 365, 819
Malhotra, R. 1995, AJ, 110, 420
Mamajek, E. E. 2012, ApJ, 754, L20
Mardling, R. A. & Lin, D. N. C. 2002, ApJ, 573, 829
Marois, C., Lafrenière, D., Doyon, R., Macintosh, B., & Nadeau, D. 2006, ApJ, 641, 556
Marois, C., Macintosh, B., Barman, T., et al. 2008, Science, 322, 1348
Marois, C., Zuckerman, B., Konopacky, Q. M., Macintosh, B., & Barman, T. 2010, Nature, 468, 1080
Masana, E., Jordi, C., & Ribas, I. 2006, A&A, 450, 735
Mason, B. D., Wycoff, G. L., Hartkopf, W. I., Douglass, G. G., & Worley, C. E. 2001, AJ, 122, 3466
Mayor, M., Pepe, F., Queloz, D., et al. 2003, The Messenger, 114, 20
Mayor, M. & Queloz, D. 1995, Nature, 378, 355
Moro-Martín, A. 2012, ArXiv e-prints
Moro-Martín, A. & Malhotra, R. 2002, AJ, 124, 2305
Mouillet, D., Larwood, J. D., Papaloizou, J. C. B., & Lagrange, A. M. 1997, MNRAS, 292, 896
Mustill, A. J. & Wyatt, M. C. 2009, MNRAS, 399, 1403
Noyes, R. W., Hartmann, L. W., Baliunas, S. L., Duncan, D. K., & Vaughan, A. H. 1984, ApJ, 279, 763
Quillen, A. C. 2006, MNRAS, 372, L14
Reche, R., Beust, H., Augereau, J.-C., & Absil, O. 2008, A&A, 480, 551
Reiners, A. & Schmitt, J. H. M. M. 2003, A&A, 398, 647
Rousset, G., Lacombe, F., Puget, P., et al. 2003, in Society of Photo-Optical Instrumentation Engineers (SPIE) Conference Series, Vol. 4839, Society of Photo-Optical Instrumentation Engineers (SPIE) Conference Series, ed. P. L. Wizinowich & D. Bonaccini, 140–149
Shaya, E. J. & Olling, R. P. 2011, ApJS, 192, 2
Soummer, R., Pueyo, L., & Larkin, J. 2012, ApJ, 755, L28
Stapelfeldt, K. R., Holmes, E. K., Chen, C., et al. 2004, ApJS, 154, 458
Stapelfeldt, K. R., Krist, J. E., Bryden, G. C., & Plavchan, P. 2012, in American Astronomical Society Meeting Abstracts, Vol. 220, American Astronomical Society Meeting Abstracts 220, 506.03
Stark, C. C. & Kuchner, M. J. 2008, ApJ, 686, 637
Stark, C. C. & Kuchner, M. J. 2009, ApJ, 707, 543
Thébault, P. 2012, A&A, 537, A65
Thébault, P. & Augereau, J.-C. 2007, A&A, 472, 169
Thebault, P., Kral, Q., & Ertel, S. 2012, A&A, 547, A92
Thébault, P., Kral, Q., & Ertel, S. 2012, ArXiv e-prints
Torres, C. A. O., Quast, G. R., da Silva, L., et al. 2006, A&A, 460, 695
Trilling, D. E., Bryden, G., Beichman, C. A., et al. 2008, ApJ, 674, 1086
van Leeuwen, F. 2007, A&A, 474, 653
Watson, C. A., Littlefair, S. P., Diamond, C., et al. 2011, MNRAS, 413, L71
Wisdom, J. 1980, AJ, 85, 1122
Wyatt, M. C. 1999, PhD thesis, Royal Observatory, Blackford Hill, Edinburgh EH9 3HJ, UK
Wyatt, M. C. 2004, in American Institute of Physics Conference Series, Vol. 713, The Search for Other Worlds, ed. S. S. Holt & D. Deming, 93–102
Wyatt, M. C. 2005, A&A, 440, 937

Wyatt, M. C. & Dent, W. R. F. 2002, MNRAS, 334, 589
Wyatt, M. C., Dermott, S. F., & Telesco, C. M. 2000, in Astronomical Society of the Pacific Conference Series, Vol. 219, Disks, Planetesimals, and Planets, ed. G. Garzón, C. Eiroa, D. de Winter, & T. J. Mahoney, 289
Wyatt, M. C., Dermott, S. F., Telesco, C. M., et al. 1999, ApJ, 527, 918

Appendix A: SPIRE images of ζ^2 Reticuli

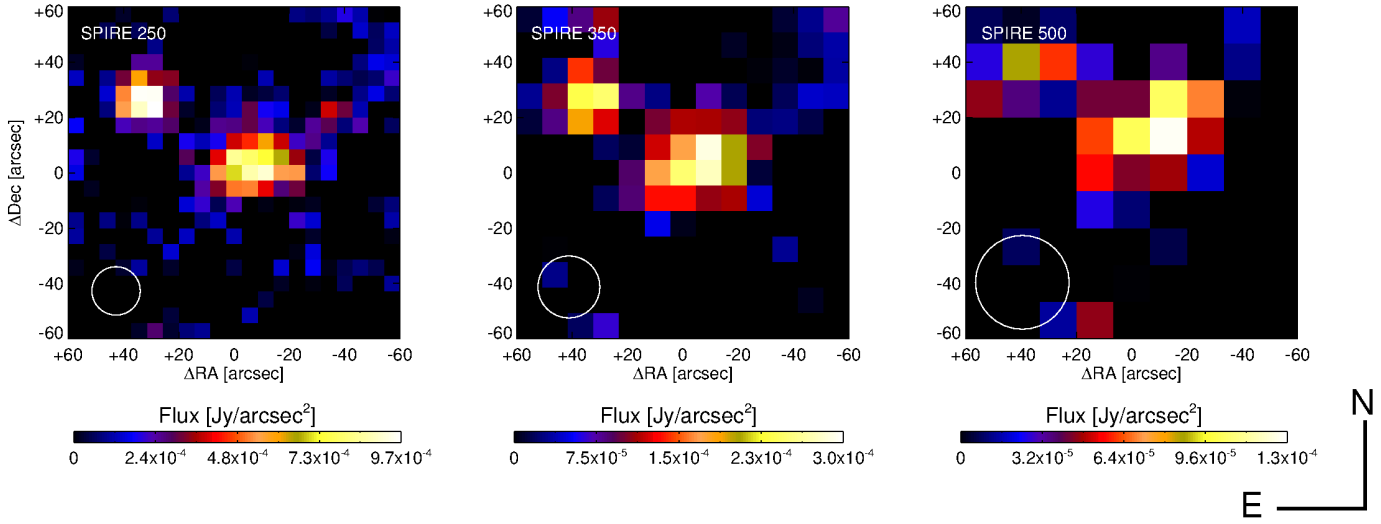

Fig. A.1. *Herschel*/SPIRE images of ζ^2 Reticuli at 250, 350, and 500 μm (left–right). The images were reduced using the standard reduction scripts ofn HIPE, version 8.2, and SPIRE CAL 8.1. Image orientation is north up, east left. The pixel scales are 6″, 10″, and 14″ at 250, 350, and 500 μm, respectively. The SPIRE beam FWHM in each band is denoted by the white circle in the bottom-left corner of each image.

Wavelength (μm)	Stellar flux (mJy)	Disk+star flux (mJy)
250	2.03 ± 0.03	59.72 ± 6.70
350	1.04 ± 0.02	24.68 ± 6.89
500	0.51 ± 0.10	20.29 ± 7.66

Table A.1. Predicted stellar fluxes and SPIRE flux measurements of the star-disk system at 250, 350, and 500 μm (Eiroa et al. 2013).

Appendix B: Inclination of ζ^2 Reticuli

Observations of the debris disk surrounding ζ^2 Reticuli reveal a double-lobed asymmetric feature. The inclination of this system relative to the line of sight is a key parameter for correctly interpreting the observations. If the system is seen pole-on, one would expect the observed feature to be the signature of resonant clumps, whereas an eccentric ring signature would be more plausible if the system were observed edge-on.

In general, observations suggest that stellar and disk inclinations are aligned (Watson et al. 2011; Guilloteau et al. 2011). Under this assumption, one can estimate the disk inclination from the observed stellar inclination. Consequently, we aim here to measure the star's inclination i, that is, the angle formed by its rotation axis with respect to the line of sight. With this convention, the system is seen pole-on if $i = 0°$, and edge-on if $i = 90°$.

The method used requires knowing the following stellar properties: the colour index $(B - V)$, the radius $R_\star$, the projected rotational velocity, $v_{\rm rot}\sin(i)$, and finally $R'_{\rm HK}$, an activity indicator defined as $F'_{\rm HK}/\sigma T_\star^4$, where $F'_{\rm HK}$ is the chromospheric flux in the H and K lines of Ca II, and $T_\star$ is the effective star temperature. These properties for ζ^2 Reticuli are summarised in Table B.1.

We first used the activity/rotation diagram built by Noyes et al. (1984), which plots $\log(R'_{\rm HK})$ versus $\log({\rm Ro})$ and shows a relationship between these two quantities for late-type stars. ${\rm Ro} = P_{\rm rot}/\tau_{\rm c}$ is the Rossby number, $P_{\rm rot}$ is the rotational period of the star, and $\tau_{\rm c}$ a model-dependent typical convective time, called the turnover time. Using Fig. 6(b) of Noyes et al. (1984) and the observed value of $\log(R'_{\rm HK}) = -4.79$ found by Henry et al. (1996) for ζ^2 Reticuli allows us to estimate $\log(P_{\rm rot}/\tau_{\rm c}) \sim 0.185 \pm 0.085$.

Then, using equation (4) of Noyes et al. (1984), where x is defined with the star colour index $(B - V)$ by $x = 1 - (B - V)$, one can estimate $\tau_{\rm c}$:

$$\log \tau_{\rm c} = \begin{cases} 1.362 - 0.166x + 0.025x^2 - 5.323x^3 & , x > 0 \\ 1.362 - 0.14x & , x < 0 \end{cases} . \quad \text{(B.1)}$$

ζ^2 Reticuli has a colour index $(B - V) = 0.60$ (Johnson et al. 1966), which gives $\tau_{\rm c} = 9.10$ days. The corresponding range of possible rotation periods is $P_{\rm rot} \sim 14.20 \pm 2.75$ days.

Table B.1. Stellar properties of ζ^2 Reticuli.

Stellar property	Value	Reference
$(B-V)$	0.60	1
$R_\star$ ($R_\odot$)	$\sim 0.965 \pm 0.05$	2
$L_\star$ ($L_\odot$)	0.97	3
$T_\star$ (K)	5851	3
$v_{\rm rot} \sin i$ (km/s)	2.7 ± 0.3	4
$\log(R'_{\rm HK})$	-4.79 ± 0.03	5
log(Ro)	$\sim 0.185 \pm 0.085$	2
τ_c (days)	~ 9.10	2
$P_{\rm rot}$ (days)	$\sim 14.20 \pm 2.75$	2
$v_{\rm rot}$ (km/s)	$\sim 3.42 \pm 0.66$	2
$i(^\circ)$	$\sim 65.5^{+24.5}_{-31.5}$	2

References. (1) Johnson et al. (1966); (2) this study; (3) Eiroa et al. (2013); (4) Reiners & Schmitt (2003); (5) Henry et al. (1996).

Since the equatorial rotation velocity is defined as $v_{\rm rot} = 2\pi R_\star / P_{\rm rot}$, knowing the stellar radius $R_\star$ allows us to obtain a range of possible values for $v_{\rm rot}$. Using $T_\star$ and $L_{\rm bol}$ and corrections prescribed by Masana et al. (2006), we found that for ζ^2 Reticuli, $R_\star = 0.965 R_\odot \pm 0.05$. The corresponding value of equatorial velocity is $\sim 3.42 \pm 0.66$ km/s.

We compared this with the independent measurement of $v_{\rm rot} \sin i$ by Reiners & Schmitt (2003). They found $v_{\rm rot} \sin(i) = 2.7 \pm 0.3$ km/s, which combined with the calculated rotational velocity, allows us to estimate the stellar inclination. We found that the inclination can range from 34° to 90° (see Fig B.1). This is very consistent with an inclined disk.

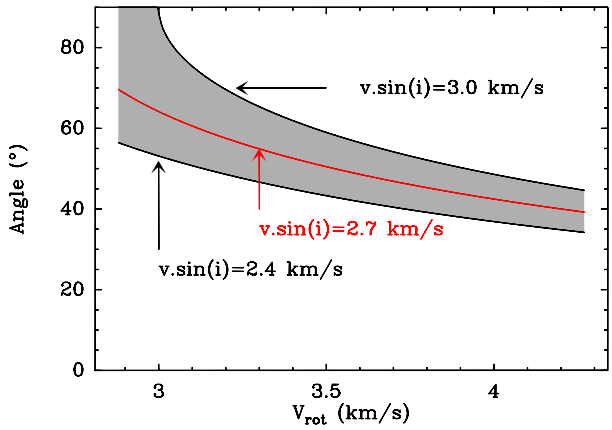

Fig. B.1. Possible inclination angles (taken from the pole) for ζ^2 Reticuli as a function of $v_{\rm rot}$ ranging between $\sim$ 2.76 and 4.08 km/s, where i is computed using the values of $v_{\rm rot} \sin(i) = 2.7 \pm 0.3$ km/s (Reiners & Schmitt 2003). The acceptable zone for the inclination is grey-shaded.

However, two angles are required to fully constrain the stellar rotation and disk axis. Therefore a degree of freedom remains and different orientations may lead to the same inclination i. Namely, the range of possible orientations leading to a same inclination is the set of axes describing a solid angle $2\pi \sin i$ about the line of sight. But the number of axes that lead to the same inclination increases with i, since it follows a $\sin i$ distribution. This means that the inclinations in a range $[34°; 90°]$ are not equiprobable. The probability for a given inclination to be between i and $i + di$, provided it is in the range $[34°; 90°]$, can thus be written

$$dP(i) = \frac{\sin i di}{\int_{34°}^{90°} \sin i di} \quad , \tag{B.2}$$

and the probability to find inclinations between i_1 and i_2 in the range $[34°; 90°]$ is

$$P(i \in [i_1; i_2]) = \frac{\int_{i_1}^{i_2} \sin i di}{\int_{34°}^{90°} \sin i di} \quad . \tag{B.3}$$

Applying this to the case of ζ^2 Reticuli, among the possible ranges of $[34°; 90°]$, we have an $\sim$ 50% chance that the observed inclination is in the range $[65.5°; 90°]$. Thus the system inclination is $i = 65.5^{\circ +24.5}_{-31.5}$. Consequently, the disk is more probably seen almost edge-on, with a pure edge-on configuration not ruled out.

Because of the large uncertainties, this constraint does not really allow us to conclude with absolute confidence whether the disk exhibits an eccentric ring or resonant clumps. However, resonant structures are in general thin structures that tend to be hidden

by non-resonant bodies and are difficult to detect, even in case of pole-on observations (Reche et al. 2008). This argument clearly supports the interpretation of Eiroa et al. (2010), who favoured an eccentric ring structure with $e \gtrsim 0.3$ seen edge-on and extending from $\sim$ 70 to $\sim$ 120 AU.

Appendix C: Constraints on ζ^2 Ret set by direct imaging

VLT/NaCo (Lenzen et al. 2003; Rousset et al. 2003) Ks-band data were retrieved from the ESO archive (ID 086.C-0732(A); PI: Löhne, 71574). Two epochs were available in August 2010 and November 2010, the former missing photometric calibration therefore only the latter was used to set detection limits on the presence of bound companions. Nevertheless, both data sets were reduced and no companion was detected. The data from November 11, 2010 were obtained in field stabilized-mode with five manual offsets of the derotator to simulate field rotation, with the S27 camera providing a pixel scale of 27 mas/pixel. Twenty image cubes with a DITxNDIT of 1.5s x 42 were obtained for a total observing time on target of 21min. The semi-transparent mask C_0.7_sep_10 with a diameter of 0.7″ and a central transmission of 3.5×10^{-3} was used. Each individual image was bad pixel-corrected and flat-fielded. Background subtraction was made for each cube using the closest sky images. The images were rencentred using a Gaussian fit of the attenuated central star. The data were selected within each data cube using criteria based on the attenuated central star flux and the encircled energy between 0.4″ and 0.55″. The images were then binned every 6s and derotated into a reference frame where the pupil was stabilized in order to simulate angular differential imaging (ADI, Marois et al. 2006). In this reference frame, the total field rotation provided by the manual offsets plus the natural pupi/field rotation is 17°. This data cube was then reduced using principal components analysis (PCA, Soummer et al. 2012), retaining four components out of 105.

The noise in the final reduced image was estimated using a sliding nine pixel-wide box to obtain a preliminary map of detection limits in magnitude. We corrected this map by computing the flux losses due to the PCA reduction. They were estimated by injecting fake planets into the data cube at a $10-\sigma$ level and processing the data again. Last, these detection limits in magnitude were converted into detection limits in masses, using the COND (Baraffe et al. 2003) or BT-settl models (Allard et al. 2011), assuming an age of 2 Gyr. The 2D-detection limits derived with the COND evolutionary models is presented in Fig. C.1

[1] UJF-Grenoble 1 / CNRS-INSU, Institut de Planétologie et d'Astrophysique de Grenoble (IPAG) UMR 5274, Grenoble, F-38041, France
[2] LESIA, Observatoire de Paris, 92195, Meudon, France
[3] Instituto Nacional de Astrofísica, Óptica y Electrónica, Luis Enrique Erro 1, Sta. Ma. Tonantzintla, Puebla, Mexico
[4] Universidad Autónoma de Madrid, Dpto. Física Teórica, Módulo 15, Facultad de Ciencias, Campus de Cantoblanco, E-28049 Madrid, Spain
[5] European Southern Observatory, Casilla 19001, Santiago 19, Chile
[6] Dpt de Astrofísica, Centro de Astrobiología (INTA-CSIC), ESAC Campus, P.O.Box 78, E-28691, Villanueva de la Cañada, Madrid, Spain
[7] Aurora Technology B.V., ESA-ESAC, P.O. Box 78, 28691, Villanueva de la Cañada, Madrid, Spain
[8] Jet Propulsion Laboratory, California Institute of Technology, 4800 Oak Grove Drive, Pasadena, CA 91109, USA
[9] NASA Goddard Space Flight Center, Exoplanets and Stellar Astrophysics, Code 667, Greenbelt, MD 20771, USA
[10] Rutherford Appleton Laboratory, Chilton OX11 0QX, UK
[11] Department of Physics and Astrophysics, Open University, Walton Hall, Milton Keynes MK7 6AA, UK
[12] Christian-Albrechts-Universität zu Kiel, Institut für Theoretische Physik und Astrophysik, Leibnizstr. 15, 24098 Kiel, Germany

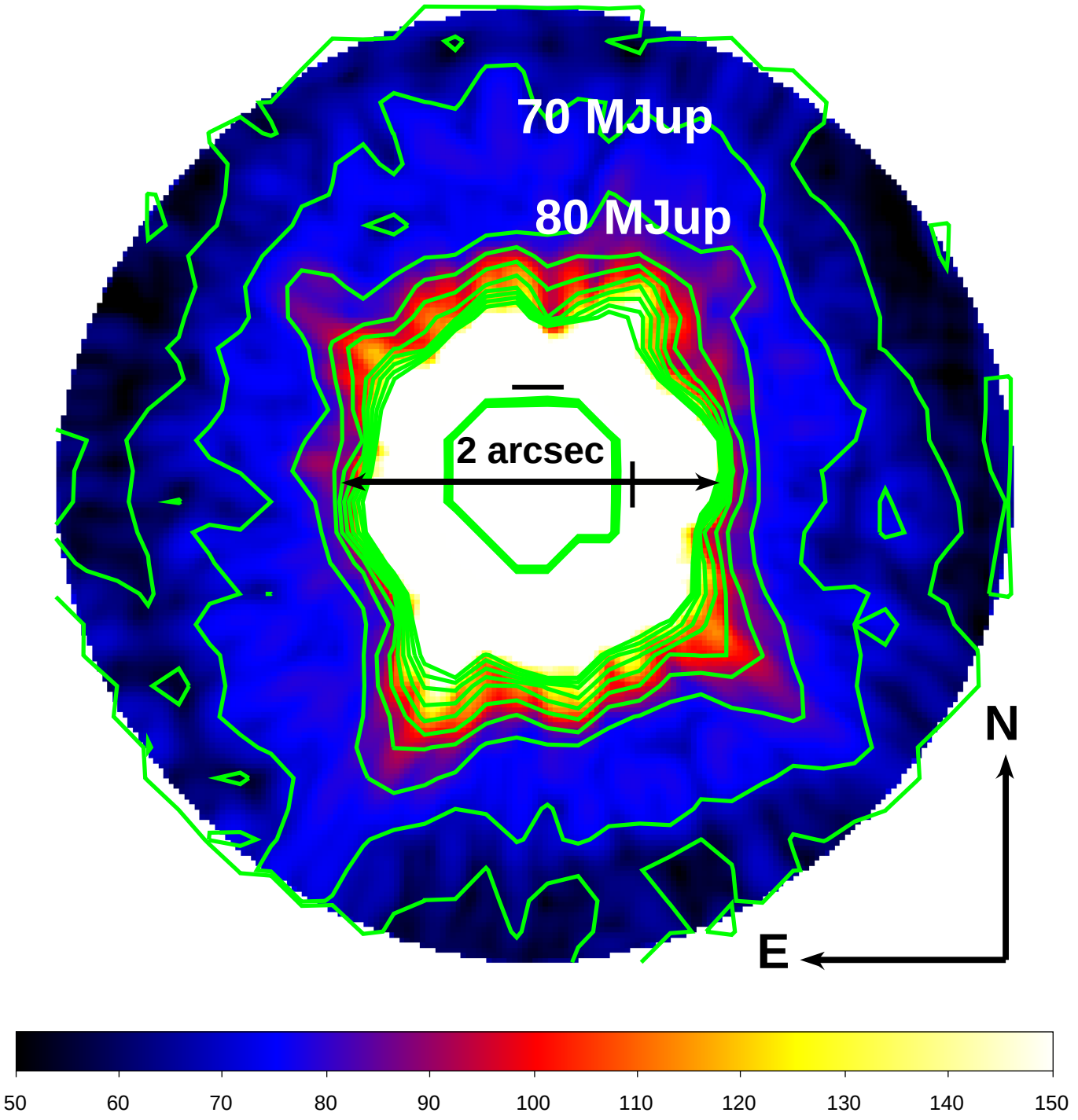

Fig. C.1. Map of the detection limits in Jupiter masses set by the COND evolutionary models. The contours range from 60 to 150 $M_{\rm Jup}$ with a step of 10 $M_{\rm Jup}$.

Chapter 4

On the dynamical history of the Fomalhaut system Faramaz et al., in prep

Contents

4.1 The Fomalhaut system

Fomalhaut (α Psa) is a 440 Myr old (Mamajek 2012) A3V star, located at 7.7 pc (van Leeuwen 2007a; Mamajek 2012). As first revealed by HST, Fomalhaut is surrounded by an eccentric dust ring ($e = 0.11 \pm 0.01$) with a sharp inner edge at 133 AU and extending up to 158 AU (see Figure 4.1 and Kalas et al. 2005).

This eccentric shape hinted at the presence of a massive body orbiting inside the belt on an eccentric orbit, dynamically shaping the belt (Quillen 2006; Deller & Maddison 2005). This hypothesis was furthermore confirmed by the direct detection of a companion near the inner edge of the belt, Fomalhaut b (hereafter Fom b) (Kalas et al. 2008). The nature of Fom b has been intensely discussed since its discovery because it is observed at visible wavelengths, but remain undetected in the infrared (Kalas et al. 2008; Marengo et al. 2009; Janson et al. 2012). The consensus today is that it is a planetary body, surrounded by a population of dust, either in the form of a planetary ring system (Kalas et al. 2008), or a dust cloud resulting from a collision between satellites (Kennedy & Wyatt 2011; Kenyon et al. 2014).

Further observations of this body led to the detection of its orbital motion. Based on the available astrometric points on four epochs over eight years, the first attempts to constrain its orbit showed that it is surprisingly extremely eccentric, nearly coplanar and close to apsidal alignment with the belt, so that the orbit inevitably crosses it ($a_b \sim 110 - 120$ AU and $e_b \sim 0.92 - 0.94$, Graham et al. 2013; Beust et al. 2014).

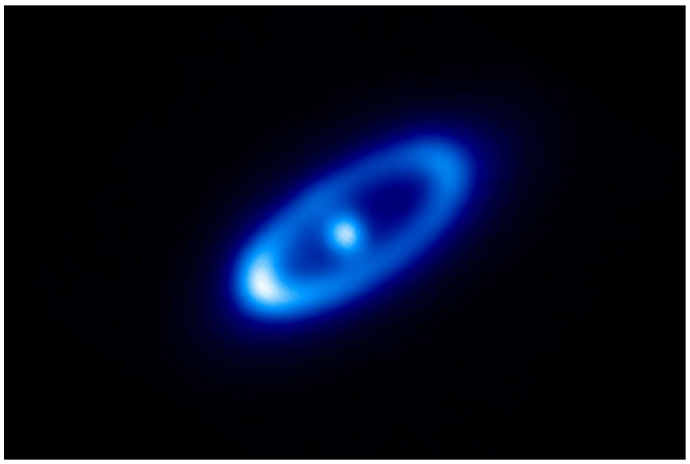

(a) Herschel/PACS image, Acke et al. (2012)

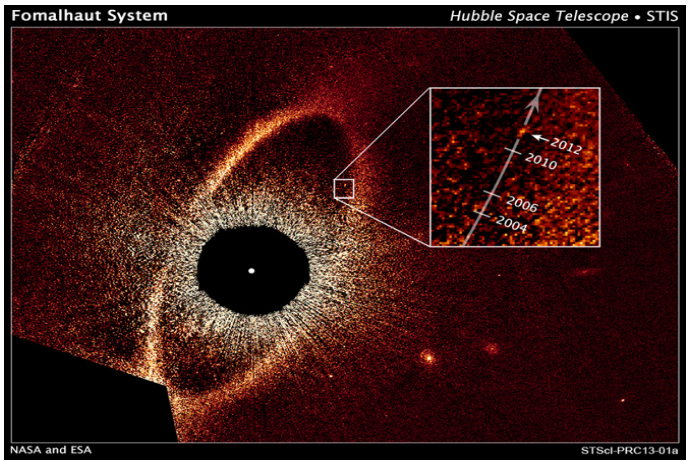

(b) HST image, Kalas et al. (2013)

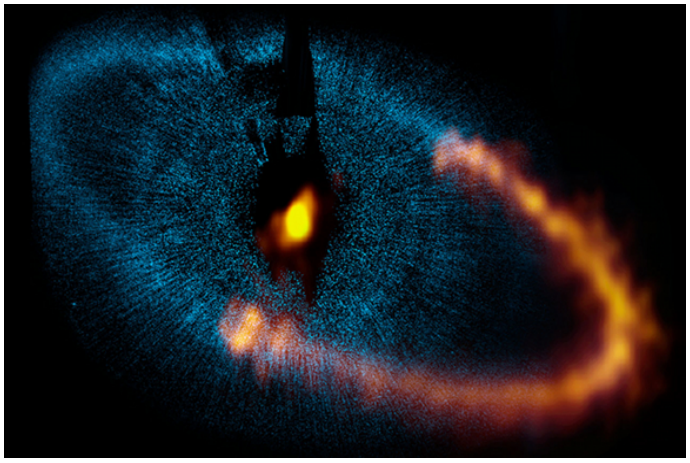

(c) Combined ALMA & HST images

Figure 4.1 – Observations of the debris disk of Fomalhaut with **(a)** Herschel/PACS, **(b)** Hubble Space Telescope (HST), and **(c)** ALMA, with a composite image showing the dust ring surrounding the star Fomalhaut. The optical image from the Hubble Space Telescope is shown in blue, with ALMA observations in orange. The star at the center has been masked. Source: ALMA: ESO/NAOJ/NRAO; visible light image: NASA/ESA Hubble Space Telescope.

Detailed recent dynamical investigations by Beust et al. (2014) revealed that this orbital configuration is not compatible with the shape of the disk and the age of the system (see Appendix B). This study showed that irrespective of its mass, Fom b is very probably not responsible for the sculpting of the observed dust ring. Indeed, if Fom b is sub-Earth or Earth sized, then it is just not massive enough to efficiently influence the ring. If Fom b is more massive, then it has a secular action on the dust ring and inevitably drives particles towards high eccentricity, which occurs in any case before the age of the star. Moreover, Beust et al. (2014) shows that if the perturber is massive enough to efficiently affect the disk, the pericenter-glow dynamics that applies in the low eccentricity regime cannot be transposed to the case where the perturber is very eccentric. Indeed, in this case, the transient elliptic disk is not apsidally aligned with the perturbing planet, and is tilted of $\sim 70°$ instead. This does not match the orbital determination for Fom b, but it must be noted that the determination of the orbital alignment is only accurate within a few tens of degrees.

Typically, with a super-Earth sized Fom b, the present-day disk eccentricity is obtained ∼10-20 Myr after the beginning of the simulation. This would imply Fom b to have been put on its orbit that time ago. But if Fom b was put on its present-day orbit a few 10^7 yrs ago by some scattering event, necessarily this event was caused by another, more massive planet which very probably controls the dynamics of the ring more efficiently than Fom b itself. A dynamical study of Tamayo (2014) also suggests that the best scenario that matches the observational constraints is this of a super-Earth Fom b with an undetected belt-shaping Saturn-mass planet.

Considering that the orbit of Fom b is highly eccentric with an apastron beyond the outer edge of the belt and a periastron that could be as low as a few AU (Beust et al. 2014), and that the putative Fom c would move on a less eccentric orbit located slightly inside the inner edge of the belt, then inevitably both orbits are expected to cross each other. This raises the question of the dynamical stability of Fom b. In this scenario, its present day orbit could just be a transient configuration. It could have been put there by a more or less recent scattering event, potentially with Fom c (Beust et al. 2014), and could be subject to an ejection in a more or less near future. The more massive is Fom c, the shorter the survival timescale of Fom b. In Beust et al. (2014), it is argued that Fom c should probably be ∼Saturn-sized to be able to shape the belt while not ejecting Fom b too quickly from its present-day orbit, just to make it likely for us to witness the transient configuration today.

One of the goals of this thesis is to investigate the issues of the generation of the present-day orbital configuration of Fom b, and to discuss whether models involving Fom c only can explain both the orbit of Fom b and the shape of the outer Kuiper-belt. We wish to examinate how Fom b, starting from a configuration inner to Fom c could have been put on its present-day orbit by a recent scattering event with Fom c.

4.2 Modelling approach

The basic assumption of our study is that Fom c is significantly more massive that Fom b. This is supported by a recent study (Beust et al. 2014) showing that Fom b is probably a low-mass object and that the eccentric disk shape is controlled by another, more massive object, presumably Fom c. We use N-body simulations to investigate the ability of the putative Fom c to put Fom b on its present-day orbit and the typical timescale for this to happen starting from various initial configurations.

Thanks to the mass difference between both objects, Fom b will be treated in this work as a massless test-particle perturbed by Fom c. Our second assumption is that Fom b was originally on an orbit inner to that of Fom c.

The configuration of the system is illustrated in Figure 4.2. In this section, we present our numerical set-up as well as theoretical background on the production of Fom b-like orbits, either by a direct scattering event or via mean-motion resonances.

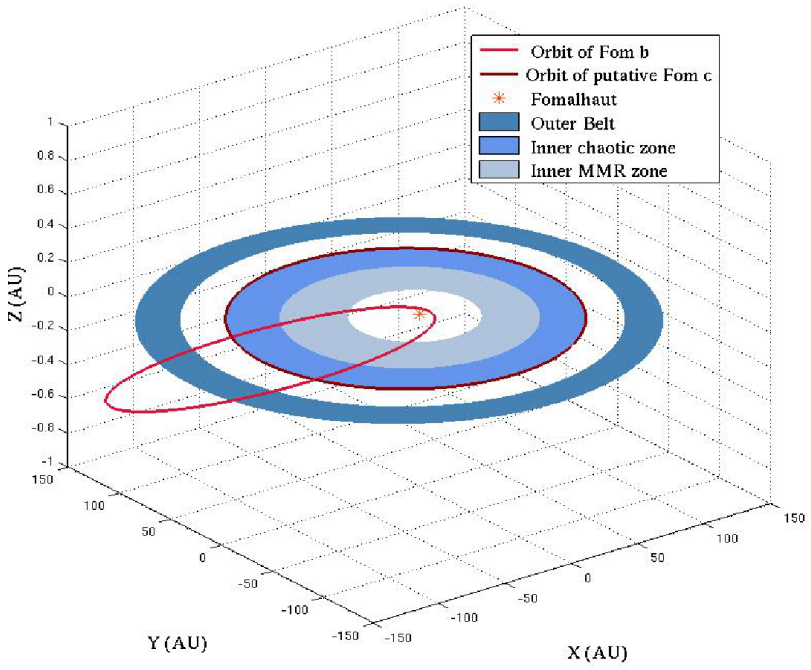

Figure 4.2 – Schematic configuration of the Fomalhaut system. The outer Kuiper belt extends from 133 to 158 AU and has an eccentricity of 0.1. The orbit of Fom b has $a_b = 120\,\mathrm{AU}$ and $e_b = 0.94$, that is, the peak values derived by Beust et al. (2014). Since Fom b has a low inclination relative to the outer belt and is nearly apsidally aligned with it, we represent this orbit as coplanar and apsidally aligned with the belt for sake of simplicity. We represent as well the presumed orbit of the putative Fom c, and the regions of potential origin for Fom b investigated in this paper, that is, the chaotic zone of Fom c and the region where mean-motion resonances which may generate orbits crossing the chaotic zone of Fom c are localised.

4.2.1 Expected routes to form Fom b-like orbits

Driving Fom b from an orbit located inside this of Fom c to its present-day orbit means drastically increasing its semi-major axis and its eccentricity. The most straightforward mechanism to achieve this is a scattering event caused by a close encounter. Such events are expected to occur in the chaotic zone around Fom c outlined above. Only a close encounter event can induce sudden changes of the eccentricity and semi-major axis of a test-particle, potentially in a way that sets it on a Fom b-like orbit.

To undergo a scattering event, a particle must cross the chaotic zone at some point on its orbit. It can have formed there or have formed more deeply inside and then have suffered an orbital evolution that caused its orbit to furthermore cross the chaotic zone.

Particles moving initially in the chaotic zone have very few chances to survive there more than a few 10^7 yrs, i.e., much less than the age of the star. Hence we think that models involving a Fom b that formed deeper inside the orbit of Fom c and was furthermore driven to cross the chaotic zone are more suited to our purpose.

Since the putative belt-shaping Fom c is an eccentric perturber, and since particles trapped in some mean-motion resonances can sometimes see their eccentricity increased to very large values, especially when in MMR with an eccentric perturber (see Section 2.5), MMRs with Fom c therefore constitute valuable routes to cause a low-mass Fom b progenitor to cross the chaotic zone of Fom c, where it may suffer a scattering event setting in on its current orbit. Moreover, material in MMRs need some time to reach the eccentricity required to cross the chaotic zone, which can thus delay a scattering event. If this delay were to be comparable to the age of the system, this would explain why the unstable present-day configuration is witnessed.

4.2.2 N-body simulations

The numerical set-up of the orbital parameters and the mass of the putative Fom c was chosen considering constraints on the belt-shepherding planet retrieved from previous dynamical studies and observational constraints. Based on dynamical investigations, Chiang et al. (2009) found an upper-mass limit of $3\,M_{\rm Jup}$, a lower semi-major axis limit of $\sim 101.5\,$AU, and an orbital eccentricity of $\sim 0.11 - 0.13$, while Quillen (2006) found that the belt-shaping planet should rather be Neptune or Saturn-sized, with a semi-major axis of $\sim 120\,$AU and an orbital eccentricy of ~ 0.1. On the other hand, Rodigas et al. (2013) found a mass of $\sim 7.6 \pm 4.6\,M_{\rm Jup}$, a lower semi-major axis limit of $\sim 85\,$AU, and an orbital eccentricity of ~ 0.11. Observational constraints from Janson et al. (2012); Galicher et al. (2013) and Currie et al. (2013) gave a detection limit of $\sim 1 - 3\,M_{\rm Jup}$ at these distances.

Therefore, we arbitrarily chose a mass of $m_c = 3\,M_{\rm Jup}$ for Fom c and will discuss the impact of this mass on our results later. We considered that the belt inner edge, located at 133 AU, was created by the chaotic zone around Fom c. The mass of Fomalhaut was set to $M_\star = 1.92\,{\rm M}_\odot$ (Mamajek 2012). Using Eq. (2.43), we derived a semi-major axis of $a_c = 107.8\,$AU. We set the orbital eccentricity of Fom c to be $e_c = 0.1$ as to match the observed ellipticity of the belt.

In order to investigate the scenarios outlined above, we ran several simulations with different initial sets of particles, that is, potential Fom b planets, each of them corresponding to either a specific MMR or a wide range of semi-major axes including both MMRs and the chaotic zone relative to Fom c. The initial conditions of our simulations are all summarised in Table 4.1.

Each of these test-particles populations are assumed to be coplanar with the orbit of Fom c. Orbital inclinations with respect to the orbit of Fom c orbit were randomly distributed between 0 and 3°, while the eccentricities were distributed between 0 and 0.05. All remaining initial angles, that is, the longitude of periastron, the longitude of ascending node, and initial mean anomaly, were randomly drawn between 0 and 2π in a uniform way. For each simulation, the initial semi-major axes of the test-particles were also uniformly and randomly distributed between boundaries that were specific to each of them.

Run A is dedicated to study the dynamics of 250,000 particles widely distributed radially, which covers both the chaotic zone and the locations of the MMRs, for comparison. The initial semi-major axes of the test-particles were distributed randomly between $[40\,{\rm AU}; 110\,{\rm AU}]$. Here the upper limit corresponds to the apastron of Fom c minus one Hill radii, to take into account the eccentricity of Fom c, and the lower limit extends the distribution of the test-particles slightly further in than the 4:1 MMR.

Table 4.1 – Characteristics of all initial sets of particles used in our numerical study. In all runs, Fom c itself is assumed to be a $3\,M_{\rm Jup}$ planet orbiting Fomalhaut with semi-major axis $a_c = 107.8\,$AU and eccentricity $e_c = 0.1$. All sets of particles are ring-like belts particles extending radially between boundaries given below, eccentricities randomly chosen between 0 and 0.05, and inclinations between 0 and 3° relative to Fom c's orbital plane. Run A contains 250,000 particles and runs B–H contain 100,000 particles.

Run #	Dynamical status relative to Fom c	Semi-major axis extent a (AU)	Theoretical resonance location $a_{\rm MMR}$ (AU)
A	Overall inner disk	40-110	-
B	4:1 MMR	40.3–45.3	42.8
C	7:2 MMR	44.3–49.3	46.8
D	3:1 MMR	49.3–54.3	51.8
E	8:3 MMR	53.6–58.6	56.1
F	5:2 MMR	56.0–61.0	58.5
G	7:3 MMR	58.8–63.8	61.3
H	2:1 MMR	65.4–70.4	67.9

Runs B–H from Table 4.1 focus on rings of 100,000 test-particles centered on specific MMRs with Fom c. Not all MMRs needed actually to be tested. As long a they keep trapped in a MMR, the semi-major axes of test-particles do not vary significantly, as they only undergo small amplitude secular variations around the theoretical MMR value (see Table 4.1).

This remains true even as their eccentricity approaches 1. Therefore, their apastron cannot grow higher than twice the theoretical $a_{\rm MMR}$ value, and we limited ourselves to MMRs achieving this condition. Note that the further in the MMR is located, the higher the eccentricity of a test-particles should increase in order for its orbit to cross the chaotic zone. Therefore, it is expected in a general manner that the most inner MMRs such as the 3:1 and 4:1 should be less efficient routes to generate orbits comparable to that of Fom b in our scenario.

The ability of a MMR to set a test-particle on a orbit sufficiently eccentric to cross the chaotic zone, or even the orbit of Fom c, can be evaluated thanks to phase-space diagrams, as shown in Section 2.5. For each of the MMRs that we investigated, we present phase diagrams which allowed us to evaluate the co-evolution of e, the eccentricity of test-particles, and ν, the orientation of their periastron compared to that of Fom c, for test-particles initially on low eccentricity orbits ($e < 0.05$) and with ν between 0 and 2π.

These diagrams show the trajectory followed by a test-particle along time in the (e, ν) space when in a given MMR in Figure 4.3. We put this in perspective with the crossing of the chaotic zone of Fom c, which allows us to evaluate the behaviour expected from the MMRs investigated in this paper.

It is expected that the 2:1, 7:3, 5:2, 3:1, and 4:1 MMRs allow test-particles to cross the chaotic zone of Fom c, where they will be allowed to be scattered and possibly be set on a Fom b-like orbit. This is not the case for the 8:3 and 7:2 MMRs, although in the Solar System Main Asteroid belt, they generate high eccentricity particles thanks to an overlap with a secular resonance with Saturn (Yoshikawa 1989). Such a fortuitous configuration has only few chances to apply here. Moreover, as our simulations only consider Fom c as massiver perturber, no secular resonance is to be expected here. We nevertheless decided to keep these MMRs in our set of simulations in order to quantify this effect.

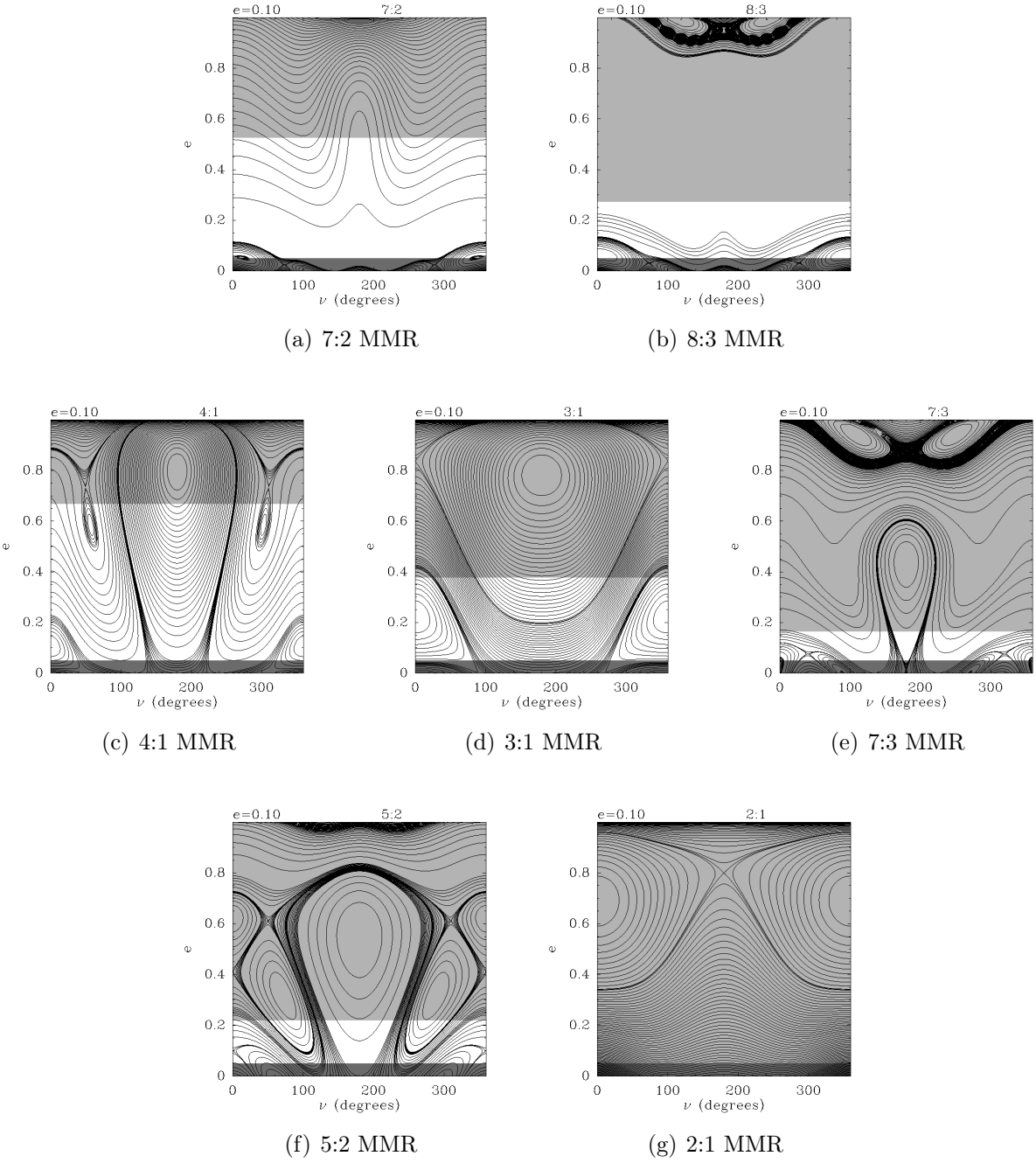

(a) 7:2 MMR (b) 8:3 MMR

(c) 4:1 MMR (d) 3:1 MMR (e) 7:3 MMR

(f) 5:2 MMR (g) 2:1 MMR

Figure 4.3 – Phase diagrams of the MMRs that we investigated. Our initial conditions are figured in dark grey and the chaotic zone of Fom c in light grey. The chaotic zone of Fom c is considered to extend from $3.5\,R_H$ inner to the periastron of Fom c, to $3.5\,R_H$ outer to the apastron of Fom c. Particles which start on a trajectory allowing it to cross the chaotic zone may then be scattered and set on a Fom b-like orbit.

In low eccentricity regime, the radial extent of a MMR is typically $\sim 0.1\%$ of the semi-major axis of the perturber, that is, ~ 0.1 AU here (Beust & Morbidelli 1996). At high eccentricity, it is typically ~ 20 times wider, that is, ~ 2 AU. We considered therefore that a radial extent of several AU is largely sufficient to investigate a particular resonance. Resonances were thus examined closely by distributing the semi-major axes of the test particles over 5 AU wide ranges centered on the theoretical location of the resonance (Table 4.1).

In all cases, the system was evolved over 100 Myr, that is $\sim 1/4$ of the age of Fomalhaut, using the symplectic N-body code SWIFT-RMVS (Levison & Duncan 1994). We used a typical timestep of $\sim 1/20$ of the smallest orbital period. This ensures a conservation of energy with a typical error of $\sim 10^{-6}$ on relative energy. We took snapshots of the particles orbits every 10^5 yrs.

4.3 A resonant origin for Fom b

In our simulations, we identified test-particles which were set on a Fom b-like orbit, which we defined as an orbit with eccentricity and semi-major axis in the 95% level of confidence intervals found by Beust et al. (2014), that is, with $e \in [0.69; 0.98]$ and $a \in [81; 415]$ AU. Other constraints have been derived by Beust et al. (2014) regarding the orientation of the orbit of Fom b : it is almost coplanar with the outer Kuiper-belt, and more or less apsidally aligned with it. However, these constraints are weaker than those on the semi-major axis and eccentricity. Therefore, we will examinate the orientation of the Fom b-like orbits that we identified in a second time. All these constraints are summarised in Table 4.2.

Table 4.2 – Summary of the constraints on the orbit of Fom b as found by Beust et al. (2014).

Parameter	Value	Remark
a (AU)	81–415	95% level of confidence
e	0.69–0.98	95% level of confidence
i (°)	0–29	67% level of confidence
ν (°)	± 30–40	$\sim$ 70% level of confidence

4.3.1 A first two-step scenario

Broad distribution, inner to the putative Fom c

We first investigated the dynamical status exhibited by the test-particles, integrated over the 100 Myr of the Run A, as a function of their initial semi-major axes in Figure 4.4. In Figure 4.4(a), the chaotic zone of Fom c shows through a large proportion of unbound orbits above ~ 70 AU, while low eccentricity orbits – $e < 0.2$ – were preferentially adopted below this limit. This is in accordance with the theoretical inner boudary of the chaotic zone, that is $\sim 3\,R_H$ inner to the periastron of Fom c. The total proportion of snapshots in a Fom b-like orbit dynamical status is less than 1%, and thus they are not visible here. In Figure 4.4(b), we present a zoom-in of the top-panel to show them.

As expected, MMRs increased the eccentricity of test-particles, and possibly led them to leave the system. Although it was able to increase the eccentricity of test-particles, the 4:1 MMR did not generate any Fom b-like orbit.

The density of snapshots in a Fom b-like status in the cases of the 3:1 and 7:3 MMRs was low compared to that of the chaotic zone, while interestingly, this density was greater in the cases of the 5:2 and 2:1 MMRs. This does not mean that the probability for being set on a Fom b-like orbit is greater for these MMRs, but rather that Fom b-like orbits generated from these MMRs are more stable, as one can see in Table 4.3, where we summarise the average time spent by a test-particles on a Fom b-like orbit as a function of their origin, and show for comparison the distribution of the origin of these test-particles.

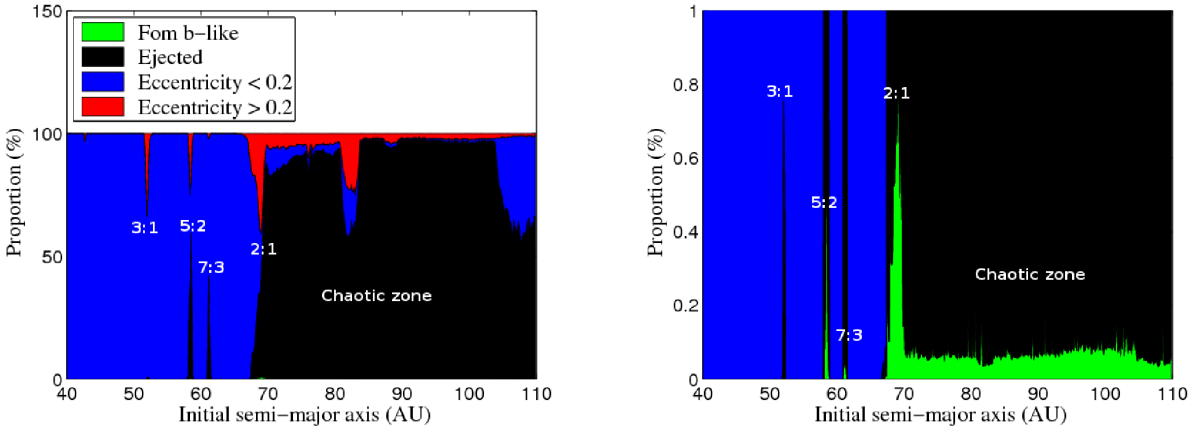

(a) Whole distribution

(b) Zoom-in on the Fom b-like orbits

Figure 4.4 – Proportion of the time spent on orbits of different dynamical status as a function of the initial semi-major axes of the test-particles.

The total proportion of particles which were set at a moment or another on a Fom b-like orbit in our run is $\sim 20\%$, where indeed $\sim 90\%$ of these test-particles originated from the chaotic zone, and the 5:2 and 2:1 MMRs produced the Fom b-like orbits with the largest mean lifetimes ($\sim 1\,\mathrm{Myr}$), although these remain largely inferior to the age of the system.

Table 4.3 – Summary of the results of Run A : distribution of the test-particles being set on a Fom b-like orbit and average time spent by a particle on a Fom b-like orbit, $\bar{t}_{\mathrm{Fom\,b}}$.

Dynamical status relative to Fom c	Distribution of Fom b-like particles (%)	$\bar{t}_{\mathrm{Fom\,b}}$ (Myr)
3:1 MMR	2.0×10^{-2}	0.13
5:2 MMR	1.15	1.0
7:3 MMR	0.45	0.2
2:1 MMR	5.35	1.4
Chaotic zone	93.0	0.21

The sample of Fom b-like orbits from Run A may be sufficient to retrieve first clues on the formation of these orbits, in particular, to show that MMRs may play a crucial part here, but it is probably not sufficient to fully compare the efficiency and specificities of each MMR. Therefore we present in the following subsection the results of Runs B–H for individual MMRs. Since these runs achieved a better sampling of MMRs, it allowed us to examine more in depth the results of Run A.

The 7:2 and 8:3 MMRs

No Fom b-like orbit was produced in the Runs C and E, that is, for the 7:2 and 8:3 MMRs respectively, which is in accordance with the results of the Run A. As we have seen in the previous section from the diagrams of the 7:2 and 8:3 resonances shown in Figure 4.3, it was obvious that test-particles initially on low-eccentricity orbits would not be able to cross the chaotic zone of Fom c, and therefore, not be able to be scattered on a Fom b-like orbit. Indeed, in both cases, none of the test-particles of the run were ever set on an eccentricity greater than 0.2.

As was mentionned previously, these two MMRs need to overlap with secular resonances to trigger an increase of the eccentricity of the test-particles. They were thus expected not to be an efficient mechanism to generate Fom b-like orbits, if not unefficient at all.

The 4:1, 3:1 and 7:3 MMRs

No Fom b-like orbit was produced in the Run B for the 4:1 MMR, in accordance with the results of the Run A. The diagram for this MMR shows that some of our test-particles would be expected to cross the chaotic zone of Fom c, and that the production of Fom b-like orbits would be expected. So does for the 3:1 MMR, which produced very rare Fom b-like orbits in the Run A, which is confirmed by results of Run D. As mentioned in the previous section, it was expected that the most inner MMRs would be less efficient at producing Fom b-like orbits, since their location require a more signifant increase for test-particles to cross the chaotic zone of Fom c than MMRs located closer to Fom c.

Very interestingly, the 3:1 MMR delayed the production of Fom b-like orbits by $\sim 30 - 40\,\mathrm{Myr}$ compared to other MMRs, which strongly reflects the delay potentially induced by the gradual increase of the eccentricity of a resonant test-particle before it is able to be scattered.

The results of the Run G, that is, for the 7:3 MMR, are in accordance with the results of the Run A : the Fom b-like orbits produced were rare ($\sim 1\%$). Moreover, they were theoretically expected as shown in the phase-diagram for this MMR. The average time spent by test-particles on a Fom b-like orbit is $\sim 0.3\,\mathrm{Myr}$, and the maximum time spent on a Fom b-like orbit for an individual particle does not exceed 40 Myr. The delay induced in the generation of Fom b-like orbits by this MMR is much smaller than the age of the system ($\sim 3\,\mathrm{Myr}$).

The 5:2 and 2:1 MMRs

The MMRs for which test-particles have greater probabilities to be set on a Fom b-like orbit are the 5:2 and 2:1 MMRs. Their phase diagrams revealed that a great number of particles will cross the chaotic zone of Fom c (see Figure 4.3). In particular, the 2:1 MMR is not expected itself to sustain large increases in eccentricity, but it appears to be fortuitously located at the boundary of the chaotic zone of Fom c with our parameters, and more particularly, with the mass chosen for Fom c. The impact of the mass of Fom c will be discussed later. In the present case, the increase in eccentricity needed is very small and test-particles have easily crossed the chaotic zone of Fom c. These two MMRs seem to be valid routes to form Fom b-like orbits. However, in both cases, although rare test-particles adopted a Fom b-like orbit over more than 40 Myr, the average time spent on a Fom b-like orbit is $\lesssim 2\,\mathrm{Myr}$, and the delay induced in the generation of Fom b-like orbits by these MMRs is much smaller than the age of the system ($\sim 1 - 2\,\mathrm{Myr}$).

Summary

Combining the results for individual MMRs and for the chaotic zone, we summarise in Table 4.4 different probabilities which characterise the production of Fom b-like orbits : $P_{\mathrm{Fom\,b}}$ is the probability to be set on a Fom b-like orbit, P_{orient} is the probability for a Fom b-like orbit to have an orientation compatible with that observed for Fom b, that is, $i \in [0°, 30°]$ and $\nu \in [-40°, 40°]$, $P_{>10\,\mathrm{Myr}}$ is the probability for a Fom b-like orbit to have a lifetime greater than 10 Myr. We summarise as well the average time $\bar{t}_{\mathrm{Fom\,b}}$ spent by test-particles which were set on a Fom b-like orbit, and the delay in the generation of Fom b-like orbits induced by MMRs.

Table 4.4 – For each individual run that produced Fom b-like orbits, probability $P_{\text{Fom b}}$ for being set on a Fom b-like orbit, that is, the proportion of the 100,000 test-particles of our initial sample set at least once on a Fom b-like orbit, average time $\bar{t}_{\text{Fom b}}$ spent by these test-particles in this configuration, probability $P_{>10\,\text{Myr}}$ for a Fom b-like orbit to have a lifetime greater than 10 Myr and probability P_{orient} for a Fom b-like orbit to have an orientation comparable to that of Fom b. We indicate as well any delay in the generation of Fom b-like orbits.

Dynamical status relative to Fom c	$P_{\text{Fom b}}$ (%)	$\bar{t}_{\text{Fom b}}$ (Myr)	$P_{>10\,\text{Myr}}$ (%)	P_{orient} (%)	Delay (Myr)
3:1 MMR	9.7×10^{-2}	3.8	11.3	4.4	~ 30
5:2 MMR	3.8	1.2	2.4	17.6	~ 2
7:3 MMR	1.3	0.24	2.2×10^{-1}	39.6	~ 3
2:1 MMR	20.1	1.6	3.5	15.2	~ 1
Chaotic zone	35.5	0.21	8.5×10^{-2}	48.5	0

Moreover, for each region of interest, one can retrieve the probability to be set on a Fom b-like orbit as a function of time, which, ponderated by the corresponding probabilities $P_{\text{Fom b}}$, $P_{>10\,\text{Myr}}$ and P_{orient} allowed us to fully compare the efficiency of each region of interest to produce orbits fully comparable to the orbit of Fom b and which have lifetimes greater than 10 Myr, as shown in Figure 4.5.

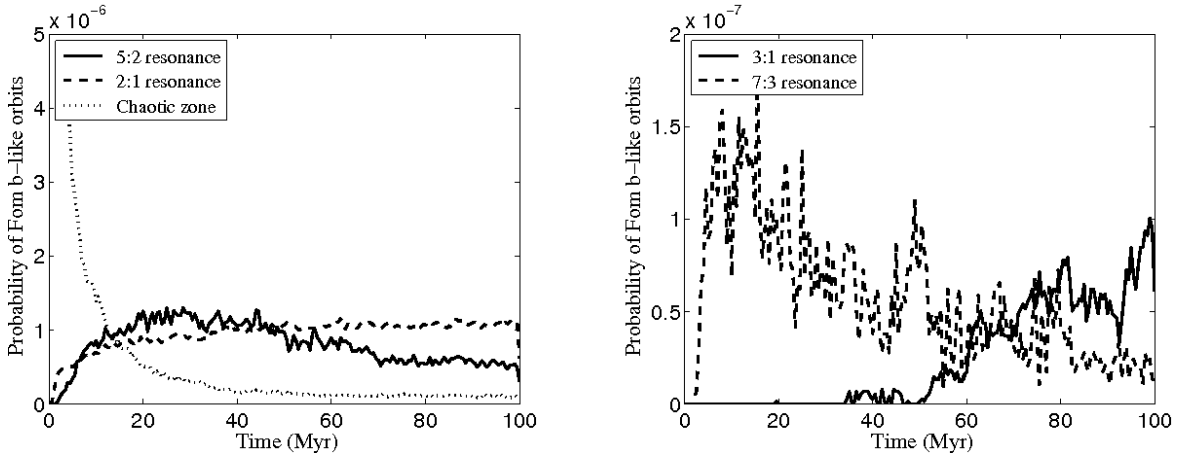

(a) For the 2:1 and 5:2 MMRs, and the chaotic zone

(b) For the 3:1 and 7:3 MMRs

Figure 4.5 – Probability to be set on a Fom b-like orbit with a lifetime greater than 10 Myr and with an orientation comparable to that of Fom b as a function of the time and the origin of the test-particles.

All these results give first insights on the most probable origin and dynamical history of Fom b in our scenario. The probability to be set on a Fom b-like orbit fully comparable to that of Fom b and which survives longer than 10 Myr is smaller by an order of magnitude for the 3:1 and 7:3 MMRs compared to the chaotic zone and the 5:2 and 2:1 MMRs. The chaotic zone of Fom c is very efficient at producing Fom b-like orbits, but these are highly unstable and the probability to be set on a Fom b-like orbit decreases very quickly during the first $\sim 10\,\text{Myr}$, where its efficiency to produce Fom b-like orbits becomes smaller than these of the 2:1 and 5:2 MMRs. Therefore, the chaotic zone, the 3:1, and the 7:3 MMRs may not be the best ways to explain the orbit and dynamical history of Fom b.

On the other hand, the 2:1 and 5:2 MMRs are very efficient at producing Fom b-like orbits, and which have a longer lifetime, and appear to be the most probable origins for Fom b in our scenario.

4.3.2 On the mass and eccentricity of Fom c

The mass of Fom c is a crucial parameter, which controls the ability of a given MMR to produce Fom b-like orbits by varying the size of the chaotic zone, but also very importantly, controls dynamical timescales, that is, the delay induced by a given MMR in the production of Fom b-like orbits and the survival timescale of Fom b-like orbits. Indeed, one can notice that with a $3\,M_{\rm Jup}$ Fom c such as in our simulations, the delay imparted on the production of Fom b-like orbits is of several Myr at most. However, given the age of the Fomalhaut system ($\sim 440\,$Myr) and the fact that an unstable two-planets system such as that hypothetised could not survive more than several 10 Myr, this delay should be of the order of 100 Myr for the mechanism to be valid.

Increasing dynamical timescales means reducing the mass of Fom c, and thus, reducing the size of its chaotic zone. This implies that particles must aquire higher eccentricities to cross the chaotic zone, and thus, have the opportunity to be scattered on a Fom b-like orbit. MMRs are therefore expected to become less efficient at producing Fom b-like orbits with decreasing mass of Fom c. We illustrate this aspect on Figure 4.6, where we show phase diagrams of the 5:2 and 2:1 MMRs for different masses of Fom c. One can see that as soon as the mass of Fom c decreases to $1\,M_{\rm Jup}$, the 2:1 MMR is not expected to be efficient any longer to produce Fom b-like orbits, which was confirmed by additional simulations. In the case of the 5:2 MMR, the mass of Fom c can decrease as low as $0.1\,M_{\rm Jup}$ (Saturn-sized) and Fom b-like orbits are still expected to be produced, although at a lower rate.

Additional simulations for this case revealed that Fom b-like orbits can be produced via the 5:2 MMR when $m_c = 0.25$–$0.5\,M_{\rm Jup}$, and their production is very interestingly delayed by timescales comparable to the age of the system (see Table 4.5). Moreover, for $m_c = 0.5 - 1\,M_{\rm Jup}$, the time spent in average by a test-particle in a Fom b-like orbit configuration has increased up to $\sim 6\,$Myr. This time is smaller for $m_c = 0.25\,M_{\rm Jup}$, however, Fom b-like orbits started to be produced very late.

Table 4.5 – Case of the 5:2 MMR with 0.1–0.5–1 $M_{\rm Jup}$. For each individual run that produced Fom b-like orbits, probability $P_{\rm Fom\,b}$ for being set on a Fom b-like orbit, that is, the proportion of the 100,000 test-particles of our initial sample set at least once on a Fom b-like orbit, average time $\bar{t}_{\rm Fom\,b}$ spent by these test-particles in this configuration, probability $P_{>10\,\rm Myr}$ for a Fom b-like orbit to have a lifetime greater than 10 Myr and probability $P_{\rm orient}$ for a Fom b-like orbit to have an orientation comparable to that of Fom b. We indicate as well any delay in the generation of Fom b-like orbits.

m_c ($M_{\rm Jup}$)	$P_{\rm Fom\,b}$ (%)	$\bar{t}_{\rm Fom\,b}$ (Myr)	$P_{>10\,\rm Myr}$ (%)	$P_{\rm orient}$ (%)	Delay (Myr)
1	1.2	5.7	10.1	14.2	$\sim$ 30–40
0.5	0.16	6.4	7.5	20.2	$\sim$ 100–150
0.25	1.6×10^{-2}	3.5	12.5	49.2	$\sim$ 350
0.1	-	-	-	-	-

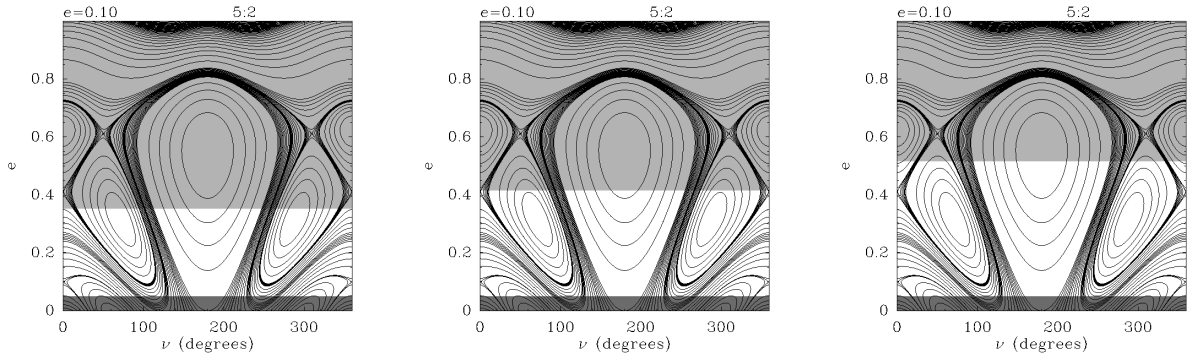

(a) 5:2 MMR with $m_c = 1\,M_{\rm Jup}$ (b) 5:2 MMR with $m_c = 0.5\,M_{\rm Jup}$ (c) 5:2 MMR with $m_c = 0.1\,M_{\rm Jup}$

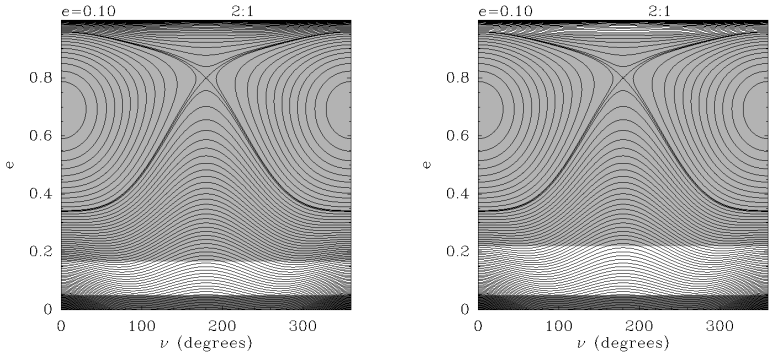

(d) 2:1 MMR with $m_c = 1\,M_{\rm Jup}$ (e) 2:1 MMR with $m_c = 0.5\,M_{\rm Jup}$

Figure 4.6 – Phase diagrams for the 5:2 MMR, with Fom c of mass **(a)** 1, **(b)** 0.5, and **(c)** 0.1 $M_{\rm Jup}$, and for the 2:1 MMR, with Fom c of mass **(d)** 1, and **(e)** 0.5 $M_{\rm Jup}$. Our initial conditions are figured in dark grey and the chaotic zone of Fom c in light grey. The chaotic zone of Fom c is considered to extend from $3.5\,R_H$ inner to the periastron of Fom c, to $3.5\,R_H$ outer to the apastron of Fom c. Particles which start on a trajectory allowing it to cross the chaotic zone may then be scattered and set on a Fom b-like orbit.

The production of Fom b-like orbits via the 2:1 MMR is extremely sensitive to the mass of Fom c and it appears not to be the most probable origin of Fom b in our scenario. The best candidate is therefore the 5:2 MMR, which is much less sensitive to the mass of Fom c in its production of Fom b-like orbits, and therefore a more robust route for Fom b to have been set on its current orbit. Moreover, this mechanism as produced by a 0.25–0.5 M_{Jup} Fom c can delay the apparition of Fom b-like orbits by timescales comparable to the age of the system, while increasing their lifetime. A lower mass limit of 0.1 M_{Jup} on the belt-shaping Fom c can be set. These timescales are more in accordance with our witnessing of the orbit of Fom b.

Moreover, a 0.25–0.5 M_{Jup} Fom c would allow Fom b not to be ejected too quickly from its present-day orbit, as underlined by Beust et al. (2014). Finally, a 0.25–0.5 M_{Jup} Fom c is completely in accordance with the shaping the outer belt into the observed eccentric ring, as shown by Quillen (2006).

Finally, the initial eccentricity of Fom c is a also crucial paramater. Indeed, the trajectories offered in the phase-space to test-particles in resonance are very sensitive to the eccentricity of the perturber that creates these resonances. An orbital eccentricity as small as 0.1 for Fom c is actually necessary to produce Fom b-like orbits because particles are allowed in this case to reach the eccentricities necessary for them to cross the close encounter zone of Fom c. This can be seen on Figure 4.7. Again, this eccentricity is fully compatible with the eccentricity of the belt-shaping planet.

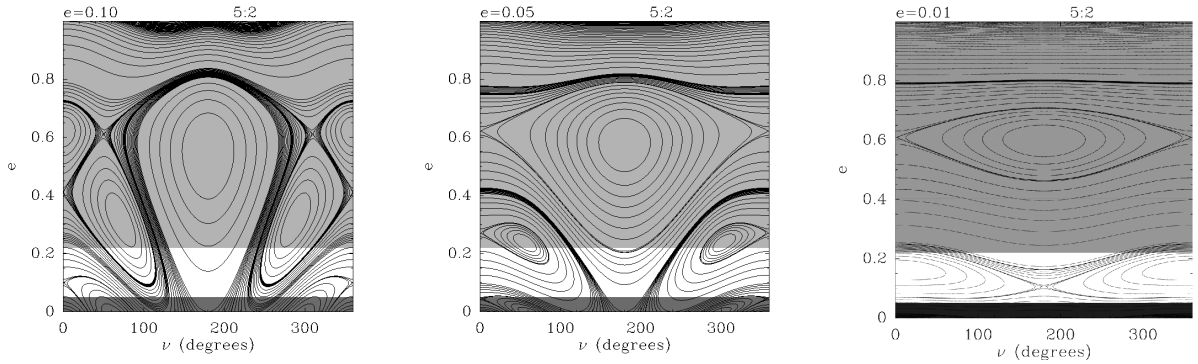

(a) With $e_c = 0.1$ (b) With $e_c = 0.05$ (c) With $e_c = 0.01$

Figure 4.7 – Phase diagrams for the 5:2 MMR, with Fom c of eccentricity **(a)** 0.1, **(b)** 0.05, and **(c)** 0.01. Our initial conditions are figured in dark grey and the chaotic zone of Fom c in light grey. The chaotic zone of Fom c is considered to extend from 3.5 R_H inner to the periastron of Fom c, to 3.5 R_H outer to the apastron of Fom c. Particles which start on a trajectory allowing it to cross the chaotic zone may then be scattered and set on a Fom b-like orbit.

A plausible dynamical scenario for the Fomalhaut system would then be a two-steps dynamical process in which Fom b originates from the 5:2 MMR with the belt-shaping, 0.1 eccentric, and Neptune-Saturn mass Fom c, and was set recently on its current orbit after a scattering event with Fom c. However, a noticable feature of the Fom b-like orbits witnessed in our simulations is that a significant proportion of them corresponded to orbits fully compatible with that of Fom b : indeed, $\sim 40\%$ of the Fom b-like orbits formed had $i \in [0°, 30°]$ and $\nu \in [-40°, 40°]$, that is, in the $\sim 70\%$ level of confidence, as shown in in Figure 4.8. This demanded an explanation, which allowed to refine the dynamical scenario proposed in this section.

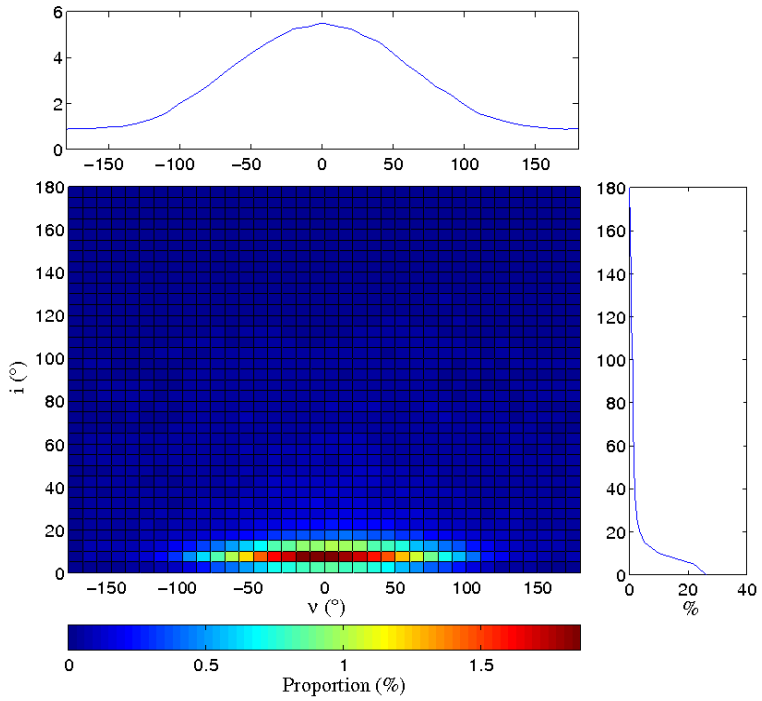

Figure 4.8 – Distribution in inclination and longitude of periastron with respect to this of Fom c of Fom b-like orbits.

4.4 Apsidal alignement and refinement of the scenario

4.4.1 An unexpected feature : apsidal alignment

A notable feature of our results is that the Fom b-like orbits formed tend to be apsidally aligned with the orbit of Fom c in a very general manner, even when these originated directly from the chaotic zone of Fom c, where they were expected to suffer random encounters and thus be put on randomly apsidally aligned Fom b-like orbits (see Figure 4.9). This hints at the fact that the whole dynamical process of production of Fom b-like orbits is more complex than previously thought. We have so far proposed a two-steps scenario, where a test particle firstly reaches the chaotic zone of Fom c on timescales comparable to the age of the system via a MMR mechanism with Fom c, and where this test-particle secondly suffers a close-encounter with Fom c.

However, a closer study of the whole dynamical behaviour of a test-particle along the two-steps process that we have proposed, and in particular an exam of the orbits resulting from close-encounters with Fom c, shows that an additional third step involving secular interactions with Fom c is not only required, but also explains the tendency for apsidal alignment.

4.4.2 Close-encounters with Fom c

Close-encounters can be investigated analytically in a very simple manner considering the Tisserand parameter C_T of a test particle, as defined by Eq. (2.44). We assume coplanarity between Fom c and the test-particle, and considered a particle initially locked in a MMR with Fom c, having a nearly constant semi-major axis a_{MMR} and a growing eccentricity. We will call here e the eccentricity it has reached when crossing the chaotic zone, where it suffers one or many close encounter episodes with Fom c.

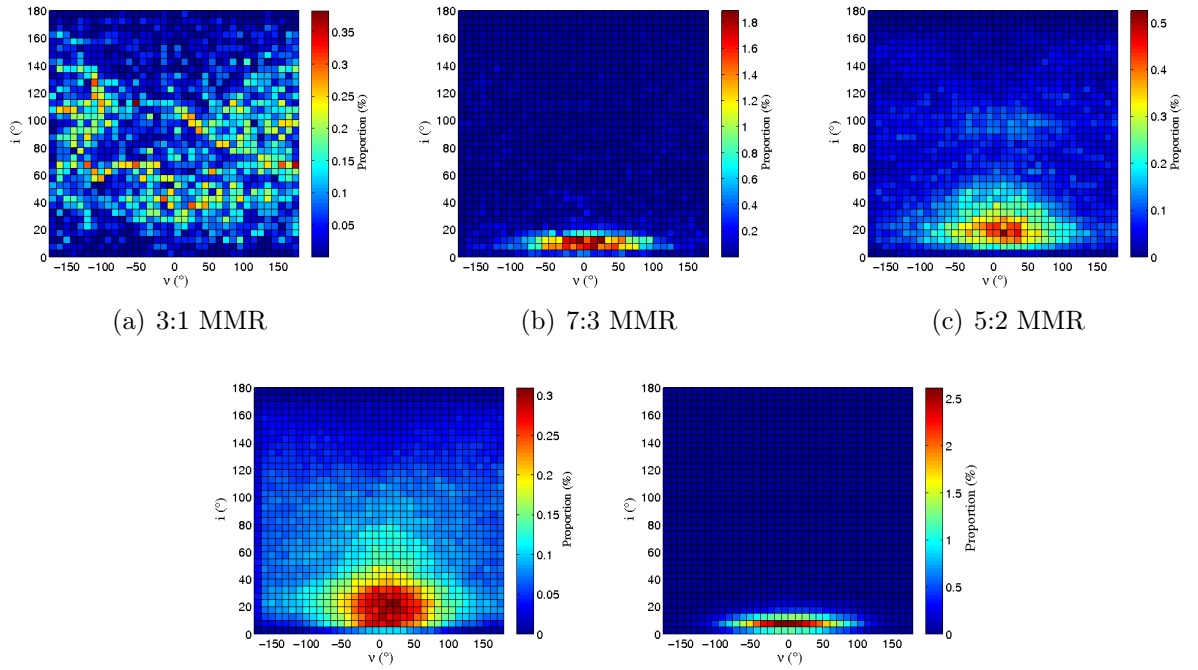

(a) 3:1 MMR (b) 7:3 MMR (c) 5:2 MMR

(d) 2:1 MMR (e) Chaotic zone

Figure 4.9 – Distribution in inclination i and longitude of periastron ν with respect to this of Fom c of Fom b-like orbits produced in the case of the **(a)** 3:1, **(b)** 7:3, **(c)** 5:2, and **(d)** 2:1 MMRs, and **(e)** the chaotic zone.

Afterwards, its semi-major axis a and eccentricity e' are related to a_{MMR} and e by the conservation of the Tisserand parameter:

$$\frac{a_c}{a_{\mathrm{MMR}}} + 2\sqrt{\frac{a_{\mathrm{MMR}}}{a_c}}\sqrt{1-e^2} = \frac{a_c}{a'} + 2\sqrt{\frac{a'}{a_c}}\sqrt{1-e'^2} \quad . \tag{4.1}$$

Depending on the resonance considered, there are constraints on a_{MMR} and e for the orbit to be able to cross the chaotic zone. For instance, in the case of the 5:2 MMR with a $3\,M_{\mathrm{Jup}}$ Fom c, we must have $0.2 \lesssim e \lesssim 0.8$. This naturally translates to constraints on a' and e' via Eq. (4.1). Note that these constraints depend on the mass of Fom c, since this parameter controls the width of the chaotic zone and thus the values of eccentricities allowed to the test-particles.

Constraints on a' can also be derived via our definition of a Fom b-like orbit, namely $81\,\mathrm{AU} \leq a' \leq 415\,\mathrm{AU}$. Once this constraints are incorporated into Eq. (4.1), this leads to constraints on the eccentricity e' that the test-particle can have after the close-encounter and when having a semi-major axis compatible with the definition of a Fom b-like orbit:

$$e' = \left[1 - \frac{1}{4}\left(C_T - \frac{a_c}{a'}\right)^2 \frac{a_c}{a'}\right]^{1/2} \quad . \tag{4.2}$$

The resulting possible eccentricities after a close-encounter are displayed in Figure 4.10 for the 5:2 MMR and for the chaotic zone. In the chaotic zone case, the limits on e are simply the limits set by our initial conditions on the eccentricity of the test-particles, that is, $e \leq 0.05$.

Figure 4.10 reveals that the eccentricity after the scattering event(s) rarely exceeds ~ 0.6–0.7, whereas the minimum eccentricity required for the orbit to be fully qualified of Fom b-like is 0.69. It thus seems that directly generating Fom b-like orbits from (even multiple) close encounters is difficult.

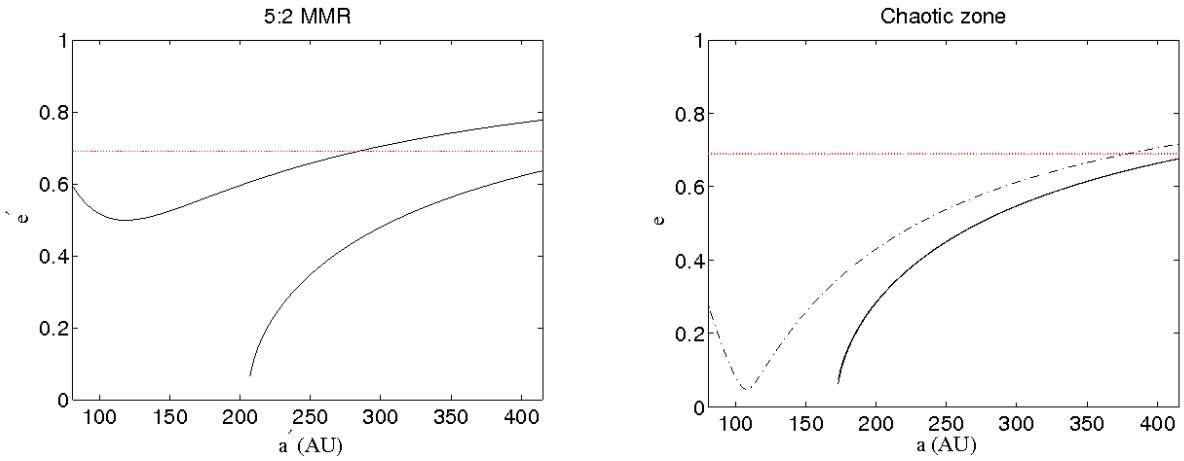

(a) 5:2 MMR

(b) Chaotic zone

Figure 4.10 – Theoretical eccentricities e' adopted by test-particles after a close-encounter with Fom c which has set them on an orbit with semi-major axis compatible with the orbit of Fom b. **(a)** The 5:2 MMR will constrain the semi-major axis to a_{MMR} and will allow a test-particle to cross the chaotic zone of Fom c for values of eccentricity e between 0.2 and 0.8, hence the configurations (a', e') allowed to a particle after its encounter with Fom c are comprised between two curves. **(b)** Close-encounters occur in the chaotic zone of Fom c, with initially low-eccentricity particles ($0 < e < 0.05$), but here the semi-major axis can span values from the inner edge of the chaotic zone to the semi-major axis of Fom c. Therefore, there is a total of four curves on this plot, two curves for each boundary value in semi-major axis, but due to the small span in eccentricity, these are very close and appear as a single one. The horizontal red dotted line figures the minimum eccentricity required for an orbit to be compatible with that of Fom b.

4.4.3 Further secular evolution with Fom c

However, after being scattered, the test-particle is no longer in resonant evolution, but in secular evolution with Fom c. The effect of a secular evolution with an eccentric perturber is that a test-particle will reach its maximum orbital eccentricity when being apsidally aligned with the eccentric perturber, as illustrated in Figure 4.11, which shows a phase diagram of this secular Hamiltonian for a particle having $a'/a_c = 1.2$, assuming coplanarity of both orbits and $e_c = 0.1$. (see also Section 2.4).

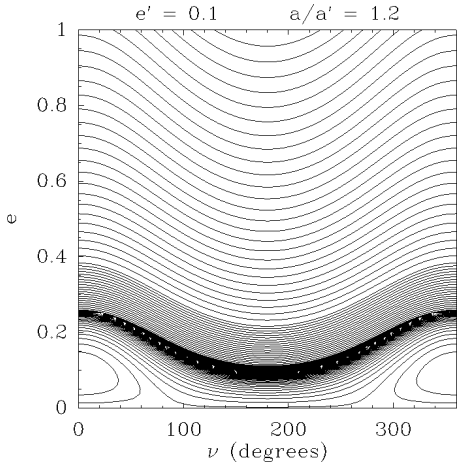

Figure 4.11 – Example of secular evolution of a test-particle under the dynamical influence of Fom c, for a typical semi-major axis ratio of $a/a_c = 1.2$.

Following Figure 4.10, let us assume that after the close-encounter episode, the particle appears in this diagram at $e \simeq 0.7$. Then, its further secular evolution can be readily seen in the phase-space diagram of Figure 4.11, and following the Hamiltonian level curve it appears on. It actually depends on the starting value of ν. If the particle starts at $\nu \simeq 0$, the secular evolution will cause its eccentricity to first decrease, and in any case never overcome the starting eccentricity. This particle will never reach a Fom b-like orbit. Conversely, a particle starting at $\nu \simeq 180°$ will undergo a secular eccentricity increase that will drive it above $e = 0.8$ near $\nu = 0$. At this point the particle has now reached a Fom b-like configuration. But $\nu \simeq 0$ exactly means apsidal aligenment. The key point here is that in the level curves of Figure 4.11, the maximum eccentricity is reached at $\nu = 0$ (see also Section 2.4). Therefore, secular evolution after the close-encounter episode can help moving to higher eccentricies and also provide an explanation for the apsidal alignment of Fom b with Fom c, and thus with the outer belt shaped by Fom c.

4.4.4 A three-step dynamical scenario

The dynamical scenario that we propose for the Fomalhaut system, and which now contains three steps, is the following:

1. *Mean-Motion Resonances between Fom b and the suspected Fom c :* Fom b is likely to have formerly resided in an inner mean-motion resonance (MMR) with the additional planet, as illustrated in Figure 4.12(a). MMRs with an eccentric perturber such as the belt-shaping putative Fom c induce a gradual eccentricity increase, which can lead Fom b to cross the chaotic zone of Fom c, where it can then be scattered by Fom c on its current orbit, as illustrated in Figure 4.12(b).

The dynamical timescale involved in this process, that is, the typical time necessary for Fom b to reach a sufficient orbital eccentricity from its MMR position and be scattered on its current orbit, strongly depends on the mass of the putative Fom c. In particular, the scattering event can be delayed by timescales comparable to the age of the system with a Neptune or Saturn-sized Fom c, which would explain why Fom b was recently set on its orbit.

2. *Close-encounter with the suspected Fom c :* inspection of the close-encounters between Fom b and the putative Fom c reveals that these can set Fom b on an orbit with a semi-major axis compatible with that of Fom b, but that they also preferentially produce orbits which are not eccentric enough to be compatible with that of the observed one ($a = 81 - 415\,\mathrm{AU}$ and $e = 0.69 - 0.98$, in the 95% level of confidence Beust et al. 2014).

3. *Secular evolution with the suspected Fom c :* an additional eccentricity increase can be provided by the mean of secular evolution of Fom b under the influence of the putative eccentric Fom c, which is indeed mainly expected at semi-major axes with $a = 81{-}415\,\mathrm{AU}$. However, this eccentricity increase is accompanied by an apsidal alignment with the belt-shaping Fom c, and thus with the belt, which may explain the tendency for the observed orbit to be apsidally aligned with the belt, as illustrated in Figure 4.12(c).

The whole process is summarised and illustrated in Figure 4.12 and 4.13. It shows the secular evolution of the semi-major axis a, eccentricity e, and longitude of periastron ν of one particle extracted from our simulation, initially trapped in 5:2 MMR with Fom c. Up to $\sim 1.8\,\mathrm{Myr}$ the particle remains in the resonance while its eccentricity increases. Then it enters a chaotic phase characterised by encounters with Fom c. After $\sim 2.2\,\mathrm{Myrs}$, there are no more encounters, but the particle keeps being secularly perturbed by Fom c. Starting this third phase at $e \simeq 0.6$ and $\nu \simeq 180°$, it evolves towards larger eccentricities and $\nu = 0$. After $\sim 3\,\mathrm{Myrs}$ it has reached a Fom b-like state.

4.5 Conclusions and perspectives

The scattering events generating orbits fully comparable to the orbit of Fom b, either in terms of semi-major axis and eccentricity, but also in near-coplanarity and apsidal alignment with the belt-shaping putative Fom c, is a very robust mechanism when generated by a perturber with an eccentricity 0.1, whether these orbits are primarily due to a scattering event, or secondarily, via a MMR. However, MMRs are the most probable route for Fom b to have been set on its current orbit in our scenario. Indeed, primary scattering events scatter the material out of the system on timescales much shorter than the age of the system, while MMRs tend to delay the production of Fom b-like orbits, potentially by timescales comparable to the age of the Fomalhaut system. This delay increases with decreasing mass of Fom c, and so does the average lifetime of Fom b-like orbits. However, the ability of a MMR to bring test-particles in the chaotic zone of Fom c, and thus the efficiency of a MMR to produce Fom b-like orbits, decreases with decreasing mass of Fom c. Therefore, the mass of Fom c should be sufficient for a given MMR to produce Fom b-like orbits, but should not exceed a given value in order for the production of Fom b-like orbits to be delayed by timescales compatible with its detection at the age of the system. The MMR which realises this compromise the best is the 5:2 MMR. New constraints on the mass of the unseen Fom c in our scenario are $m_c = 0.25 - 0.5\,M_{\mathrm{Jup}}$.

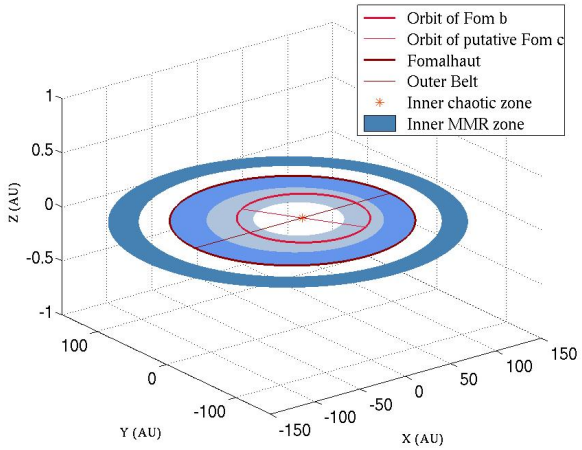

(a) Initial configuration

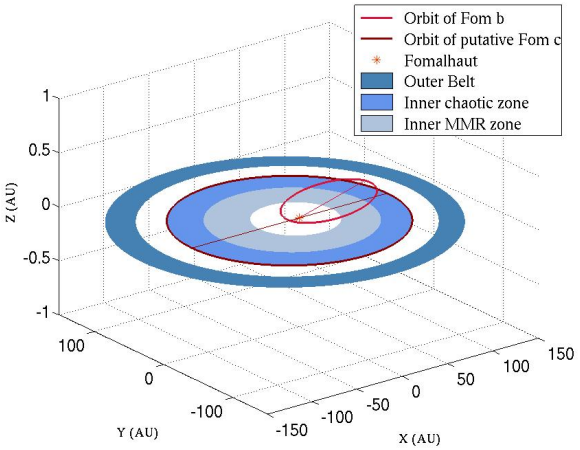

(b) Intermediary configuration

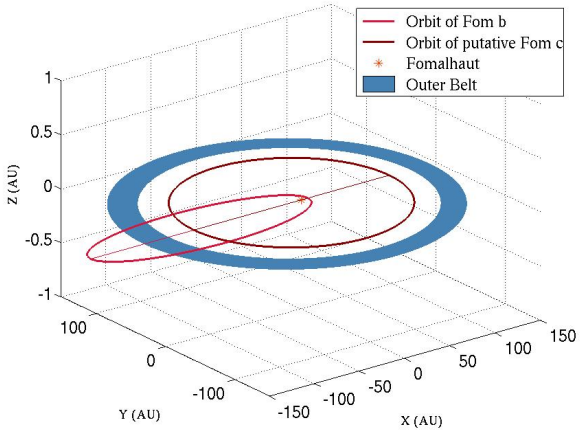

(c) Final configuration

Figure 4.12 – **(a)** Probable initial configuration of the Fomalhaut system. Fom b is in MMR with the belt shaping eccentric Fom c. **(b)** Probable intermediary configuration of the Fomalhaut system. MMRs with an eccentric perturber generate very eccentric orbits, which leads Fom b to cross the chaotic zone of Fom c and be scattered by it on its current orbit. **(c)** Probable current configuration of the Fomalhaut system.

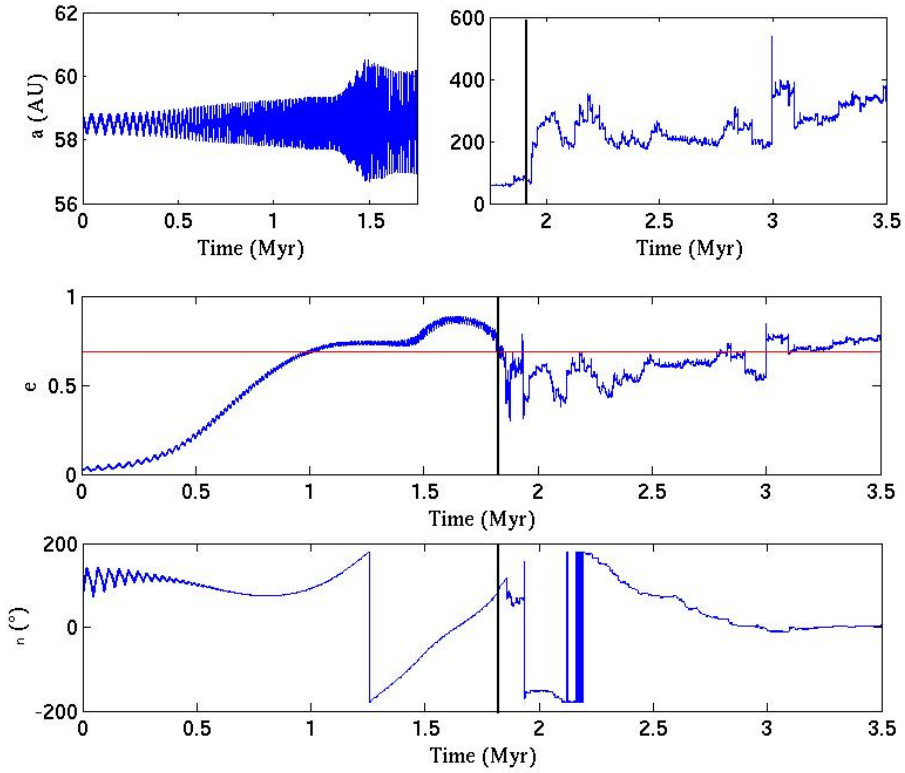

Figure 4.13 – **Example of the three-step process that may have led Fom b on its current orbit.** We display the evolutions in time of the semi-major axis a, eccentricity e, and longitude of periastron ν of a massless test-particle initially in 5:2 MMR with a $3\,M_{\rm Jup}$ Fom c, with semi-major axis $a_c = 108.6\,\mathrm{AU}$ and orbital eccentricity $e_c = 0.1$. Note that this process can be generated via several other MMRs. The test-particle endures a three-step dynamical evolution, starting with a resonant evolution, where its semi-major axis suffers small oscillations around the exact resonant location, and its eccentricity largely increases, while co-evolving with the longitude of periastron. The vertical black line at $\sim 2\,\mathrm{Myr}$ indicates the second step of the process, that is, a close-encounter with Fom c when the highly eccentric orbit of the test-particle leads its orbit to cross the chaotic zone of Fom c. Note that this delay of several Myr with a Jupiter-sized Fom c increases up to several 100 Myr with a Saturn or Neptune-sized Fom c. The semi-major axis of the test-particle is compatible with this of Fom b after the close-encounter, but its eccentricity remains smaller than 0.69 *(horizontal red line)*, and thus is incompatible with that of Fom b. The third step consists mainly in a secular evolution of the test-particle with the eccentric Fom c, although its orbit endures small chaotic variations. This secular evolution allows the eccentricity to increase and become greater than 0.69, which occurs when there is an apsidal alignment between the perturber and the test-particle, that is, when the longitude of periastron of the test-particle is close to zero.

These constraints are compatible with the witnessing of a transient planetary system configuration, where the orbits of Fom b and Fom c cross each other, and that is sufficiently stable to be witnessed (Beust et al. 2014). Finally, it is also crucial that MMRs are generated by a perturber with an eccentricity ~ 0.1 such as this of Fom c in order to produce Fom b-like orbits. These constraints are fully compatible with the shaping of the outer belt (Quillen 2006).

Considering that it would have been difficult to form Fom b from resonant material, since eccentricities and thus relative velocities of solids are increased, which thus challenges their accretion, it is most probable that there were migration processes in this system.

Fom b and/or Fom c are very likely to have migrated in order for Fom b to find itself at a MMR location. An outward migration process has been put forward to explain the presence of the belt-shaping planet at a distance of the order of 100 AU from its host star by Crida et al. (2009). This mechanism implies migration of a pair of planets in MMR : if the inner planet is more massive than the outer one, both planets can migrate outwards in a common gap in the gaseous protoplanetary disk. However, the eccentricity of these planets are excited by their MMR configuration, but also damped by the gaseous disk (Crida et al. 2008). In Crida et al. (2009), this resulted into planets with orbital eccentricities too moderate ($\sim 0.02 - 0.03$) to be compatible with that of the belt-shaping planet. Planetesimal-driven migration could both explain the outward migration of the belt-shaping planet and its orbital eccentricity, since the abscence of gas prevents orbital eccentricities to be damped during this migration process. However, as for the early migration scenario, this would involve the presence of another massive body inner to the belt shaping planet, which questions the compatibility of our scenario with an additional putative Fom d.

Finally, a significant and broad population of small bodies were set on highly eccentric orbits via MMRs in our scenario. As the eccentricity of a resonant test-particle increases while its semi-major axis suffers only small relative variations, its periastron will obviously decrease. This means that a significant amount of material has spent some time in the inner parts of the system, and this might be linked with the presence of two inner belts in the Fomalhaut system, a hot, very close, at $\sim 0.1 - 0.3\,\mathrm{AU}$, and another, warm, at $\sim 2\,\mathrm{AU}$ (Lebreton et al. 2013).

Far from being paradoxal, the configuration of the Fomalhaut system is in fact logical, that is, if there are clues for a perturber on a 0.1 eccentric orbit in a system, bodies on Fom b-like orbits should be expected to be present in the system, in a continuous way as long as material is available either in the chaotic zone or at MMR locations, and also once a given MMR starts producing Fom b-like orbits, which can be delayed very late in the life of a system. This suggests that warm and hot inner belts potentially resulting from this process may start to be produced very late in the history of a system. In the same manner that it might explain the presence of inner belts in the Fomalhaut system, this may also give a solution to the yet unexplained detection of numerous hot belts in systems older than 100 Myr, and which contain levels of dust surprisingly large at such ages (Absil et al. 2013; Ertel et al. 2014, 30% of stars). Bonsor et al. (2012), Bonsor et al. (2014), and Raymond & Bonsor (2014) and have investigated whether scattering of planetesimals by a chain of planets or subsequent to planetary migration, as well as a combination of both, as possible mechanisms to explain the presence of such hot belts over several 100 Myr. However, if these mechanism may explain the origin of this dust, they require that the dust is replenished over the system's age, and thus, will ultimately fade with time. The three-step process revealed in this paper involves one should not necessarily assume that hot belts in systems older than 100 Myr have been sustained over the system's age, and suggest that some of these hot belts may be related to the presence of a massive and slightly eccentric planet in the system (see Sect. 6.3).

Article : Insights on the dynamical history of the Fomalhaut system – Investigating the Fom c hypothesis

Astronomy & Astrophysics manuscript no. main
July 12, 2014

Insights on the dynamical history of the Fomalhaut system

Investigating the Fom c hypothesis

V. Faramaz[1,2], H. Beust[1,2], J.-C. Augereau[1,2], P. Kalas[3], and J.R. Graham[3]

[1] Univ. Grenoble Alpes, IPAG, F-38000 Grenoble, France
[2] CNRS, IPAG, F-38000 Grenoble, France
[3] Department of Astronomy, 601 Campbell Hall, University of California at Berkeley, Berkeley, CA 94720, USA

Received; Accepted

ABSTRACT

Context. The eccentric shape of the debris disk observed around the star Fomalhaut was first attributed to Fom b, a companion detected near the belt inner-edge, but new constraints on its orbit revealed that it is belt-crossing, highly eccentric ($e \sim 0.6 - 0.9$), and can hardly account for the shape of the belt. The best scenario to explain this paradox is that there is another massive body in this system, Fom c, which drives the debris disk shape. The resulting planetary system is highly unstable, which hints at a dynamical scenario involving a recent scattering of Fom b on its current orbit, potentially with the putative Fom c.
Aims. Our goal is to give insights on the probability for Fom b to have been set on its highly eccentric orbit by a close-encounter with the putative Fom c. We aim to study in particular the part played by mean-motion resonances with Fom c, which could have brought Fom b sufficiently close to Fom c for it to be scattered on its current orbit, but also delay this scattering event.
Methods. We assumed that Fom c is much more massive than Fom b, that is, Fom b behaves as a mass-less test-particle compared to Fom c. This allowed us to use N-body numerical simulations and to study the influence of Fom c on a population of mass-less test-particles, that is, to study the generation of Fom b-like orbits by direct scattering events or via mean-motion resonance processes. We assumed that Fom b originated from an orbit inner to that of the putative Fom c.
Results. We found that the generation of orbits similar to that of Fom b, either in term of dimensions or orientation, is a robust process and a consequence of interactions of inner material with an eccentric massive body such as the putative Fom c. We found that mean-motion resonances can delay the production of Fom b-like orbits on timescales comparable to the age of the system, thus explaining the witnessing of an unstable configuration.
Conclusions. We conclude that Fom b probably originated from an inner resonance with Fom c, which is at least Neptune-Saturn size, and was set on its current orbit by a scattering event with Fom c. Since Fom b could not have formed from material in resonance, our scenario also hints at former migration processes in this planetary system.

Key words. Circumstellar matter – Planetary systems – Methods: N-body Simulations – Celestial mechanics – Fomalhaut – ζ^2 Reticuli

1. Introduction

Fomalhaut (α Psa) is a 440 Myr old (Mamajek 2012) A3V star, located at 7.7 pc (van Leeuwen 2007; Mamajek 2012). As revealed by HST, Fomalhaut is surrounded by an eccentric dust ring ($e = 0.11 \pm 0.01$) with a sharp inner edge at 133 AU and extending up to 158 AU (Kalas et al. 2005). This eccentric shape hinted at the presence of a massive body orbiting inside the belt on an eccentric orbit, dynamically shaping the belt (Quillen 2006; Deller & Maddison 2005). This hypothesis was furthermore confirmed by the direct detection of a companion near the inner edge of the belt, Fomalhaut b (hereafter Fom b) (Kalas et al. 2008). The nature of Fom b has been intensely discussed since its discovery because it is observed at visible wavelengths, but remain undetected in the infrared (Kalas et al. 2008; Marengo et al. 2009; Janson et al. 2012). The consensus today is that it is a planetary body, surrounded by a population of dust, either in the form of a planetary ring system (Kalas et al. 2008), or a dust cloud resulting from a collision between satellites (Kennedy & Wyatt 2011; Kenyon et al. 2014). Further observations of this body led to the detection of its orbital motion. Based on the available astrometric points, the first attempts to constrain its orbit showed that it is surprisingly extremely eccentric, nearly coplanar and close to apsidal alignment with the belt, so that the orbit inevitably crosses it ($a_b \sim 110 - 120$ AU and $e_b \simeq 0.92 - 0.94$, Graham et al. 2013; Beust et al. 2014). Detailed recent dynamical investigations (Beust et al. 2014) revealed that this orbital configuration is not compatible with the shape of the disk and the age of the system. A low eccentricity belt like the one observed might indeed be produced by this perturber, but irrespective of the mass of Fom b, it appears to be a transient feature that evolves to very high eccentricities and possibly to its destruction on timescales much smaller than the age of the system.

The most straightforward solution to this apparent paradox is to suppose the presence of a second more massive and yet undetected body in the system (hereafter named Fom c), which is responsible for the disk shaping because of a predominant dynamical influence. This implies that Fom b is rather a low-mass body compared to the putative Fom c, but other arguments suggest this. As shown by Beust et al. (2014), even with no Fom c and given its orbit, a massive Fom b would lead to a rapid destruction of the observed belt. Moreover, if Fom b was massive enough,

Send offprint requests to: V. Faramaz
Correspondence to: Virginie.Faramaz@obs.ujf-grenoble.fr

it would trigger a more or less rapid secular orbital precession of the orbit of Fom c. This could prevent Fom c from sustaining the belt asymmetry. A dynamical study of Tamayo (2014) also suggests that the best scenario that matches the observational constraints is that of a super-Earth Fom b with an undetected belt-shaping Saturn-mass planet. Finally, a low-mass Fom b is also compatible with recent photometric studies, which suggest that it is no more than Earth- or Super-Earth sized (Janson et al. 2012; Galicher et al. 2013).

Considering that the orbit of Fom b is highly eccentric with an apastron beyond the outer edge of the belt and a periastron that could be as low as a few AU (Beust et al. 2014), and that the putative Fom c would move on a less eccentric orbit located slightly inside the inner edge of the belt, then inevitably both orbits are expected to cross each other. This raises the question of the dynamical stability of Fom b. In this scenario, its present day orbit could just be a transient configuration. It could have been put there by a more or less recent scattering event, potentially with Fom c (Beust et al. 2014), and could be subject to an ejection in a more or less near future. The more massive is Fom c, the shorter the survival timescale of Fom b. In Beust et al. (2014), it is argued that Fom c should probably be ~Saturn-sized to be able to shape the belt while not ejecting Fom b too quickly from its present-day orbit, just to make it likely for us to witness the transient configuration today.

The goal of this paper is to investigate the issues of the generation of the present-day orbital configuration of Fom b. In this work, we discuss whether models involving Fom c only can explain both the orbit of Fom b and the shape of the outer Kuiper-belt. We examinate how Fom b, starting from a configuration inner to Fom c could have been put on its present-day orbit by a scattering event with Fom c. We show that mean-motion resonances may play a crucial role by delaying this scattering event. We outline our method and our expectations in Sect. 2, and display our results in Sect. 3. We discuss these results in Sect. 4. In particular, we investigate the influence of the eccentricity and the mass of Fom c, which reveal to be crucial parameters controlling the mechanism that generates orbits comparable to that of Fom b. The mechanism itself is also shown to be more complex than originally thought and is investigated in more details. We give our conclusions in Sect. 5.

2. Method

The basic assumption of our study is that Fom c is significantly more massive that Fom b. This is supported by a recent study (Beust et al. 2014) showing that Fom b is probably a low-mass object and that the eccentric disk shape is controlled by another, more massive object, presumably Fom c. We use N-body simulations to investigate the ability of the putative Fom c to put Fom b on its present-day orbit and the typical timescale for this to happen starting from various initial configurations. Thanks to the mass difference between both objects, Fom b will be treated in this work as a massless test-particle perturbed by Fom c. Our second assumption is that Fom b was originally on an orbit inner to that of Fom c. The configuration of the system is illustrated in Fig. 1.

In this section, we present our numerical set-up as well as theoretical background on the production of Fom b-like orbits, either by a direct scattering event or via mean-motion resonances.

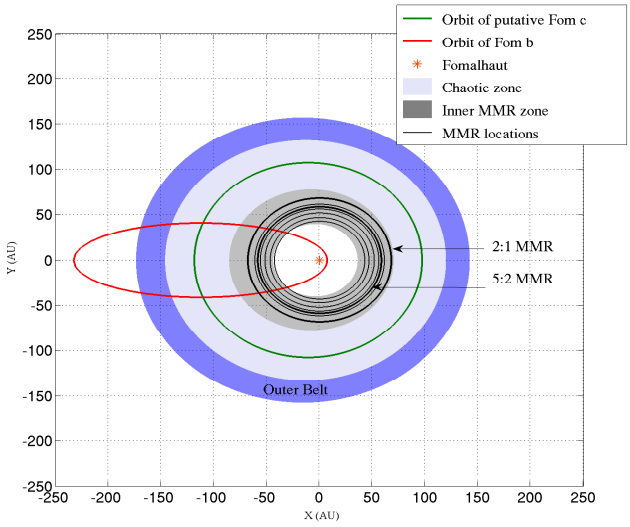

Fig. 1. Schematic configuration of the Fomalhaut system. The outer Kuiper belt extends from 133 to 158 AU and has an eccentricity of 0.1. The orbit of Fom b has $a_b = 120$ AU and $e_b = 0.94$, that is, the peak values derived by Beust et al. (2014). Since Fom b has a low inclination relative to the outer belt and is nearly apsidally aligned with it, we represent this orbit as coplanar and apsidally aligned with the belt for sake of simplicity. We represent as well the presumed orbit of the putative Fom c, and the regions of potential origin for Fom b investigated in this paper, that is, the chaotic zone of Fom c and the region where mean-motion resonances which may generate orbits crossing the chaotic zone of Fom c are localised.

2.1. The putative Fom c

The numerical set-up of the orbital parameters and the mass of the putative Fom c was chosen considering constraints on the belt-shepherding planet retrieved from previous dynamical studies and observational constraints.

Based on dynamical investigations, Chiang et al. (2009) found an upper-mass limit of $3\,M_{Jup}$, a lower semi-major axis limit of ~ 101.5 AU, and an orbital eccentricity of $\sim 0.11-0.13$, while Quillen (2006) found that the belt-shaping planet should rather be Neptune or Saturn-mass, with a semi-major axis of ~ 120 AU and an orbital eccentricy of ~ 0.1. On the other hand, Rodigas et al. (2013) found a mass of $\sim 7.6 \pm 4.6\,M_{Jup}$, a lower semi-major axis limit of ~ 85 AU, and an orbital eccentricity of ~ 0.11. Observational constraints from Janson et al. (2012) and Currie et al. (2013) gave a detection limit of $\sim 1-3\,M_{Jup}$ at these distances.

Therefore, we arbitrarily chose a mass of $m_c = 3\,M_{Jup}$ for Fom c and will discuss the impact of this mass on our results in Sect. 4. We followed the approach of Quillen (2006); Chiang et al. (2009) and Duncan et al. (1989), and considered that the belt inner edge, located at 133 AU, was created by the chaotic zone around Fom c, that is, the region where material is on a highly unstable orbit. In this context, the location of the inner edge should correspond to the outer boundary of the chaotic zone of Fom c. The chaotic zone of a planet is defined as the region where mean-motion resonances overlap. The width of this zone, Δa, depends on the mass of the planet, m_{planet}, and its semi-major axis a_{planet}. It reads :

$$\frac{\Delta a}{a_{planet}} = \frac{a_{edge} - a_{planet}}{a_{planet}} = 1.5\mu^{2/7} \quad , \qquad (1)$$

where $\mu = m_{planet}/M_\star$ (Wisdom 1980; Duncan et al. 1989). The mass of Fomalhaut was set to $M_\star = 1.92\,M_\odot$ (Mamajek 2012). Consequently, one can deduce the semi-major axis of a planet of a given mass that generates a disk inner edge at 133 AU:

$$a_{planet} = \frac{a_{edge}}{1 + 1.5\mu^{2/7}} \quad . \tag{2}$$

We derived a semi-major axis of $a_c = 107.8$ AU. We set the orbital eccentricity of Fom c to be $e_c = 0.1$ as to match the observed ellipticity of the belt.

This is in agreement with other studies which showed that the chaotic zone extends radially up to $\sim 3 - 3.5R_H$ around the planet's orbit (Ida et al. 2000; Kirsh et al. 2009), where R_H is the Hill radius defined by

$$R_H = a_c \left(\frac{m_c}{3M_\star}\right)^{1/3} \quad . \tag{3}$$

Eq. 3 gives then $R_H = 8.54$ AU, and with $a_c = 107.8$ AU, the inner edge of the belt at 133 AU is indeed distant of $\sim 3R_H$ from Fom c.

2.2. Producing Fom b-like orbits from originally quiescent orbits

Driving Fom b from an orbit located inside this of Fom c to its present-day orbit means drastically increasing its semi-major axis and its eccentricity. The most straightforward mechanism to achieve this is a scattering event caused by a close encounter. Such events are expected to occur in the chaotic zone around Fom c outlined above. Only a close encounter event can induce sudden changes of the eccentricity and semi-major axis of a test-particle, potentially in a way that sets it on a Fom b-like orbit.

To undergo a scattering event, a particle must cross the chaotic zone at some point on its orbit. It can have formed there or have formed more deeply inside and then have suffered an orbital evolution that caused its orbit to furthermore cross the chaotic zone. Particles moving initially in the chaotic zone have very few chances to survive there more than a few 10^7 yrs, i.e. much less than the age of the star. Hence we think that models involving a Fom b that formed deeper inside the orbit of Fom c and was furthermore driven to cross the chaotic zone are more suited to our purpose.

To lead an inner orbit to cross the chaotic zone, its semi-major axis and/or its eccentricity must be increased. A major semi-major axis change can only be achieved by a scattering event with other unknown planets prior to crossing the chaotic zone of Fom c. Of course, this cannot be excluded, but implies the hypothetical presence of at least a third planet, with potentially similar timescale problems as with close encounters with Fom c. Here we will investigate models involving Fom c only.

For a low-mass Fom b forming inside the orbit of Fom c on a low eccentricity orbit, the only way to make it reach the chaotic zone with no scattering event by another inner planet is to drastically increase its eccentricity by trapping Fom b in near mean-motion resonance with Fom c. Regular secular perturbations triggered by Fom c on particles moving deeply inside its orbit are indeed known not to much affect their semi-major axes. Moreover, particles moving outside resonances are expected to undergo only moderate amplitude regular eccentricity fluctuations. Conversely, particles trapped in some mean-motion resonances can sometimes see their eccentricity increased to very large values and therefore constitute valuable routes to cause a Fom b progenitor to cross the chaotic zone of Fom c.

Mean motion resonances (hereafter MMR) between a particle and a perturber (here Fom c), usually noted n : p, where n and p are integers, concern particles with orbital periods achieving the p/n commensurability with that of the perturber. The integer $q = |n - p|$ is called the order of the resonance. MMRs occur at specific locations relative to the orbit of the perturber. Resonances with $n > p$ correspond to *inner* resonances, that is, particles orbiting inside the orbit of the perturber, while $n < p$ denotes *outer* resonances.

Particles trapped in MMRs are characterized by the libration of a characteristic resonant angle (see Beust & Morbidelli 1996; Morbidelli & Moons 1995, for details) and small amplitude semi-major axis librations ($\lesssim 0.1$AU) around the exact resonance location. If the eccentricity of the perturber is zero (or very small), then the secular evolution of the eccentricity is coupled with that of the semi-major axis, so that the eccentricity only undergoes small amplitude variations. But if the eccentricity of the perturber is non-zero, the eccentricity modulations can have much larger amplitudes. Yoshikawa (1989) showed that this is particularly relevant for inner MMRs like the 4:1, 3:1 or 5:2. This mechanism is thought to be responsible for the generation of the Kirkwood gaps in the solar system (Wisdom 1983), and it has been claimed to trigger the Falling Evaporating Bodies (FEBs, that is, star-grazing evaporating planetesimals, or comets) mechanism towards β Pictoris (Beust & Morbidelli 1996, 2000). As soon as the eccentricity of the perturber overcomes ~ 0.05, this mechanism is able to increase the eccentricity of resonant particles up to large values in the cases of the 3:1, 5:2, 7:3 and 2:1 resonances, and even virtually ~ 1 in the case of the 4:1 resonance. In the asteroid belt, other resonances can also be active provided it overlaps with the ν_6 secular resonance (Yoshikawa 1989). Moreover, as we shall see in Sect. 3, material in MMRs need some time to reach the eccentricity required to cross the chaotic zone, which can thus delay a scattering event. If this delay were to be comparable to the age of the system, this would explain why the unstable present-day configuration is witnessed.

2.3. Initial sets of particles

In order to investigate the scenarios outlined above, we ran several simulations with different initial sets of particles, that is, potential Fom b planets, each of them corresponding to either a specific MMR or a wide range of semi-major axes including both MMRs and the chaotic zone relative to Fom c. The initial conditions of our simulations are all summarised in Table 1. Each of these test-particles populations are assumed to be coplanar with the orbit of Fom c. Orbital inclinations with respect to the orbit of Fom c orbit were randomly distributed between 0 and 3°, while the eccentricities were distributed between 0 and 0.05. All remaining initial angles, that is, the longitude of periastron, the longitude of ascending node, and initial mean anomaly, were randomly drawn between 0 and 2π in a uniform way.

For each simulation, the initial semi-major axes of the test-particles were also uniformly and randomly distributed between boundaries that were specific to each of them.

Run A is dedicated to study the dynamics of 250,000 particles widely distributed radially, which covers both the chaotic zone and the locations of the MMRs, for comparison. The initial semi-major axes of the test-particles were distributed randomly between [40 AU; 110 AU]. Here the upper limit corresponds to the apastron of Fom c minus one Hill radii, to take into account the eccentricity of Fom c, and the lower limit extends the distribution of the test-particles slightly further in than the 4:1 MMR.

Table 1. Characteristics of all initial sets of particles used in our numerical study. In all runs, Fom c itself is assumed to be a $3\,M_{Jup}$ planet orbiting Fomalhaut with semi-major axis $a_c = 107.8$ AU and eccentricity $e_c = 0.1$. All sets of particles are ring-like belts of test-particles extending radially between boundaries given below, eccentricities randomly chosen between 0 and 0.05, and inclinations between 0 and 3° relative to Fom c's orbital plane. Run A contains 250,000 particles and runs B–H contain 100,000 particles.

Run #	Dynamical status relative to Fom c	Semi-major axis extent a (AU)	Theoretical resonance location $a_{n:p}$ (AU)
A	Broad distribution	40-110	-
B	4:1 MMR	40.3–45.3	42.8
C	7:2 MMR	44.3–49.3	46.8
D	3:1 MMR	49.3–54.3	51.8
E	8:3 MMR	53.6–58.6	56.1
F	5:2 MMR	56.0–61.0	58.5
G	7:3 MMR	58.8–63.8	61.3
H	2:1 MMR	65.4–70.4	67.9

Runs B–H from Table 1 focus on rings of 100,000 test-particles centered on specific MMRs with Fom c. Not all MMRs needed actually to be tested. As long a they keep trapped in a MMR, the semi-major axes of test-particles do not vary significantly, as they only undergo small amplitude secular variations around the theoretical MMR value (see Table 1). This remains true even as their eccentricity approaches 1. Therefore, their apastron cannot grow higher than twice the theoretical $a_{n:p}$ value, and we limited ourselves to MMRs achieving this condition. Note that the further in the MMR is located, the higher the eccentricity of a test-particles should increase in order for its orbit to cross the chaotic zone. Therefore, it is expected in a general manner that the most inner MMRs such as the 3:1 and 4:1 should be less efficient routes to generate orbits comparable to that of Fom b in our scenario.

The ability of a MMR to set a test-particle on a orbit sufficiently eccentric to cross the chaotic zone, or even the orbit of Fom c, can be evaluated thanks to phase-space diagrams. For each of the MMRs that we investigated, we present phase space diagrams which allowed us to evaluate the co-evolution of e, the eccentricity of test-particles representing Fom b, and ν, the orientation of their periastron compared to that of Fom c, for test-particles initially on low eccentricity orbits ($e < 0.05$) and with ν between 0 and 2π, with $\nu = 0$ correspoonding to an apsidal alignement of the two orbits. These diagrams show the trajectory followed by a test particle along time in the (e, ν) space when in a given MMR in Fig. 2. We put this in perspective with the crossing of the chaotic zone of Fom c, which allows to evaluate the behaviour expected from the MMRs investigated in this paper.

It is expected that the 2:1, 7:3, 5:2, 3:1, and 4:1 MMRs allow test-particles to cross the chaotic zone of Fom c, where they will be allowed to be scattered and possibly be set on a Fom b-like orbit. This is not the case for the 8:3 and 7:2 MMRs, although in the solar system asteroid belt, they generate high eccentricity particles thanks to an overlap with a secular resonance with Saturn. Such a fortuitous configuration has only few chance to apply here. Moreover, as our simulations only consider Fom c as massiver perturber, no secular resonance is to be expected here. We nevertheless decided to keep these MMRs in our set of simulations in order to quantify this effect.

In low eccentricity regime, the radial extent of a MMR is typically $\sim 0.1\%$ of the semi-major axis of the perturber, that is, ~ 0.1 AU here (Beust & Morbidelli 1996). At high eccentricity, it is typically ~ 20 times wider, that is, ~ 2 AU. We considered therefore that a radial extent of several AU is largely sufficient to investigate a particular resonance. Resonances were thus examined closely by distributing the semi-major axes of the test particles over 5 AU wide ranges centered on the theoretical location of the resonance (Table 1).

In all cases, the system was evolved over 100 Myr, that is $\sim 1/4$ of the age of Fomalhaut, using the symplectic N-body code SWIFT-RMVS (Levison & Duncan 1994). We used a typical timestep of $\sim 1/20$ of the smallest orbital period. This ensures a conservation of energy with a typical error of $\sim 10^{-6}$ on relative energy. We took snapshots of the particles orbits every 10^5 yrs.

In the next section, we present our findings about the production of orbits similar to that of Fom b in our scenario, that is, the ability of the putative Fom c to set much less massive bodies on orbits similar to that of Fom b when these originate from the parts of the system inner to Fom c.

3. Results

In this section, we first retrieve general results from Run A and then present results of Runs B–H for individual MMRs. In our simulations, we identified particles which were set on a Fom b-like orbit, which we defined as an orbit with eccentricity and semi-major axis in the 95% level of confidence intervals found by Beust et al. (2014), that is with $e \in [0.69; 0.98]$ and $a \in [81; 415]$ AU. Other constraints have been derived by Beust et al. (2014) regarding the orientation of the orbit of Fom b: it is almost coplanar with the outer Kuiper-belt, and more or less apsidally aligned with it. However, these constraints are weaker than those on the semi-major axis and eccentricity. Therefore, we will examinate the orientation of the Fom b-like orbits that we identified in a second time. All these constraints are summarized in Table 2.

Table 2. Summary of the constraints on the orbit of Fom b as found by Beust et al. (2014).

Parameter	Value	Remark
a (AU)	81–415	95% level of confidence
e	0.69–0.98	95% level of confidence
i (°)	0–29	67% level of confidence
ν (°)	± 30–40	~ 70% level of confidence

3.1. Broad distribution, inner to the putative Fom c

We first investigated the dynamical status exhibited by the test-particles, integrated over the 100 Myr of the run, as a function of their initial semi-major axes in Fig. 3. In the top-panel, the chaotic zone of Fom c shows through a large proportion of unbound orbits above $\sim$ 70 AU, while low eccentricity orbits – $e < 0.2$ – were preferentially adopted below this limit. This is in accordance with the theoretical inner boudary of the chaotic zone, that is $\sim 3R_H$ inner to the periastron of Fom c. The total proportion of snapshots in a Fom b-like orbit dynamical status is less than 1%, and thus they are not visible here. On the bottom-panel of Fig. 3, we present a zoom-in of the top-panel to show them.

As expected, MMRs increased the eccentricity of test-particles, and possibly led them to leave the system. Although

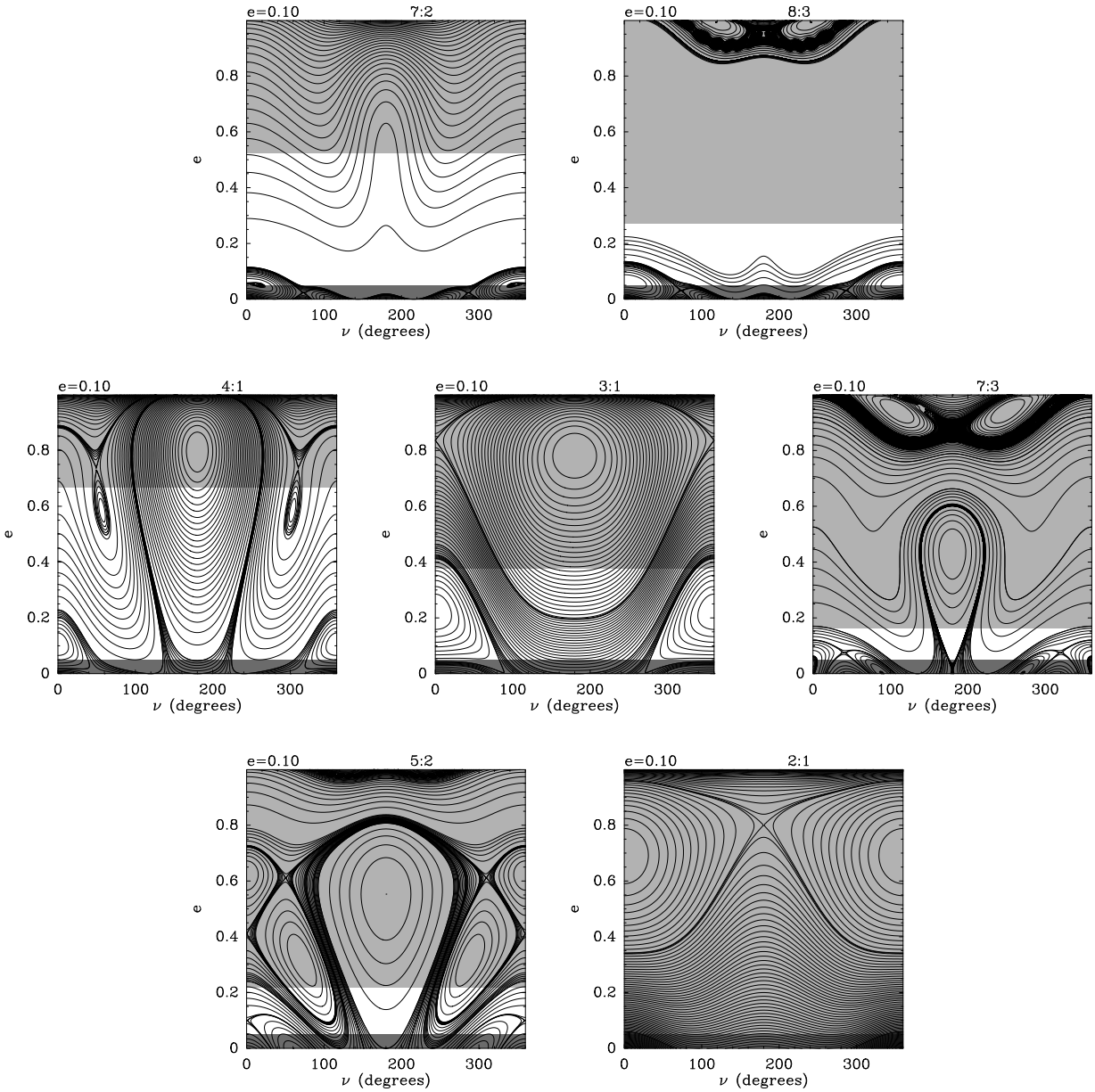

Fig. 2. Theoretical phase diagrams of the MMRs that we investigated. Our initial conditions are figured in dark grey and the chaotic zone of Fom c in light grey. The chaotic zone of Fom c is considered to extend from $3.5R_H$ inner to the periastron of Fom c, to $3.5R_H$ outer to the apastron of Fom c. Particles which start on a trajectory allowing it to cross the chaotic zone may then be scattered and set on a Fom b-like orbit.

it was able to increase the eccentricity of test-particles, the 4:1 MMR did not to generate any Fom b-like orbit. The density of snapshots in a Fom b-like status in the cases of the 3:1 and 7:3 MMRs was low compared to that of the chaotic zone, while interestingly, this density was greater in the cases of the 5:2 and 2:1 MMRs. This does not mean that the probability for being set on a Fom b-like orbit is greater for these MMRs, but rather that Fom b-like orbits generated from these MMRs are more stable, as one can see in Table 3, where we summarise the average time spent by a test-particles on a Fom b-like orbit as a function of their origin, and show for comparison the distribution of the origin of these test-particles. The total proportion of particles which were set at a moment or another on a Fom b-like orbit in our run is ∼ 20%, where indeed ∼ 90% of these test-particles originated from the chaotic zone, and the 5:2 and 2:1 MMRs produced the Fom b-like orbits with the largest mean lifetimes (∼ 1 Myr), although these remain largely inferior to the age of the system.

Table 3. Summary of the results of Run A: distribution of the test-particles being set on a Fom b-like orbit and average time spent by a particle on a Fom b-like orbit, $\bar{t}_{Fomb}$.

Dynamical status relative to Fom c	Distribution of Fom b-like particles (%)	$\bar{t}_{Fomb}$ (Myr)
3:1 MMR	2.0×10^{-2}	0.13
5:2 MMR	1.15	1.0
7:3 MMR	0.45	0.2
2:1 MMR	5.35	1.4
Chaotic zone	93.0	0.21

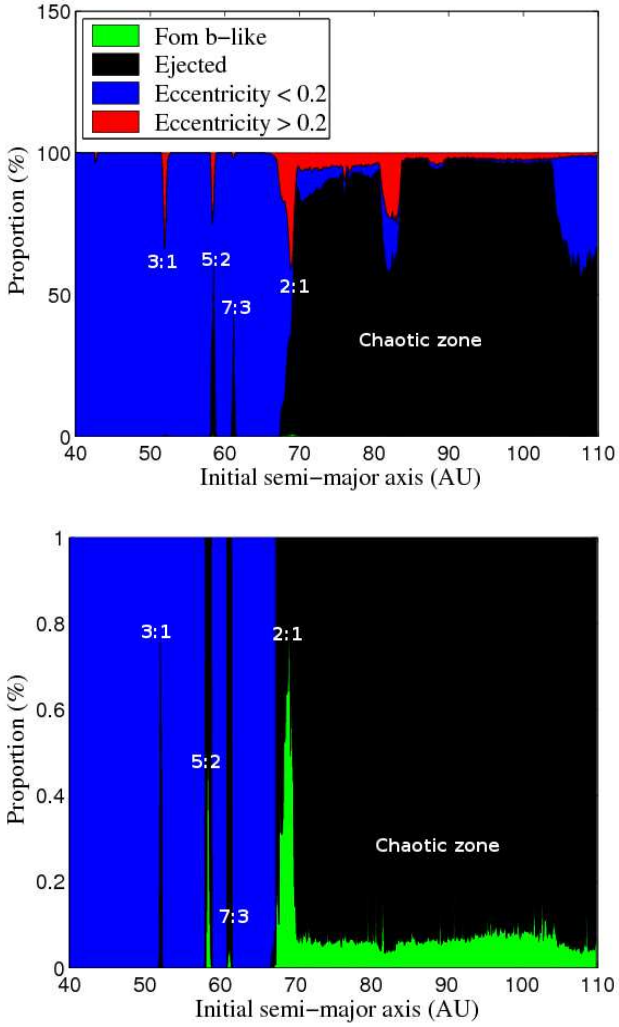

Fig. 3. Proportion of the time spent on orbits of different dynamical status as a function of the initial semi-major axes of the test-particles.

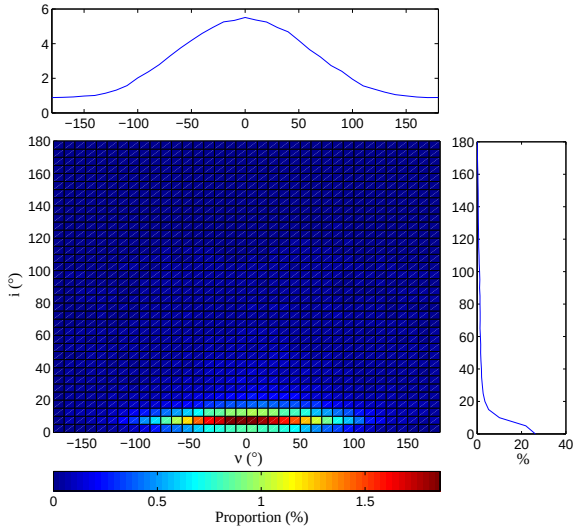

Fig. 4. Distribution in inclination and longitude of periastron with respect to this of Fom c of Fom b-like orbits.

In our definition of a Fom b-like orbit, we did not take into account the orientation of these orbits. However, constraints on the orbit of Fom b also showed that it is rather coplanar and apsidally aligned with the belt, which, in our scenario, involves that the orbit of Fom b is also coplanar and apsidally aligned with that of Fom c, since it is the planet that shapes the belt and gives it its apsidal orientation. Therefore, we show in Fig. 4 the orientation of Fom b-like orbits, that is their inclination i and the direction of their periastron with respect of that of Fom c, ν. A significant proportion of them corresponded to these criterions: indeed, $\sim$ 40% of the Fom b-like orbits formed had $i \in [0°, 30°]$ and $\nu \in [-40°, 40°]$, that is, in the $\sim$ 70% level of confidence. This shows that the production of orbits fully comparable to that of Fom b, either in terms of semi-major axis and eccentricity, but also in terms of relative inclination to the disk and apsidal orientation, is extremely common, even in the chaotic zone. The reasons for this to happen are discussed further in Sect. 4.3.

The sample of Fom b-like orbits from Run A may be sufficient to retrieve first clues on the formation of these orbits, in particular, to show that MMRs may play a crucial part here, but it is probably not sufficient to fully compare the efficiency and specificities of each MMR. Therefore we present in the following subsection the results of Runs B–H, that is for individual MMRs. Since these runs achieved a better sampling of MMRs, it allowed us to examine more in depth results of Run A.

3.2. Individual MMRs

The results from Run A suggested that the 4:1, 7:2, and 8:3 MMRs do not produce any Fom b-like orbit. They also suggested that the 3:1 and 7:3 MMRs produce rare and unstable Fom b-like orbits, while the 5:2 and 2:1 MMRs tend to be very efficient in comparison, and produce Fom b-like orbits which are the most stable, although on timescales much smaller than the age of the system ($\sim$ 1 Myr). We present hereafter the results of Runs B–H for individual MMRs.

3.2.1. The 7:2 and 8:3 MMRs

No Fom b-like orbit was produced in the Runs C and E, that is, for the 7:2 and 8:3 MMRs respectively, which is in accordance with the results of the Run A.

As we have seen in the previous section from the diagrams of the 7:2 and 8:3 resonances shown in Fig. 2, it was obvious that test-particles initially on low-eccentricity orbits would not be able to cross the chaotic zone of Fom c, and therefore, not be able to be scattered on a Fom b-like orbit. Indeed, in both cases, none of the test-particles of the run were ever set on an eccentricity greater than 0.2. As was mentionned previously, these two MMRs need to overlap with secular resonances to trigger an increase of the eccentricity of the test-particles. They were thus expected not to be an efficient mechanism to generate Fom b-like orbits, if not unefficient at all.

3.2.2. The 4:1, 3:1 and 7:3 MMRs

No Fom b-like orbit was produced in the Run B for the 4:1 MMR, in accordance with the results of the Run A. The diagram for this MMR shows that some of our test-particles would be expected to cross the chaotic zone of Fom c, and that the production of Fom b-like orbits would be expected. So does for the 3:1 MMR, which produced very rare Fom b-like orbits in the Run A,

which is confirmed by results of Run D. As mentioned in the previous section, it was expected that the most inner MMRs would be less efficient at producing Fom b-like orbits, since their location require a more signifant increase for test-particles to cross the chaotic zone of Fom c than MMRs located closer to Fom c.

Very interestingly, the 3:1 MMR delayed the production of Fom b-like orbits by $\sim 30 - 40$ Myr compared to other MMRs, which strongly reflects the delay potentially induced by the gradual increase of the eccentricity of a resonant test-particle before it is able to be scattered. It is however notable that the 3:1 MMR generated Fom b-like orbits with completely random orientation, which critically reduces the chance of apsidal alignement between Fom b and the dust belt (see top-left-panel of Fig. 5).

The results of the Run G, that is, for the 7:3 MMR, are in accordance with the results of the Run A: the Fom b-like orbits produced were rare ($\sim 1\%$). Moreover, they were theoretically expected as shown in the phase-diagram for this MMR. The average time spent by test-particles on a Fom b-like orbit is ~ 0.3 Myr, and the maximum time for an individual particle does not exceed 40 Myr. The delay induced in the generation of Fom b-like orbits by this MMR is much smaller than the age of the system (~ 3 Myr). However, the Fom b-like orbits produced by this MMR are also similar with the observed orbit of Fom b in terms of orientation (see top-middle-panel of Fig. 5).

3.2.3. The 5:2 and 2:1 MMRs

The MMRs for which test-particles have greater probabilities to be set on a Fom b-like orbit, that is, the 5:2 and 2:1 MMRs, also produced a significant proportion of orbits with orientation comparable to that of Fom b (see top-right and bottom-left panels of Fig. 5).

Their phase-space diagrams revealed that a great number of particles will cross the chaotic zone of Fom c (see Fig. 2). In particular, the 2:1 MMR is not expected itself to sustain large increases in eccentricity, but it appears to be fortuitously located at the boundary of the chaotic zone of Fom c with our parameters, and more particularly, with the mass chosen for Fom c. The impact of the mass of Fom c will be discussed in Sect. 4.2. In the present case, the increase in eccentricity needed is very small and test-particles have easily crossed the chaotic zone of Fom c. These two MMRs seem to be valid routes to form orbits comparable to this of Fom b. However, in both cases, although rare test-particles adopted a Fom b-like orbit over more than 40 Myr, the average time spent on a Fom b-like orbit is $\lesssim 2$ Myr, and the delay induced in the generation of Fom b-like orbits by these MMRs is much smaller than the age of the system ($\sim 1 - 2$ Myr)

3.3. Summary

Combining the results for individual MMRs and for the chaotic zone, we summarise in Table 4 different probabilities which characterize the production of Fom b-like orbits: P_{Fomb} is the probability to be set on a Fom b-like orbit, P_{orient} is the probability for a Fom b-like orbit to have an orientation compatible with that observed for Fom b, that is $i \in [0°, 30°]$ and $\nu \in [-40°, 40°]$, $P_{>10\,Myr}$ is the probability for a Fom b-like orbit to have a lifetime greater than 10 Myr. We summarise as well the average time $\bar{t}_{Fomb}$ spent by test-particles which were set on a Fom b-like orbit, and the delay in the generation of Fom b-like orbits induced by MMRs.

Moreover, for each region of interest, one can retrieve the probability to be set on a Fom b-like orbit as a function of time, which, ponderated by the corresponding probabilities P_{Fomb}, $P_{>10\,Myr}$ and P_{orient} allowed us to fully compare the efficiency of each region of interest to produce orbits fully comparable to the orbit of Fom b and which have lifetimes greater than 10 Myr, as shown in Fig. 6.

Table 4. For each individual run that produced Fom b-like orbits, probability P_{Fomb} for being set on a Fom b-like orbit, that is, the proportion of the 100,000 test-particles of our initial sample set at least once on a Fom b-like orbit, average time $\bar{t}_{Fomb}$ spent by these test-particles in this configuration, probability $P_{>10\,Myr}$ for a Fom b-like orbit to have a lifetime greater than 10 Myr and probability P_{orient} for a Fom b-like orbit to have an orientation comparable to that of Fom b. We indicate as well any delay in the generation of Fom b-like orbits.

Dynamical status relative to Fom c	P_{Fomb} (%)	$\bar{t}_{Fomb}$ (Myr)	$P_{>10\,Myr}$ (%)	P_{orient} (%)	Delay (Myr)
3:1 MMR	9.7×10^{-2}	3.8	11.3	4.4	~ 30
5:2 MMR	3.8	1.2	2.4	17.6	~ 2
7:3 MMR	1.3	0.24	2.2×10^{-1}	39.6	~ 3
2:1 MMR	20.1	1.6	3.5	15.2	~ 1
Chaotic zone	35.5	0.21	8.5×10^{-2}	48.5	0

All these results give first insights on the most probable origin and dynamical history of Fom b in our scenario. The probability to be set on a Fom b-like orbit fully comparable to that of Fom b and which survives longer than 10 Myr is smaller by an order of magnitude for the 3:1 and 7:3 MMRs compared to the chaotic zone and the 5:2 and 2:1 MMRs. The chaotic zone of Fom c is very efficient at producing Fom b-like orbits, but these are highly unstable and the probability to be set on a Fom b-like orbit decreases very quickly during the first ~ 10 Myr, where its efficiency to produce Fom b-like orbits becomes smaller than these of the 2:1 and 5:2 MMRs. Therefore, the chaotic zone, the 3:1, and the 7:3 MMRs may not be the best ways to explain the orbit and dynamical history of Fom b.

On the other hand, the 2:1 MMR is very efficient at producing Fom b-like orbits, and which have a longer lifetime. However, their orientation is much less probable to be comparable with this of Fom b. Finally, although the 5:2 MMR produces less Fom b-like orbits than the 2:1 MMR, it produces Fom b-like orbits with comparable lifetime, and additionally, produces Fom b-like orbits with orientation fully comparable to this of Fom b in a very significant proportion. Therefore, the 5:2 and 2:1 MMRs appear to be the most probable origin of Fom b in our scenario.

Surprisingly, Fom b-like orbits originating from the chaotic zone have an orientation comparable to this of Fom b, in even greater proportions than MMRs. This is indeed surprising because one would rather have expected some specific MMRs to be able to generate such a significant tendency for apsidal alignement, since they may cause a preferential geometry of close-encounters, while random encounters in the chaotic zone would have had expected to generate randomly orientated Fom b-like orbits. Instead, the apsidal alignement feature appears to be very common, excepted for the 3:1 MMR.

We discuss our results and investigate the influence of the eccentricity and mass of Fom c in the next section. These parameters reveal to be crucial since the former controls the ability of Fom c to generate Fom b-like orbits via MMRs and the latter controls the delay in the generation these orbits. We further investigate the mechanism that generates Fom b-like orbits and the origin of the observed common apsidal alignement in more details.

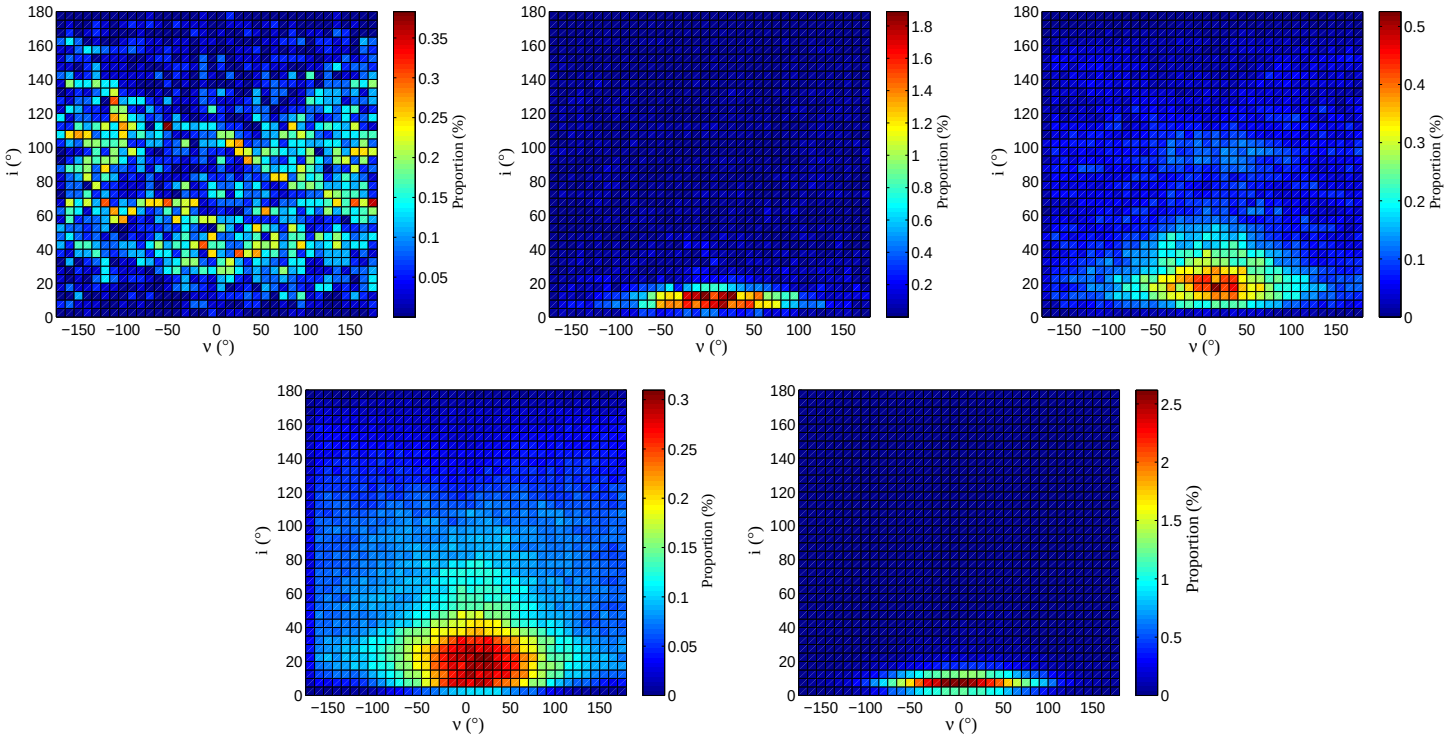

Fig. 5. Distribution in inclination and longitude of periastron with respect to this of Fom c of Fom b-like orbits produced in the case of the 3:1, 7:2, 5:2, and 2:1 MMRs, and the chaotic zone, from top to bottom and left to right, respectively.

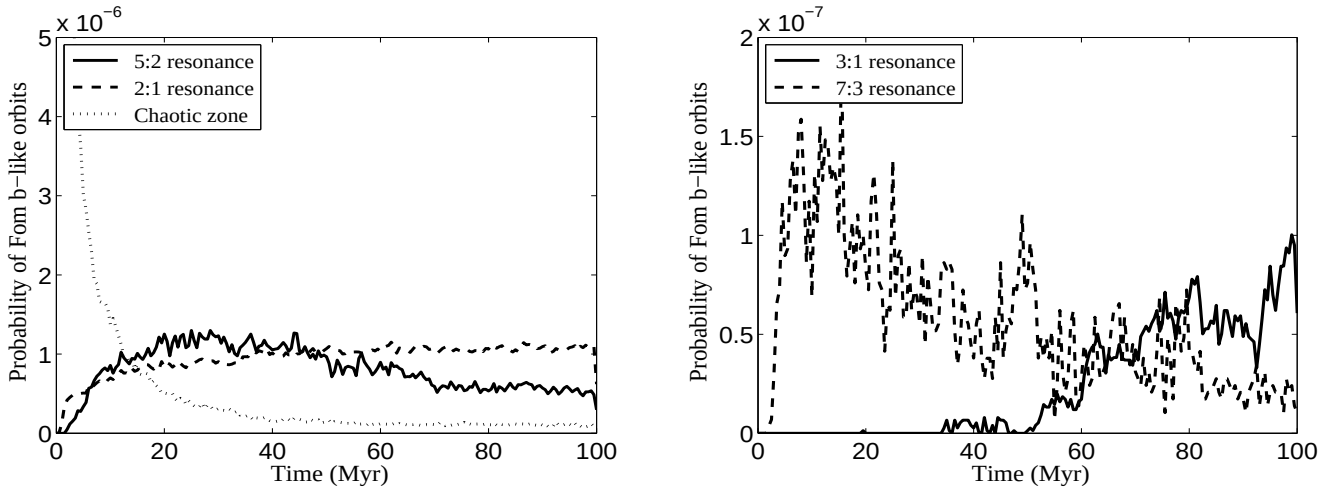

Fig. 6. Probability to be set on a Fom b-like orbit with a lifetime greater than 10 Myr and with an orientation comparable to that of Fom b as a function of the time and the origin of the test-particles.

4. Discussion

In this section, we further investigate the influence of the orbital eccentricity and mass of Fom c. We focus especially on the 2:1 and 5:2 MMRs, which, as we have seen in the previous section, seem so far to be the best routes to have led Fom b on its current orbit in our scenario. We also investigate further the process that generates Fom b-like orbits and the tendency for those to be apsidally aligned with the putative Fom c and the outer belt in a very general manner.

4.1. Eccentricity of Fom c

The initial eccentricity of Fom c is a crucial paramater. Indeed, the trajectories offered in the phase-space to test-particles in resonance are very sensitive to the eccentricity of the perturber that creates these resonances. An orbital eccentricity as small as 0.1 for Fom c is actually necessary to produce Fom b-like orbits because particles are allowed in this case to reach the eccentricities necessary for them to cross the close encounter zone of Fom c. This can be seen on Fig. 7. Another simulation (not shown here) studying the 5:2 resonance with a Fom c on an orbit with eccentricity 0.05 revealed as expected that the number of particles set on a Fom b-like orbit decreases dramatically. Only ∼ 0.5% of the particles of the run were indeed set on such an orbit. Moreover,

the time spent by these on a Fom b-like orbit did not even exceed 10 Myr, with an average of ~ 0.3 Myr. Another run with a Fom c on a circular orbit did not produce any Fom b-like orbit, as expected. Therefore, Fom b-like orbits can be considered a natural consequence of Fom c having an eccentricity of 0.1. Note that is is fully compatible with the measured eccentricity of the dust belt. If we believe that Fom c controls the dynamics of the dust belt, then secular (pericenter glow) theory (Wyatt 2005) shows that the disk is expected to achieve a bulk eccentricity comparable to that of the perturbing planet.

4.2. Mass of Fom c

The mass of Fom c is also a crucial parameter, which controls the ability of a given MMR to produce Fom b-like orbits by varying the size of the chaotic zone, but also very importantly, controls dynamical timescales, that is, the delay induced by a given MMR in the production of Fom b-like orbits and the survival timescale of Fom b-like orbits.

Since the Hill radius and thus the width of the chaotic zone increases with the mass of Fom c ($\propto m_c^{1/3}$), for a same planetary semi-major axis, a less massive Fom c is expected to generate a thinner chaotic zone that small bodies in MMR will be then less probable to cross. Therefore, one should expect less Fom b-like orbits to be generated with less massive Fom c. This can be shown by examining the minimum eccentricity needed for a test-particle in MMR to reach the chaotic zone of Fom c, because it depends only on the mass of Fom c for each MMR. Indeed, if we assume that the inner boundary of the chaotic zone of Fom c is $a_{in} = a_c - 3R_H$, then Eq. (3) gives:

$$a_{\rm in} = a_{\rm c}\left[1 - 3\left(\frac{m_{\rm c}}{3M_\star}\right)^{1/3}\right] \quad . \tag{4}$$

A particle will cross the chaotic zone as soon as it apoastron reaches the inner boundary of the chaotic zone. The apoastron Q of a test-particle in MMR reads:

$$Q = a_{\rm MMR}(1+e) \quad , \tag{5}$$

where e is the eccentricity of the test-particle and $a_{\rm MMR}$ is the semi-major axis of the resonance. If we assume the particle to be trapped in a $p+q:p$ MMR (p and q integers) with Fom c, then we have:

$$a_{\rm MMR} = a_{\rm c}\left(\frac{p}{p+q}\right)^{2/3} \quad . \tag{6}$$

Consequently, the particle crosses the choatic zone only if $e \geq e_{\rm min}$, where $e_{\rm min}$ reads

$$e_{\rm min} = \left[1 - 3\left(\frac{m_{\rm c}}{3M_\star}\right)^{1/3}\right]\left(\frac{p}{p+q}\right)^{-2/3} - 1 \quad . \tag{7}$$

From Eq. (7) we can see that a less massive Fom c will require MMRs to make test-particles acquire higher eccentricities to reach the chaotic zone of Fom c, and thus to enable the production of Fom b-like orbits. MMRs are therefore expected to become less efficient at producing Fom b-like orbits with decreasing mass of Fom c. We illustrate this aspect on Fig. 8, where we show phase-diagram of the 5:2 and 2:1 MMRs for different masses of Fom c. In the case of the 5:2 MMR, the mass of Fom c can decrease as low as 0.1 $M_{\rm Jup}$ (Saturn-sized) and Fom b-like orbits are still expected to be produced, although at a lower rate. On the other hand, one can see that as soon as the mass of Fom c decreases to 1 $M_{\rm Jup}$, the 2:1 MMR is not expected to be efficient any longer to produce Fom b-like orbits.

Therefore, additional simulations were run for these two MMRs, identical to Run F, with lower masses for Fom c (see Table 5).

Table 5. Characteristics of initial sets of particles used to study the 5:2 and 2:1 MMRs. Fom c itself is assumed to be orbiting Fomalhaut with semi-major axis $a_c = 107.8$ AU and eccentricity $e_c = 0.1$. Our sets of particles are made of 100,000 ring-like belts particles extending radially between boundaries given below, eccentricities randomly chosen between 0 and 0.05, and inclinations between 0 and 3° relative to Fom c's orbital plane.

Run #	Dynamical status relative to Fom c	Semi-major axis extent (AU)	Theoretical resonance location (AU)	m_c ($M_{\rm Jup}$)
F1	5:2 MMR	56.0–61.1	58.5	1.0
F2				0.5
F3				0.25
F4				0.1
H1	2:1 MMR	65.4–70.4	67.9	1.0
H2				0.5

Interestingly, the occurrence of Fom b-like orbits is delayed by $\sim$ 30 Myr in both MMRs with a 1 $M_{\rm Jup}$ Fom c. This reflects the fact that a less massive Fom c increases dynamical timescales, and in particular, the timescale necessary for the test-particles to reach a sufficient eccentricity to cross the chaotic zone, and be scattered. We summarize in Table 6 the proportion of the 100,000 test-particles of our initial sample set at least once on a Fom b-like orbit, and the probabilities that characterise the production of Fom b-like orbits.

Table 6. For each individual run that produced Fom b-like orbits, probability $P_{\rm Fomb}$ for being set on a Fom b-like orbit, that is, the proportion of the 100,000 test-particles of our initial sample set at least once on a Fom b-like orbit, average time $\bar{t}_{\rm Fomb}$ spent by these test-particles in this configuration, probability $P_{>10\,\rm Myr}$ for a Fom b-like orbit to have a lifetime greater than 10 Myr and probability $P_{\rm orient}$ for a Fom b-like orbit to have an orientation comparable to that of Fom b. We indicate as well any delay in the generation of Fom b-like orbits.

MMR	m_c ($M_{\rm Jup}$)	$P_{\rm Fomb}$ (%)	$\bar{t}_{\rm Fomb}$ (%)	$P_{>10\,\rm Myr}$ (%)	$P_{\rm orient}$ (Myr)	Delay
	3	20.1	1.6	3.5	15.2	~ 1
2:1	1	1.1×10^{-1}	1.4	1.8	41.9	~ 30
	0.5	0	-	-	-	-
	3	3.8	1.2	2.4	17.6	~ 2
5:2	1	6.3×10^{-2}	0.9	0	38.7	$\sim$ 30–40
	0.5	0	-	-	-	
	0.1	0	-	-	-	

For both MMRs, the proportion of particles set on a Fom b-like orbits is sharply decreasing with the mass of Fom c and is almost zero with 1 $M_{\rm Jup}$. The time spent in average by a test-particle on its Fom b-like orbit is very short $\sim$ 1 Myr. In addition, the Fom b-like orbits produced via the 5:2 MMR when m_c = 1 $M_{\rm Jup}$ are highly unstable (none of them survived longer than 10 Myr). However, since the production of Fom b-like orbits is delayed, test-particles may be set on a Fom b-like orbit later than

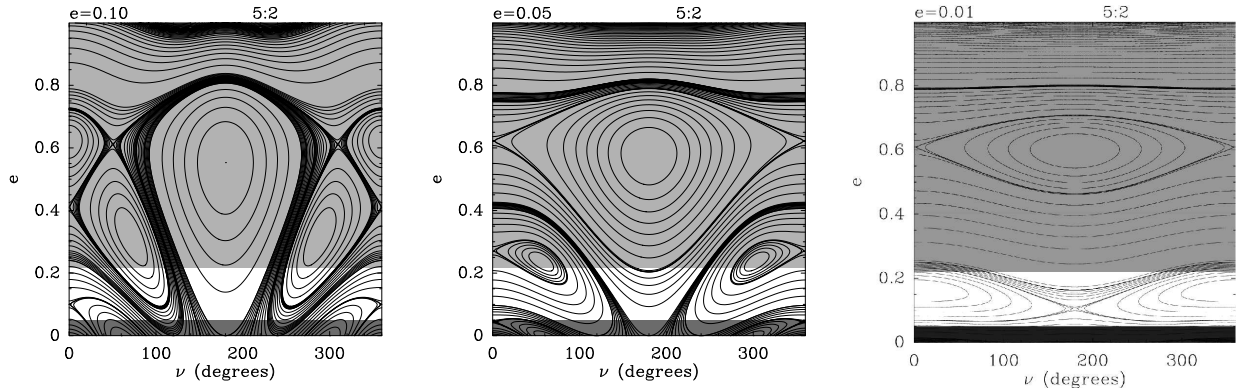

Fig. 7. Phase diagram for the 5:2 MMR, with Fom c of eccentricity 0.1, 0.05, and 0.01, from left to right, respectively. Our initial conditions are figured in dark grey and the chaotic zone of Fom c in light grey. The chaotic zone of Fom c is considered to extend from $3.5R_H$ inner to the periastron of Fom c, to $3.5R_H$ outer to the apastron of Fom c. Particles which start on a trajectory allowing it to cross the chaotic zone may then be scattered and set on a Fom b-like orbit.

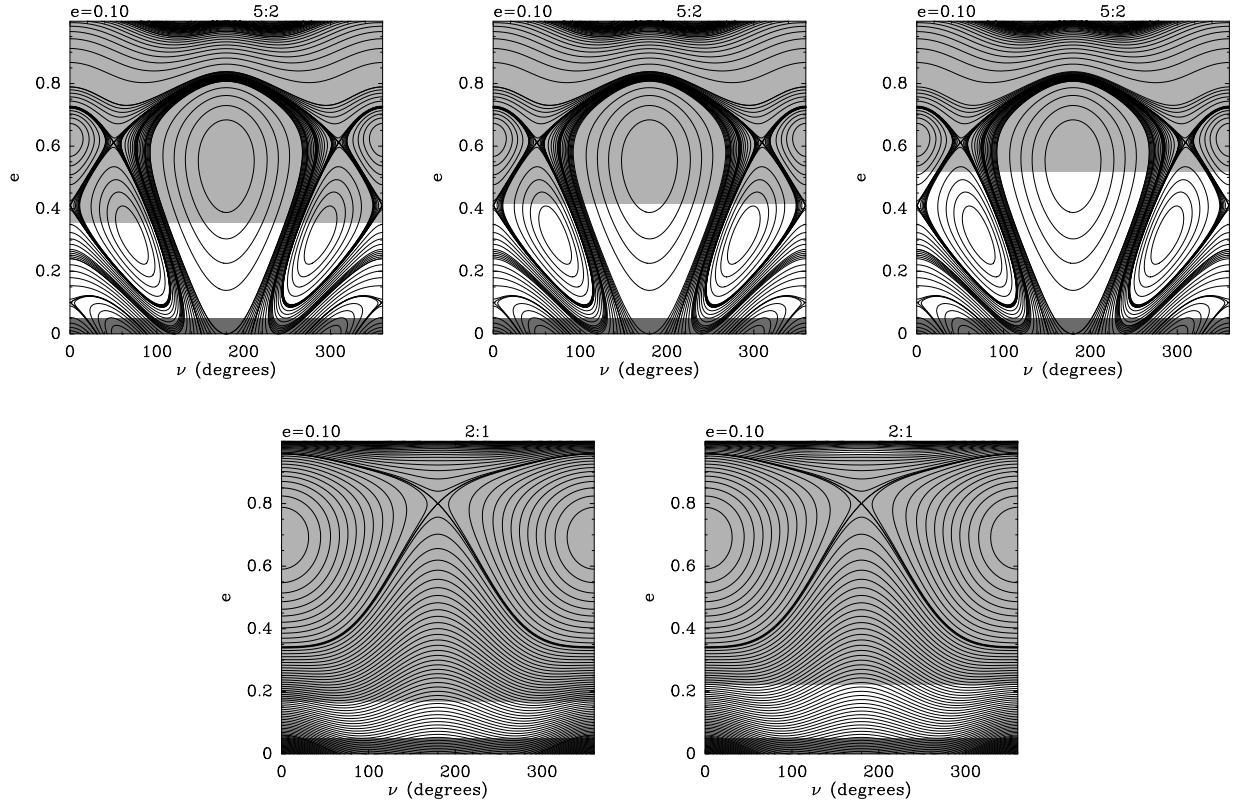

Fig. 8. *Top:* Phase diagrams for the 5:2 MMR, with Fom c of mass 1, 0.5, and 0.1 M_{Jup}, from left to right. *Top:* Phase diagrams for the 2:1 MMR, with Fom c of mass 1, and 0.5 M_{Jup}, from left to right. Our initial conditions are figured in dark grey and the chaotic zone of Fom c in light grey. The chaotic zone of Fom c is considered to extend from $3.5R_H$ inner to the periastron of Fom c, to $3.5R_H$ outer to the apastron of Fom c. Particles which start on a trajectory allowing it to cross the chaotic zone may then be scattered and set on a Fom b-like orbit.

the 100 Myr of the run, and test-particles on a Fom b-like orbit at the end of the run may survive longer in this configuration. Therefore, these quantities are to be considered with caution and as lower limits.

No test-particle was set on a Fom b-like orbit for masses below $1\,M_{Jup}$, which was clearly expected in the case of the 2:1 MMR, but not in the case of the 5:2, for which particles are still expected to be able to cross the chaotic zone and Fom b-like orbits to be produced. Again, this feature may be due to the fact that the delay in the production of Fom b-like orbits is expected to increase when the mass of Fom c decreases. In other words, these orbits may start being produced after the 100 Myr of the run when $m_c = 0.5\,M_{Jup}$. Therefore, we run again the simulations F1–F4 and extend the runs over 500 Myr in order to test this hypothesis.

In the case where $m_c = 1\,M_{Jup}$, the proportion of test-particles set on a Fom b-like orbit increases actually up to 1% over 500 Myr. As we were expecting, Fom b-like orbits can be produced via the 5:2 MMR when $m_c = 0.25$–$0.5\,M_{Jup}$, and their

production is very interestingly delayed on timescales comparable to the age of the system (see Table 6).

For $m_c = 0.5 - 1\,M_{Jup}$, the time spent in average by a test-particle in a Fom b-like orbit configuration has increased up to ~ 6 Myr. This time is smaller for $m_c = 0.25\,M_{Jup}$, however, as mentionned, Fom b-like orbits started to be produced very late.

Table 7. Case of the 5:2 MMR with 0.1–0.5–1 M_{Jup}. For each individual run that produced Fom b-like orbits, probability P_{Fomb} for being set on a Fom b-like orbit, that is, the proportion of the 100,000 test-particles of our initial sample set at least once on a Fom b-like orbit, average time $\bar{t}_{Fomb}$ spent by these test-particles in this configuration, probability $P_{>10\,Myr}$ for a Fom b-like orbit to have a lifetime greater than 10 Myr and probability P_{orient} for a Fom b-like orbit to have an orientation comparable to that of Fom b. We indicate as well any delay in the generation of Fom b-like orbits.

m_c (M_{Jup})	P_{Fomb} (%)	$\bar{t}_{Fomb}$ (Myr)	$P_{>10\,Myr}$ (%)	P_{orient} (%)	Delay (Myr)
1	1.2	5.7	10.1	14.2	$\sim$ 30–40
0.5	0.16	6.4	7.5	20.2	$\sim$ 100–150
0.25	1.6×10^{-2}	3.5	12.5	49.2	$\sim$ 350
0.1	0	-	-	-	-

Note that while varying the mass of Fom c in our simulations, we kept the same semi-major axis value, although the constraint for Fom c to shape the inner edge of the outer belt at 133 AU involves that this semi-major should increase with decreasing mass of Fom c. However, as we have seen, the capacity of a perturber to bring test-particles in its chaotic zone via MMR does not depend on the semi-major axis of the perturber, and therefore, our results would still be valid if we applied the constraint mentionned above. The only effect that a greater semi-major axis would have is to increase the dynamical timescales, and thus, our results are all the more valid.

The production of Fom b-like orbits via the 2:1 MMR is extremely sensitive to the mass of Fom c and it appears not to be the most probable origin of Fom b in our scenario. The best candidate is therefore the 5:2 MMR, which is much less sensitive to the mass of Fom c in its production of Fom b-like orbits, and therefore a more robust route for Fom b to have been set on its current orbit. Moreover, this mechanism as produced by a 0.25–0.5 M_{Jup} Fom c can delay the apparition of Fom b-like orbits on timescales comparable to the age of the system, while increasing their lifetime. A lower mass limit of 0.1 M_{Jup} on the belt-shaping Fom c can be set. These timescales are more in accordance with our witnessing of the orbit of Fom b. Moreover, a 0.25–0.5 M_{Jup} Fom c would allow Fom b not to be ejected too quickly from its present-day orbit, as underlined by Beust et al. (2014). Finally, a $0.25 - 0.5\,M_{Jup}$ Fom c is completely in accordance with the shaping the outer belt into the observed eccentric ring, as shown by Quillen (2006).

4.3. Preferential apsidal orientation

A notable feature of our results is that the Fom b-like orbits formed tend to be apsidally aligned with the orbit of Fom c in a very general manner, even when these originated directly from the chaotic zone of Fom c, where they were expected to suffer random encounters and thus be put on randomly apsidally aligned Fom b-like orbits. This hints at the fact that the whole dynamical process of production of Fom b-like orbits is more complex than previously thought. We have so far proposed a two-steps scenario, where a test particle firstly reaches the chaotic zone of Fom c on timescales comparable to the age of the system via a MMR mechanism with Fom c, and where this test-particle secondly suffers a close-encounters with Fom c.

However, a closer study of the whole dynamical behaviour of a test-particle along the two-steps process that we have proposed, and in particular an exam of the orbits resulting from close-encounters with Fom c, shows that an additional third step involving secular interactions with Fom c is not only required, but also explain the tendency for apsidal alignement.

4.3.1. Close-encounters with Fom c

Close-encounters can be investigated analytically in a very simple manner considering the Tisserand parameter C_T of a test particle. If we assume here coplanarity between Fom c and the test-particle, this quantity reads

$$C_T = \frac{a_c}{a} + 2\sqrt{\frac{a}{a_c}}\sqrt{1-e^2} \quad , \tag{8}$$

where a_c is the semi-major axis of Fom c, and where a and e are the semi-major axis and eccentricity of the test-particle.

Tisserand parameter is closely related to the Jacobi invariant which is a conserved quantity in the framework of the circular restricted 3-body system, even after close encounters. Here the perturber (Fom c) has moderate but non-zero eccentricity. Strictly speaking, C_T is thus not conserved, but detailed studies focusing on Jupiter perturbed comets showed that in most cases, C_T remained preserved within $\sim 1\,\%$ despite the eccentricity of Jupiter (Carusi et al. 1995). Here the assumed eccentricity (0.1) is only twice that of Jupiter, so that we expect C_T to be perserved within a few percents in close encounters. This accuracy is sufficient for our analysis.

Consider a particle initially locked in a MMR with Fom c, having a neary constant semi-major axis a_{MMR} and a growing eccentricity. Assume it has reached eccentricity e when crossing the chaotic zone. Then it suffers one or many close encounter episodes with Fom c. Afterwards, its semi-major axis a and eccentricity e' are related to a_{MMR} and e by the conservation of the Tisserand parameter:

$$\frac{a_c}{a_{MMR}} + 2\sqrt{\frac{a_{MMR}}{a_c}}\sqrt{1-e^2} = \frac{a_c}{a'} + 2\sqrt{\frac{a'}{a_c}}\sqrt{1-e'^2} \quad . \tag{9}$$

Depending on the resonance considered, there are constraints on a_{MMR} and e for the orbit to be able to cross the chaotic zone. For instance, in the case of the 5:2 MMR with a $3\,M_{Jup}$ Fom c, we must have $0.2 \lesssim e \lesssim 0.8$. This naturally translates to constraints on a' and e' via Eq.(9). Note that these constraints depend on the mass of Fom c, since this parameter controls the width of the chaotic zone and thus the values of eccentricities allowed to the test-particles.

Constraints on a' can also be derived via our definition of a Fom b-like orbit, namely $81, AU \leq a' \leq 415$ AU. Once this constraints are incorporated into Eq. 9, this leads to constraints on the eccentricity e' that the test-particle can have after the close-encounter and when having a semi-major axis compatible with the definition of a Fom b-like orbit:

$$e' = \left[1 - \frac{1}{4}\left(C_T - \frac{a_c}{a'}\right)^2 \frac{a_c}{a'}\right]^{1/2} \quad . \tag{10}$$

This resulting possible eccentricities after a close-encounter are displayed in Fig. 9 for the 5:2 MMR and for the chaotic zone.

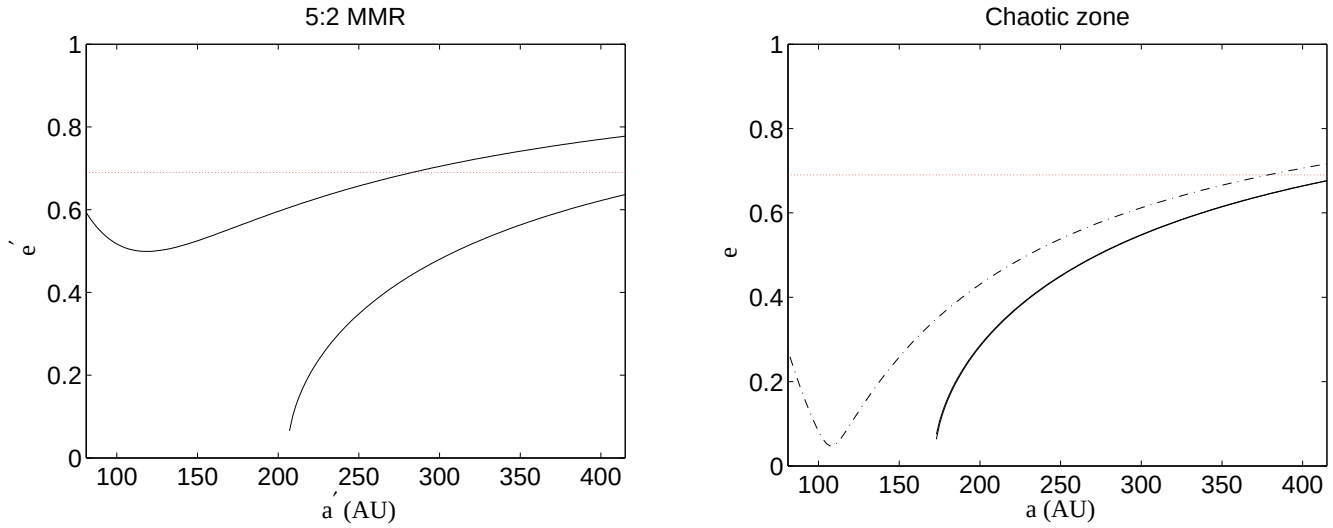

Fig. 9. Theoretical eccentricities e' adopted by test-particles after a close-encounter with Fom c which has set them on an orbit with semi-major axis compatible with the orbit of Fom b. On the left panel, the 5:2 MMR will constrain the semi-major axis to $a_{\rm MMR}$ and will allow a test-particle to cross the chaotic zone of Fom c for values of eccentricity e between 0.2 and 0.8, hence the configurations (a', e') allowed to a particle after its encounter with Fom c are comprised between two curves. On the right panel, close-encounters occur in the chaotic zone of Fom c, with initially low-eccentricity particles ($0 < e < 0.05$), but here the semi-major axis can span values from the inner edge of the chaotic zone to the semi-major axis of Fom c. Therefore, there is a total of four curves on this plot, two curves for each boundary value in semi-major axis, but due to the small span in eccentricity, these are very close and appear as a single one. The horizontal red dotted line figures the minimum eccentricity required for an orbit to be compatible with this of Fom b.

In the chaotic zone case, the limits on e are simply the limits set by our initial conditions on the eccentricity of the test-particles, that is, $e \leq 0.05$.

Figure 9 reveals that the eccentricity after the scattering event(s) rarely exceeds ~ 0.6–0.7, whereas the minimum eccentricity required for the orbit to be fully qualified of Fom b-like is 0.69. It thus seems that directly generating Fom b like orbits from (even multiple) close encounters is difficult. But, as we detail it below, secular evolution after the close encounter episode can help moving to higher eccentricies and also provide explanation for the apsidal alignment with Fom c.

4.3.2. Further secular evolution with Fom c

Particles initially locked in a MMR with Fom c, and that have undergone a close encounter episode keep being perturbed in a secular manner with Fom c even after the last encounter. This behaviour can be investigated semi-analytically in a similar way as we did in the resonant case in Sect. 2 (Fig. 2). Now, as the particle is no longer locked in a MMR with Fom c, it secular motion can be described performing a double average of the interaction Hamiltonian over both orbits (see background theory in Beust et al. 2014). This is illustrated in Fig. 10, which shows a phase diagram of this secular Hamiltonian for a particle having $a'/a_{\rm c} = 1.2$, assuming coplanarity of both orbits and $e_{\rm c} = 0.1$. Following Fig. 9, let us assume that after the close encounter episode, the particle appears in this diagram at $e' \simeq 0.7$. Then is further secular evolution can be readily seen of Fig. 10 following the Hamiltonian level curve it appears on. It actually depends on the starting value of ν. If the particle stars at $\nu \simeq 0$, the secular evolution will cause its eccentricity to first decrase and in any case never overcome the starting eccentricity. This particle will never reach a Fom b-like orbit. Conversely, a particle starting at $\nu \simeq 180°$ will undergo a secular eccentricity increase that will drive it above $e' = 0.8$ near $\nu = 0$. At this point the particle has now reached a Fom b-like configuration.

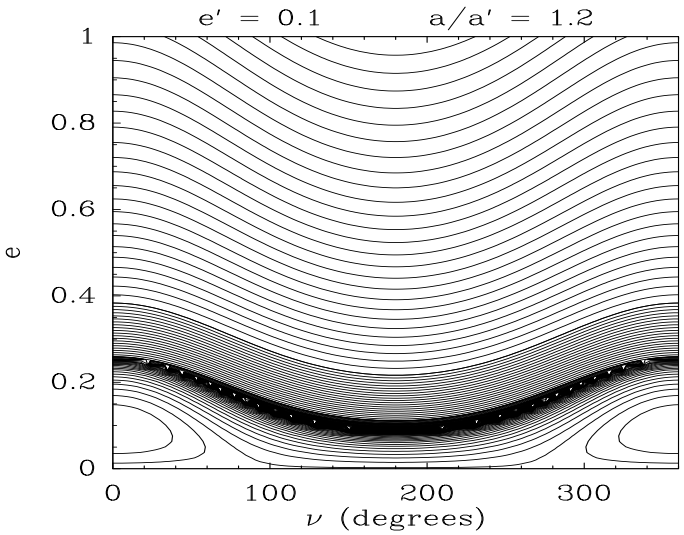

Fig. 10. Example of secular evolution of a test-particle under the dynamical influence of Fom c, for a typical semi-major axis ratio of $a/a_{\rm c} = 1.2$.

But $\nu \simeq 0$ exactly means apsidal alignment. The key point here is that in the level curves of Fig. 10, the maximum eccentricity is reached at $\nu = 0$. This description is actually a high eccentricity equivalent to the analytical pericenter glow theory described by Wyatt (2005). According to this scenario, low eccentricity particles perturbed by a low eccentricity planet undergo a secular eccentricity evolution where the maximum eccentricity is reached together with apsidal alignment (see Wyatt 2005 and Beust 2014 for details). This configuration corresponds indeed to the bottom curves of Fig. 10. Here our Fom b progenitors move at large eccentricity on the upper curves of Fig. 10, so that a full analytical formulation of the motion is not possible. But the qualitative result remains: the maximum eccentricity is reached for $\nu = 0$.

So, our three steps scenario is now the following: Particles trapped in MMRs with Fom c first undergo a resonant eccentricity increase at ∼constant semi-major axis up to a point they cross the chaotic zone. Then in a second phase they have one or several close encounters with Fom c that extract them from the MMR and drastically change their semi-major axes, bringing them to a a' value compatible with Fom b-like orbits and to $e' \simeq 0.7$. In the third phase, they keep being secularly perturbed by Fom c at constant a', while their eccentricities fluctuate. The particles starting the third phase close to $\nu \simeq 0$ keep evolving below $e' \simeq 0.7$ and never reach a Fom b-like state. But hose appearing at $\nu \simeq 180^\circ$ undergo a further eccentricity evolution above $e' \simeq 0.7$ that drives them to Fom b-like orbits when $\nu = 0$ is reached. We claim that Fom b could be one of these particles, initially originating from an inner MMR (typically the 5:2 one which is among the most efficient ones), and now having reached $e' \gtrsim 0.8$ and apsidal alignment (i.e., $\nu \simeq 0$) with Fom c.

Figure 11 exactly illustrates this three steps scenario. It shows the semi-major axis, eccentricity and longitude or periastron secular evolution of one particle extracted from our simulation, initially trapped in 5:2 MMR with Fom c. Up to ~ 1.8 Myr the particle remains in the resonce while its eccentricity increases. Then it enters a chaotic phase characterized by encounters with Fom c. After ~ 2.2 Myrs, there are no more encounters, but the particle keeps being secularly perturbed by Fom c. Starting this third phase at $e' \simeq 0.6$ and $\nu \simeq 180^\circ$, it evolves towards larger eccentricities and $\nu = 0$. After ~ 3 Myrs it has reached a Fom b-like state.

5. Conclusion

The scattering events generating orbits fully comparable to the orbit of Fom b, either in terms of semi-major axis and eccentricity, but also in near-coplanarity and apsidal alignement with the belt-shaping putative Fom c, is a very robust mechanism when generated by a perturber with an eccentricity 0.1, whether these orbits are primarily due to a scattering events, or secondarily, via a MMR. However, MMRs are the most probable route for Fom b to have been set on its current orbit in our scenario. Indeed, primary scattering events scatter the material out of the system on timescales much shorter than the age of the system, while MMRs tend to delay the production of Fom b-like orbits, potentially on timescales comparable to the age of the Fomalhaut system. This delay increases with decreasing mass of Fom c, and so does the average lifetime of Fom b-like orbits. However, the ability of a MMR to bring test-particles in the chaotic zone of Fom c, and thus the efficiency of a MMR to produce Fom b-like orbits, decreases with decreasing mass of Fom c. Therefore, the mass of Fom c should be sufficient for a given MMR to produce Fom b-like orbits, but should not exceed a given value in order for the production of Fom b-like orbits to be delayed by timescales compatible with its detection at the age of the system. The MMR which realises this compromise the best is the 5:2 MMR. New constraints on the mass of the unseen Fom c in our scenario are $m_c = 0.25{-}0.5\,M_{Jup}$. These constraints are compatible with the witnessing of a transient planetary system configuration where the orbits of Fom b and Fom c cross each other that is sufficiently stable to be witnessed (Beust et al. 2014), and observational constraints. Finally, it is also crucial that MMRs are generated by a perturber with an eccentricity ~ 0.1 such as this of Fom c in order to produce Fom b-like orbits. These constraints are fully compatible with the shaping of the outer belt (Quillen 2006). Considering that it would have been difficult to form Fom b from resonant material, since eccentricities and thus relative velocities of solids are increased, which thus challenges their accretion, it is most probable that there were migration processes in this system. Fom b and/or Fom c are very likely to have migrated in order for Fom b to find itself at a MMR location. An outward migration process has been put forward to explain the presence of the belt-shaping planet at a distance of the order of 100 AU from its host star by Crida et al. (2009). This mechanism implies migration of a pair of planets in MMR: if the inner planet is more massive than the outer one, both planets can migrate outwards in a common gap in the original gaseous protoplanetary disk. However, the eccentricity of these planets are excited by their MMR configuration, but also damped by the gaseous disk (Crida et al. 2008). In Crida et al. (2009), this resulted into planets with orbital eccentricities too moderate ($\sim 0.02 - 0.03$) to be compatible with that of the belt-shaping planet. Planetesimal-driven migration at later stages of the system evolutions, when gas has dissipated, could both explain the outward migration of the belt-shaping planet and its orbital eccentricity, since the abscence of gas prevents orbital eccentricities to be damped during this migration process. However, as for the early migration scenario, this would involve the presence of another massive body inner to the belt shaping planet, which questions the compatibility of our scenario with an additional putative Fom d.

Finally, a significant and broad population of small bodies were set on highly eccentric orbits via MMRs in our scenario. As the eccentricity of a resonant test-particles increases while its semi-major axis suffers only small relative variations, its periastron will obviously decrease. This means that if a population of small bodies was residing in the vicinity of Fom c, Fom b, or simply in MMR, a significant amount of this material has spent some time in the inner parts of the system, and this might be linked with the presence of two inner dust belts in the Fomalhaut system, a hot, very close, at $\sim 0.1 - 0.3$ AU, and another, warm at about 2 AU (Lebreton et al. 2013). This will be the subject of a forthcoming paper (Faramaz et al. in prep).

Far from being paradoxal, the configuration of the Fomalhaut system is in fact logical, that is, if there are clues for a perturber on a 0.1 eccentric orbit in a system, bodies on Fom b-like orbits should be expected to be present in the system, in a continuous way as long as material is available either in the chaotic zone or at MMR locations, and also once a given MMR starts producing Fom b-like orbits, which can be delayed very late in the life of a system. This suggests that warm and hot inner dusty belts potentially resulting from this process may start to be produced very late in the history of a system. In the same manner that it might explain the presence of inner dust belts in the Fomalhaut system, this may also give a solution to the yet unexplained detection of numerous hot belts in systems older than 100 Myr, and which contain levels of dust surprisingly large at such ages (Absil et al. 2013; Ertel et al. 2014, 12 to 30% of stars). Bonsor et al. (2012) and Bonsor et al. (2014) have respectively investigated whether scattering of planetesimals by a chain of planets or subsequent to planetary migration, as possible mechanisms to explain the presence of such hot belts over several 100 Myr. The three-step process revealed in this paper involves one should not necessarily assume that hot belts in systems older than 100 Myr have been sustained over the system's age, and suggest that some of these hot belts may be related to the presence of a massive and slightly eccentric planet in the system.

Aknowledgements:

The authors acknowledge the support of the ANR-2010 BLAN-0505-01 (EXOZODI). Computations presented in this paper

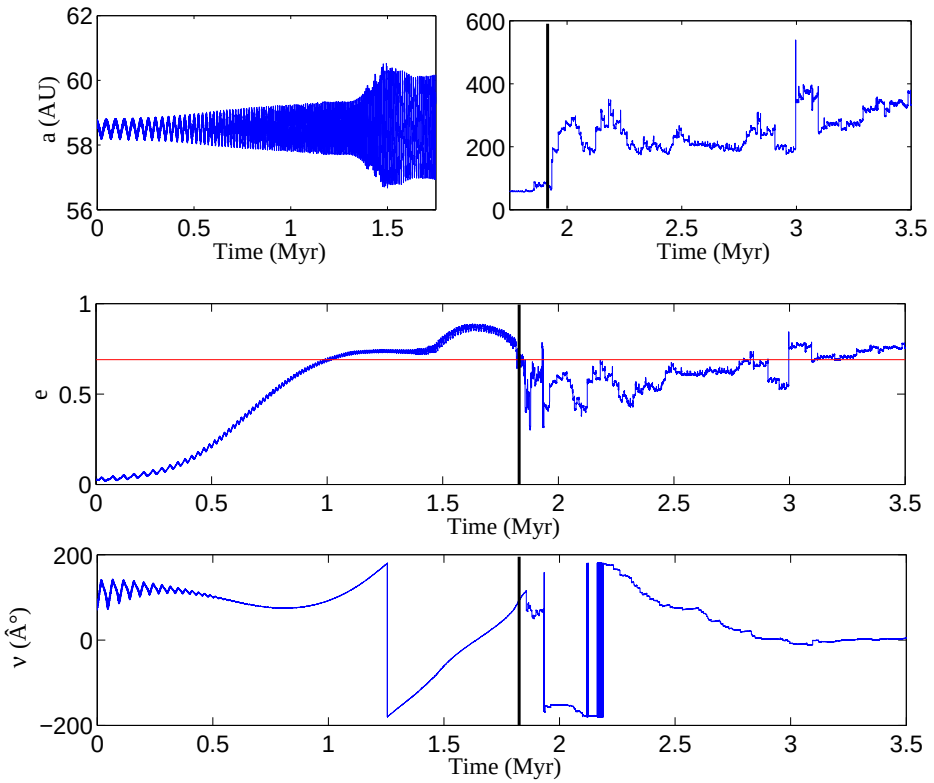

Fig. 11. Example evolution of the semi-major axis, eccentricity and longitude of periastron of a test-particle set on a Fom b-like orbit via the 5:2 MMR route, from top to bottom, respectively. The semi-major axis evolution is splitted into the resonant regime, on left, and the secular regime, on right. During its resonant evolution, the test-particle endures only small variations of its semi-major axis, while its eccentricity increases. Its suffers a close encounter with Fom c at high eccentricity because its orbits crosses the chaotic zone of Fom c. After the close encounters, its semi-major axis is compatible with that of Fom b. However, its eccentricity is not, as is figured by the horizontal red line which indicates the minimum eccentricity required for an orbit to be compatible with that of Fom b. The eccentricity gradually increases due to secular evolution and finally reaches Fom b compatible values at ~ 3 Myr. As can be seen on the bottom-panel, this evolution of the eccentricity is accompanied by an evolution of the longitude of periastron, which tends to zero, and thus, to an apsidal alignement of the orbit with this of Fom c.

were performed at the Service Commun de Calcul Intensif de l'Observatoire de Grenoble (SCCI) on the super-computer funded by the Agence Nationale pour la Recherche under contracts ANR-07-BLAN-0221, ANR-2010-JCJC-0504-01 and ANR-2010-JCJC-0501-01.

References

Absil, O., Defrère, D., Coudé du Foresto, V., et al. 2013, A&A, 555, A104
Beust, H., Augereau, J.-C., Bonsor, A., et al. 2014, A&A, 561, A43
Beust, H. & Morbidelli, A. 1996, Icarus, 120, 358
Beust, H. & Morbidelli, A. 2000, Icarus, 143, 170
Bonsor, A., Augereau, J.-C., & Thébault, P. 2012, A&A, 548, A104
Bonsor, A., Raymond, S. N., Augereau, J.-C., & Ormel, C. W. 2014, ArXiv e-prints
Carusi, A., Kresák, Ľ., & Valsecchi, G. B. 1995, Earth Moon and Planets, 68, 71
Chiang, E., Kite, E., Kalas, P., Graham, J. R., & Clampin, M. 2009, ApJ, 693, 734
Crida, A., Masset, F., & Morbidelli, A. 2009, ApJ, 705, L148
Crida, A., Sándor, Z., & Kley, W. 2008, A&A, 483, 325
Currie, T., Cloutier, R., Debes, J. H., Kenyon, S. J., & Kaisler, D. 2013, ApJ, 777, L6
Deller, A. T. & Maddison, S. T. 2005, ApJ, 625, 398
Duncan, M., Quinn, T., & Tremaine, S. 1989, Icarus, 82, 402
Ertel, S., Augereau, J.-C., Thébault, P., et al. 2014, in IAU Symposium, Vol. 299, IAU Symposium, ed. M. Booth, B. C. Matthews, & J. R. Graham, 338–339
Galicher, R., Marois, C., Zuckerman, B., & Macintosh, B. 2013, ApJ, 769, 42
Graham, J. R., Fitzgerald, M. P., Kalas, P., & Clampin, M. 2013, in American Astronomical Society Meeting Abstracts, Vol. 221, American Astronomical Society Meeting Abstracts, 324.03
Ida, S., Bryden, G., Lin, D. N. C., & Tanaka, H. 2000, ApJ, 534, 428
Janson, M., Carson, J. C., Lafrenière, D., et al. 2012, ApJ, 747, 116
Kalas, P., Graham, J. R., Chiang, E., et al. 2008, Science, 322, 1345
Kalas, P., Graham, J. R., & Clampin, M. 2005, Nature, 435, 1067
Kennedy, G. M. & Wyatt, M. C. 2011, MNRAS, 412, 2137
Kenyon, S. J., Currie, T., & Bromley, B. C. 2014, ApJ, 786, 70
Kirsh, D. R., Duncan, M., Brasser, R., & Levison, H. F. 2009, Icarus, 199, 197
Lebreton, J., van Lieshout, R., Augereau, J.-C., et al. 2013, A&A, 555, A146
Levison, H. F. & Duncan, M. J. 1994, Icarus, 108, 18
Mamajek, E. E. 2012, ApJ, 754, L20
Marengo, M., Stapelfeldt, K., Werner, M. W., et al. 2009, ApJ, 700, 1647
Morbidelli, A. & Moons, M. 1995, Icarus, 115, 60
Quillen, A. C. 2006, MNRAS, 372, L14
Rodigas, T. J., Malhotra, R., & Hinz, P. M. 2013, ArXiv e-prints
Tamayo, D. 2014, MNRAS, 438, 3577
van Leeuwen, F., ed. 2007, Astrophysics and Space Science Library, Vol. 350, Hipparcos, the New Reduction of the Raw Data
Wisdom, J. 1980, AJ, 85, 1122
Wisdom, J. 1983, Icarus, 56, 51
Yoshikawa, M. 1989, A&A, 213, 436

Chapter 5

Planetesimal-driven migration in binary systems

Contents

The planetary systems discovered to date exhibit a wide variety of architectures, and our solar system is far from being a generic model. One of the mechanisms that determines the morphology of a planetary system is the planetary migration. It is expected that the presence of a stellar binary companion modifies the conditions of migration, and potentially lead to the formation of different system's architectures. This phenomenon is probably significant, since at least half of stellar systems are binary systems.

One of the goals of this thesis was to explore the impact of a stellar companion on migration processes through N-body codes. It was therefore necessary, in first instance, to determine at once what was the state of the art in this field, what type of study was necessary and achievable mainly through N- body codes. As we shall see, the usual inwards direction of late migration processes such as those expected as a result from interactions between a planet and planetesimals may be reversed to outwards by a circumstellar binary companion.

5.1 Why planetesimal-driven migration?

I will focus here on the essential knowledge of the different migration processes around a single star or as part of a binary system, as well as numerical tools dedicated to their study, and finally conclude on the type of study needed and achievable thanks to N-body codes.

5.1.1 Migration around a single star

The first extrasolar planet discovered around 51 Peg in 1995 was very surprising (Mayor & Queloz 1995), because51 Peg b is a Jupiter-like gas giant planet, which orbits very close to its host star and has in consequence an orbital period which is extremely short (only 4 days). It is seven to eight times closer than Mercury is to the Sun, which was not considered in the previous planetary formation models. Indeed, such a planet is supposed to have a solid core composed of materials that can not condense so close to the star, since the temperature conditions do not allow these materials to be present in solid form there.

Other planets of this type, called "hot" planets, have been discovered since, and the most likely dynamical scenario that explains the presence of these planets where they could not have formed is that these planets formed farther from their star and migrated towards it while of after having formed (Lin et al. 1996). This phenomenom had also been predicted and studied on a smaller scale for a planet-satellite system, and thus the theoretical framework was already established long before the discovery of evidences for planetary migration processes in star-planet systems (Goldreich & Tremaine 1980). As might be expected, the models have known major developments since.

Planetary migration results from exchanges of angular momentum between a planet and the material present with it in the system, that is, a disk of gas and/or solid material. A planet divides the disk inside which it forms in three parts : an inner and an outer region, both separated by the co-orbital zone, where material is stabilised on so-called horseshoe orbits (see Fig. 1 of Kley & Nelson 2012).

Exchanges of angular momentum between a planet and the material contained in the disk occurs when the material endures deviations from its Keplerian trajectory because of the planet [1]. However, it is important to distinguish the material undergoing large deviations, that is, close-encounters, and which can pass from an orbit inner to the planet to an outer orbit (or vice versa), from the material undergoing only small deviations and under secular evolution of the planet.

Indeed, in both cases, weak or strong deviations, angular momentum exchanges between the planet and the material are possible, but the physical processes at work in these two types of exchanges are very different. As we shall see later, these processes are actually antagonists and require separate descriptions. It is obvious that the closer the material is to the planet, the stronger will be the deviations it suffers. The area where large deviations occur, also called close-encounter zone, marks thus the boundary between the coorbital zone and the rest of the disk, which only undergoes small deflections and secular perturbations.

Slow Type I & II migration

If the planet mass is sufficient (very roughly of the order of Mars' Armitage 2010), it creates density waves in the inner and outer parts of the disk, which results from the small deviations generated by the planet. These waves undergo differential Keplerian rotation as they propagate radially, thus appearing under the form of spiral arms (see e.g. Fig.1 in Kley & Nelson 2012). As a response, these density waves exert a gravitational torque on the planet, inducing an exchange of angular momentum between the planet and the disk.

In this case, angular momentum is transferred from inner to outer material and interactions are repulsive. On the one hand, the inner spiral tends to push the planet outwards and make it gain angular momentum, since it exerts a positive torque on it.

[1] See Sect. 2.6

On the other hand, the outer spiral tends to push the planet inwards, making it loose angular momentum while exerting a negative torque on it.

Clearly, torques from the inner and outer parts of the disk tend to cancel out, and as a consequence, the planet effective migration is due to an unbalance between the magnitude of these torques. These magnitudes, and ipso facto the speed and direction of migration, depends delicately on the physical details of the disk (Kley & Nelson 2012). However, the torque exerted by the outer parts of the disk generally predominates, which leads to an inward planetary migration.

In this case, planets migrate in one of slow migration regimes: if the planet is completely embedded in the disk, its migration regime is called Type I, while if it is massive enough to overcome viscous refilling of its neighbourhood, it opens a gap and is said to migrate in the Type II regime. Both Type I and II migration preferentially take place during the protoplanetary phase, that is, during the early phase of planetary systems formation and evolution in massive gaseous disks. This phase typically lasts 10 Myrs, which is the timescale for the disk to devoid itself of its gaseous part.

Fast Type III and Planetesimal-driven migration

Angular momentum exchange with material residing in the vicinity of the co-orbital zone is also possible, but the process involved is completely different. In this region, material suffers close-encounters and may cross the planet orbit. Here, unlike the migration mechanism discussed in the previous section, the interactions are not repulsive, but attractive, and the angular momentum passes on from outer to inner material.

By pulling inner/outer material out/in, the planet looses/gain angular momentum and tend to migrate inwards/outwards. This mechanism is the Type III "fast/rapid/runaway" migration. Like slow migration modes, this type of migration relies on a desequilibrium of angular momentum exchanges between material localised inner or outer to the planet.

As Armitage (2010) points out, the calculation of the torque exerted by co-rotating gaseous material is still subject to a great uncertainty and is a field of active research. This is due to the fact that this torque depends very precisely on the physical state of the disk.

However it is considered a standard phenomenon in a disk of solid particles, where the effect of the co-orbital torque is predominant (Ward 1991; Ida et al. 2000). Indeed, this mechanism is quite well understood in the case of a dynamically cold disk of planetesimals. This is the planetesimal-driven migration mechanism, hereafter PDM, which due to a scattering bias favouring interactions with inner material, tends to make the planets migrate inwards (Kirsh et al. 2009). This mechanism takes place after the protoplanetary phase, when the gas has left the system, and thus rather represents later stages of planetary systems evolution.

5.1.2 Dedicated numerical tools

The goal here being to use N-body codes, I review here the numerical tools typically dedicated to planetary migration, which as we have seen, takes different forms, and some of which will be hardly affordable with the codes that we want to use. Since it involves interaction with solids kilometer-sized planetesimals, the PDM is obviously the aspect of planetary migration most likely to be approached with a N-body code.

For other migration regimes, that is, in gaseous disks, two types of codes are used: hydrodynamical grid-based codes, and SPH (Smooth Particle Hydrodynamics) codes, where the disk is treated as a set of particles whose dynamics includes the effects of viscosity due to their gaseous nature. Migration regimes of Type II and III are extremely sensitive to physical details of the disk and involve very narrow regions of interest near the co-orbital zone and the gap created by the planet, which are therefore low density regions.

Since, the resolution level of a disk is determined by the mesh size of the grid for the hydrodynamic codes, and the density of particles for SPH codes, the use of hydrodynamic codes is widely favoured to study the Type II and III migration, because these codes allow the use of nested meshes with different resolutions for different regions of the disk.

Finally, the Type I migration involving the action of gravitational torques generated by a much wider region of the disk, the study of this migration regime is studied using both types of codes, hydrodynamic and SPH. It would be possible to modify a N-body code to address this type of migration regime, however, as we shall see later, this type of migration has been studied extensively, including in binary systems. However, the effect of a binary companion on the most easily affordable migration regime through N-body codes, the PDM, has been little discussed.

5.1.3 Influence of a stellar binary companion

General effects

With the presence of stellar binary companion, disks are naturally expected not to be as dynamically quiet as if they were in a system with a single star (Zhou et al. 2012).

Similarly to planet opening a gap in a disk when its ability to empty its vicinity is more powerful than its ability to refill the emptied zone, a stellar companion truncates the disk where its gravitational (gap-opening) torques balance its viscous (gap-closing) torques (Kley 2000). In the case the disk is circumprimary, it is typically truncated at one third of the binary's separation, whereas the size of the cavity created in a circumbinary disk is roughly thrice the binary separation. (Artymowicz & Lubow 1994; Holman & Wiegert 1999; Pichardo et al. 2005).

In addition, within the disk remaining after truncation, the effects of a circumstellar binary companion are still being felt. In particular, it causes a relative increase in the speed between the solids, which increases their difficulty to assemble to form planets. Therefore, the favorable planetary formation region in a binary system can be extremely reduced, depending on the distance and the mass ratio between the two stars of the couple (Thébault et al. 2006).

In addition to truncation effects, a binary companion may severely alter a disk structure if for instance, its orbit is misaligned with the disk or if it is eccentric. It can cause the disk to be warped, twisted or even disrupted in the first case (Larwood et al. 1996; Fragner & Nelson 2010) or cause the disk to be eccentric and precess in the second case. These effects are by no mean rare and negligible, since the distibution of binaries orbital eccentricities is broad, with a mean value 0.4-0.5 (Duquennoy & Mayor 1991).

Moreover, when a planet forms inside such disks, it does not only form in a environment which is dynamically disturbed by the binary, but it also endures itself changes in its orbital elements, which may also affect the disk in return. Consequently, planetary systems formation and evolution processes are expected to be much more complicated in binary systems and strongly affected by nonlinear effects, which are difficult to analyse by analytical methods. Thus, as Zhou et al. (2012) points out, studies of these aspects strongly rely on numerical simulations.

Effects on planetary migration

So far, studies of the influence of a stellar companion on planetary migration processes have mainly focused on migration in gaseous disks. The circumbinary case, that is, when the planetary system orbits the two components of the binary system, has been extensively studied by Pierens & Nelson (2008b,a, 2007). Their work showed that low-mass planets tend to migrate inwards toward the couple of stars and interact together, either by merging, deviating themselves or adopting resonant configurations. More massive planets, like Jupiter, rather tend to interact directly with the binary companion and adopt a 4:1 mean-motion resonance with it.

However, the most common case is where the planetary system is orbiting one of the components of the binary star system, studied by Kley & Nelson (2008). Their study shows that protoplanetary cores mainly migrate inwards. However, the closer the core is initially located near the unstable zone created by the binary companion, the greater is the orbital eccentricity it adopts, at such point that only the action of gaseous material, which by friction and braking tends to circularise the orbit, can be considered to explain the stability of a core in these regions. Moreover, the migration rate decreases during phases of high eccentricities, and this study also shows that the orbital eccentricity induced on the core is the result of both the direct effect of the binary companion and of the disturbed disk, which confirms the action of nonlinear effects in binary systems.

Late migration such as PDM also causes inward migration of a planet in a single star system, but concerning this type of migration regime, the influence of a circumstellar binary companion has been little discussed. Moreover, since this type of migration involves interactions of a planet with planetesimals, conducting a study of the impact of a circumstellar binary companion on this late migration process is clearly achievable by the use of N-body codes.

5.2 PDM in single star systems: the theory

First evidences for PDM were found in our own Solar System : for instance, the existence of a population of Kuiper-Belt Objects (KBOs) trapped in 3:2 mean motion resonance with Neptune is best explained by models implying resonance trapping during an outwards migration of Neptune (Malhotra 1993, 1995). The mechanism itself was first studied by Hahn & Malhotra (1999) in the frame of the Solar System, precisely to provide an explanation for Neptune's outwards migration. It was first conceived as a source-sink model, where the presence of a second body, namely Jupiter, is at the origin of the asymmetry of angular momentum exchanges between Neptune and inner or outer material. Indeed, by scattering material inner to Neptune out of the system and giving birth to the Oort cloud, Jupiter reduced the quantity of inner material available for Neptune to interact with. Therefore, Neptune preferentially interacted with outer material, thus migrating outwards. In this model, the presence of a second body is necessary to create an asymmetry of angular momentum exchanges.

The problem was revisited by Kirsh et al. (2009), as Hahn & Malhotra (1999) numerical simulations where showing a tendendy for Neptune to migrate inwards before Jupiter could even create asymmetrical exchanges of angular momentum. The study of Kirsh et al. (2009) combines the setting of a theoretical frame and numerical simulations, showing that single planets around single stars tend to migrate inwards in a planetesimal disk.

PDM is due to interactions with strongly deflected planetesimals in the vicinity of the planet, during which angular momentum passes on from outer to inner material.

As a consequence, the first issue in studying PDM is to be able to determine where is this material, that is, to determine which planetesimals may suffer close-encounters. As seen in Section 2.6, close encounters occur in the planet's chaotic zone, which extends between 1 and $3 - 3.5\,R_H$ around the planet.

Kirsh et al. (2009) chose a more precise definition of the encounter zone, based on a dynamical criterion, by using the Tisserand parameter, defined by Eq. (2.44). Indeed, this quantity increases with the distance to the planet which allows one to define the value of the Tisserand parameter for close encounters $C_{T,\mathrm{enc}}$ with:

$$C_{T,\mathrm{enc}} = C_T(a = a_p + 3.5\,R_H, e = 0, i = 0) \quad , \tag{5.1}$$

where all particles with $C_T < C_{T,\mathrm{enc}}$ and which cannot approach the planet closer than a Hill radius are on orbits crossing the planet encounter zone.

The Tisserand parameter increases with distance to the planet, however, it increases asymmetrically on each side of the planet. Indeed, the close-encounter zone extends farther from the planet in the outer part of the disk, thus leading to think that interactions with outer material will be favoured, and generate an outwards migration of the planet.

However, one must also consider the typical timescale between two successive interactions, called the synodic period T_{syn} and defined by:

$$T_{\mathrm{syn}} = \frac{2\pi}{|\frac{2\pi}{T_p} - \frac{2\pi}{T}|} \quad . \tag{5.2}$$

As for the case of the precession timescale, seen in Chapter 3, the synodic timescale is also a quantity which is highly variable accross the region of interest, here the close-encounter region. In fact, it is so sensitive that T_{syn} are much shorter for material inner to the planet, and it is sufficient to reverse the effects of the natural spatial asymmetry of the co-orbital zone, making in fact interactions with inner material clearly favoured, thus leading to an inwards migration.

As we shall see in the next section, it is not necessary to simulate a planet effective migration to put in evidence the asymmetry favouring interactions with inner material, and thus predict an inwards migration. However, additional simulations of Kirsh et al. (2009) including effective migration of the planet, and therefore the effect of planetesimals on it, confirms the tendency for inwards migration with typical planetesimal surface density profiles, as it has been also found in the simulations of Fernandez & Ip (1984); Hahn & Malhotra (1999); Gomes et al. (2004)

In the next section, I will detail my first attempts to adapt their method to the study of PDM in binary systems.

5.3 Influence of a binary companion: first results Faramaz et al. (2014a)

I first reproduced the results of Kirsh et al. (2009), before studying the impact of a circumstellar binary companion. Therefore, I used the same initial conditions, and considered a planet of mass $m_p = 4.5 M_\oplus$, semi-major axis $a_p = 25$AU, on a circular and zero inclination orbit around a solar-mass star. This planet is surrounded by a disk of 10^5 massless and collisionless test-particles, extending radially over five R_H on each side of the planet, which results into a belt of total width $10\,R_H = 4.3\,$AU. The disk surface density is set to $\Sigma \propto a^{-1}$, which implies an initial distribution in semi-major axes with regular spacing of 4.3×10^{-5}AU.

The eccentricities and inclinations of the test-particles follow Rayleigh distribution with $RMS_e = 2RMS_i = 10^{-4}$ (where i is in radians), while their remaining orbital angles are uniformely distributed in $[0, 2\pi]$.

The evolution of this system over 800 planetary orbits is computed using the N-body code Swift-RMVS Levison & Duncan (1994). Kirsh et al. (2009) used SyMBA instead and chose a timestep of one year, that is, 1/125th of the planet orbital period. We chose to adopt the same timescale, however, it must be noted that with Swift-RMVS, the use of a typical timestep of the order of 1/20th of the smallest orbital period involved should be sufficient. Since planetesimals are here considered as massless test-particles, their action on the planet is not computed and therefore, the effective migration of the planet is not realised in our simulations. However, as we shall see, this approach is sufficient to show that there exists a bias in the close-encounters favouring interactions of the planet with inner material, and thus, generating an inwards migration.

The status of the system status is examined after each planetary orbit : close-encounters experienced by the test-particles are recorded over the last three quarters of the simulation, and counting separately close-encounters with material inner and outer to the planet. The criterion for a particle to have suffered a scattering event between two outputs is that its eccentricity changes by more than a tenth of the hill factor χ, defined by

$$\chi = \left(\frac{m_p}{3M_\star}\right)^{1/3} \quad . \tag{5.3}$$

One can then derive the probability for a planetesimal to undergo a close-encounter as a function of its distance from the planet, and therefore its Tisserand parameter, and compare these probabilities for inner and outer material. Our results, shown on Figure 5.1(a), are identical to those of Kirsh et al. (2009). Kirsh et al. (2009) also showed that this result depends only weakly on the semi-major axis of the planet. This is confirmed by the results of another simulation with $a_p = 10\,\mathrm{AU}$ (see Figure 5.1(b)).

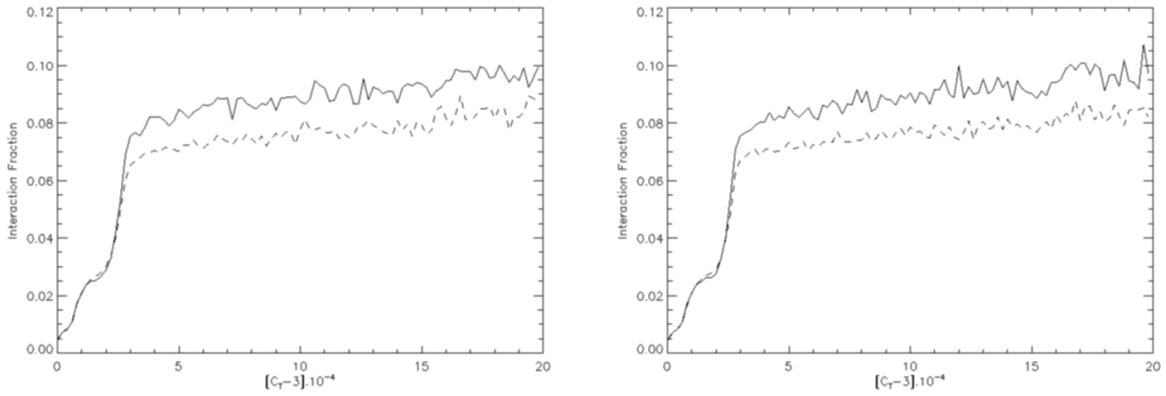

(a) With a planet at 25 AU

(b) With a planet at 10 AU

Figure 5.1 – Probability for a test-particle to suffer a close-encounter with a planet over a planetary orbit, as a function of the Tisserand parameter. The planet has a mass $4.5\,M_\oplus$, and is on a circular and zero inclination orbit with a semi-major axis **(a)** $a_p = 25\,\mathrm{AU}$ and **(b)** $a_p = 10\,\mathrm{AU}$, around a solar-mass star. The distinction is made between particles from regions inner to the planet with $a < a_p$ (solid line) and the particle from regions outer to the planet with $a > a_p$ (doted line).

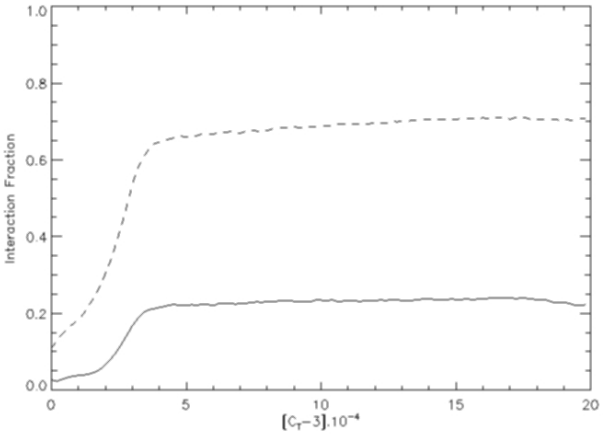

Figure 5.2 – Probability for a test-particle to suffer a close-encounter with a planet over a planetary orbit, as a function of the Tisserand parameter. The planet has a mass $4.5\,M_\oplus$, and is on a circular and zero inclination orbit with a semi-major axis $a_p = 10\,\mathrm{AU}$, around a solar-mass star, and with a stellar binary companion of a solar mass orbiting the system with a semi-major axis of 100 AU and on a circular and coplanar orbit. The distinction is made between particles from regions inner to the planet with $a < a_p$ (solid line) and the particle from regions outer to the planet with $a > a_p$ (doted line).

The goal here is to study the impact of a binary companion on planetesimal-driven migration. Therefore, I followed the approach of Kirsh et al. (2009) described above and extended the calculation of probability of interaction with a planet at 10 AU to the case where the system is orbited by a stellar binary companion of a solar-mass at 100 AU, on a circular and zero inclination orbit (thus coplanar with the disk and the orbit of the planet). The results are shown in Figure 5.2.

At first glance, the interactions are not only more numerous than in the case of a single planet, but very interestingly, exchanges angular momentum are now biased towards outer material. This indicates that, in the presence of a binary companion, the direction of migration is reversed and the planet migrates outwards, in the direction of the binary companion. However, these results should be considered with great caution.

The main limitation of this approach is that the context is no longer that of the three-body problem when adding a binary companion to the system. Therefore, the Tisserand parameter is no longer a constant, because the binary companion will generate secular variations of the planet and the planetesimals orbital elements. Moreover, the orbits of planetesimals are expected to suffer non-linear perturbations of their orbit, as a result of the perturbations induced on the planet by the binary companion. Thus even if the motion of the system's components are accurately simulated with the N-body code, the data processing, and therefore, the detection of an asymmetry, suffers errors compared with the case where the system contains no companion binary.

Since close-encounters are detected thanks to a change in eccentricity, the most important aspect to consider here is the ability of the binary companion to generate secular variations in the eccentricity of the planetesimals, which mimic close encounters. If this is the case, this will lead to false positives in the detection of close-encounters.

Moreover, these variations depend on the distance to the binary, and are thus expected to vary accross the planetesimal disk if this one is wide enough.

More precisely, the closer the particles are from the binary companion, the greater the variations in their eccentricity is expected, and one could then wonder if the reverse of asymmetry could not simply be due to this. To quantify this effect and answer this question, we run a simulation identical to the previous one, excepted we remove the planet, and use a fictive fixed circular planetary orbit of semi-major axis 10 AU to compute the particles Tisserand parameter. Indeed, since the planet is in secular evolution with the binary companion, its semi-major axis can be considered to be constant, and this allows to study the secular effects only, and ignore the non-linear effects induced by the perturbations suffered by the planet. The result is that all the particles suffer changes in their eccentricity that mimic close encounters, independently from their location across the belt. The relative difference of interactions between inner and outer material as a function of the Tisserand parameter is shown in Figure 5.3.

We can conclude from this that the binary companion alone cannot be responsible for the reverse of asymmetry, that is, the eccentricity variations induced on the planetesimals is not sensitive enough to sustain an asymmetry across the planet close-encounter zone and the asymmetry witnessed in Figure 5.2 is thus most probably the result of a non-linear effect of the variations of the orbital elements of the planet as an effect of the binary companion.

However, these variations are expected to be of secular nature, that is, the semi-major axis of the planet is a constant in average and therefore, by taking this into account as in the simulation where we take a fixed fictive planet, we have seen that this cannot sustain an asymmetry either. Therefore, the probabilities increase of an order of magnitude can be explained by the fact that the binary companion mimics eccentricity increases and close encounters for the planetesimals, however, this increase is not asymmetric at all across the close-encounter zone, and therefore, although the data processing suffers errors, the asymmetry in interactions is most probably real.

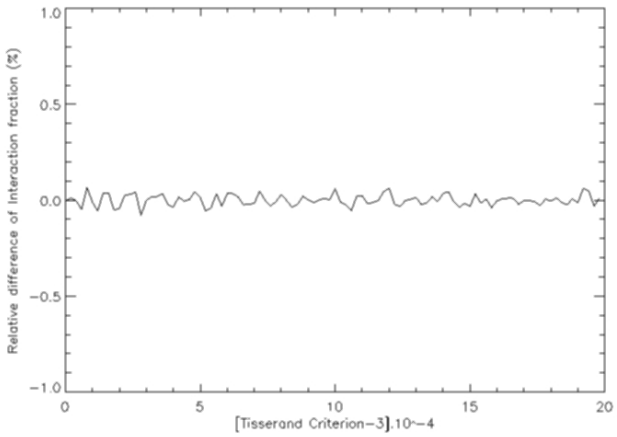

Figure 5.3 – Relative difference of interactions between inner and outer material as a function of the Tisserand parameter for a fictive planet of mass $4.5\,M_{\oplus}$, on a circular and zero inclination orbit at 10 AU around a $1\,M_{\odot}$ star, and with a stellar binary companion of $1\,M_{\odot}$, on a circular and zero inclination orbit at 100 AU.

5.4 Conclusion and Perspectives

The results of our study suggest that binary companions could reverse the direction of PDM from inwards to outwards, but clearly, the study of this impact should be studied in a more accurate manner. This can be achieved by using for instance the N-body code SyMBA because it allows one to simulate an effective migration of a planet, since it includes the action of planetesimals on said planet. A study of Payne et al. (2009) already suggested that a binary companion could sustain outwards PDM, however, their simulations included an outer disk of planetesimals only, and therefore, outward migration was sutained even in absence of a binary companion. Clearly, one should move beyond this simplified approach and achieve extensive numerical simulations, involving a large number of interacting planetesimals for a sufficient resolution.

Depending on the the available computational capabilities, one might want to reduce the computational needs. N-body simulations with the Swift-RMVS code consume one order of magnitude less CPU-time than SyMBA simulations, since they do not compute the effect of the planetesimals on the planet. However, such simulations also provide snapshots of instantaneous amounts of material a planet interacts with, and could be used as a basis for semi-analytical methods. For instance, combining this information with the theoretical synodic period would allow one to derive the real amounts of material the planet is expected to interact with over time, and unravel any asymmetry in the exchanges of angular momentum. This would most probably not give insights on the migration rate, but at least on the direction of migration, and using this approach could allow to limit the use of SyMBA simulations and thus save computational time, especially in the frame of a parametric exploration of the characteristics of the disk, the planet and the binary companion.

Finally, if this phenomenon is to be confirmed, it could provide an explanation for the puzzling planetary systems configurations found in close binary systems (see Sect. 6.1).

Chapter 6

Perspectives

Contents

The diversity of exoplanetary systems often questions our formation and evolution models, however, these models have been primarily built on the study of our solar system, which turns out to be quite exceptional, because it contains nearly circular orbits and involves a single star. By focusing on the dynamical history of systems containing eccentric perturbers, and the impact of a second star on the architecture of exoplanetary systems, this thesis opens the way to a more appropriate view of exoplanetary systems and their broad diversity.

6.1 Architecture of exoplanetary systems in close binaries

With the increasing number of detected exoplanets, and since at least half of the stars are part of a binary or more multiple system, it is not surprising that a significant number of exoplanets were detected in such systems (60 exoplanets, Roell et al. 2012). Of course, one can expect that the presence of a stellar binary companion affects planetary systems formation and evolution, all the more when it is closely separated from the planet-bearing star. Indeed, if it was found by Roell et al. (2012) that the characteristics of exoplanetary systems in wide binary systems, where the stars are separated by at least 100 AU, differ very little from planetary systems around single stars, the architecture of exoplanetary systems in close binaries, with separation $\sim 20\,\mathrm{AU}$, is much more puzzling.

Five exoplanets were found in such systems: Gl86 (Queloz et al. 2000; Lagrange et al. 2006), HD 41 004 (Zucker et al. 2004), γ Cephei (Hatzes et al. 2003; Neuhäuser et al. 2007; Endl et al. 2011), HD 196 885 (Correia et al. 2008; Chauvin et al. 2011), and α Centauri B (Dumusque et al. 2012). Three of these planets – HD 196 885 Ab, HD 41 004 Ab,γ Cep Ab – were detected close to the orbital stability limit imposed by the binary companion, but even more curiously, in the region where the accretion of a solid core is severely handicapped by the binary companion, and where they are not believed to have formed in situ (Thebault & Haghighipour 2014).

Kley & Nelson (2008) studied the specific case of the γ Cephei system and used this case as a proxy to study the influence of a stellar companion on planetary migration. They showed that it was possible to find a model explaining the current orbital configuration of the planet in the system of γ Cephei, provided that a protoplanetary core has migrated inwards after having formed.

As a consequence, migration scenarios in gaseous disk struggle to provide an explanation for the configuration of these systems. Indeed, since a planet is supposed to migrate inwards towards its host star, even in the presence of a binary companion, then one must always assume in this type of model that the planet formed further from its host star, and therefore closer to the region where the binary companion specifically prevents the formation of planets (see, e.g., Thebault & Haghighipour 2014, for more details).

A more natural assumption would be that this planet, along with these in the HD 41 004 and HD 196 885 systems, have formed instead closer to their host stars in a better environment, and then migrated outwards in the direction of the binary companion. However, this type of migration can not be assured in a gaseous disk.

The results of our study suggest that a binary companion could affect the late stages of evolution of planetary systems by reversing the natural direction of migration of PDM from inwards to outwards, as seen in Chapter 5, which may provide an explanation for the configurations of these systems. This phenomenon should be confirmed, but also studied in more details, and in particular, its sensitivity to the mass and distance of the binary companion, as well as those of the migrating planet, should be investigated. As suggested in Chapter 5, the study of this phenomenon would involve parametric explorations and intensive use of numerical simulations, as well as the developement of dedicated numerical or semi-analytical analysis techniques.

6.2 Exoplanetary systems in time

Eccentric perturbers can create eccentric patterns in debris disks, and as seen in this thesis with the case of ζ^2 Reticuli , can sustain this asymmetry on Gyr timescales as seen in Chapter 3. However, if there is clear evidence for an eccentric perturber in this system, this one is also expected to be distant of several tens of AU from its host star, which renders its detection very difficult, since usual detection techniques are biased towards short period objects. This is not the case of direct imaging techniques, however, these are challenging to apply here, because their sensitivity does not allow them yet to detect faint emissions from Gyr-old planets.

The arrival of new instruments such as VLT-SPHERE (Beuzit et al. 2010), or Gemini-GPI (Graham et al. 2007), will complete our knowledge of the most outer parts of extrasolar systems and how these are populated by giant planets. Indeed, SPHERE and GPI will offer direct detection of planets more massive than Jupiter up to 100 AU from their host star.

Moreover, SPHERE will be able to detect planetary systems over a large spectrum of ages, up to Gyr-old systems, and hopefully, it may allow the detection of the perturber predicted in this thesis in the ζ^2 Reticuli system. As underlined in Chapter 3, this perturber could also be further characterised by studying its imprints on the debris disk in a more accurate manner, which involves obtaining better constraints on the disk geometry. The capabilities of ALMA to provide such informations were already mentioned in Chapter 3, but the capabilities of SPHERE regarding this aspect are also remarkable.

SPHERE observations of the debris disk of HR 4796, shown in Figure 6.1, and which was historically the first disk presenting signs of perturbations by an eccentric planet and a pericenter-glow like ζ^2 Reticuli , allowed to obtain a level of precision unachieved by previous observations. These images will allow to place much better constraints on the disk spatial structures suggested by previous observations (Mouillet et al. 1997a; Augereau et al. 1999; Schneider et al. 1999; Wyatt et al. 1999; Thalmann et al. 2011; Lagrange et al. 2012; Wahhaj et al. 2014; Milli et al. 2014). In particular the belt possess sharp inner and outer edges, which may give evidence for planets beyond the limit that outer Kuiper belts have been expected to set on the extent of a planetary system. It is actually not the first time that a belt is found to possess sharp inner and outer edges thanks to new instrumental capabilities. ALMA observations of the Fomalhaut system outer belt have led Boley et al. (2012) to consider a scenario involving the shaping of this belt by two perturbers on each side of the belt. In addition, distortions are suspected in the disk of HR 4796, which gives clues for a complex dynamical history. The informations provided by SPHERE observations will provide strong constraints on the spatial features of this debris disk, which in turn, will enable a very detailed dynamical modelling, and thus set more precise constraints on the planetary system responsible for these features, and which remains undetected as of yet.

Detailed dynamical modelling of spatial features in debris disk can in fact be a powerful indirect detection and characterisation method, and lead to the posterior discovery of hidden planets, as was the case for the Fomalhaut and β Pictoris systems. This illustrates the fact that considering interactions between planets and the small solid components in a planetary system provides a handful of informations which can then be modelled to help characterise a planetary system and its dynamical history. Of course, this strongly relies on the use of numerical tools, which take great advantage of improvements in computational capabilities, and evolve towards tools which take always more phenomena into account, and in particular, collisional aspects (See for instance Thébault 2012; Kral et al. 2013). These improvements will permit to achieve modelling at a level of detail which will match that of the forthcoming observations.

The systems of HR 4796 and β Pictoris, which are relatively young, with ages not exceedding several 10 Myrs, and the older $\sim$ 440 Myr Fomalhaut system, are most probably the debris disks we know the most details about, which makes them benchmarks to feed our theories and models of planetary systems formation and evolution.

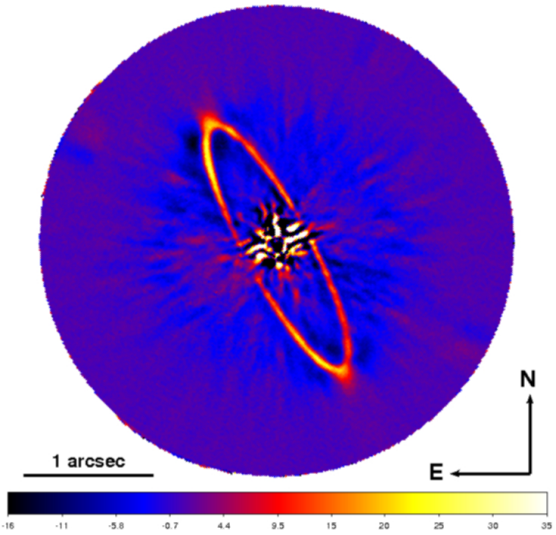

Figure 6.1 – SPHERE-IRDIS observations of the debris disk of HR 4796. *Source :* ESO Press release

The understanding of such documented systems has and will greatly benefit from dynamical studies, in the mutual feedback process between dynamical modelling, which feed on observations, and observations which feed on theoretical predictions to test.

As already mentioned, Gyr-old systems are faint and thus rarely accessible to current instrumental sensitivities, and there is thus a lack of informations on mature systems. However, the study of Gyr-old and mature systems which bear signs of dynamical histories very different from this of our Solar system is crucial to shed light on how diverse the long-term evolution of planetary systems can be. The study of ζ^2 Reticuli could help filling this lack. The knowledge of the system of ζ^2 Reticuli and its debris disk would clearly benefit from detailed observations such as those achieved for the HR 4796 system with SPHERE, or those achievable with ALMA or JWST.

6.3 An answer to the origin of exozodiacal dust?

The hot dust in the inner regions of extrasolar planetary systems, within a few astronomical units from a star, is known as exozodiacal dust, or exozodi. The grains are small and thus essentially unbound due to radiation pressure. Therefore, the hot exozodis need to be replenished, but in-situ replenishement by collisional evolution of a population of planetesimals as in a cold debris disk does not work for exozodis, because planetesimals could not survive long enough so close to the star for this process to take place (see, e.g., Augereau 2009). However, large amounts of exozodiacal dust were detected in numerous systems, and their occurrence rate is estimated to be $\sim 15-20\%$ around solar-type stars (Absil et al. 2013; Ertel et al. 2014), with no apparent correlation with the age of the system.

This has motivated several studies to unravel the origin of these levels of dust, and particularly how these levels could be maintained over a system's age of order of 100 Myrs. The evaporation of comets is thought to be the most effective exozodiacal dust production mechanism, however, the generation of a population of comets requires itself an explanation. Bonsor et al. (2012), Bonsor et al. (2014), and Raymond & Bonsor (2014) have investigated whether scattering of planetesimals by a chain of planets or subsequent to planetary migration, as well as a combination of both, as possible mechanisms. However, if these mechanism may explain the origin of this dust, they require that the dust is replenished over the system's age, and thus, will ultimately fade with time.

The study of the dynamical history of the Fomalhaut system has shown that eccentric planetary perturbers in the outer parts of a planetary system are able to set low-mass material such as those contained in debris disks on highly eccentric orbits in a robust manner, which may result into the cometary activity required to produce an exozodi (Chapter 4).

Moreover, the generation of these eccentric orbits could be delayed by very significant timescales, up to several 100 Myr with Neptune-Saturn mass perturbers, which also indicates that warm and hot inner belts potentially resulting from this process may start to be produced very late in the history of a system. Therefore the production of an exozodi in this scenario would have the crucial advantage of not requiring that the levels of dust are maintained over the system's age.

Following the approach of Bonsor et al. (2012) and Bonsor et al. (2014), the question of whether this mechanism could feed an exozodi at a sufficient rate could be addressed using for instance N-body simulations with a massive planet and massless test-particles representing the planetesimals. The method consists in tracking planetesimals as they reach below a given distance of several AU from their host star under the influence of an eccentric massive planet.

This allows one to estimate the mass flux in the innermost parts of the system : assuming that these planetesimals will endure a collisional activity there, one can estimate the maximum levels of dust a given mechanism can produce.

More importantly, the presence of hot inner dust belts could provide indirect evidence of eccentric planets. This would be a particularly helpful indirect characterisation method in the case of systems older than 100 Myr, since as the study of Fomalhaut reveals, this could be related with Neptune-Saturn mass planets in the outer parts of a system, whereas these planets are precisely part of the least accessible planets through classical detection and imaging methods. In that sense, it could be for instance particularly helpful to confirm any correlation between eccentric outer perturbers and inner dust belts.

6.4 Conclusion

The major conclusion which can probably be drawn from this work is that the interplay between all the components of a planetary system can be extremely complex, and thus that refinements in our planetary systems evolution models will be achieved by considering exoplanetary systems as a whole, from their smallest to biggest components, from their most inner to most outer parts, and at all possible timescales.

Complementary observations of instruments such as SPHERE, ALMA, JWST, HARPS, GPI, and Kepler, therefore covering all the scales of a planetary system, either in term of spatial scales, components size scales, and timescales, will help us to consider planetary systems in their globality. The complementarity of these observations with dynamical modelling will allow us to understand exoplanetary system in a much more accurate manner, and to grasp a comprehensive picture of their diversity.

Appendix

Appendix A

The ζ^2 Reticuli system

Contents

A.1 Inclination of ζ^2 Reticuli

Observations of the debris disk surrounding ζ^2 Reticuli reveal a double-lobed asymmetric feature. The inclination of this system relative to the line of sight is a key parameter for correctly interpreting the observations. If the system is seen pole-on, one would expect the observed feature to be the signature of resonant clumps, whereas an eccentric ring signature would be more plausible if the system were observed edge-on.

In general, observations suggest that stellar and disk inclinations are aligned (Watson et al. 2011; Guilloteau et al. 2011). Under this assumption, one can estimate the disk inclination from the observed stellar inclination. Consequently, we aim here to measure the star's inclination i, that is, the angle formed by its rotation axis with respect to the line of sight. With this convention, the system is seen pole-on if $i = 0°$, and edge-on if $i = 90°$.

The method used requires knowing the following stellar properties: the colour index $(B - V)$, the radius $R_\star$, the projected rotational velocity, $v_{\rm rot} \sin(i)$, and finally $R'_{\rm HK}$, an activity indicator defined as $F'_{\rm HK}/\sigma T_\star^4$, where $F'_{\rm HK}$ is the chromospheric flux in the H and K lines of Ca II, and $T_\star$ is the effective star temperature. These properties for ζ^2 Reticuli are summarised in Table A.1.

We first used the activity/rotation diagram built by Noyes et al. (1984), which plots $\log(\mathrm{R}'_{\rm HK})$ versus $\log(\mathrm{Ro})$ and shows a relationship between these two quantities for late-type stars. $\mathrm{Ro} = P_{\rm rot}/\tau_{\rm c}$ is the Rossby number, $P_{\rm rot}$ is the rotational period of the star, and $\tau_{\rm c}$ a model-dependent typical convective time, called the turnover time. Using Fig. 6(b) of Noyes et al. (1984) and the observed value of $\log(R'_{\rm HK}) = -4.79$ found by Henry et al. (1996) for ζ^2 Reticuli allows us to estimate $\log(P_{\rm rot}/\tau_{\rm c}) \sim 0.185 \pm 0.085$.

Table A.1 – Stellar properties of ζ^2 Reticuli . (1) Johnson et al. (1966); (2) this study; (3) Eiroa et al. (2013); (4) Reiners & Schmitt (2003); (5) Henry et al. (1996).

Stellar property	Value	Reference
$(B-V)$	0.60	1
$R_\star$ ($\mathrm{R}_\odot$)	$\sim 0.965 \pm 0.05$	2
$L_\star$ ($L_\odot$)	0.97	3
$T_\star$ (K)	5851	3
$v_{\rm rot} \sin i$ (km/s)	2.7 ± 0.3	4
$\log(R'_{\rm HK})$	-4.79 ± 0.03	5
$\log(\mathrm{Ro})$	$\sim 0.185 \pm 0.085$	2
$\tau_{\rm c}$ (days)	~ 9.10	2
$P_{\rm rot}$ (days)	$\sim 14.20 \pm 2.75$	2
$v_{\rm rot}$ (km/s)	$\sim 3.42 \pm 0.66$	2
$i(^\circ)$	$\sim 65.5^{+24.5}_{-31.5}$	2

Then, using Eq. (4) of Noyes et al. (1984), where x is defined with the star colour index $(B-V)$ by $x = 1-(B-V)$, one can estimate $\tau_{\rm c}$:

$$\log \tau_{\rm c} = \begin{cases} 1.362 - 0.166x + 0.025x^2 - 5.323x^3 & , x > 0 \\ 1.362 - 0.14x & , x < 0 \end{cases} . \tag{A.1}$$

ζ^2 Reticuli has a colour index $(B-V) = 0.60$ (Johnson et al. 1966), which gives $\tau_{\rm c} = 9.10$ days. The corresponding range of possible rotation periods is $P_{\rm rot} \sim 14.20 \pm 2.75$ days.

Since the equatorial rotation velocity is defined as $v_{\rm rot} = 2\pi R_\star / P_{\rm rot}$, knowing the stellar radius $R_\star$ allows us to obtain a range of possible values for $v_{\rm rot}$. Using $T_\star$ and $L_{\rm bol}$ and corrections prescribed by Masana et al. (2006), we found that for ζ^2 Reticuli , $R_\star = 0.965 R_\odot \pm 0.05$. The corresponding value of equatorial velocity is $\sim 3.42 \pm 0.66$ km/s.

We compared this with the independent measurement of $v_{\rm rot} \sin i$ by Reiners & Schmitt (2003). They found $v_{\rm rot} \sin(i) = 2.7 \pm 0.3$ km/s, which combined with the calculated rotational velocity, allows us to estimate the stellar inclination. We found that the inclination can range from 34° to 90° (see Fig A.1). This is very consistent with an inclined disk.

However, two angles are required to fully constrain the stellar rotation and disk axis. Therefore a degree of freedom remains and different orientations may lead to the same inclination i. Namely, the range of possible orientations leading to a same inclination is the set of axes describing a solid angle $2\pi \sin i$ about the line of sight. But the number of axes that lead to the same inclination increases with i, since it follows a $\sin i$ distribution. This means that the inclinations in a range $[34°; 90°]$ are not equiprobable.

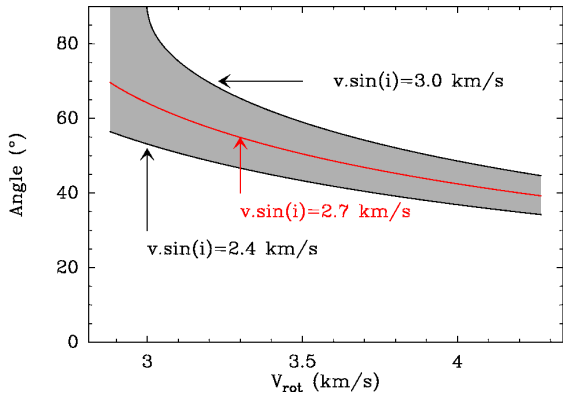

Figure A.1 – Possible inclination angles (taken from the pole) for ζ^2 Reticuli as a function of $v_{\rm rot}$ ranging between ~ 2.76 and 4.08 km/s, where i is computed using the values of $v_{\rm rot}\sin(i) = 2.7 \pm 0.3$ km/s (Reiners & Schmitt 2003). The acceptable zone for the inclination is grey-shaded.

The probability for a given inclination to be between i and $i + di$, provided it is in the range $[34°; 90°]$, can thus be written

$$dP(i) = \frac{\sin i di}{\int_{34°}^{90°} \sin i di} \quad , \tag{A.2}$$

and the probability to find inclinations between i_1 and i_2 in the range $[34°; 90°]$ is

$$P(i \in [i_1; i_2]) = \frac{\int_{i_1}^{i_2} \sin i di}{\int_{34°}^{90°} \sin i di} \quad . \tag{A.3}$$

Applying this to the case of ζ^2 Reticuli, among the possible ranges of $[34°; 90°]$, we have an $\sim$ 50% chance that the observed inclination is in the range $[65.5°; 90°]$. Thus the system inclination is $i = 65.5^{\circ +24.5}_{-31.5}$. Consequently, the disk is more probably seen almost edge-on, with a pure edge-on configuration not ruled out.

Because of the large uncertainties, this constraint does not really allow us to conclude with absolute confidence whether the disk exhibits an eccentric ring or resonant clumps. However, resonant structures are in general thin structures that tend to be hidden by non-resonant bodies and are difficult to detect, even in case of pole-on observations (Reche et al. 2008). This argument clearly supports the interpretation of Eiroa et al. (2010), who favoured an eccentric ring structure with $e \gtrsim 0.3$ seen edge-on and extending from ~ 70 to ~ 120 AU.

A.2 Constraints on ζ^2 Ret set by direct imaging

VLT/NaCo (Lenzen et al. 2003; Rousset et al. 2003) Ks-band data were retrieved from the ESO archive (ID 086.C-0732(A); PI: Löhne, 71574). Two epochs were available in August 2010 and November 2010, the former missing photometric calibration therefore only the latter was used to set detection limits on the presence of bound companions. Nevertheless, both data sets were reduced and no companion was detected. The data from November 11, 2010 were obtained in field stabilized-mode with five manual offsets of the derotator to simulate field rotation, with the S27 camera providing a pixel scale of 27 mas/pixel. Twenty image cubes with a DITxNDIT of 1.5s x 42 were obtained for a total observing time on target of 21min. The semi-transparent mask C_0.7_sep_10 with a diameter of 0.7″ and a central transmission of 3.5×10^{-3} was used. Each individual image was bad pixel-corrected and flat- fielded. Background subtraction was made for each cube using the closest sky images. The images were rencentred using a Gaussian fit of the attenuated central star. The data were selected within each data cube using criteria based on the attenuated central star flux and the encircled energy between 0.4″ and 0.55″. The images were then binned every 6s and derotated into a reference frame where the pupil was stabilized in order to simulate angular differential imaging (ADI, Marois et al. 2006). In this reference frame, the total field rotation provided by the manual offsets plus the natural pupi/field rotation is 17°. This data cube was then reduced using principal components analysis (PCA, Soummer et al. 2012), retaining four components out of 105.

The noise in the final reduced image was estimated using a sliding nine pixel-wide box to obtain a preliminary map of detection limits in magnitude. We corrected this map by computing the flux losses due to the PCA reduction. They were estimated by injecting fake planets into the data cube at a $10 - \sigma$ level and processing the data again. Last, these detection limits in magnitude were converted into detection limits in masses, using the COND (Baraffe et al. 2003) or BT-settl models (Allard et al. 2011), assuming an age of 2 Gyr. The 2D-detection limits derived with the COND evolutionary models is presented in Fig. A.2

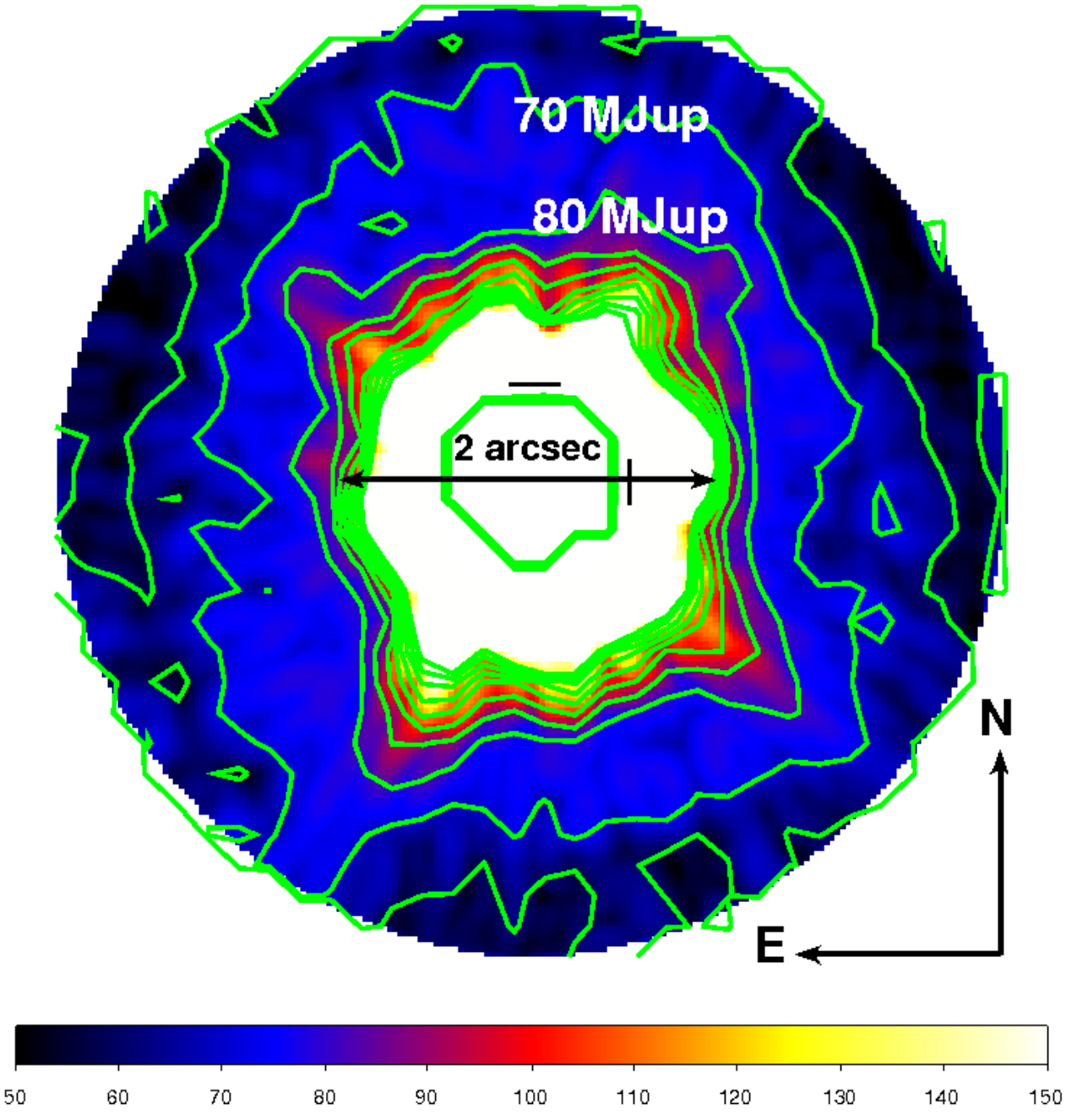

Figure A.2 – Map of the detection limits in Jupiter masses set by the COND evolutionary models. The contours range from 60 to 150 $M_{\rm Jup}$ with a step of 10 $M_{\rm Jup}$.

Appendix B

Article : An independent determination of Fomalhaut b's orbit and the dynamical effects on the outer dust belt, Beust et al. (2014)

Astronomy & Astrophysics manuscript no. fomb-orbit
November 21, 2013

An independent determination of Fomalhaut b's orbit and the dynamical effects on the outer dust belt

H. Beust[1], J.-C. Augereau[1], A. Bonsor[1], J.R. Graham[3], P. Kalas[3] J. Lebreton[1], A.-M. Lagrange[1], S. Ertel[1], V. Faramaz[1], and P. Thébault[2]

[1] UJF-Grenoble 1 / CNRS-INSU, Institut de Planétologie et d'Astrophysique de Grenoble (IPAG) UMR 5274, Grenoble, F-38041, France
[2] Observatoire de Paris, Section de Meudon, F-92195 Meudon Principal Cedex, France
[3] Department of Astronomy, University of California at Berkeley, Berkeley, CA 94720, USA

Received 8 July 2013; Accepted 13 November 2013

ABSTRACT

Context. The nearby star Fomalhaut harbours a cold, moderately eccentric ($e \sim 0.1$) dust belt with a sharp inner edge near 133 au. A low-mass, common proper motion companion, Fomalhaut b (Fom b), was discovered near the inner edge and was identified as a planet candidate that could account for the belt morphology. However, the most recent orbit determination based on four epochs of astrometry over eight years reveals a highly eccentric orbit ($e = 0.8 \pm 0.1$) that appears to cross the belt in the sky plane projection.
Aims. We perform here a full orbital determination based on the available astrometric data to independently validate the orbit estimates previously presented. Adopting our values for the orbital elements and their associated uncertainties, we then study the dynamical interaction between the planet and the dust ring, to check whether the proposed disk sculpting scenario by Fom b is plausible.
Methods. We used a dedicated MCMC code to derive the statistical distributions of the orbital elements of Fom b. Then we used symplectic N-body integration to investigate the dynamics of the dust belt, as perturbed by a single planet. Different attempts were made assuming different masses for Fom b. We also performed a semi-analytical study to explain our results.
Results. Our results are in good agreement with others regarding the orbit of Fom b. We find that the orbit is highly eccentric, is close to apsidally aligned with the belt, and has a mutual inclination relative to the belt plane of $< 29°$ (67% confidence). If coplanar, this orbit crosses the disk. Our dynamical study then reveals that the observed planet could sculpt a transient belt configuration with a similar eccentricity to what is observed, but it would not be simultaneously apsidally aligned with the planet. This transient configuration only occurs a short time after the planet is placed on such an orbit (assuming an initially circular disk), a time that is inversely proportional to the planet's mass, and that is in any case much less than the 440 Myr age of the star.
Conclusions. We constrain how long the observed dust belt could have survived with Fom b on its current orbit, as a function of its possible mass. This analysis leads us to conclude that Fom b is likely to have low mass, that it is unlikely to be responsible for the sculpting of the belt, and that it supports the hypothesis of a more massive, less eccentric planet companion Fomalhaut c.

Key words. Planetary systems – Methods: numerical – Celestial mechanics – Stars: Fomalhaut – Planets and satellites: dynamical evolution and stability – Planet-disk interactions

1. Introduction

The presence of circumstellar dust orbiting the nearby (d = 7.7 pc; Mamajek 2012; van Leeuwen 2007) A3V star Fomalhaut (α Psa, HD 216956, HIP 113368) has been known for a long time through its thermal emission (Aumann 1985). The spatial structure of its debris disk was furthermore specified by direct imaging (Holland et al. 2003; Kalas et al. 2005). HST coronographic images by Kalas et al. (2005) have revealed a large dust belt in optical scattered light, extending between 133 au and 158 au and modeled as a moderately eccentric ring ($e = 0.11 \pm 0.1$) with a 13.4 ± 1.0 au offset between its centre and the star. The investigators suggest that an undetected planet could account for these features, as supported by numerical (Deller & Maddison 2005) and semi-analytic studies (Quillen 2006).

Kalas et al. (2008) then reported the detection of a planet candidate (subsequently termed Fomalhaut b, hereafter Fom b) orbiting the star at 119 au, only 18 au inside the dust belt, thus strongly supporting its putative shepherding role for the inner edge of the belt. The optical detections of Fom b with HST/ACS were confirmed by two independent analyses of the data (Currie et al. 2012; Galicher et al. 2013). Since Fom b was *not* detected at infrared wavelengths (Kalas et al. 2008; Marengo et al. 2009; Janson et al. 2012), it has been suggested that Fom b could represent starlight reflected from dust grains, possibly bound to a planet in the form of a large planetary ring (Kalas et al. 2008) or a cloud due to the collisional erosion of irregular planetary satellites (Kennedy & Wyatt 2011).

The mass and orbit of Fom b continues to require better constraints. An accurate knowledge of these parameters would clearly help define its interaction with the dust ring orbiting Fomalhaut. It is not possible to constrain Fom b's mass (hereafter m) from photometry because the emission detected is likely dominated by the circumplanetary dust scattering. Dynamical modeling of its interaction with its environment is therefore a valuable way to derive constraints. Kalas et al. (2008) give a conservative upper limit $m < 3$ Jupiter masses (hereafter $M_{\rm Jup}$), while Chiang et al. (2009) reduces it to possibly $0.5\,M_{\rm Jup}$, under the assumption that the planet is responsible for the sculpting of the dust ring. Based on photometric estimates, Currie et

Send offprint requests to: H. Beust
Correspondence to: Herve.Beust@obs.ujf-grenoble.fr

Table 1. Summary of compiled astrometric data of Fom b relative to Fomalhaut

UT Date	Declination (δ, mas)		Right Ascension (α, mas)	
	K13	G13	K13	G13
Oct. 25/26, 2004	9175 ± 17	9190 ± 20	−8587 ± 24	−8590 ± 20
Jul. 17/20, 2006	9365 ± 19	9360 ± 20	−8597 ± 22	−8640 ± 20
Sep. 13, 2010	9822 ± 44	9790 ± 30	−8828 ± 42	−8810 ± 30
May 29/31, 2012	10016 ± 37		−8915 ± 35	

K13 = Kalas et al. (2013); G13 = Galicher et al. (2013)

al. (2012) claim $m < 2\,M_{\rm Jup}$, but other recent studies (dynamical or photometric) suggest a possibly much lower mass in the super-Earth regime (Janson et al. 2012; Kennedy & Wyatt 2011; Galicher et al. 2013). According to Janson et al. (2012), the recent non-detection of Fom b at $\lambda = 4.5\,\mu$m in thermal infrared excludes any Jovian-sized planet, and is rather compatible with a $\sim 10\,M_\oplus$ object.

Based on the first two epochs of HST detections in 2004 and 2006, separated by only 1.7 years, Fom b's orbit was initially thought to be nearly circular or moderately eccentric ($e = 0.11$–0.13 Chiang et al. 2009) and coplanar with the outer dust belt, as its orbital motion was detected nearly parallel to its inner edge. This constraint was deduced assuming that Fom b is responsible for the belt's inner edge sculpting. This assumption was nevertheless recently questioned by Boley et al. (2012) who suggest the presence of other shepherding planets, in particular outside the outer edge of the ring. Fom b was recovered at a third (2010) and fourth (2012) epoch using HST/STIS coronagraphy (Kalas et al. 2013), allowing accurate measurements of its sky-plane motion when all four epochs of astrometry are combined. These investigators independently developed a Markov chain Monte Carlo code to estimate the orbital elements (Graham et al. 2013), producing a surprising result that the orbit of Fomalhaut b is highly eccentric, and will appear to cross the dust belt in the sky plane projection.

The purpose of this paper is first to perform an independent analysis of the available astrometric data of Fom b to derive refined orbital constraints using a Markov-Chain Monte Carlo (MCMC) method that was developed by one of us (H. Beust) and already used to fit β Pic b's orbit (Chauvin et al. 2012). This independent analysis confirms the eccentric nature of the orbit, and that it is very probably coplanar with the disk and apsidally aligned (Sect. 2). In Sect. 3 we numerically investigate the dynamics of the Fomalhaut system including Fom b and the dust belt. We present in Sect. 4 a semi-analytical study to explain the numerical result we derive. Our conclusions are presented in Sect. 5.

2. Orbital fitting

2.1. Astrometric data

Fom b was observed with HST/ACS/HRC and HST/STIS at four epochs in 2004, 2006, 2010 and 2012. A detailed analysis and the corresponding astrometric data are given in Kalas et al. (2013). Galicher et al. (2013) also give independently derived astrometric measurement for all epochs before 2012. All these data are summarised in Table 1. While both sets of data are mutually compatible within their respective error bars, we note a slight difference between data from Kalas et al. (2013) and those from Galicher et al. (2013). To check the sensitivity of our orbital determination, we chose then to perform our orbital analysis with two independent sets of data: a first one with all data from Kalas et al. (2013), and a second one with the Galicher et al. (2013) data for the 2004, 2006 and 2010 data points, and the 2012 measurement from Kalas et al. (2013).

2.2. Orbital fit

The detected orbital motion with four epochs is in principle sufficient to try a first orbital determination. This is nevertheless not a straightforward task. Given the long expected orbital period of Fom b (hundreds of years), our four astrometric epochs cover only a tiny part of the orbit. We thus expect any orbital determination to come with large error bars. In this context, a standard least-square fitting procedure like Levenberg-Marquardt (Press et al. 1992) may produce meaningless results with huge error bars, as the χ^2 surface is probably very chaotic with many local minima. This was confirmed by our first attempts. Therefore we moved to a more robust statistical approach using the Markov-Chain Monte Carlo (MCMC) Bayesian analysis technique (Ford 2005, 2006). This technique applied to astrometric orbits was already successfully used to constrain the orbit of the giant planet β Pic b (Chauvin et al. 2012). We use here the same code for Fom b. We assume $d = 7.7$ pc and $M = 1.92\,M_\odot$ for the distance and the mass of Fomalhaut (van Leeuwen 2007; Mamajek 2012) After convergence of the Markov chains (10 simultaneously), a sample of 500,000 orbits (out of $\sim 10^7$) is picked up randomly in the chains of orbital solutions. This sample is assumed to represent the probability (posterior) distribution of Fom b's orbit. This distribution is presented in Figs. 1 and 2.

Figure 1 shows histograms of the distribution of individual orbital elements. In each plot we show two histograms. The black one corresponds to the first MCMC run (using Kalas et al. (2013) data), and the red one corresponds to the second run (using Galicher et al. (2013) data for epochs before 2012). The reference frame $OXYZ$ with respect to which the orbit is referred to is chosen as usual in such a way that the OZ axis points towards the Earth (hence the OXY plane corresponds to the plane of the sky); the OX axis points towards North. In the framework of this formalism, the astrometric position of the planet relative to the central star reads:

$$x = \Delta\delta = r\,(\cos(\omega+f)\cos\Omega - \sin(\omega+f)\cos i\sin\Omega) \quad (1)$$

$$y = \Delta\alpha = r\,(\cos(\omega+f)\sin\Omega + \sin(\omega+f)\cos i\cos\Omega) \quad (2)$$

where Ω is the longitude of the ascending node (measured counterclockwise from North), ω is the argument of periastron, i is the inclination, f is the true anomaly, and $r = a(1-e^2)/(1+e\cos f)$, where a stands for the semi-major axis and e for the eccentricity. With this convention, an $i = 0$ inclination would correspond to a prograde pole-on orbit, $i = 90°$ to a edge-on viewed orbit (like β Pictoris b), and $i = 180°$ to a pole-on retrograde orbit.

In Figure 1, the distributions of Ω and ω appear twofold, with two distinct peaks separated by 180°. This is due to a degeneracy in the Keplerian formalism. It can be seen from Eqs. 1 and 2 that changing simultaneously Ω and ω to $\Omega+\pi$ and $\omega+\pi$ leads to the same orbital model. Consequently these orbital parameters are only determined with a ±180° degeneracy. However, their sum $\Omega+\omega$ and difference $\Omega-\omega$ are unambiguously determined. It is easy to rewrite Eqs. 1 and 2 as a function of $\Omega+\omega$ and $\Omega-\omega$ instead of ω and Ω:

$$x = r\left(\cos^2\frac{i}{2}\cos(\Omega+\omega+f) + \sin^2\frac{i}{2}\cos(f+\omega-\Omega)\right) \quad (3)$$

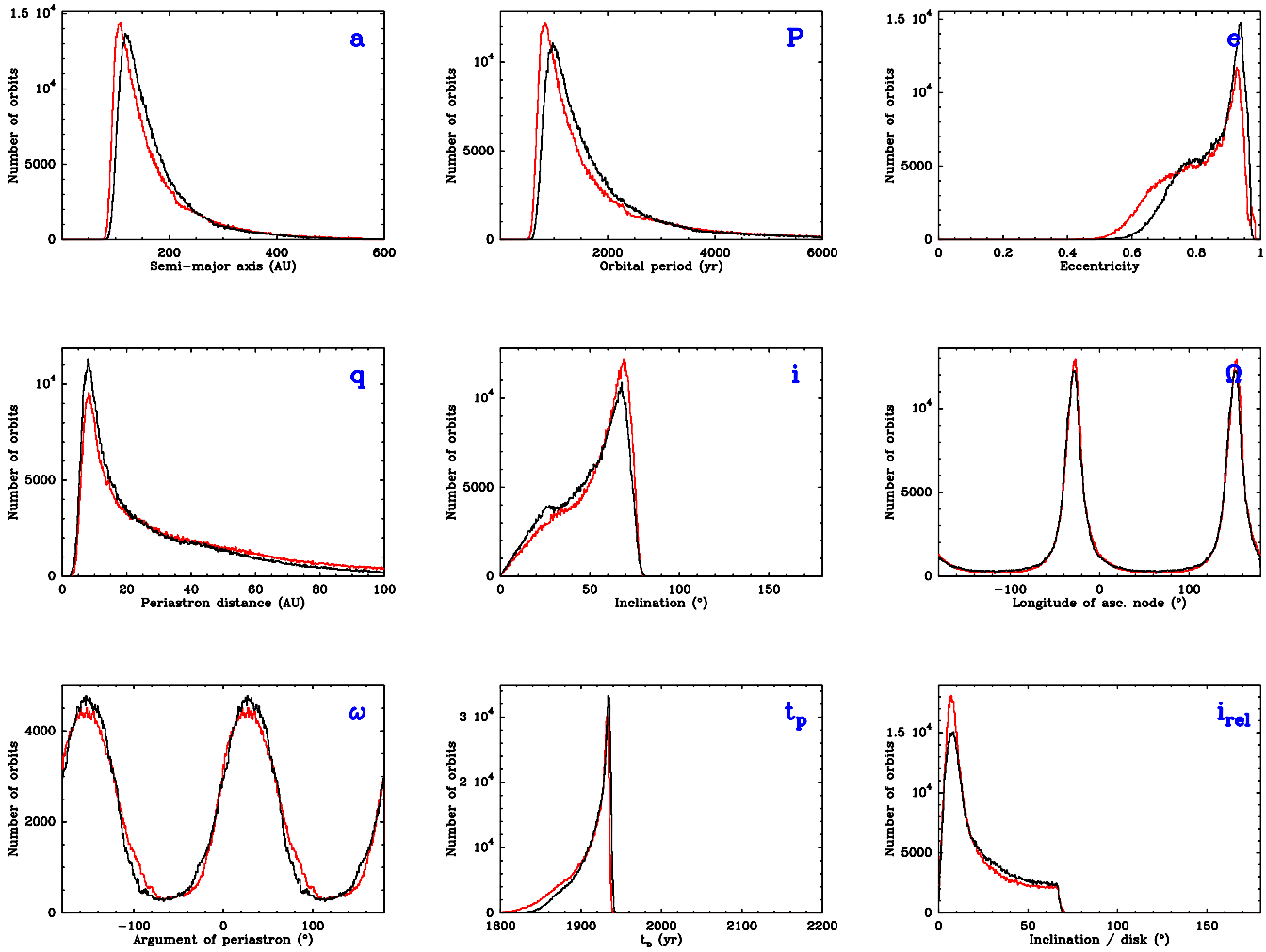

Fig. 1. Resulting MCMC distribution of the orbital elements of Fom b's orbit. In all plots, the black curves correspond to the first run using the full Kalas et al. (2013) data, and the red one to the second run using Galicher et al. (2013) data before 2012. Upper row, from left to right: semi-major axis (a), orbital period (P), eccentricity (e); second row, id: periastron (q), inclination (i), longitude of ascending node (Ω); third row, id: argument of periastron (ω), time for periastron passage (t_p), and inclination relative to the disk plane ($i_{\rm rel}$)

Table 2. Summary of various statistical parameters resulting from the MCMC distribution of Fom b's orbital solutions (run with Kalas et al. (2013) data)

Parameter	Peak value	Median	67% confidence interval	95% confidence interval	Kalas et al. (2013) 95% interval
Semi-major axis (a, au)	120	160	81 – 193	81 – 415	126.6 – 242.9
Orbital Period (P, yr)	999	1522	554 – 2028	554 – 5116	1028 – 2732
Eccentricity (e)	0.94	0.87	0.82 – 0.98	0.69 – 0.98	0.694 – 0.952
Periastron (q, au)	7.8	20.	2.7 – 33	2.7 – 77.8	6 – 74
Time for periastron (t_p, yr AD)	1935	1922	1910 – 1944	1869 – 1944	1800 – 2000
Inclination (i, °)	67	55	43 – 81	15. – 81.	31.9 – 71.5
Inclination relative to the disk ($i_{\rm rel}$, °)	6.1	17.	0 – 29	0 – 61	5 – 29
Argument of periastron (ω, °)	−148 or 33				−19.2 – 52.9
Longitude of ascending node (Ω, °)	−28 or 152				141.1 – 172.8

$$y = r\left(\cos^2\frac{i}{2}\sin(\Omega+\omega+f) - \sin^2\frac{i}{2}\sin(f+\omega-\Omega)\right) \quad ,(4)$$

We used those formulas in our MCMC code, which in fact fits $\Omega+\omega$ and $\Omega-\omega$. This avoids erratic changes in the solution between degenerate solutions, and subsequently ensures convergence of the chains. So, each time an orbital solution is taken in the chains with fitted values for $\Omega+\omega$ and $\Omega-\omega$, it results in two solutions with similar orbital parameters but different (Ω,ω) sets. This is why we have dual peaks distributions for Ω and ω.

The only way to eliminate the degeneracy is to obtain information regarding the OZ axis. This can be radial velocity data points, or information about which side of the orbit in foreground in the images. In the case of βPictoris, information about the Keplerian gas disk help to fix the ambiguity. But here no such

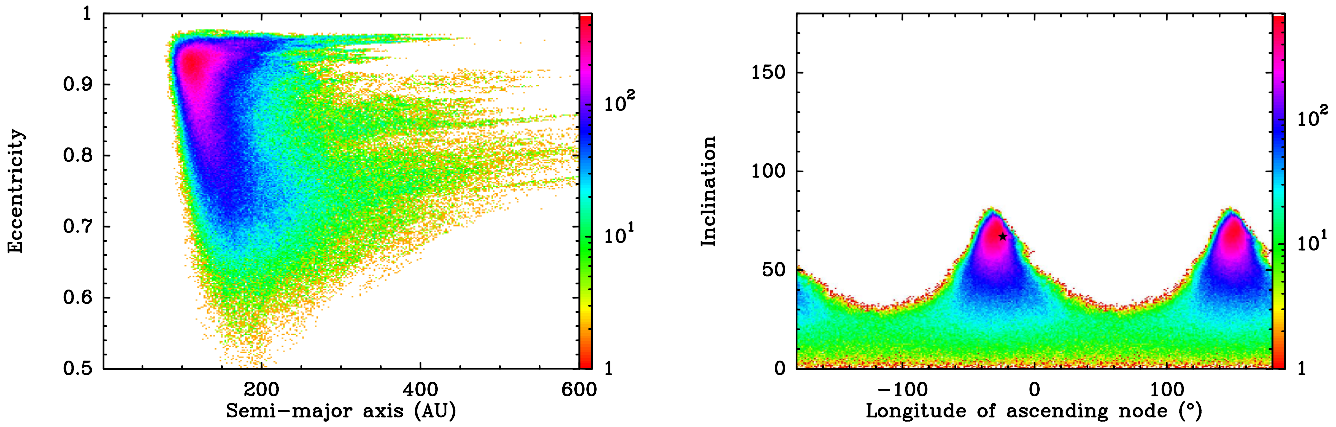

Fig. 2. Resulting 2D MCMC distribution of Fom b's orbital elements for two couples of parameters, for the run with the full Kalas et al. (2013) data: semi-major axis (a) – eccentricity (e) (left); longitude of ascending node (Ω) – inclination (i) (right). The color scale represents the joint 2D density of solutions for the considered set of parameters. In the right plot, the star indicates the corresponding location of the mid-plane of the dust disk (Kalas et al. 2005). The same plot using Galicher et al. (2013) data is almost identical

information is available for Fomalhaut, so we keep all possible solutions.

Figure 1 shows orbital distributions with well identified peaks, although this could appear surprising given the paucity of the data points. Detailed statistical parameters such as peak values and confidence intervals for various parameters are given in Table 2. The semi-major axis appears to peak at $\sim$ 110–120 au, a value comparable to the present day location of Fom b with respect to the star, but surprisingly, the eccentricity is very high. The peak of the eccentricity distribution is $\sim$ 0.92–0.94 (depending on the data set taken), virtually all solutions have $e \gtrsim 0.5$–0.6, and even $e \gtrsim 0.8$ with a 70% confidence level. It must be noted that the eccentricity distribution never extends up to $e = 1$. No solution with $e \geq 0.98$ is derived in the distribution. Thus we are confident in the fact that Fom b is actually bound to Fomalhaut, although it may be on a very eccentric orbit. As a consequence of this high eccentricity, the periastron value of the orbit is small with a peak value of 7–8 au, and subsequently the apoastron is $\gtrsim$ 200 au with a high confidence level. Figure 2 (left) shows a 2D joint probability map for a and e, for the first run only. We clearly see a peak of solutions around ($a = 120$ au, $e = 0.94$). A similar plot built with the data from the second run would appear nearly identical with a peak around ($a = 110$ au, $e = 0.92$).

There are indeed very few differences between the histograms derived from the two independent runs. The semi-major axis distribution appears slightly shifted towards shorter values in the second run (red curves, use of Galicher et al. (2013) data), with a peak appearing at $a = 110$ au instead of $a = 120$ au. Similarly, the eccentricity peaks at $e = 0.92$ in the second run instead of $e = 0.94$. These are the only noticeable differences between the two resulting distributions, all remaining differences barely reaching the level of the noise in the histograms. The differences are in all cases far below the bulk uncertainty on the corresponding parameters and therefore not very significant. We may therefore consider our orbital determination as robust. In the following, the dynamical study are performed with a Fom b orbit with $a = 120$ au and $e = 0.94$, i.e. corresponding to the peak values in the first run. The use of $a = 110$ au and $e = 0.92$ (the peak values for the second run) appears not to change anything noticeable to the dynamical behaviour we describe below.

The inclination distribution in Fig. 1 shows that all solutions are with $i < 90°$, confirming a prograde orbit. The inclination peaks at 66.7°, a value very close to the disk inclination quoted by Kalas et al. (2005). The longitude of ascending node exhibits (due to the quoted degeneracy) two peaks separated by 180° at −27.8° and 152.2°. This is again very close to the $PA = 156°$ of the belt ellipse quoted by Kalas et al. (2005). As our longitudes of nodes are counted counterclockwise from North like PAs, these similarities of values are a strong indication in favour of a coplanarity, or near coplanarity between the dust belt and Fom b's orbit. We therefore plot in Figure 1 the statistical distribution of the mutual inclination $i_{\rm irel}$ between Fom b's orbit and the dust disk, assuming the inclination and PA values given by Kalas et al. (2005). We see a sharp peak at 6.3°, which clearly suggests quasi-coplanarity. The fact that the peak is not at $i_{\rm rel} = 0$ does not necessarily indicate a non-coplanarity. Due to the error bars on the disk orbit parameters, strict coplanarity ($i_{\rm rel} = 0$) is just less probable than a few degrees offset. If the direction vector perpendicular to Fom b's orbit was drawn randomly on a sphere, the natural statistical distribution for $i_{\rm rel} = 0$ would be $\propto \sin i_{\rm rel}$. This is equivalent to saying that the coplanar configuration would be the least probable one if the orientation of Fom b's orbital plane was distributed randomly. Now, if we consider that error bars on the determination on the dust ring orbital plane and on our determination of Fom b's orbital plane lead to an uncertainty of $\sim 10°$ on the determination of $i_{\rm rel}$, this means that we add a stochastic component to our measurement of $i_{\rm rel}$, which should follow the $\propto \sin i_{\rm rel}$ distribution, at least up to $\sim 10°$. This is enough to create a peak in the MCMC distribution of $i_{\rm rel}$ that appears offset from the pure coplanar configuration by a few degrees.

Note also that when computing $i_{\rm rel}$, due to the Keplerian degeneracy, two mutual inclinations could be deduced for each solution. We systematically chose the lower one. This shows also up in Fig. 2 (right), which shows a 2D joint probability map for Ω and i, for the first run (full Kalas et al. (2013) data). We clearly identify the two peaks. The star indicates now the corresponding values for the dust disk taken from Kalas et al. (2005), which fall

very close to the peaks of the distribution. This unambiguously suggests coplanarity or quasi-coplanarity.

The argument of periastron ω peaks at −148.3 or 31.7. Kalas et al. (2005) report that the periastron of the elliptic dust belt is at PA=170°. Taking into account the PA of the disk and its inclination, we derive an argument of periastron $\omega_{\rm disk} = -148.9°$, which is extremely close to our peak value of ω. While this could be considered a strong indication for Fom b's orbit to be apsidally aligned with the elliptic dust belt, the real alignment may not be this perfect given the uncertainties of ω and $\omega_{\rm disk}$. The uncertainty on ω_{disk} is roughly ±25°, and that on our ω determination is comparable. A a result the agreement within less than 1° between both values could be a pure coincidence. All we can stress looking at the whole ω distribution is that we have apsidal alignment within less than ±30–40° with a good level of confidence (∼ 70%).

The conclusions is that we confirm the orbital determination of Fom b independently inferred by Kalas et al. (2013). The inclination distributions are compatible (within a sign convention in Kalas et al. (2013)), as well as the Ω and ω distribution, although only single peak distributions are given in Kalas et al. (2013). The shapes of the semi-major axis and eccentricity distributions are noticeably similar. The eccentricity and semi-major axis intervals are very similar, except the that our semi-major axis distribution extends a bit lower and our eccentricity distribution a bit higher (Table 2). We also confirm that Fom b's orbit is very probably nearly coplanar and apsidally aligned within a few tens of degrees with the dust belt.

3. Numerical study assuming coplanarity

3.1. Pericenter glow for low eccentricity orbits

We thus conclude like Kalas et al. (2013) that a dust belt crossing orbit for Fom b is consistent with the data. This automatically raises the question of the long-term stability of this configuration. Thus we move now to a dynamical study to address this issue. fomb's orbit turns out to be nearly coplanar and apsidally aligned with the elliptic dust ring. This is a strong indication for a pericenter glow phenomenon.

Pericenter glow occurs when a disk of planetesimals orbiting a star is secularly perturbed by a planet moving on an eccentric orbit. We briefly recall here the theory, which is described in detail in Wyatt et al. (1999) and Wyatt (2005). We consider the motion of a planetesimal perturbed by the planet. We use Laplace-Lagrange theory, based on an expansion of the disturbing function in ascending powers of eccentricities and inclinations and a truncation to second order, assuming that eccentricities and inclinations remain low (Murray & Dermott 1999). This causes the secular system to become linear. The analytical solution for the planetesimal eccentricity can be described for the eccentricity variables as

$$z(t) \equiv e \times \exp(I\varpi) = Be' + e_{\rm p} \exp\left(I(At + \beta_0)\right) \quad . \tag{5}$$

Here $z(t)$ is the complex eccentricity and $I^2 = -1$; e is the planetesimal's eccentricity while e' is that of the planet; $\varpi = \omega + \Omega$ is the longitude of periastron with respect to the direction of the planet's periastron. B and A are coefficients that depend on the orbital configuration of the two bodies via Laplace coefficients (see Wyatt 2005, for details). The first term in Eq. (5) is a fixed forced eccentricity due to the eccentricity of the perturbing planet. The second term is a proper oscillating term with additional parameters $e_{\rm p}$ and β_0 that depend on the initial conditions.

Consider now that we start with an initially cold disk, i.e., planetesimals on circular orbits ($z(0) = 0$). This could be the case at the end of the protoplanetary phase, because before the disappearance of the gas, the eccentricity of all solid particles tend to be damped by gas drag. Then obviously $\beta_0 = \pi$ and $e_{\rm p} = Be'$, so that the full solution now reads

$$z(t) = Be' \left(1 - \exp(IAt)\right) \quad . \tag{6}$$

The complex eccentricity $z(t)$ describes a circle path in complex plane with radius Be', centered on the point $(Be', 0)$. It results from Eq. (6) that the maximum eccentricity $e_{\rm max} = 2Be'$ is reached for $At \equiv \pi[2\pi]$, when $\varpi = 0$. This means that the maximum eccentricity in the secular evolution is reached when the planetesimal is apsidally aligned with the planet.

When $e' \neq 0$, Wyatt (2005) showed that a steady-state regime is reached after a transient phase characterised by spiral structures. In the steady-state regime all planetesimals are at various phases on their secular eccentricity cycle, but those which are close to their peak eccentricity are approximately apsidally aligned with the planet. The global result is an elliptic dust ring apsidally aligned with the planet.

From an observational point of view, the pericenter side of the ring appears more luminous, thanks to a more efficient scattering of stellar light by the dust particles produced by the planetesimals. The same applies also to thermal emission, as grains are hotter near pericenter. This phenomenon termed pericenter glow was invoked to explain many observed asymmetric global structures in debris disks, such as HR 4796 (Wyatt et al. 1999; Moerchen et al. 2011), HD 141569 (Wyatt 2005) or more recently ζ^2 Reticuli (Faramaz et al. 2013). Concerning Fomalhaut, the dynamical study by Chiang et al. (2009), based on a moderately eccentric orbit of Fom b shepherding the dust ring were made in this framework.

Fomalhaut's dust ring and Fom b's orbit share many characteristics that are typical of pericenter glow: an eccentric ring with an offset centre, coplanar and apsidally aligned with Fom b. It is therefore tempting to invoke it here. But the linear theory outlined above holds for moderately eccentric orbits that do not cross each other. Here with $e = 0.94$, we are far from any linear regime. It is then important to characterise what happens in the high eccentricity regime. This must be done numerically.

3.2. Pericenter glow phenomenon with highly eccentric perturbers

We present now a numerical study of the Fomalhaut system, to properly address the case of high eccentricity orbits. We take an initial ring of 10^5 massless particles (i.e., planetesimals) between 110 au and 170 au, i.e., extending wider than the observed ring, and we add a planet orbiting on an orbit corresponding to our best fit: $a = 120$ au and $e = 0.94$. The initial eccentricities of the particles are randomly sorted between 0 and 0.05, while their inclinations with respect to the planet's orbital plane are chosen between 0 and 3°. The dynamics of this system is integrated using the symplectic N-body code Swift_rmvs (Levison & Duncan 1994) which takes into account close encounters between the planet and the disk particles. The integration is extended up to 500 Myr, i.e, a bit longer than the estimated age of Fomalhaut (440 Myr; Mamajek 2012).

Taking into account close encounters is indeed important here. As the planet's orbit crosses the disk we expect to have many encounters. The perturbing action of the planet onto the disk particles is twofold: all particles crossing the planet's path

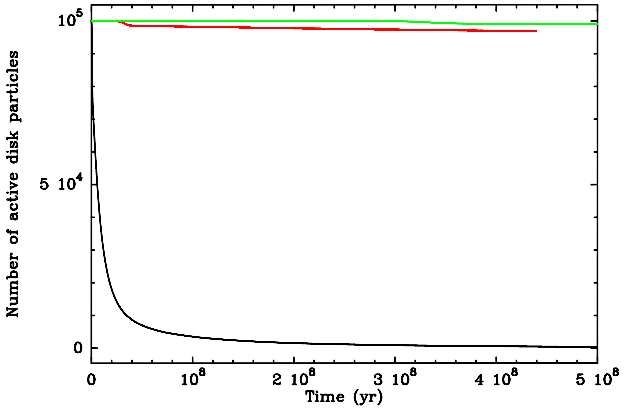

Fig. 4. Evolution of the number of active disk particles as a function of time in the simulations described in Figs. 3 (black), 5 (red) and 6 (green). All missing particles have been ejected by close encounters. This phenomenon mainly concerns the $m = 1\,M_{\rm Jup}$ case.

within a few Hill radii undergo a close encounter that most of the time scatters them out of the disk; but as long as the particles do not encounter the planet, they are subject to a secular evolution more or less comparable to the one described in the previous section. We expect any global shaping of the disk to be due to secular perturbations rather than close encounters, as close encounters rather have a destructive effect on the disk.

The balance between the two effects (secular and close encounters) depends actually on the mass of Fom b, which we will consider to be a free parameter.

3.2.1. Massive planet

We first present a run with a massive planet, i.e., $m = 1\,M_{\rm Jup}$, but still fitting the observational constraints (Janson et al. 2012). The result is shown in Fig. 3. We represent here upper views of the particle disk and semi-major axis versus eccentricity plots, at the beginning of the simulation and at two subsequent epochs: $t = 5$ Myr and $t = 100$ Myr. As early as $t = 5$ Myr, the disk appears extremely perturbed and actually no longer assumes a disk shape. Many particles have already had a close encounter with the planet and have been scattered. Interestingly, a few disk particles have been trapped in co-orbiting orbits (or 1:1 resonance) with the planet. At $t = 100$ Myr, i.e., well below the age of Fomalhaut, these are no longer present. The disk now contains fewer particles. Many of them have been lost in close encounters with the planet. To illustrate this, we plot in Fig. 4 the number of remaining disk particles (i.e., those particles which have not been ejected yet) as a function of time. Starting from 10^5, we see that it is reduced to 4000 at $t = 100$ Myr and to 400 at $t = 500$ Myr. We can then safely claim that this situation does not match the observation, unless the planet was very recently scattered ($\lesssim 10$ Myr; see Fig. 4) onto its present orbit. Over any longer time-scale, the disk is virtually destroyed by close encounters, which are just too efficient here with such a massive planet. In fact, even a few Myrs is already too long. The disk particles reach high eccentricities much earlier than that. An average eccentricity of 0.1 for the disk particles, which we should consider as matching the observations, is reached only $\sim 3 \times 10^4$ yr after the beginning of the simulations. As a result any subsequent configuration must be considered as incompatible with the observation.

3.2.2. Super-Earth planet

We come now to a similar simulation, but with a lower mass for Fom b. Figure 5 presents a simulation with a mass $m = 0.02\,M_{\rm Jup} = 6.28\,M_\oplus$ (Super-Earth regime). The disk is represented at three epochs: $t = 5$ Myr, $t = 20$ Myr and $t = 440$ Myr, i.e., the estimated age of Fomalhaut. We do not show the initial disk, as it is identical to that in Fig. 3. At $t = 5$ Myr, we note a drastic difference with the previous simulation. The disk now still assumes a disk shape with a moderate ($e \sim 0.2$) eccentricity. This disk configuration actually roughly matches the observed disk, but the elliptic disk is not apsidally aligned with the planet's orbit. It instead appears rotated by $\sim 70°$. This contradicts both our orbital determination, which suggests apsidal alignment, and the predictions of the standard pericenter glow theory. This is actually due to the high eccentricity of Fom b; see explanation in Sect. 4.

At $t = 20$ Myr, the disk still assumes this elliptic shape with a similar angular tilt with respect to the planet's apsidal line. But now the disk particles have reached much higher eccentricities ($\sim 0.6 - \sim 1$), causing the disk to no longer resemble the observed one. In fact, the bulk eccentricity of the disk increases continuously with time. At $t = 5$ Myr it is ~ 0.2, while at $t = 20$ Myr it is $\gtrsim 0.6$. An average disk eccentricity of 0.1, considered as a good match to the observations, is reached earlier than $t = 5$ Myr, in fact at $t = 2$ Myr (plot not shown here). But even in that case, the disk appears tilted the same way as at $t = 5$ Myr.

At $t = 440$ Myr, the particles' eccentricities have spread over all possible values. The disk no longer assumes a ring shape. This indeed appears to be the case much earlier in the simulation. After $t = 20$ Myr, the particles' eccentricity keep increasing up to high values, and the disk structure is already lost at $t =\sim 80$ Myr. In fact the situation at $t = 440$ Myr with $m = 0.02\,M_{\rm Jup}$ is comparable to that at $t = 5$ Myr with $m = 1\,M_{\rm Jup}$, except that less particles have been lost in close encounters.

3.2.3. Sub-Earth regime

Figure 6 presents now a simulation with a mass $m = 0.002\,M_{\rm Jup} = 0.628\,M_\oplus$ (Earth or sub-Earth regime). The epochs represented are now $t = 40$ Myr, $t = 200$ Myr and $t = 440$ Myr. The main difference is that at all 3 epochs, the disk still assumes an elliptic disk shape. But as with $m = 0.02\,M_{\rm Jup}$, the global disk eccentricity increases to reach high values. This is of course due to the increase of the eccentricity of the disk particles which keep being apsidally tilted by $\sim 70°$ with respect to the planet's orbit. In fact, the situation at $t = 40$ Myr with $m = 0.002\,M_{\rm Jup}$ is somewhat comparable to that at $t = 5$ Myr with $m = 0.02\,M_{\rm Jup}$, and the situation at $t = 200$ Myr with $m = 0.002\,M_{\rm Jup}$ also compares with that at $t = 20$ Myr with $m = 0.02\,M_{\rm Jup}$. An average disk eccentricity of 0.1 is reached at ~ 20 Myr.

It must be specified that this last simulation may be less realistic than the others, in the sense that the planet's mass is now lower than the mass of the dust disk. According to Wyatt & Dent (2002) and Chiang et al. (2009), a mass of planetesimals ranging between $3\,M_\oplus$ and $20\,M_\oplus$ is required to sustain the dust disk over the age of the star. This issue is investigated further in Sect. 4.3.

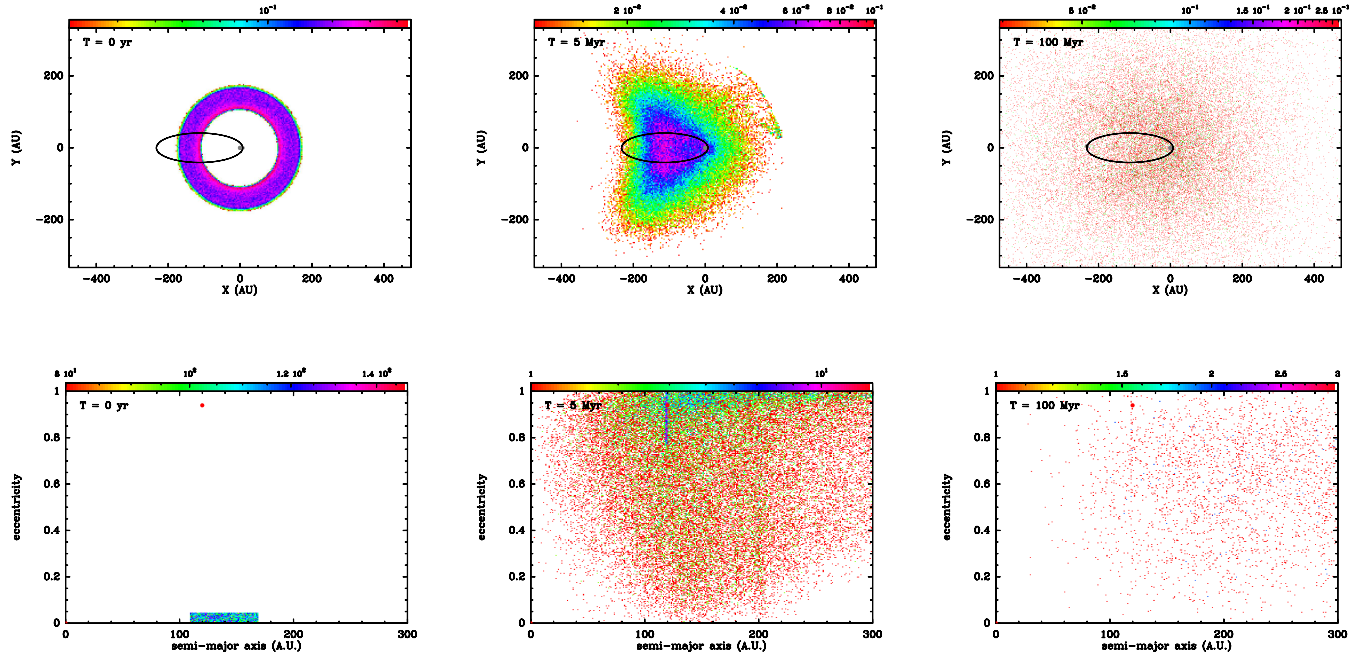

Fig. 3. Result of the N-body integration with a perturbing planet with $m = 1\,M_{\rm Jup}$. We display here upper views of the planetesimal disk together with the planet's orbit (top) and semi-major axis – eccentricity diagrams of the disk (bottom), at three epochs: beginning of the simulation ($t = 0$, left), at $t = 5$ Myr (middle) and $t = 100$ Myr (right). The color scale is proportional to the projected densities of particles (top plots) and of orbits in (a, e) space (bottom plots). The red circles represent the location of the star and of the planet. The planet's orbit is sketched as a black ellipse.

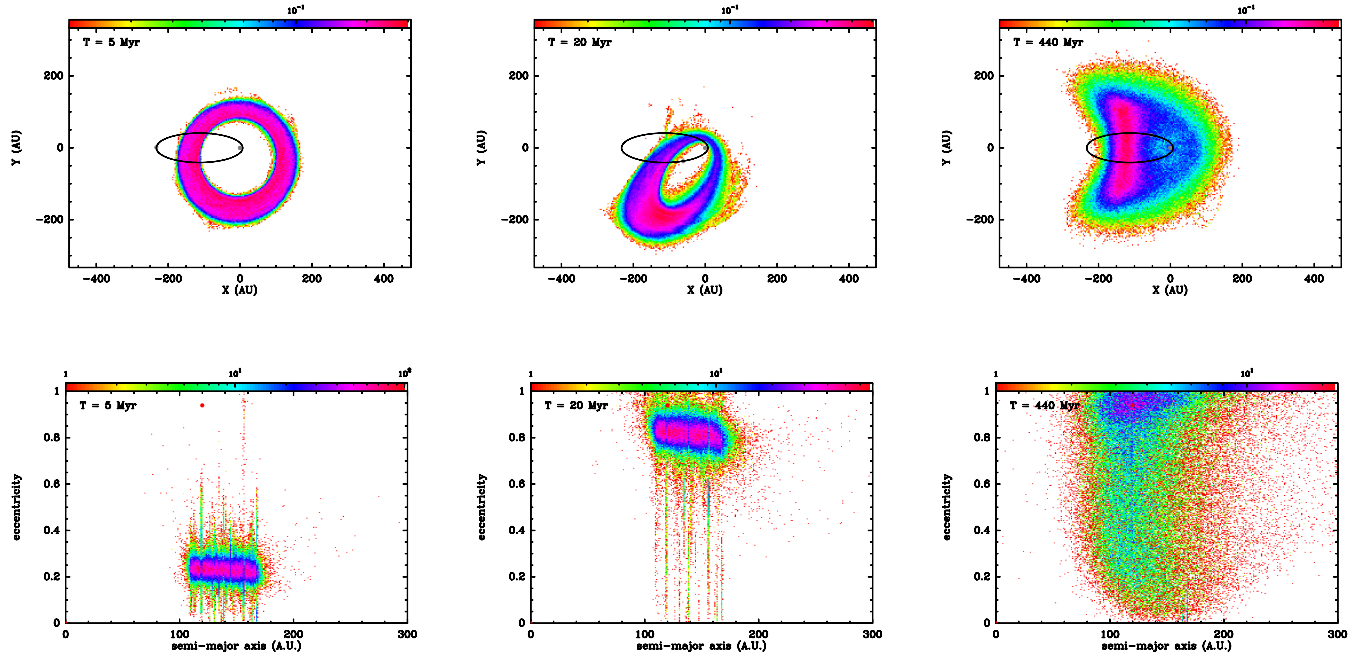

Fig. 5. Result of the N-body integration with a perturbing planet with $m = 0.02\,M_{\rm Jup}$. The conventions are the same as in Fig. 3. Three epochs are represented: $t = 5$ Myr (left), $t = 20$ Myr (middle) and $t = 440$ Myr (right).

3.2.4. Discussion

The three simulations described above with different masses for Fom b present similarities and differences. The comparison between the various outputs reveals comparable sequences: the disk is first perturbed to assume an elliptic shape. This is due to an increase of the eccentricities of the particles, while their longitudes of periastron remain more or less constrained to $\sim 70°$ with respect to the apsidal line of the planet. Then the global eccentricity increases to reach very high values. Afterwards, the particles spread in eccentricities and the structure of the disk is lost. The main difference resides in the time-scale of this pro-

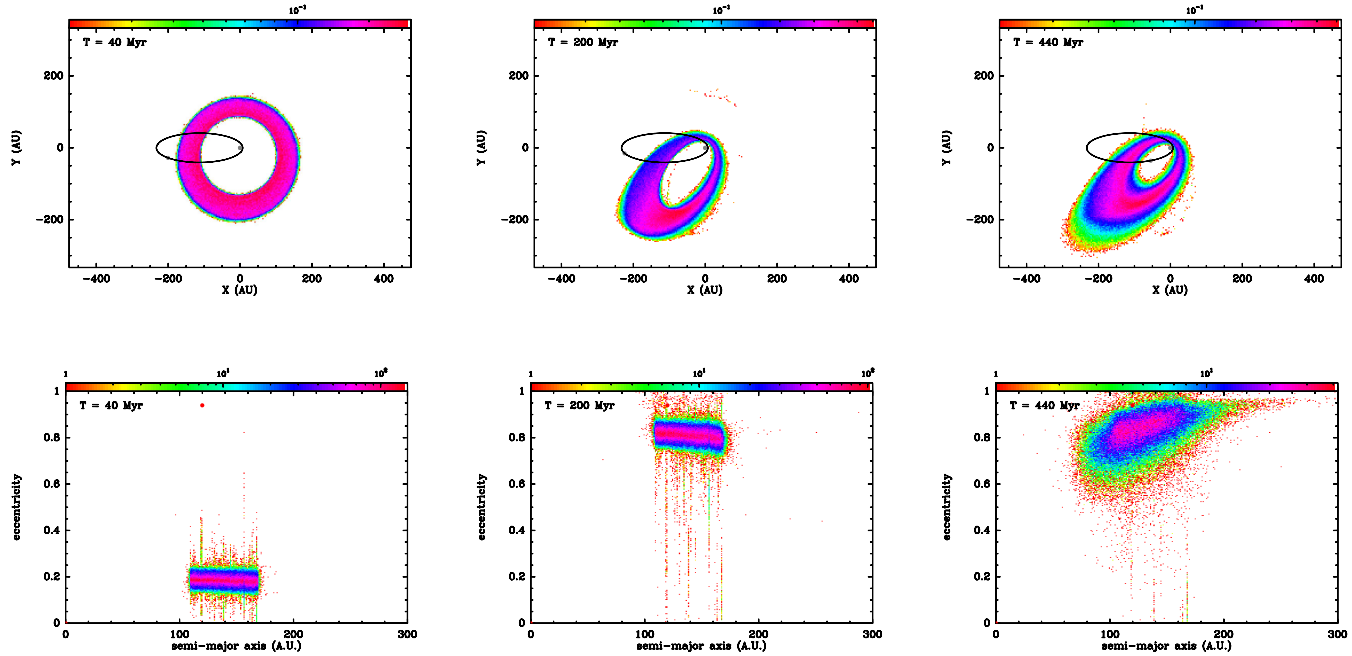

Fig. 6. Result of the N-body integration with a perturbing planet with $m = 0.002\ M_{\rm Jup}$. The conventions are the same as in Fig. 3. Three epochs are represented: $t = 40$ Myr (left), $t = 200$ Myr (middle) and $t = 440$ Myr (right).

cess. At $t = 5$ Myr with $m = 1\ M_{\rm Jup}$ the particles have already very high eccentricities, and the structure of the disk is already getting lost. At $t = 440$ Myr with $m = 0.002\ M_{\rm Jup}$ we are barely reaching this stage after the disk particles have seen their eccentricities increase. Comparing the three runs, the time-scale of the process turns out to be roughly inversely proportional to the planet's mass. This is characteristic for a secular process, as the secular disturbing function due to the planet is proportional to its mass while the topology of the Hamiltonian depends only weakly on the planet's mass (see next section).

Another difference between the three simulations resides in the loss of particles. Obviously the higher the mass, the more efficiently particles are lost. Particle loss is due to scattering by close encounters. As expected, more massive planets are more efficient at scattering particles. With $m = 1\ M_{\rm Jup}$, particle scattering actually dominates the dynamics after ~ 5 Myr, so that there is virtually no particle left at the age of the star. This is conversely not the case for low mass planets. Figure 4 shows that the loss of particles, although it is present, is not significant over a time-scale of Fomalhaut's age. Thus we may stress that for low mass planets, the dynamics is essentially secular, and that close encounters are negligible. Note that this does not necessarily mean that there are no close encounters. There are inevitably encounters, but they are less numerous, thanks to a shorter Hill sphere. However, as the Hill radius scales as $m^{1/3}$, the effect should not be so drastic. The other reason is that for a low mass planet, it would take many subsequent encounters to actually eject a particle.

We also tried to vary the orbital configuration, in particular to add a few degrees inclination (5°) to the planet with respect to the disk mid-plane. This appeared not to produce significant changes in the global results describe here, so that our conclusion still hold and may be regarded as robust.

It turns out that with the orbit we deduced from our fitting procedure, assuming a low mass for Fom b is enough to prevent the destruction of the disk by scattering close encounters over a time-scale corresponding to the age of the star, even if the planet crosses the disk. The secular perturbations by the planet succeed in rendering the disk eccentric, but they inevitably drive the particles towards very high eccentricities that do not match the observation. Depending on the mass assumed for Fom b an average disk eccentricity of 0.1 is reached between a few 10^6 to a few 10^7 yr after the beginning of the simulations, which is still far below the age of the system. Moreover, even when its global eccentricity matches the observation, the disk appears not apsidally aligned with the planet's orbit, which does not match the conclusion of our orbital fit (Sect. 2). This is also in contradiction with the pericenter glow dynamics, where the particles get their maximum eccentricities when they are apsidally aligned with the planet, causing the global disk figure to be aligned similarly. The linear pericenter glow analysis obviously does no longer apply here. This is a consequence of the very high eccentricity assumed for the planet, as we detail below.

4. Semi-analytical study

4.1. Theoretical background

We consider a massless disk particle moving in the gravitational field of the star Fomalhaut with mass M and the planet Fom b with mass m. The motion of the particle is thus described in the framework of the restricted three body system. The Hamiltonian of the particle's motion then reads in stellocentric reference frame

$$H = -\frac{GM}{2a} - Gm\left(\frac{1}{|\boldsymbol{r}-\boldsymbol{r'}|} - \frac{\boldsymbol{r}\cdot\boldsymbol{r'}}{r'^3}\right) \quad , \tag{7}$$

where G is the gravitational constant, a is the particle's semi-major axis in stellocentric referential frame, and $\boldsymbol{r}$ and $\boldsymbol{r'}$ are the position vectors of the particle and the planet in the same referential frame. We shall restrict ourselves to the planar problem,

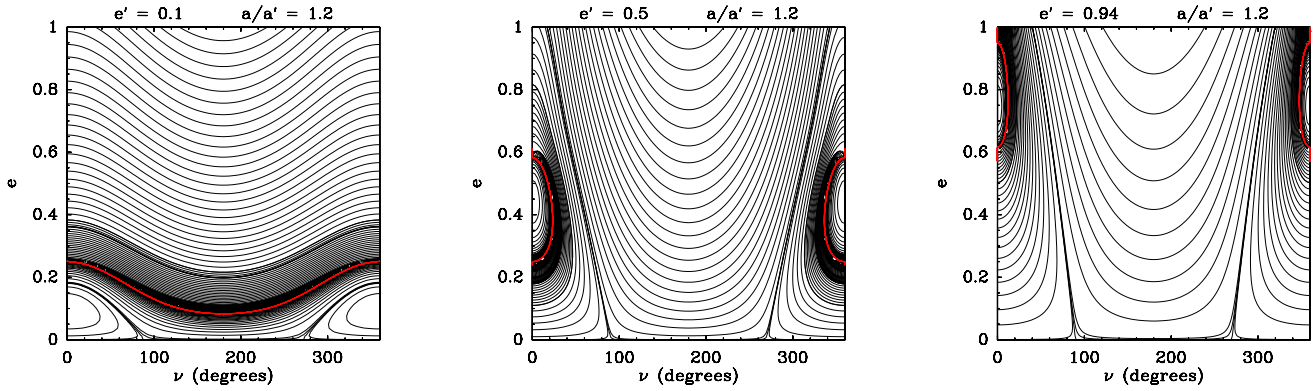

Fig. 7. Phase portraits of secular averaged Hamiltonian $\overline{H}$ for different values of the perturber's eccentricity e' and a fixed semi-major axis ratio $a/a' = 1.2$, as a function of the longitude of periastron of the particle relative to that of the perturber $\nu = \varpi - \varpi'$. The red curves separate regions where the orbits actually cross from region where they do not. In the case $e' = 0.1$ (left), the orbits do not cross below the red curve, while for $e' = 0.5$ and $e' = 0.94$, they do not cross inside the curves around $\nu = 0$.

where all three bodies move in the same plane. With this assumption, the Hamiltonian H reduces to two degrees of freedom.

The secular dynamics of the particle is then studied taking the time average of H over both orbits

$$\overline{H} = \frac{1}{4\pi^2} \int_0^{2\pi} \int_0^{2\pi} H(\lambda, \lambda') \, \mathrm{d}\lambda' \, \mathrm{d}\lambda \quad , \tag{8}$$

where λ and λ' are the mean longitudes of the particle and of the planet respectively. This averaged Hamiltonian describes accurately the secular motion of the particle as long as i) there is no close encounter between the particle and the planet, ii) the two bodies are not locked in a mean-motion resonance. We will assume that both conditions are fulfilled, even when both orbits cross each other. The numerical study showed indeed that as long as we do not take too high a mass for Fom b, scattering by close encounters remains a minor phenomenon (Fig. 4). Similarly, most planetesimals in our simulation are very probably not in resonance with Fom b, as mean-motion resonances usually cover small areas in semi-major axis. In fact, to enhance resonance structures, additional mechanisms such as planet migration are required (Reche et al. 2008; Wyatt 2003).

The averaged Hamiltonian $\overline{H}$ cannot in general be expressed in closed form. A full analytical treatment requires first to perform an expansion of H before averaging. There are two ways to do this. The first is to assume that both orbits have very different sizes. Then H can be written in ascending powers of r/r' (or r'/r depending on which orbit is the wider) using Legendre polynomials. The final averaging is then written in ascending powers of a'/a (or a/a'), where a and a' are the semi-major axes. The second way to average is to consider that both orbits may be of comparable sizes, but that the eccentricities and inclinations are and will remain low. H is then expanded in ascending powers of eccentricities and inclinations using Laplace coefficients and then averaged over both orbital motions. This second technique, once truncated to second order in eccentricities and inclinations, leads to describing the pericenter glow phenomenon.

We stress that none of these techniques can be applied here. As Fom b's orbit crosses the disk, the disk particles' orbits cannot be considered as significantly wider or smaller than Fom b's, and the very high eccentricity we determine for Fom b prevents from using any technique based on an expansion in ascending powers of eccentricity. A semi-analytical study is nevertheless possible. As we consider the planar problem, the Hamiltonian H has two degrees of freedom. But the averaged Hamiltonian $\overline{H}$ has only one, as thanks to the averaging process, the semi-major axis is a secular invariant. Considering then that a is a secular invariant, $\overline{H}$ is basically a function of only two dependant variables, namely the eccentricity e and the longitude of periastron ϖ. It is even more relevant to describe it as a function of e and of $\nu = \varpi' - \varpi$, where ϖ' is the longitude of periastron of the planet. It is then possible, for a given semi-major axis value a, to compute numerically the value of $\overline{H}$ for various sets of variables (ν,e), and to draw level curves of $\overline{H}$ in (ν,e) space. As $\overline{H}$ is itself a secular invariant, any secular evolution must be done following one of these level curves. This technique of phase portrait drawing has already proved efficiency to describe non-linear dynamics, such as in resonant configurations in the β Pictoris case (Beust & Morbidelli 1996; Beust & Valiron 2007).

4.2. Application to a test particle perturbed by Fom b

The result in the case of a disk test particle perturbed by Fom b is shown in Fig. 7 for three planet eccentricity values (from left to right): $e = 0.1$, $e = 0.5$, $e = 0.94$. Of course, given our orbital determination, the latter value is more relevant for Fom b. The semi-major axis ratio was fixed to $a/a' = 1.2$, as typical of the situation under study. Assuming indeed $a' = 120$ au for Fom b, $a/a' = 1.2$ leads to $a = 144$ au, i.e., a typical particle in the middle of the dust belt (Kalas et al. 2005). We also checked nearby a/a' values also representative for various belt particles. We do not show the corresponding phase portraits here. The Hamiltonian topology described in Fig. 7 turns out indeed to be only slightly affected by the fixed a/a' value, so that the

conclusions we derive here with $a/a' = 1.2$ still hold. Similarly, the mass ratio between the planet and the star was fixed to $m/M = 10^{-6}$ to build the phase portraits, i.e., an Earth-sized planet. Changing m/M appears not to change anything noticeable to the shape of the Hamiltonian level curves, so that we do not show corresponding phase portraits which are virtually identical to those displayed here. This can be understood easily. The variable part of H, which is responsible for the topology, is just proportional to m. Therefore changing m only scales that variable part accordingly but does not affect the global topology.

In the phase portraits of Fig. 7, the red curve separates regions where both orbits not only overlap in distance, but actually cross each other (assuming they are coplanar) from regions where they do not. We first describe the $e' = 0.1$ case (left plot). We note an island of ν-libration around $\nu = 0$ surrounded by smooth ν-circulating curves. We stress that this phase portrait actually faithfully describes the pericenter glow phenomenon. Any particle moving along a ν-circulating curve will be subject to a precession of ν (i.e., of the longitude of periastron ϖ) coupled with an eccentricity modulation, and the maximum eccentricity will be reached for $\nu = 0$, i.e., when both orbits are apsidally aligned. This is characteristic for pericenter glow, and this secular evolution exactly matches the circular path of $z(t)$ in complex plane described above. The same applies to particles moving in the ν-libration island around $\nu = 0$. This corresponds to cases where the circular $z(t)$ path does not encompass the zero point. This situation can be viewed as a secular resonance where ϖ no longer circulates.

The situations with $e' = 0.5$ and $e' = 0.94$ are different. With $e' = 0.5$, the island of ν-libration around $\nu = 0$ is still present, but it reaches now much higher eccentricities. It actually encircles a small region in (ν, e) space where both orbits do not cross. But the main difference concerns the circulating curves. They all reach very high eccentricities, virtually $e = 1$. This means that any particle starting at low eccentricity is about to evolve to this very high eccentricity regime, unless it is subject to a close encounter before. Contrary to what could be suggested from the phase portrait, these particles do not pass beyond $e = 1$, i.e., they are not ejected by the secular process. Our numerical simulations show that they pass through a very high eccentricity maximum before going down in the diagram (see below). This does not show up in Fig. 7, but can be understood in terms of orbital energy. As the semi-major axis a is a secular invariant, so is the orbital energy $-GM/2a$ (the fixed part of Hamiltonian H). It thus remains negative, hence the particle remains bound to the star. The only way to eject a particle here is to have a close encounter which has the ability to affect the orbital energy.Strictly speaking, ν does not circulate in this regime, but rather librates around $\nu = 180°$. Such $\nu = 180°$-librating curves are in fact already present in the $e' = 0.1$ case, but only in the very high eccentricity regime (top of the diagram). With $e' = 0.5$, this regime extends down to low eccentricities and the ν-circulating regime has disappeared.

The situation at $e' = 0.94$ is similar to that with $e' = 0.5$, except that it is even more drastic. The island of ν-libration is now confined to a tiny region close to $\nu = 0$ at high eccentricity. As a consequence, nearly all particles initially at low eccentricity in the disk must evolve to the very high eccentricity regime. We claim that this phase portrait exactly describes the dynamics observed in Figs. 5 and 6. We must specify here that the level curves of Fig. 7 are explored in a fixed sense that is imposed by Hamiltonian dynamics. For $e' = 0.94$, basically the left part of the diagram $\nu < 180°$ corresponds to growing eccentricities, while the right part $\nu > 180°$ corresponds to decreasing eccentricities. Now, consider a disk of particles initially at low eccentricities and random ν values. Following the $\overline{H}$ level curves, all particles will see their eccentricity grow when they reach $60° \lesssim \nu \lesssim 90°$. Irrespective of their initial ν value, they will all have similar longitudes of periastron during their eccentricity growth phase up to $e \simeq 1$. This is the exact origin of the eccentric disk tilted by $\sim 70°$ we observe in Figs. 5 and 6. Remember that in these simulations we had chosen the perturbing planet in such a way that $\varpi' = 0$, so that $\nu = \varpi$.

To illustrate this, we plot in Fig. 8 snapshots of the simulations described in Figs. 5 and 6, but in (ν, e) space to better compare with Fig. 7. The first four plots (upper plots and lower left one) show the evolution with $m = 0.002\,M_{\rm Jup}$ (Fig. 6) at various epochs. The correspondence with the phase portrait in Fig. 7 is striking. We clearly see the eccentricity growth phase of the particles with constrained ν. A discrepancy can nevertheless be noted in the lower left plot (at $t = 440$ Myr) with respect to the corresponding plot in Fig. 6, where we note that the global orientation of the disk leads to suggest that most particles have $0° < \nu < 180°$, while in Fig. 8, it turns out that at the same time, they mostly have $180° < \nu < 360°$. As explained in Sect. 5, this apparent discrepancy is due to an inclination effect. At this time, most particles have indeed moved to retrograde orbits, which does not show up in the projected upper view of Fig. 6.

We also see that once the particles reach high eccentricities, they start to diffuse in the upper part of the diagram, before starting to get down to lower eccentricities in the right part of the diagram. But at this level the cloud of particles is much less concentrated in (ν, e) space, resulting in a less sharp eccentric disk. This diffusion is due to the difference in secular evolution timescales for the individual particles. All particles do not rigorously evolve at the same speed in (ν, e) space, so that they inevitably diffuse after a few cycles. This is illustrated in the fifth plot of Fig. 8 (lower middle), which corresponds now to $m = 0.02\,M_{\rm Jup}$ (Fig. 5) at $t = 200$ Myr. As pointed out above, the dynamical evolutions in both cases are almost identical, but with $m = 0.02\,M_{\rm Jup}$ it is just achieved faster, actually in a manner proportional to m, as the variable part of H is $\propto m$. The situation at $t = 200$ Myr with $m = 0.02\,M_{\rm Jup}$ can therefore also be regarded as virtually corresponding to $t = 2$ Gyr with $m = 0.002\,M_{\rm Jup}$, as long as close encounters can be neglected. At this stage, we see that the cloud of particles has diffused in all parts of the diagram. A kind of steady-state regime has been achieved where individual particles are at random phases of their evolution tracks. They still gather around $\nu \simeq 70°$ and $\nu \simeq 290°$ when their eccentricities grow or decrease, but the disk no longer achieves an eccentric ring shape (Fig. 5). This picture does not change drastically if we adopt different orbital parameters for the perturbing planet. Assuming different eccentricity and semi-major axis values, the gathering points at $\nu \simeq 70°$ and $\nu \simeq 290°$ appear to move by no more than $\sim 20°$.

It could been argued looking at the left plot of Fig. 7 that a disk of particles starting at zero eccentricity and perturbed by a planet with $e' = 0.1$ may start start to gather around $\nu \simeq 70°$ before filling all the available phase space and generate the pericenter glow phenomenon. This corresponds indeed to the transient spiral structures noted by Wyatt (2005). But this transient phase lasts at most a few Myrs (Wyatt 2005), which is very short. The steady-state regime, characterized by diffusion of particles into the phase space and subsequent apsidal alignment, sets on more quickly.

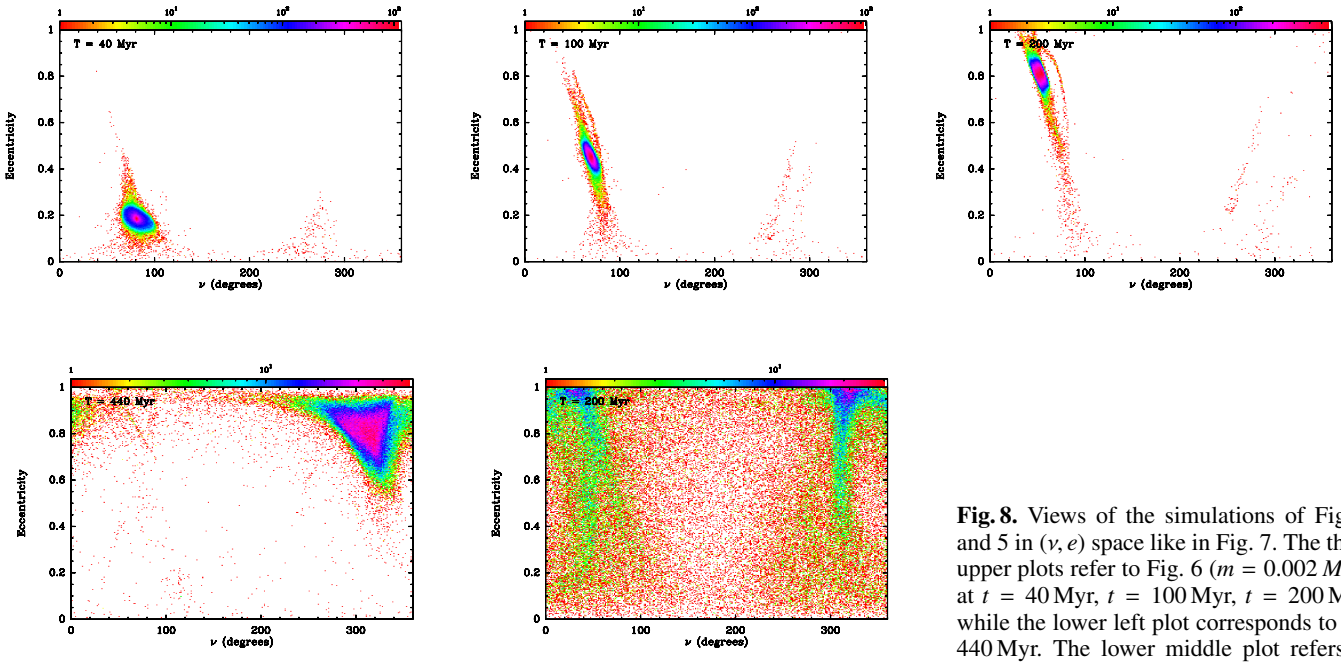

Fig. 8. Views of the simulations of Fig. 6 and 5 in (ν, e) space like in Fig. 7. The three upper plots refer to Fig. 6 ($m = 0.002\,M_{\rm Jup}$) at $t = 40$ Myr, $t = 100$ Myr, $t = 200$ Myr, while the lower left plot corresponds to $t = 440$ Myr. The lower middle plot refers to Fig. 5 ($m = 0.02\,M_{\rm Jup}$) at $t = 200$ Myr.

4.3. Disk self-gravity and very low mass regime for Fom b

As pointed out above, the simulations involving a very low mass Fom b might be unrealistic because of the neglected disk mass. In our simulations indeed, the disk is made of massless particles which do not influence Fom b's orbit nor perturb each other. This approximation remains justified as long as Fom b's mass remains higher than the disk mass. According to Wyatt & Dent (2002) and Chiang et al. (2009), a mass of planetesimals ranging between $\sim 3\,M_\oplus$ and $\sim 20\,M_\oplus$ is required to sustain the dust production in the debris disk over the age of the star. It is of course hard to derive a more accurate estimate, but obviously, when we consider a $6\,M_\oplus$ Fom b, its mass is comparable to that of the disk, and with $m = 0.6\,M_\oplus$ it is clearly below. Consequently the reality of some of our simulations may appear questionable.

Strictly speaking, addressing this issue would require to perform simulations with a self-gravitating disk over the age of the star, which would be extremely computing time consuming. It is nevertheless possible to derive the effect of the disk mass using our semi-analytical approach. As long as close encounters and mean-motion resonances are not considered, which is the case here, the secular effect of an elliptic disk is basically identical to that of a planet with the same mass and orbiting on the same orbit. In fact, the averaging process described in Eq. (8) is virtually equivalent to replacing both bodies with massive rings spread over their orbits. Terquem & Ajmia (2010) showed for instance directly that a planet perturbed by a massive inclined disk is subject to Kozai effect exactly as if it was perturbed by another planet.

The first thing we need to investigate is the secular effect of a massive ring on the orbit of Fom b. This situation can be modelled treating Fom b as a test particle initially at $a = 120$ au and $e = 0.94$, perturbed by a planet orbiting at $a' = 140$–150 au and $e' = 0.1$. This is in fact very close to the situation depicted in the left plot of Fig. 7, except that the semi-major axis ratio should be now taken as $a/a' \simeq 0.8$ instead of 1.2. The result is shown in Fig. 9, which appears indeed very similar to the left plot of Fig. 9. The initial configuration of Fom b ($e = 0.94$ and $\nu \simeq 0$)

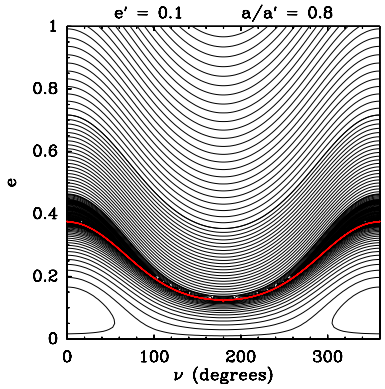

Fig. 9. A phase portrait equivalent to the left plot of Fig. 7, but with $a/a' = 0.8$. This situation mimics the dynamics of Fom b as perturbed by a massive disk (see text).

corresponds to the top curves of the phase diagram. Following any of these curves, we see that due to the disk perturbation, the periastron of Fom b is subject to precession, but that in any case, its eccentricity will never get below ~ 0.6. Figure 7 shows then that the dynamics of disk particles perturbed by a $e = 0.6$ Fom b is very similar to that with a $e = 0.94$ Fom b. We are thus confident in the fact that even if its orbit is secularly perturbed by the disk, this does not prevent Fom b from perturbing the disk particles as described above.

The second potential effect is the self-gravity of the disk, i.e., the perturbation the massive disk can rise on disk particles. This can be investigated adding a second perturbing planet to the situ-

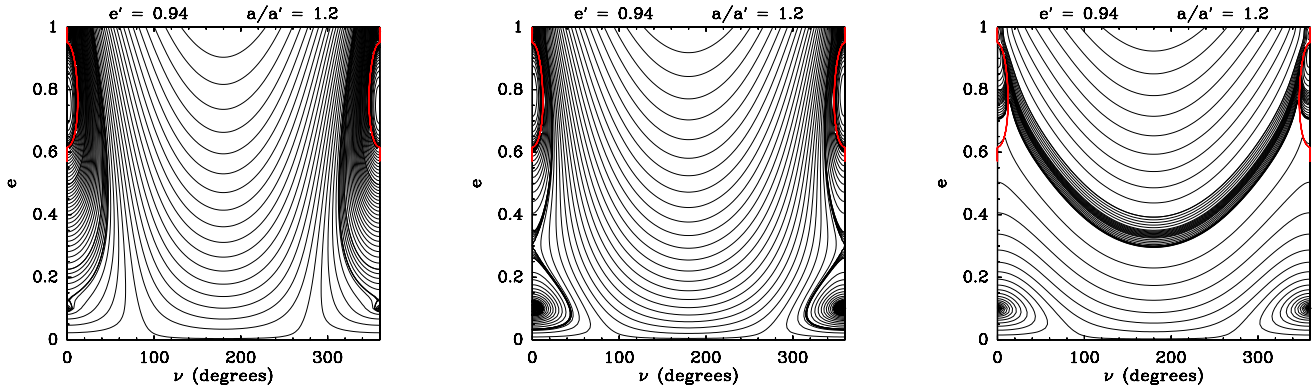

Fig. 10. Phase portraits similar to those of Fig. 7 but to which we have added a second perturbing planet (representing the disk) apsidally aligned with the first one (Fom b). The second planet is assumed to orbit at the same semi-major axis as the disk particle. The important parameter is the mass ratio ρ between the two planets. **Left plot:** $\rho = 0.1$, i.e., a disk 10 times less massive than Fom b; **Middle plot:** $\rho = 1$, disk and Fom b have equal masses; **Right plot:** $\rho = 10$, i.e., a disk 10 times more massive than Fom b.

ation depicted in Fig. 7 and averaging the resulting Hamiltonian over all orbits. This is illustrated in Fig. 10. Fom b'eccentricity is taken equal to 0.94. The planets are taken apsidally aligned to mimic the alignment between Fom b and the disk, and the second planet's semi-major axis is taken equal to that of the test particle, i.e., 1.2 times that of Fom b. The important parameter here is the mass ratio ρ between the perturbing planets, i.e., between the disk and Fom b. In Fig. 10 we show phase diagrams for $\rho = 0.1$ (left plot, disk less massive than Fom b), $\rho = 1$ (middle plot, equal masses), $\rho = 10$, (right plot, disk more massive than Fom b). With $\rho = 0.1$, the situation is very close to that of Fig. 7 with $e = 0.94$, which is not surprising as Fom b dominates the dynamics. With $\rho = 1$ (middle plot) the situation is now somewhat changed. An island of libration appears now at low eccentricity around $\nu = 0$. This island corresponds to a secular resonance pericenter glow region controlled by the second planet. But not all disk particles moving at low eccentricity are concerned by this behaviour. Contrary to a pure pericenter glow configuration (left plot of Fig. 7), those which are not trapped in the libration island actually follow a route that drives them to high eccentricity almost exactly as if the second planet was not there. Those particles are stilled controlled by the highly eccentric Fom b. Given the limited size of the libration island around ν, the latter class of particles is potentially more crowded that the former. As a result we may claim that a disk perturbed by an equal mass Fom b would still see a significant part of its particles evolve towards high eccentricities and yield a disk figure that does not match the present day observation.

With $\rho = 10$ (right plot), now the bottom part of the phase diagram closely looks like that of the left plot of Fig. 7. Only the particles initially moving at high eccentricity actually feel a noticeable perturbation by Fom b. Conversely, all particles moving at low eccentricity follow a route entirely controlled by the disk treated as a second planet. This does not explain the eccentricity of the disk, as the second planet was initially given the suitable eccentricity. All we stress here is that we expect here the disk to be no longer affected by Fom b, which is not surprising as it is now 10 times less massive than the disk.

We also checked intermediate values of ρ (not shown here). When increasing ρ from 1 to 10, the island of libration at low eccentricity around $\nu = 0$ gets higher. The transition between the regime where a significant part of the low eccentricity particles are still perturbed towards high eccentricity and that where all particles remain at low eccentricity occurs around $\rho \simeq 3.5$. As a result, even if Fom b is 3 times less massive than the disk, it can still perturb it in such a way that many particles are driven towards high eccentricities. Given the disk mass estimates by Wyatt & Dent (2002) and Chiang et al. (2009), we conclude that a super-Earth sized Fom b (like in the simulation of Fig. 5) is very probably capable of efficiently perturb the disk, while this is certainly no longer the case for a sub-Earth sized Fom b. Our corresponding simulation (Fig. 6) can therefore be considered as unrealistic given the probable mass of the disk. We nevertheless presented it here to illustrate the mechanism we describe and how its time-scale scales with the planet's mass.

We may thus distinguish two regimes : For a ~super-Earth sized Fom b and above, the dynamics outlined in the previous section holds, while for lower masses, the secular effect of Fom b is overridden by the self-gravity of the disk so that its influence of the disk is very small.

5. Vertical structures

As of yet, we only cared about planar structures, Fom b and the disk were assumed to be coplanar. This choice was indeed guided by the result of the orbital determination. However, in all simulations presented above, the disk of particles was not initially strictly planar. While Fom b was assumed to lie in the mid-plane of the disk, a random inclination between 0 and 3° was given to the particles at the beginning, as to mimic a realistic inclination dispersion within a real disk. Figures 3–6 present in fact projected upper views of the disk. We come now to discussing vertical structures in the disk and their consequences.

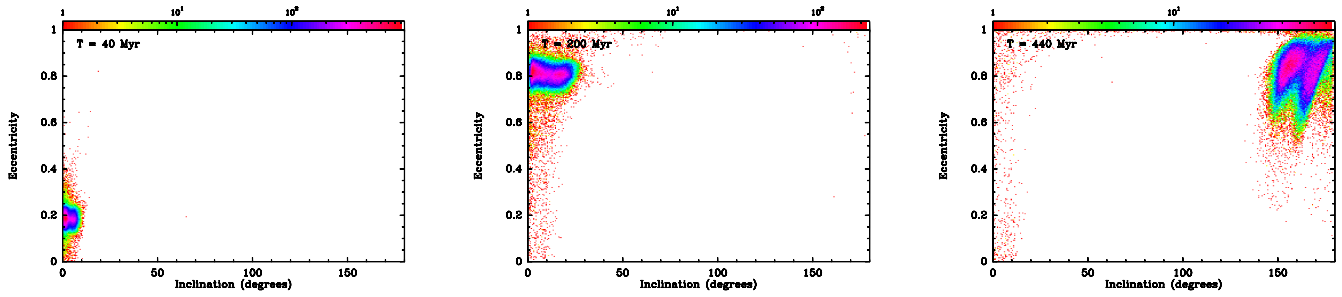

Fig. 11. Same simulation as presented in Fig. 6, but in inclination–eccentricity space (i, e), at the same corresponding times : $t = 40$ Myr (left), $t = 200$ Myr (middle), $t = 440$ Myr (right)

All the results presented below concern the simulation with the $m = 0.002\,M_{\rm Jup}$ Fom b, as it is the slowest evolving one, keeping in mind that this simulation is probably unrealistic if we consider the self-gravity of the disk. But the secular evolution we present here holds for any mass regime. For higher masses, the evolution is the same except that it occurs faster.

Figure 11 shows the same simulation as presented in Fig. 6, but in inclination–eccentricity space. We see that at the beginning of the simulation ($t = 40$ Myr), all particles are as expected still at low inclination while the eccentricities have started to grow; at $t = 200$ Myr, the eccentricities are high, but the inclinations are still moderate, although the peak inclination value of the distribution is now $\sim 30°$. Recalling that all inclinations were initially below 3°, this shows that the inclinations have grown significantly; at $t = 440$ Myr, the particles have now passed their peak eccentricity phase (see Fig. 8), but most inclinations have now jumped close to 180°, meaning they have evolved to retrograde orbits.

Basically, the typical inclination evolution of a disk particle is the following : as long as the eccentricity grows, the inclination keeps increasing while remaining moderate. When the eccentricity nearly reaches 1, the inclination rapidly jumps close to 180° and keeps evolving retrograde afterwards.

This behaviour was of course already present in Figs. 3–6, but somewhat hidden by the upper view projections. As noted above, at $t = 440$ Myr in Fig. 6, most particles seem to have $0° < \nu < 180°$, while in Fig. 8, they obviously have $180° < \nu < 360°$. This discrepancy is indeed due to the inclination. At this time, most particles already have retrograde orbits, so that once projected onto the OXY plane, the apparent longitude of periastron $\Omega + \omega \cos i$ rather corresponds to $\Omega - \omega$ than to $\Omega + \omega$. To explain this behaviour, we must get back to our semi-analytical study. The main difficulty here is that contrary to the planar problem, the averaged Hamiltonian of the particle has now two degrees of freedom. The averaged Hamiltonian is usually described by the classical canonically conjugate Delaunay variables :

$$\begin{array}{l} \omega \ , \ G = \sqrt{a(1-e^2)} \\ \Omega \ , \ G\cos i \end{array} \quad , \tag{9}$$

or similarly, introducing $\varpi = \omega + \Omega$:

$$\begin{array}{l} \varpi \ , \ P = \sqrt{a}\left(1 - \sqrt{1-e^2}\right) \\ \Omega \ , \ G\cos i \end{array} \quad , \tag{10}$$

where i is the inclination. As long as the eccentricity does not reach 1, the fact that the inclination remains moderate actually validates the planar motion which is described by the canonically conjugate variables (ϖ, P), or equivalently (ν, P). Now,

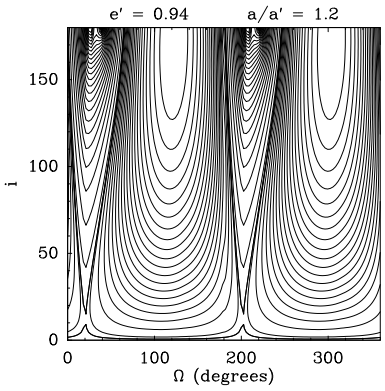

Fig. 12. A phase portrait in (Ω, i) space of the averaged spatial Hamiltonian of a massless particle perturbed by Fom b in the same conditions as in Fig. 7, computed with constant $\nu = 65°$ and $e = 0.8$. This approximately describes the secular inclination evolution of the particle during its eccentricity growth.

Fig. 7 shows that with $e' = 0.94$, a particle starting at low eccentricity will evolve towards high eccentricity with ~constant ϖ ($\nu \simeq 70°$). As ϖ and P are canonically conjugate, a ~constant ϖ means $\partial\overline{H}/\partial P \simeq 0$, which is equivalent to $\partial\overline{H}/\partial e \simeq 0$. We may thus expect the Hamiltonian to weakly depend on the eccentricity during this phase. The dynamics of the particle during the eccentricity increase will then be approximately well described drawing level curves of Hamiltonian in $(\Omega, G\cos i)$ space, or equivalently in (Ω, i) space for a fixed $\nu \simeq 70°$ and a fixed arbitrary e value .

Figure 12 shows the result of this computation, performed with fixed $\nu = 65°$ and $e = 0.8$. We see two major libration islands that inevitably drive any particle starting at low inclination towards high inclination. The Hamiltonian curves are here again explored clockwise. We checked that other choices of ν and e along the separatrix of the right plot in Fig. 7 lead to similar diagrams. Following the Hamiltonian level curves, we clearly see how the particles move towards retrograde orbits.

To check the reality of this analysis, we plot snapshots of our simulation with $m = 0.002\,M_{\rm Jup}$ (Figs. 6 and 11) in (Ω, i)

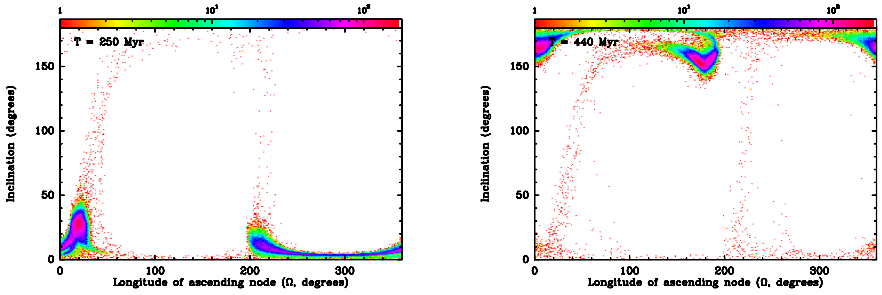

Fig. 13. Views of the simulation of Fig. 6 and in (Ω, i) space like in Fig. 12 at t = 250 Myr and t = 440 Myr

space like in Fig. 12. This is done in Fig. 13 at t = 250 Myr and t = 440 Myr. At the beginning of the simulation (not shown here), all inclinations are below 3° while the Ω values are drawn randomly. All particles appear thus in the bottom of the diagram in (Ω, i) space. This remains true for a long time as long as the inclinations remain low. At t = 250 Myr (at this time most particles have already $e > 0.8$, hence our choice of e in Fig. 12), the inclinations have started to grow with Ω value concentrated around 20° and 200°. Obviously, the particles follow a route in (Ω, i) space that is very close to the level curves of Fig. 13. At t = 440 Myr, all particles have moved in the upper part of the diagram following this route and become retrograde. Afterwards, the particles get back to low inclinations and cycle around the two island of libration in (Ω, i) space.

For higher Fom b masses like in Fig. 5 ($m = 0.02\,M_{\rm Jup}$), the same dynamics is observed but it occurs proportionally faster. At the end of the simulation, we have at each time approximately as many prograde particles as retrograde ones. The initial disk of particles now assumes a cloud shape rather than a disk shape. This is illustrated in Fig. 14, which shows the disk of particles, here again for the $m = 0.002\,M_{\rm Jup}$ case and at the same epochs as in Fig. 6, but viewed with a 67° inclination with respect to pole-on. This mimics the viewing conditions of Fom b's disk from the Earth. At t = 20 Myr, the disk still appears as a clearly eccentric disk with moderate eccentricities. This is marginally the case at t = 200 Myrs and obviously no longer applies at t = 440 Myrs. At this stage (and even earlier) the simulated disk no longer matches the observed one.

The simulations presented here assumed that the orbital plane of the perturbing Fom b is coplanar with the mid-plane of the disk. As the coplanarity is not strictly established observationally due to the uncertainties, we checked other configuration with disks inclined up to 20° with respect to the orbital plane of the planet. In all cases, the behaviour reported in the previous sections remains almost unchanged. All particles evolve towards high eccentricities and become retrograde with respect to the planet's orbital plane when reaching very high eccentricities, so that our conclusions are unchanged : the disk inevitably gets a too high eccentricity to match the observations. Moreover, due to the evolution of the inclinations of the particles, the disk no longer assumes a disk shape.

6. Discussion

6.1. Disk shaping by Fom b: an unlikely scenario ?

Our numerical and semi-analytical study shows that if the perturber is massive enough to efficiently affect the disk, the pericenter glow dynamics that applies in the low eccentricity regime cannot be transposed to the case where the perturber is very eccentric. In that case, we have a completely different dynamics where the disk particles reach very high eccentricities and high inclinations. In a first transient phase, the disk actually achieves an eccentric disk shape with growing eccentricity, but afterwards the particles diffuse in phase space and the steady-state regime does no longer correspond to an eccentric disk figure. A moderate eccentricity approximately matching the observed one is in all cases reached shortly after the beginning of the secular process. The desired time roughly scales as

$$t_{e=0.1} = \frac{0.04}{m} \quad , \tag{11}$$

where m is given in Jupiter masses and $t_{e=0.1}$ in Myrs. Reaching this stage at t = 440 Myr would indicate an extremely low planetary mass (∼ 2.3 Lunar masses). As described in the previous section, such a low mass perturber is unlikely to be able to perturb the dust ring, given its probable mass. In this regime, the dynamics of the disk is virtually unaffected by Fom b.

Alternatively, the perturbation of the disk might be recent rather than primordial. According to that scenario, Fom b's mass should be closely linked with the date of this event by Eq. (11) to generate a disk with the suitable bulk eccentricity today. This situation is nevertheless a transient phase, as the bulk disk eccentricity is supposed to keep growing. The disk can only survive in its observed configuration for a short time period comparable to $t_{e=0.1}$. As a consequence, the higher Fom b's mass, the less probable this picture is.

In all cases however, the transient elliptic disk is not apsidally aligned with the perturbing planet, which does not match our orbital determination for Fom b. However, it is difficult to derive a firm conclusion on this sole basis, as the determination of the orbital alignment is only accurate within a few tens of degrees. It must nevertheless be noted that a ∼ 70° misalignment would only be marginally compatible with the data.

Consequently, we come to a contradiction. If we forget its high eccentricity, the compared orientations of Fom b's orbit and the dust ring share all characteristics of a pericenter glow phenomenon. But our analysis revealed that pericenter glow no longer applies at the eccentricity of Fom b. Even if we consider the lowest possible eccentricity according to our MCMC distribution ($e' \simeq 0.6$, Fig. 1), Fig. 7 shows that the topology of the Hamiltonian map is already very different from that leading to pericenter glow.

We thus have two conclusions. First, Fom b is very likely to be a low mass planet (∼Earth or super-Earth sized). On a ∼ 10 Myr time-scale, a massive planet would destroy the dust ring (Fig. 3). Before that, its secular action would inevitably drive the disk particles towards high eccentricities incompatible with the observations. According to Eq. (11), this occurs within ∼ 10^5 yrs, which is very short. This would require Fom b to

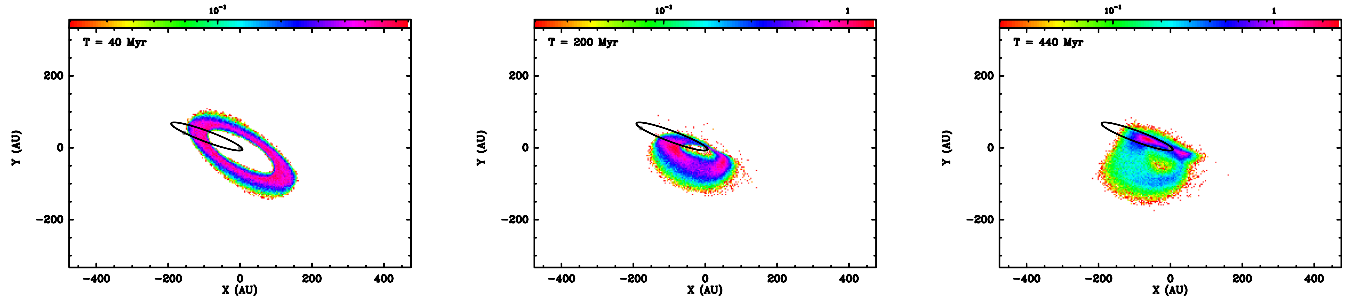

Fig. 14. Same simulation as presented in Fig. 6, at the same corresponding times (left: t = 40 Myr, middle: t = 200 Myr, right: t = 440 Myr) but the disk is now viewed with a 67° with respect to pole-on, as to mimic the viewing conditions of Fomalhaut's disk from Earth

have been put on its present day orbit more recently than that. Given the age of the star, this seems rather unlikely. We must however note that this is only an order-of-magnitude estimate. Equation (11) is actually an empirical fit that hides some unknown dependencies on the semi-major axis and the eccentricity of Fom b. Putting a lower mass limit on Fom b is less straightforward. We have seen that below ∼Earth-sized, the planet has virtually no secular effect on the disk, but this is not incompatible with the observations. It would just mean that something else than Fom b is responsible for the disk shaping. In fact, a very low mass Fom b would hardly retain enough dust around it to be detected directly. This was earlier suggested by Kennedy & Wyatt (2011) and more recently by the numerical experiments in Kalas et al. (2013). Kalas et al. (2013) propose a lower limit to the mass between Ceres and Pluto, under the assumption that the more likely models are the most long lived, and this requires a cloud of dust to be bound to a central object and have sufficient size to explain the optical luminosity. Alternatively, Fom b could also just be short lived cloud of dust with no planet mass inside, such as might be created when planetesimal in the 10–100 km size range collide with each other (Kalas et al. 2008; Galicher et al. 2013).

Our second conclusion is that Fom b can hardly be responsible for the shaping of the dust ring into a moderately eccentric ring on its own. This is actually independent of its mass. If we assume that Fom b is ∼sub-Earth sized, then it is just not massive enough to efficiently influence the ring. According to our semi-analytical study, this regime holds up to ∼Earth-sized planets. If Fom b is more massive, then it has a secular action on the dust ring and inevitably drives particles towards high eccentricity. This occurs in any case before the age of the star. Typically, with a super-Earth sized Fom b, the present-day disk eccentricity is obtained ∼ 10–20 Myr after the beginning of the simulation. This would imply Fom b to have been put on its orbit that time ago. Here again, given the age of the star, this seems unlikely, but less unrealistic than the 10^5 yrs required for a massive planet. Therefore we cannot rule out this possibility. But if Fom b was put on its present-day orbit a few 10^7 yrs ago by some scattering event, necessarily this event was caused by another, more massive planet (see below) which very probably controls the dynamics of the ring more efficiently than Fom b itself. So, irrespective of its mass, Fom b is very probably not responsible for the sculpting of the observed dust ring.

6.2. Another planet

If Fom b cannot be responsible for the disk sculpting, a subsequent conclusion is that there must be another, more massive planet shepherding the dust ring. Kalas et al. (2013) came to the same conclusion and their numerical experiments assume that a Jupiter mass planet exists with $a \sim 120$ au, $e \sim 0.1$ and serves to dynamically maintain the inner edge of the belt. Chiang et al. (2009) actually already invoked the hypothesis of another planet accounting at least partly for the forced eccentricity of the belt, concluding that given the residual proper acceleration of Fomalhaut measured by the Hipparcos satellite, a $\sim 30\,M_{\rm Jup}$ brown dwarf could be orbiting Fomalhaut at ∼ 5 au. This possibility was nevertheless ruled out by Kenworthy et al. (2013), who compiled their own observations with other direct searches for additional companions to Fomalhaut (Absil et al. 2011; Kenworthy et al. 2009). They conclude that no companion more massive than $\sim 20\,M_{\rm Jup}$ is to be expected from 4 au to 10 au and than $\sim 30\,M_{\rm Jup}$ closer. Less massive companions (Jovian-sized ?) are nevertheless not excluded. The main problem in this context is to combine the shepherding of the disk and the survival of Fom b. Basically, to confine the inner edge of the dust belt at 133 au as it is observed, a moderately eccentric Jovian-sized planet must orbit the star between ∼ 90 au and ∼ 120 au, depending on its mass (see detailed calculations by Chiang et al. 2009). But given its high eccentricity, Fom b's orbit will inevitably cross the orbit of that additional planet (let us name it Fom c hereafter), which raises the issue of its dynamical stability. Figure 1 shows indeed that Fom b's periastron is most probably as low as ∼ 8 au.

There are two ways to possibly solve this paradox (see Fig. 15). The first scenario to suppose that Fom b is locked in a secular (apsidal) resonance with Fom c that prevents the orbits to cross each other. This occurs for instance inside the loops around $\nu = 0$ delimited by the red curves in the $e' = 0.5$ and $e' = 0.94$ cases in Fig. 7. Inside these loops, the particle is subject to a secular resonance where it remains apsidally aligned with the perturbing planet, while it never crosses its path. Here the particle would be Fom b itself, while Fom c would be the perturber. This kind of locking in secular resonance has already been observed in some extrasolar systems like υ Andromedae (Chiang & Murray 2002). Although the eccentricity regime is higher here, this cannot be excluded. It would have the advantage that it would explain the apsidal alignment of Fom b with the dust ring, as both would be apsidally aligned with Fom c (the belt being apsidally aligned with Fom c thanks to pericenter glow). Figure 7 nevertheless shows that locking in secular resonance at very high eccentricity, as it is the case for Fom b,

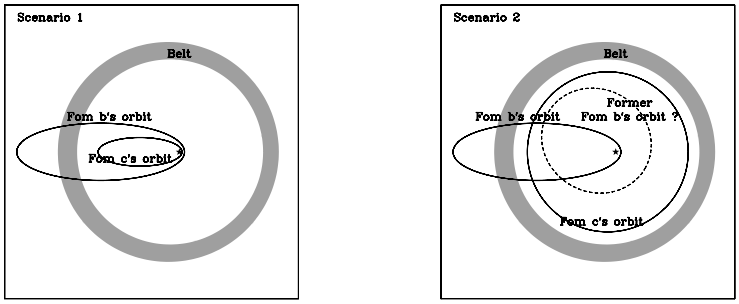

Fig. 15. Sketch of the two scenarios for Fom b and Fom c interaction. **Left :** Scenario 1, with non-crossing orbits for Fom b and Fom c, locked in apsidal resonance; **Right :** Scenario 2, with Fom b recently scattered from an inner orbit onto its present day one by a moderately eccentric Fom c. The latter orbital configuration of Fom b is supposed to be metastable.

requires a high eccentricity perturber (Fom c). As Fom c is assumed to control the dynamics of the belt instead of Fom b, one needs to explain now how the disk remains at low eccentricity, in other words, why a regular pericenter glow dynamics seems to apply to the disk with respect to Fom c despite its high eccentricity. This is in contradiction with our previous analysis, but could possibly be due to a wider separation between Fom c and the disk. Although we cannot firmly rule it out, we nevertheless consider this scenario as less probable. Obviously a dedicated parametric study is required to determine in which conditions it could eventually be possible.

The second scenario assumes that Fom b is presently on a metastable orbit (Fig. 15). In this context, Fom b would have resided initially closer to the star, and it would have been put more or less recently on its present orbit by a scattering event, possibly originating from Fom c. We are then back to the hypothesis of a transient configuration with a more or less recent scattering event. This scenario would quite naturally explain the very high eccentricity of Fom b and its puzzling belt-crossing orbital configuration. We could also possibly explain the presence of solid material around this planet, which actually renders it observable. This material could actually be captured from the dust belt each time Fom b crosses it. The plausibility of this scenario is basically a matter of time-scales compared to the masses of both planets. Figure 4 shows that after $\sim$ 100 Myr, a particle crossing the orbit of a Jovian-sized planet has only a few percent chances not to have been ejected earlier by a close encounter. It can be argued that this time-scale is not that short compared to the age of the star. This depends however on the mass of the perturber, here Fom c. Assuming a more massive Fom c would inevitably drastically shorten the ejection time-scale and render the present day observation of Fom b on its metastable orbit very unlikely. Conversely, a less massive (Saturn-sized ?) Fom c would make it more plausible, but it should remain massive enough to be able to efficiently sculpt the dust belt. Another difficulty with this scenario is that it does not provide a natural explanation for the apsidal alignment between Fom b and the dust belt. As a result of pericenter glow dynamics, the dust belt would be apsidally aligned with Fom c. It would then be necessary to explain how Fom b would have been put on an apsidally aligned orbit by the scattering action of Fom c. We must however keep in mind that the observed apsidal alignment of Fom b with the disk is not accurately constrained, so that a fortuitous near-alignment within a few tens of degrees is still possible. In that scenario, the mass of Fom b is less constrained, as its perturbing action on the disk is recent. We stress however that a massive Fom b ($\sim$Jovian) is rather unlikely, for two reasons. First, scattering a Jovian-sized planet onto a high eccentricity metastable orbit would require a very massive Fom c, which could not fit the observational limits. Second, given the efficiency of close encounters with a massive Fom b, the scattering event should have occurred very recently. Given the age of the star, we would then be very lucky to witness this event today. For these reasons, we think that a low-mass Fom b is still more likely even in this second scenario. If Fom b is less massive than the Earth, then its influence on the disk is damped by the self-gravity of the disk so that no constraint can be derived anymore this way. The only limitation is then the survival of Fom b versus close encounters with Fom c.

Both scenarios turn out to present advantages and disadvantages. The first one is a steady-state configuration where the dynamical stability of Fom b as perturbed by Fom c is not ensured, and where the sculpting of the disk in its present-day shape by a very eccentric Fom c is questionable, but that would more naturally explain the apsidal alignment between the ring and Fom b; the second one points towards transient configuration with a more or less recent scattering event that placed Fom b on its current orbit. The likelihood of the former depends on the hypothetical dynamical stability of Fom b as perturbed by Fom c and on the hypothetical existence of configurations allowing the disk to remain at low eccentricity despite Fom c's high eccentricity, while that of latter is related to the evolution and survival timescales of the transient configuration, as compared to Fomalhaut's age. We nevertheless consider that scenario as more likely than the first one.

An alternative scenario would be that the dust confinement in Fomalhaut's disk is due to its interaction with gas without any Fom c, such as suggested recently by Lyra & Kuchner (2013). As of yet this cannot be confirmed nor ruled out. As pointed out by Lyra & Kuchner (2013), the key point is the hypothetical presence of gas in Fomalhaut's disk, moreover at such a long orbital distance. We know that younger debris disks like β Pictoris actually contain gas (Brandeker et al. 2004; Lagrange et al. 1996), but for an older system like Fomalhaut, it is less obvious. Only upper limits are available (Liseau 1999).

Both scenarios imply the presence of planets with very short periastron values. Fom b itself has a probable periastron in the 7–8 au range. If scenario 1 holds, then Fom c has an even shorter periastron than that. Lebreton et al. (2013) attributed the near-

and mid-infrared interferometric excesses of Fomalhaut (see also Mennesson et al. 2013; Absil et al. 2009) to an asteroid belt at about 2 au producing a mid-infrared excess, which subsequently produces even hotter dust detected in the near-infrared. To produce the observed amount of dust, Lebreton et al. (2013) argue that the inner belt had to be somehow excited. The presence of planets with such short periastron values could actually provide the suspected source of excitation, or, more generally, may be related to the process that placed Fom b on its peculiar. In scenario 1, Fom c would have a periastron in the 2-3 au range, which would be enough to excite a belt at 2 au. The dynamical stability of this belt would even be questionable and render this scenario unlikely. In scenario 2, the scattering event that more or less recently put Fom b on its present-day orbit causes it to suddenly approach the inner belt thanks to its low periastron. This could explain the excitation of the inner belt and the enhanced dust production.

In all cases, our main conclusions are that Fom b is very probably a low mass planet, possibly orbiting on a metastable orbit, and that another, more massive planet (Fom c) is required to control the disk dynamics and to be possibly responsible for the transient orbital configuration of Fom b. The interplay between both planets is still an open issue. Further work that continues to investigate and quantify the masses and orbits of the planets are clearly required. This will be the purpose of forthcoming work.

Acknowledgements. All computations presented in this paper were performed at the *Service Commun de Calcul Intensif de l'Observatoire de Grenoble* (SCCI) on the super-computer funded by *Agence Nationale pour la Recherche* under contracts ANR-07-BLAN-0221, ANR-2010-JCJC-0504-01 and ANR-2010-JCJC-0501-01. We gratefully acknowledge financial support from the French *Programme National de Planétologie* (PNP) of CNRS/INSU, and from the ANR through contract ANR-2010-BLAN-0505-01 (Exozodi). P. Kalas and J.R. Graham acknowledge support from NSF AST-0909188 and NASA Origins NNX11AD21G.

References

Absil O., Mennesson B., Le Bouquin J.-B., 2009, ApJ 704, 150
Absil O., Le Bouquin J.-B., Berger J.-P.,et al., 2011, A&A 535, A68
Augereau J.-C., Papaloizou J.C.B., 2004, A&A 414, 1153
Aumann H.H., 1985, PASP 97, 885
Beust H., Morbidelli A., 1996, Icarus 120, 358
Beust H., Valiron P., 2007, A&A 466, 201
Boley A.C., Payne M.J., Corder S., et al., 2012, ApJL 750, L21
Brandeker A., Liseau R., Olofsson G., Fridlund M. 2004, A&A 413, 681
Chauvin G., Lagrange A.-M., Beust H., et al., 2012, A&A 542, A41
Chiang E.I., Murray N., 2002, ApJ 576, 473
Chiang E.I., Kite E., Kalas P., Graham J.R., Clampin M., 2009, ApJ 693, 734
Currie T., Debes J., Rodigas T.J., 2012, ApJL 760, L32
Deller A.T., Maddison, S.T., 2005, ApJ 625, 398
Faramaz V., Beust H., Thbault, et al., A&A, submitted
Ford E.B., 2005, AJ 129, 1706
Ford E.B., 2006, ApJ 642, 505
Galicher R., Marois C., Zuckerman B., Macintosh B., 2013, ApJ 769, 42
Graham J.R., Fitzgerald M.P., Kalas P., Clampin M., 2013, AAS 221, 324.03
Holland W.S., Greaves J.S., Dent W.R.F., et al., 2003, ApJ 582, 1141
Janson M., Carson J.C., Lafrenière D., et al., 2012, ApJ 747, 116
Kalas P., Graham J.R., Chiang E., et al., 2005, Nature 435, 1067
Kalas P., Graham J.R., Chiang E., et al., 2008, Science 322, 1345
Kalas P., Graham J.R., Fitzgerald, M.P., Clampin M., 2013, ApJ 775, 56
Kennedy G.M., Wyatt M.C., 2011, MNRAS 412, 2137
Kenworthy M.A., Mamajek E.E., Hinz P.M., et al., 2009, ApJ 697, 1928
Kenworthy M.A., Meshkat T., Quanz S.P., et al., 2013, ApJ 764, 7
Lagrange A.-M., Plazy F., Beust H., et al., 1996, A&A 310, 547
Lebreton J., van Lieshout R., Augereau J.-C., et al., 2013, A&A 555, A146
Levison H.F., Duncan M.J., 1994, Icarus 108, 18
Liseau R., 1999, A&A 348, 133
Lyra W., Kuchner M., 2013, Nature 499, 18
Mamajek E.E., 2012, ApJ 754, L20
Marengo M., Stapelfeldt K., Werner M.W., et al., 2009, ApJ 700, 1647
Mennesson B., Absil O., Lebreton J., et al., 2013, ApJ 763, 199
Moerchen M.M., Churcher L.J., Telesco C.M., 2011, A&A 526, A34
Murray C.D., Dermott S.F., 1999, Solar System Dynamics (Cambridge: Cambridge University Press)
Press W.H., Teukolsky S.A., Vetterling W.T., Flannery B.P., 1992, Numerical Recipes (Cambridge Univ. Press.)
Quillen A.C., 2006, MNRAS 372, L14
Reche R., Beust H., Augereau J.-C., Absil O., 2008 A&A 480, 551
Terquem C., Ajmia A., 2010, MNRAS 404, 409
van Leeuwen F., Hipparcos, the New Reduction of the Raw Data, ed. 2007, Astrophysics and Space Science Library, vol. 350
Wyatt M.C., Dent W.R.F., 2002, MNRAS 334, 589
Wyatt M.C., 2003, ApJ 598, 1321
Wyatt M.C., Dermott S.F., Telesco C.M., et al., 1999, ApJ 527, 918
Wyatt M.C., 2005, A&A 440, 937

Bibliography

Absil, O., Defrère, D., Coudé du Foresto, V., et al. 2013, A&A, 555, A104

Acke, B., Min, M., Dominik, C., et al. 2012, A&A, 540, A125

Allard, F., Homeier, D., & Freytag, B. 2011, in Astronomical Society of the Pacific Conference Series, Vol. 448, 16th Cambridge Workshop on Cool Stars, Stellar Systems, and the Sun, ed. C. Johns-Krull, M. K. Browning, & A. A. West, 91

Armitage, P. J. 2010, Astrophysics of Planet Formation

Arnold, V. I. 1978, Mathematical methods of classical mechanics

Artymowicz, P. & Lubow, S. H. 1994, ApJ, 421, 651

Augereau, J.-C. 2009, in SF2A-2009: Proceedings of the Annual meeting of the French Society of Astronomy and Astrophysics, ed. M. Heydari-Malayeri, C. Reyl'E, & R. Samadi, 301

Augereau, J.-C. & Beust, H. 2006, A&A, 455, 987

Augereau, J. C., Lagrange, A. M., Mouillet, D., Papaloizou, J. C. B., & Grorod, P. A. 1999, A&A, 348, 557

Augereau, J. C., Nelson, R. P., Lagrange, A. M., Papaloizou, J. C. B., & Mouillet, D. 2001, A&A, 370, 447

Augereau, J. C. & Papaloizou, J. C. B. 2004, A&A, 414, 1153

Aumann, H. H., Beichman, C. A., Gillett, F. C., et al. 1984, ApJ, 278, L23

Backman, D. E. & Paresce, F. 1993, in Protostars and Planets III, ed. E. H. Levy & J. I. Lunine, 1253–1304

Baraffe, I., Chabrier, G., Barman, T. S., Allard, F., & Hauschildt, P. H. 2003, A&A, 402, 701

Beust, H. 2003, A&A, 400, 1129

Beust, H., Augereau, J.-C., Bonsor, A., et al. 2014, A&A, 561, A43

Beust, H. & Dutrey, A. 2006, A&A, 446, 137

Beust, H. & Morbidelli, A. 1996, Icarus, 120, 358

Beust, H. & Morbidelli, A. 2000, Icarus, 143, 170

Beuzit, J.-L., Boccaletti, A., Feldt, M., et al. 2010, in Astronomical Society of the Pacific Conference Series, Vol. 430, Pathways Towards Habitable Planets, ed. V. Coudé du Foresto, D. M. Gelino, & I. Ribas, 231

Boley, A. C., Payne, M. J., Corder, S., et al. 2012, ApJ, 750, L21

Bonfils, X., Delfosse, X., Udry, S., et al. 2013, A&A, 549, A109

Bonsor, A., Augereau, J.-C., & Thébault, P. 2012, A&A, 548, A104

Bonsor, A., Raymond, S. N., Augereau, J.-C., & Ormel, C. W. 2014, ArXiv e-prints

Burns, J. A. 1976, American Journal of Physics, 44, 944

Burns, J. A., Lamy, P. L., & Soter, S. 1979, Icarus, 40, 1

Carusi, A., Kresák, Ľ., & Valsecchi, G. B. 1995, Earth Moon and Planets, 68, 71

Chambers, J. E. 1999, MNRAS, 304, 793

Chauvin, G., Beust, H., Lagrange, A.-M., & Eggenberger, A. 2011, A&A, 528, A8

Chiang, E., Kite, E., Kalas, P., Graham, J. R., & Clampin, M. 2009, ApJ, 693, 734

Clampin, M., Krist, J. E., Ardila, D. R., et al. 2003, AJ, 126, 385

Correia, A. C. M., Udry, S., Mayor, M., et al. 2008, A&A, 479, 271

Crida, A., Masset, F., & Morbidelli, A. 2009, ApJ, 705, L148

Crida, A., Sándor, Z., & Kley, W. 2008, A&A, 483, 325

Currie, T., Cloutier, R., Debes, J. H., Kenyon, S. J., & Kaisler, D. 2013, ApJ, 777, L6

Deller, A. T. & Maddison, S. T. 2005, ApJ, 625, 398

Dohnanyi, J. S. 1969, J. Geophys. Res., 74, 2531

Draine, B. T. 2003, ARA&A, 41, 241

Dumusque, X., Pepe, F., Lovis, C., et al. 2012, Nature, 491, 207

Duncan, M., Quinn, T., & Tremaine, S. 1989, Icarus, 82, 402

Duncan, M. J., Levison, H. F., & Lee, M. H. 1998, AJ, 116, 2067

Duquennoy, A. & Mayor, M. 1991, A&A, 248, 485

Eiroa, C., Fedele, D., Maldonado, J., et al. 2010, A&A, 518, L131

Eiroa, C., Marshall, J. P., Mora, A., et al. 2013, A&A, 555, A11

Endl, M., Cochran, W. D., Hatzes, A. P., & Wittenmyer, R. A. 2011, in American Institute of Physics Conference Series, Vol. 1331, American Institute of Physics Conference Series, ed. S. Schuh, H. Drechsel, & U. Heber, 88–94

Ertel, S., Augereau, J.-C., Thébault, P., et al. 2014, in IAU Symposium, Vol. 299, IAU Symposium, ed. M. Booth, B. C. Matthews, & J. R. Graham, 338–339

Ertel, S., Wolf, S., Eiroa, C., et al. 2011, in EPSC-DPS Joint Meeting 2011, 678

Ertel, S., Wolf, S., & Rodmann, J. 2012, A&A, 544, A61

Faramaz, V., Beust, H., Augereau, J.-C., et al. 2014a, in IAU Symposium, Vol. 299, IAU Symposium, ed. M. Booth, B. C. Matthews, & J. R. Graham, 212–213

Faramaz, V., Beust, H., Thébault, P., et al. 2014b, A&A, 563, A72

Fernandez, J. A. & Ip, W.-H. 1984, Icarus, 58, 109

Ford, E. B., Kozinsky, B., & Rasio, F. A. 2000, ApJ, 535, 385

Fragner, M. M. & Nelson, R. P. 2010, A&A, 511, A77

Galicher, R., Marois, C., Zuckerman, B., & Macintosh, B. 2013, ApJ, 769, 42

Goldreich, P. & Tremaine, S. 1980, ApJ, 241, 425

Gomes, R. S., Morbidelli, A., & Levison, H. F. 2004, Icarus, 170, 492

Graham, J. R., Fitzgerald, M. P., Kalas, P., & Clampin, M. 2013, in American Astronomical Society Meeting Abstracts, Vol. 221, American Astronomical Society Meeting Abstracts, 324.03

Graham, J. R., Macintosh, B., Doyon, R., et al. 2007, in Bulletin of the American Astronomical Society, Vol. 39, American Astronomical Society Meeting Abstracts, 134.02

Gray, R. O., Corbally, C. J., Garrison, R. F., et al. 2006, AJ, 132, 161

Greaves, J. S., Holland, W. S., Moriarty-Schieven, G., et al. 1998, ApJ, 506, L133

Guilloteau, S., Dutrey, A., Piétu, V., & Boehler, Y. 2011, A&A, 529, A105

Hahn, J. M. & Malhotra, R. 1999, AJ, 117, 3041

Hamilton, D. P. & Miller, M. C. 2001, in Bulletin of the American Astronomical Society, Vol. 33, AAS/Division of Dynamical Astronomy Meeting #32, 1192

Hatzes, A. P., Cochran, W. D., Endl, M., et al. 2003, ApJ, 599, 1383

Henry, T. J., Soderblom, D. R., Donahue, R. A., & Baliunas, S. L. 1996, AJ, 111, 439

Holman, M. J. & Wiegert, P. A. 1999, AJ, 117, 621

Ida, S., Bryden, G., Lin, D. N. C., & Tanaka, H. 2000, ApJ, 534, 428

Janson, M., Carson, J. C., Lafrenière, D., et al. 2012, ApJ, 747, 116

Johnson, H. L., Mitchell, R. I., Iriarte, B., & Wisniewski, W. Z. 1966, Communications of the Lunar and Planetary Laboratory, 4, 99

Kaib, N. A., Raymond, S. N., & Duncan, M. 2013, Nature, 493, 381

Kalas, P., Graham, J. R., Chiang, E., et al. 2008, Science, 322, 1345

Kalas, P., Graham, J. R., & Clampin, M. 2005, Nature, 435, 1067

Kalas, P., Graham, J. R., Fitzgerald, M. P., & Clampin, M. 2013, ApJ, 775, 56

Kant, I. 1755, Allgemeine Naturgeschichte und Theorie des Himmels

Kennedy, G. M. & Wyatt, M. C. 2011, MNRAS, 412, 2137

Kenyon, S. J., Currie, T., & Bromley, B. C. 2014, ApJ, 786, 70

Kirsh, D. R., Duncan, M., Brasser, R., & Levison, H. F. 2009, Icarus, 199, 197

Kley, W. 2000, in IAU Symposium, Vol. 200, IAU Symposium, 211P

Kley, W. & Nelson, R. P. 2008, A&A, 486, 617

Kley, W. & Nelson, R. P. 2012, ARA&A, 50, 211

Kral, Q., Thébault, P., & Charnoz, S. 2013, A&A, 558, A121

Krist, J. E., Stapelfeldt, K. R., Bryden, G., & Plavchan, P. 2012, AJ, 144, 45

Krivov, A. V. 2010, Research in Astronomy and Astrophysics, 10, 383

Krymolowski, Y. & Mazeh, T. 1999, MNRAS, 304, 720

Lagrange, A.-M., Beust, H., Udry, S., Chauvin, G., & Mayor, M. 2006, A&A, 459, 955

Lagrange, A.-M., Milli, J., Boccaletti, A., et al. 2012, A&A, 546, A38

Larwood, J. D., Nelson, R. P., Papaloizou, J. C. B., & Terquem, C. 1996, MNRAS, 282, 597

Lebreton, J., Augereau, J.-C., Thi, W.-F., et al. 2012, A&A, 539, A17

Lebreton, J., van Lieshout, R., Augereau, J.-C., et al. 2013, A&A, 555, A146

Lenzen, R., Hartung, M., Brandner, W., et al. 2003, in Society of Photo-Optical Instrumentation Engineers (SPIE) Conference Series, Vol. 4841, Society of Photo-Optical Instrumentation Engineers (SPIE) Conference Series, ed. M. Iye & A. F. M. Moorwood, 944–952

Levison, H. F. & Duncan, M. J. 1994, Icarus, 108, 18

Levison, H. F. & Duncan, M. J. 2000, AJ, 120, 2117

Lin, D. N. C., Bodenheimer, P., & Richardson, D. C. 1996, Nature, 380, 606

Löhne, T., Krivov, A. V., & Rodmann, J. 2008, ApJ, 673, 1123

Luhman, K. L., Patten, B. M., Marengo, M., et al. 2007, ApJ, 654, 570

Malhotra, R. 1993, Nature, 365, 819

Malhotra, R. 1995, AJ, 110, 420

Mamajek, E. E. 2012, ApJ, 754, L20

Mardling, R. A. & Lin, D. N. C. 2002, ApJ, 573, 829

Marengo, M., Stapelfeldt, K., Werner, M. W., et al. 2009, ApJ, 700, 1647

Marois, C., Lafrenière, D., Doyon, R., Macintosh, B., & Nadeau, D. 2006, ApJ, 641, 556

Marois, C., Macintosh, B., Barman, T., et al. 2008, Science, 322, 1348

Marois, C., Zuckerman, B., Konopacky, Q. M., Macintosh, B., & Barman, T. 2010, Nature, 468, 1080

Marshall, J. P., Moro-Martín, A., Eiroa, C., et al. 2014, A&A, 565, A15

Masana, E., Jordi, C., & Ribas, I. 2006, A&A, 450, 735

Mason, B. D., Wycoff, G. L., Hartkopf, W. I., Douglass, G. G., & Worley, C. E. 2001, AJ, 122, 3466

Mayor, M., Pepe, F., Queloz, D., et al. 2003, The Messenger, 114, 20

Mayor, M. & Queloz, D. 1995, Nature, 378, 355

Milli, J., Mawet, D., Pinte, C., et al. 2014, ArXiv e-prints

Moran, S. M., Kuchner, M. J., & Holman, M. J. 2004, ApJ, 612, 1163

Morbidelli, A. & Moons, M. 1995, Icarus, 115, 60

Moro-Martín, A. & Malhotra, R. 2002, AJ, 124, 2305

Mouillet, D., Lagrange, A.-M., Beuzit, J.-L., & Renaud, N. 1997a, A&A, 324, 1083

Mouillet, D., Larwood, J. D., Papaloizou, J. C. B., & Lagrange, A. M. 1997b, MNRAS, 292, 896

Murray, C. D. & Dermott, S. F. 1999, Solar system dynamics

Mustill, A. J. & Wyatt, M. C. 2009, MNRAS, 399, 1403

Neuhäuser, R., Mugrauer, M., Fukagawa, M., Torres, G., & Schmidt, T. 2007, A&A, 462, 777

Noyes, R. W., Hartmann, L. W., Baliunas, S. L., Duncan, D. K., & Vaughan, A. H. 1984, ApJ, 279, 763

Payne, M. J., Wyatt, M. C., & Thébault, P. 2009, MNRAS, 400, 1936

Pichardo, B., Sparke, L. S., & Aguilar, L. A. 2005, MNRAS, 359, 521

Pierens, A. & Nelson, R. P. 2007, A&A, 472, 993

Pierens, A. & Nelson, R. P. 2008a, A&A, 478, 939

Pierens, A. & Nelson, R. P. 2008b, A&A, 483, 633

Queloz, D., Mayor, M., Weber, L., et al. 2000, A&A, 354, 99

Quillen, A. C. 2006, MNRAS, 372, L14

Raymond, S. N. & Bonsor, A. 2014, MNRAS, 442, L18

Reche, R., Beust, H., Augereau, J.-C., & Absil, O. 2008, A&A, 480, 551

Reiners, A. & Schmitt, J. H. M. M. 2003, A&A, 398, 647

Rodigas, T. J., Malhotra, R., & Hinz, P. M. 2013, ArXiv e-prints

Roell, T., Neuhäuser, R., Seifahrt, A., & Mugrauer, M. 2012, A&A, 542, A92

Rousset, G., Lacombe, F., Puget, P., et al. 2003, in Society of Photo-Optical Instrumentation Engineers (SPIE) Conference Series, Vol. 4839, Society of Photo-Optical Instrumentation Engineers (SPIE) Conference Series, ed. P. L. Wizinowich & D. Bonaccini, 140–149

Schneider, G., Smith, B. A., Becklin, E. E., et al. 1999, ApJ, 513, L127

Shaya, E. J. & Olling, R. P. 2011, ApJS, 192, 2

Soummer, R., Pueyo, L., & Larkin, J. 2012, ApJ, 755, L28

Stapelfeldt, K. R., Holmes, E. K., Chen, C., et al. 2004, ApJS, 154, 458

Stapelfeldt, K. R., Krist, J. E., Bryden, G. C., & Plavchan, P. 2012, in American Astronomical Society Meeting Abstracts, Vol. 220, American Astronomical Society Meeting Abstracts 220, 506.03

Stark, C. C. & Kuchner, M. J. 2008, ApJ, 686, 637

Tamayo, D. 2014, MNRAS, 438, 3577

Thalmann, C., Janson, M., Buenzli, E., et al. 2011, ApJ, 743, L6

Thébault, P. 2012, A&A, 537, A65

Thébault, P. & Augereau, J.-C. 2007, A&A, 472, 169

Thebault, P. & Haghighipour, N. 2014, ArXiv e-prints

Thebault, P., Kral, Q., & Ertel, S. 2012, A&A, 547, A92

Thébault, P., Marzari, F., & Scholl, H. 2006, Icarus, 183, 193

Torres, C. A. O., Quast, G. R., da Silva, L., et al. 2006, A&A, 460, 695

Trilling, D. E., Bryden, G., Beichman, C. A., et al. 2008, ApJ, 674, 1086

Udry, S. & Santos, N. C. 2007, ARA&A, 45, 397

van Leeuwen, F., ed. 2007a, Astrophysics and Space Science Library, Vol. 350, Hipparcos, the New Reduction of the Raw Data

van Leeuwen, F. 2007b, A&A, 474, 653

Wahhaj, Z., Liu, M. C., Biller, B. A., et al. 2014, ArXiv e-prints

Ward, W. R. 1986, Icarus, 67, 164

Ward, W. R. 1991, in Lunar and Planetary Institute Science Conference Abstracts, Vol. 22, Lunar and Planetary Institute Science Conference Abstracts, 1463

Watson, C. A., Littlefair, S. P., Diamond, C., et al. 2011, MNRAS, 413, L71

Wisdom, J. 1980, AJ, 85, 1122

Wisdom, J. 1983, Icarus, 56, 51

Wisdom, J. & Holman, M. 1991, AJ, 102, 1528

Wisdom, J. & Holman, M. 1992, AJ, 104, 2022

Wolszczan, A. & Frail, D. A. 1992, Nature, 355, 145

Wyatt, M. C. 1999, PhD thesis, Royal Observatory, Blackford Hill, Edinburgh EH9 3HJ, UK

Wyatt, M. C. 2003, ApJ, 598, 1321

Wyatt, M. C. 2004, in American Institute of Physics Conference Series, Vol. 713, The Search for Other Worlds, ed. S. S. Holt & D. Deming, 93–102

Wyatt, M. C. 2005, A&A, 440, 937

Wyatt, M. C. & Dent, W. R. F. 2002, MNRAS, 334, 589

Wyatt, M. C., Dermott, S. F., & Telesco, C. M. 2000, in Astronomical Society of the Pacific Conference Series, Vol. 219, Disks, Planetesimals, and Planets, ed. G. Garzón, C. Eiroa, D. de Winter, & T. J. Mahoney, 289

Wyatt, M. C., Dermott, S. F., Telesco, C. M., et al. 1999, ApJ, 527, 918

Yoshida, H. 1993, Celestial Mechanics and Dynamical Astronomy, 56, 27

Yoshikawa, M. 1989, A&A, 213, 436

Zhou, J.-L., Xie, J.-W., Liu, H.-G., Zhang, H., & Sun, Y.-S. 2012, Research in Astronomy and Astrophysics, 12, 1081

Zucker, S., Mazeh, T., Santos, N. C., Udry, S., & Mayor, M. 2004, A&A, 426, 695

Remerciements

Mes premiers remerciements iront bien entendu à Hervé Beust et Jean-Charles Augereau, mes directeurs de thèse. Leurs grandes qualités humaines et scientifiques si complémentaires en font un véritable duo de choc. Le parcours n'a pas toujours été facile, j'en conviens, et en particulier pour obtenir une bourse à l'École Doctorale. Malgé tout, j'ai toujours pu compter sur leur confiance et leur soutien.

Hervé a dit autrefois de son propre directeur de thèse qu'il aimerait lui avoir apporté autant que ce qu'il avait reçu. Avec la grande humilité qui le caractérise, je me demande s'il a jamais eu l'ambition de susciter le même enthousiasme et le même sentiment de profonde gratitude chez un thésard, mais c'est désormais chose faite.

Les mots me manquent pour décrire le plaisir que j'ai eu à travailler avec eux deux, j'ai tant appris durant ces trois années... La liste des choses pour lesquelles j'aimerai les remercier est bien longue et les bons souvenirs sont nombreux... En particulier, je remercie Hervé pour m'avoir transmis la fièvre des diagrammes de phase et de la complémentarité de l'analytique et du numérique. Quant à Jean-Charles, je le remercie tout particulièrement d'avoir élargi le champ de mon espace collaboratif en me présentant à l'équipe des DUNErS et des EXOZODIerS.

Un grand merci à tous ces derniers pour la richesse et la productivité de nos discussions scientifiques! En particulier, à Carlos Eiroa pour avoir fait partie de mon jury, et aussi surtout pour m'avoir intégrée à l'équipe DUNES. À tous les co-auteurs de mes papiers. À Amy Bonsor, pour avoir propulsé ma méthodologie d'écriture dans la langue de Shakespeare. À Steve Ertel, pour sa contribution à mon proposal ALMA. À Philippe Thébault, pour m'avoir reçue à Meudon pour mettre la touche finale à mon premier papier. À Sasha Krivov, pour m'avoir invitée à Jena et m'avoir donné l'opportunité d'y présenter mes travaux. A Karl Stapelfeldt, pour avoir accepté de rapporter ma thèse et s'être déplacé depuis Washington pour assister à ma soutenance.

Merci également à Alain Lecavelier des Étangs, qui, malgré un planning déjà chargé, a immédiatement accepté de faire partie de mon jury. Un grand merci pour ses questions et interventions très pertinentes. Merci à Sean Raymond pour avoir rapporté ma thèse, et en particulier pour l'intérêt qu'il a montré pour mes travaux sur la migration planétaire.

Merci à Jonathan Ferreira, pour avoir présidé mon jury, mais aussi et surtout pour m'avoir permis d'intégrer le M2 Astro, et de l'effectuer sur deux ans pour pouvoir me permettre de maintenir l'activité professionnelle qui me faisait vivre. Sans lui, je n'aurais pas le plaisir d'écrire ces lignes, et je lui en suis profondément reconnaissante.

Merci aussi à toutes celles et ceux avec qui j'ai eu le plaisir d'interagir à l'IPAG, les chercheurs bien entendu, mais aussi le personnel technique et administratif, ainsi que celles et ceux qui s'investissent au service de calcul intensif, sans lesquels, il faut bien avouer, nous ne ferions pas grand-chose. En particulier un grand merci à Valérie, David, Marie-Hélène, Bruno et Françoise. Merci également aux membres du comité de suivi des thèses, ainsi qu'à l'équipe qui anime les visites scolaires et les soirées d'observations au grand public.

Je pense bien entendu également à toute l'équipe des joyeux thésards et post-doc avec qui j'ai eu le privilège de partager tout ou partie de ces trois années de thèse : Jérémy et Quentin, embarqués tout comme moi dans l'aventure DUNES-EXOZODI, Florian, mon co-bureau, Fabien et Layal, Fabrice, Antoine, Illya, Romane, Julien R., Julien M., et Julien V., Simon, Justine, Vianney, Rémi, Solenn, Thomas, David, Mickaël et Mikhael, Alexandre, Alexis, Nicolas, Ana, Susana... J'espère sincèrement n'omettre personne...

Mes touts derniers remerciements iront bien entendu à ma famille et mes amis, pour leur soutien indéfectible et leur tendre bienveillance. À mes grands-parents, Yvette et François, qui nous ont malheureusement quitté durant cette thèse, à mes parents, Philippe et Marielle, à ma soeur Anaïs et à mon frère Gaëtan. À Kévin, pour avoir partagé ma vie. À Andrea, en particulier pour m'avoir accueillie chez elle ces derniers mois, à Fatima, pour m'avoir motivée à prendre une semaine de vacances plus que nécessaire, à toutes mes copines les Loutres de l'Adelphia et à mes amis chambériens, qui, malgré mon planning chargé et mon manque de disponibilité, n'ont jamais abandonné ni désespéré de me voir leur consacrer un peu de ma vie sociale. Aux élèves à qui j'ai eu le privilège de transmettre un peu de mon savoir et dont j'ai eu le privilège de recevoir de la reconnaissance, ce qui m'a bien souvent remonté le moral, et en particulier à Lucas et Rémi, ainsi qu'à leur maman Sophie, qui sont tous trois venus assister à ma soutenance. A tous ceux-ci, un grand merci, et, je vous aime, tout simplement.

Enfin, des remerciements très spéciaux, que je qualifierais plutôt de "non-remerciements", et qui iront tout droit à l'ancien proviseur du Lycée Demotz de la Salle à Rumilly, qui avait conseillé à ma mère de me garder à la maison pour apprendre le tricot, conseil qu'elle a bien fait de ne pas suivre...

J'espère n'avoir oublié personne, et au cas où, je terminerais en remerciant toutes celles et ceux qui ont, de près ou de loin, contribué à cette thèse et à mon épanouissement durant celle-ci. Merci, tout simplement.

List of Figures

List of Tables